Remote Sensing from Air and Space

R. C. Olsen
Associate Professor of Physics
Naval Postgraduate School

7/9/00 3:11 PM

Apollo 17 - 1972 (AS17-148-22727)

Table of Contents

A LIDAR   **177**

B Milli-meter   **177**

C Other non-traditional forms   **177**

Chapter 1 INTRODUCTION

Remote sensing is a technique for acquiring information, or intelligence, about areas of interest from some distance. As such, this is an important element of modern warfare. In this chapter, some of the basic motivating factors for the understanding of remote sensing will be developed. A brief introduction to some typical remote sensing products will be given, as well, in order to provide perspective for subsequent chapters.

A Order of Battle

The material in these notes is organized according to an ongoing usage of the paradigm provided by "Order of Battle", or OOB. This is largely associated with the counting of "things", but not entirely. Indeed, one thing for which care must be taken - don't limit the levels of information to simple 'counting'. We also need to pay attention to non-literal forms of information. Still, a large fraction of what we want to accomplish can be done by using this structure. Order of Battle has a number of forms, such as Ground Order of Battle (GOB), Air Order of Battle (AOB), etc. Some of the things one might like to know are enumerated according to this pattern:

1) Ground Order of Battle (GOB) - including logistics
2) Air Order of Battle (AOB)
3) Electronic Order of Battle (EOB)
4) Naval Order of Battle (NOB)
5) Industrial Order of Battle (IOB)
6) Cyber Order of Battle (COB)
7) Space Order of Battle (SOB)

What items characterize these OOB types? Taking GOB as an example, one might like to know about:
- Vehicles – numbers, locations, types…
  - e.g. armor (tanks) – operational status (fueled, hot, armed), capabilities, etc.
- Troops – numbers, arrangement, types…
- Defenses – mine fields, geography, missiles, chem/bio, camo, decoys…
- Infrastructure – roads, bridges…

Other examples follow.

1 Air Order of Battle
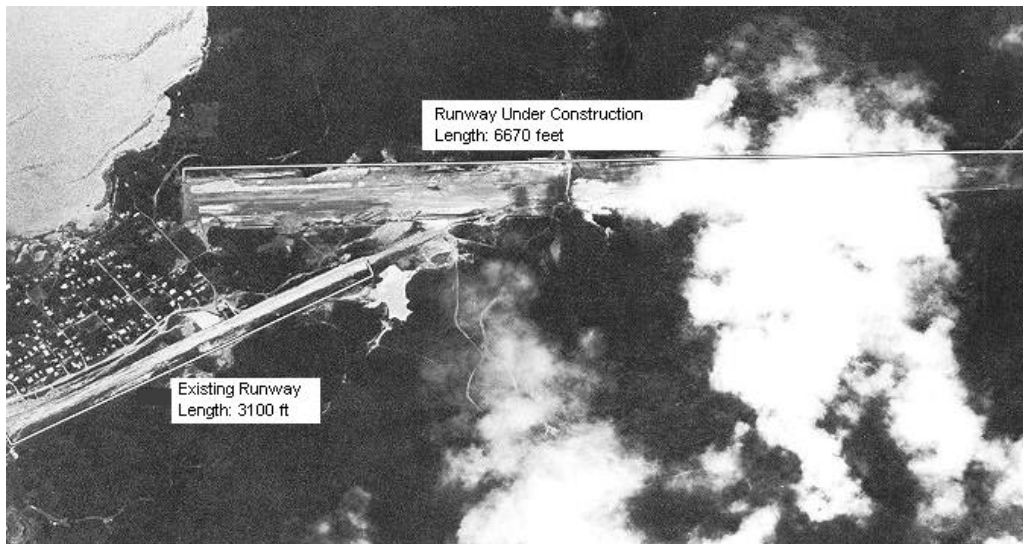
Figure 1-1. SR-71 image, Bluefields, Nicarauga, New runway under construction, 2 January 1982.   http://www.fas.org/irp/imint/nic_13.htm

For AOB, you might want to know about:

- Planes – numbers, kinds, versions, unit IDs, operational status, armament, pilots, locations…
- Airfields – runway length, composition (material- asphalt, dirt, concrete), capacity, locations, bunkers, fuel (capacity, how full)
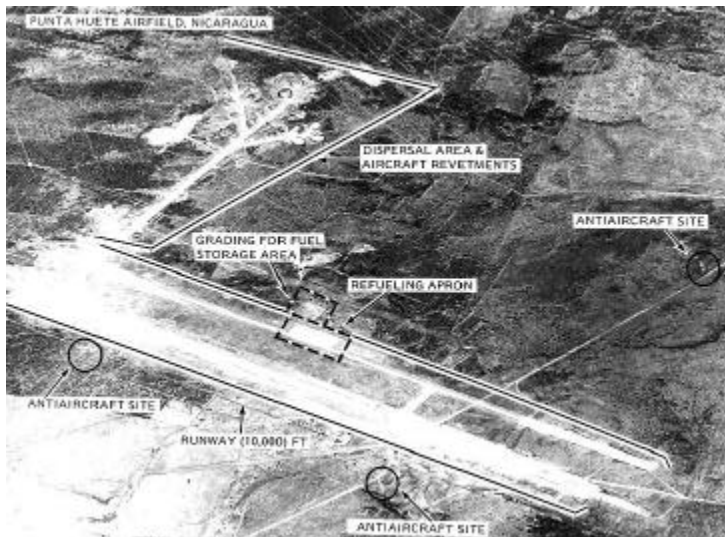
Figure 1-2. SR-71 image, Punta Huete Airfield, Nicarauga.
http://www.fas.org/irp/imint/nic_16.htm

Expanding on the general topics noted above, an ever more detailed list can be developed, as shown in the table here.

Air Order of Battle				
Planes	Type	Fighter	Weapons	Air-to-Air
				Air-to-Ground
			Sensors	FLIR
				Radar
				Visible
				EW
		Bomber		
		Tanker		
		Transport	Civilian	
			Military	
		Trainer		
		EW		
		Reconnaissance		
	Number			
	Locations	Bunkers		
		Runway		
		Aprons		
Runways	Length			
	Composition	(material- asphalt, dirt, concrete)		
	Direction			
	Approach	Terrain		
		Lighting		
		Weather		
		Ground Controllers		
Logistics	Supply Lines/ Lines of Communication			
POL	Fuel Tanks	Capacity		
		Type of Fuel		
		Fill Factor		
Pilots	Number			
	Ranks			
	Training			
	Experience			
Defenses	Weapons	AA guns		
		AA Missiles		
	Radar	Frequency		
		Range		
		Location		
		Type		
	Locations	FOV		

2 Electronic Order of Battle

Figure 1-3. TARPS, (Tactical Airborne Reconnaissance Pod System) Umm al Aysh SATCOM, Federation of American Scientists Image, http://www.fas.org/irp/imint/alaysh.htm

- Defenses – SAM, radars…
  - Radars (technical details, and admittedly more SIGINT than IMINT) – frequencies, PRF, scan type, pulse width, mode-changing…
  - Radars – locations, ranges, operational patterns, networked?, EW requirements…
  - Radar Types - Air search, Surface search, Fire control, Target trackers.
- Communications – nodes, types (HF, µwave, fiber, etc.), commercial vs. military, encryption, interception and denial…
- Power – dams, power grid…

Figure 1-4. KH4 Corona image - Sary Shagan Operational Hen House Radar, http://www.fas.org/irp/imint/4_hen5.htm

3 Space Order of Battle

For SOB, you might want to know about two classes of things:
1) On the ground: launchers (boosters), pad or infrastructure, communications ground sites, and payloads
2) In space: communications (relays), payloads, orbital elements, constellations
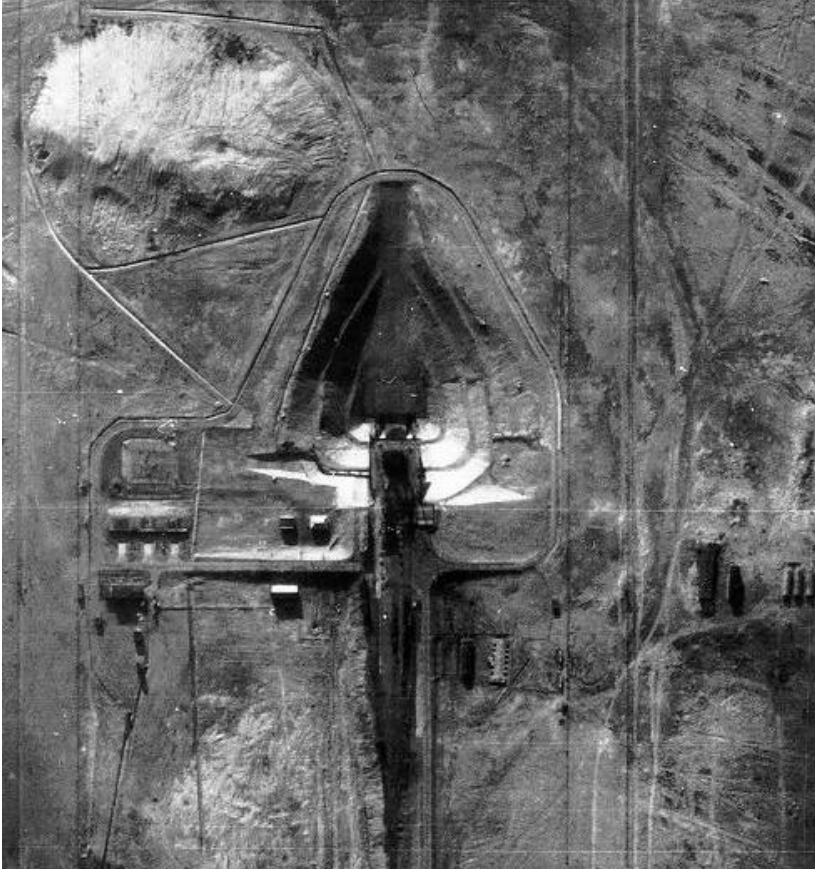
Figure 1-5. U2 image of SS-6 / Sputnik Launch Pad, Baikonur
http://www.fas.org/irp/imint/u-2_tt.htm

4 Naval Order of Battle

Figure 1-6. U-2 image of Soviet submarine pens,
http://www.fas.org/irp/imint/u-2_sub.htm
Sayda Guba, or Olenya Guba?

B Happy Snaps

In order to begin our study, we take an introductory look at images (often historical), which illustrate the range of data types found in the remote sensing community, and indicate how what we learn from remote sensing varies with spatial resolution and wavelength. We begin with whole earth visible imagery. The cover plate image from Apollo 17 is an early illustration. In sequence, below, we progress from resolution of 1 km to better than 1 meter. Following this will be a look at infrared and radar.

1 Visible

a GOES - whole earth

GOES 9 - visible image, 9 June 1995, 1815 UTC. The GOES 9 visible imager acquires an image once every 15 minutes at a spatial resolution of 1 km. The familiar nightly weather news will frequently be illustrated by images from one of the GOES satellites.
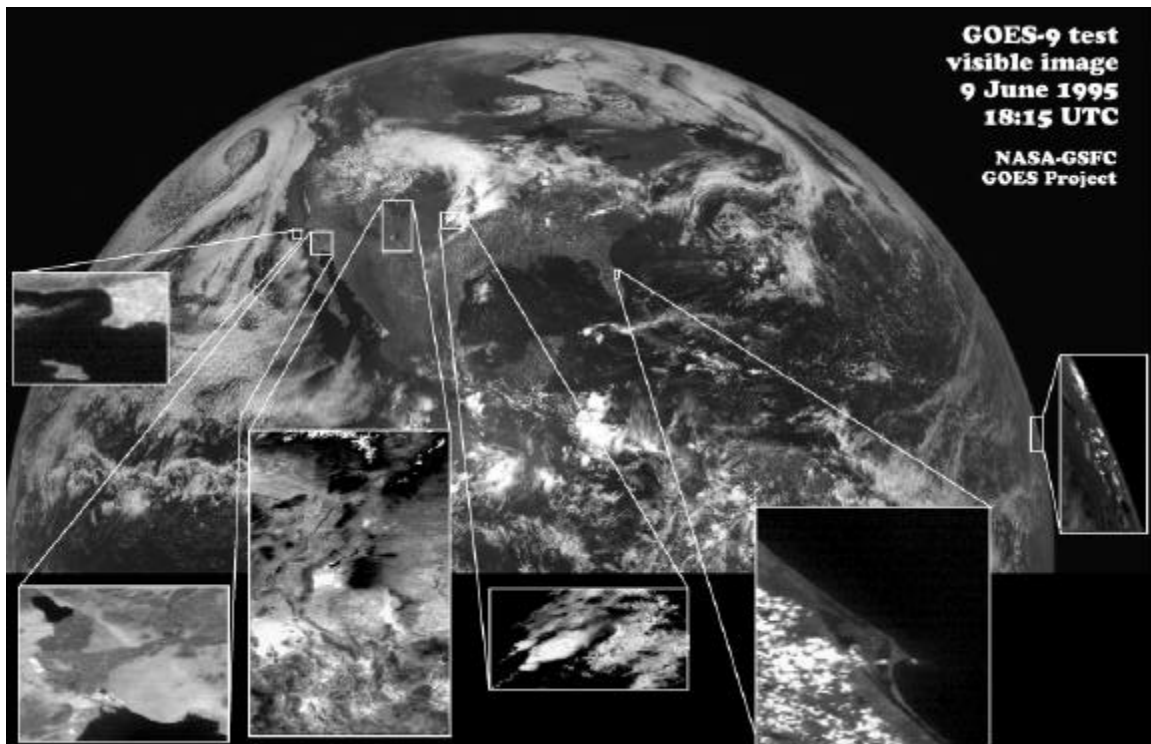
Figure 1-7 GOES-9 visible image, 9 June 1995, 18:15 UTC.

What value do such data have for the military? Clouds are a major element in modern warfare, directly affecting the ability of pilots and autonomous weapons to locate their targets. From the perspective of the sequence of images that begin here, this image also illustrates the beginning of an important set of trades between spatial resolution, frequency of coverage, and area of coverage. High altitude satellites, such as the geosynchronous weather satellites, provide large area coverage, more or less continuously. As noted above, the scanners produce an image every 15-30 minutes, at a spatial resolution of 1 km.

b DMSP (0.5 km), Earth at Night Landsat 5

A military variant on the more commonly seen weather satellites is given by DMSP. A low light capability gives DMSP the additional ability to see city lights, large fires (oil wells, forest fires), and the northern lights (aurora borealis). Such images provide some less-obvious value - for example, as indications of industrial capability. The image here is at a spatial resolution of 2.6 km. The imager is designed to see clouds at night (via moonshine), and the city lights saturate the photo-multiplier tube detectors (photon counters).

East Coast US at Night
NGDC DMSP Data Archive
01 February 1994
OLS-Smooth, Visible Band
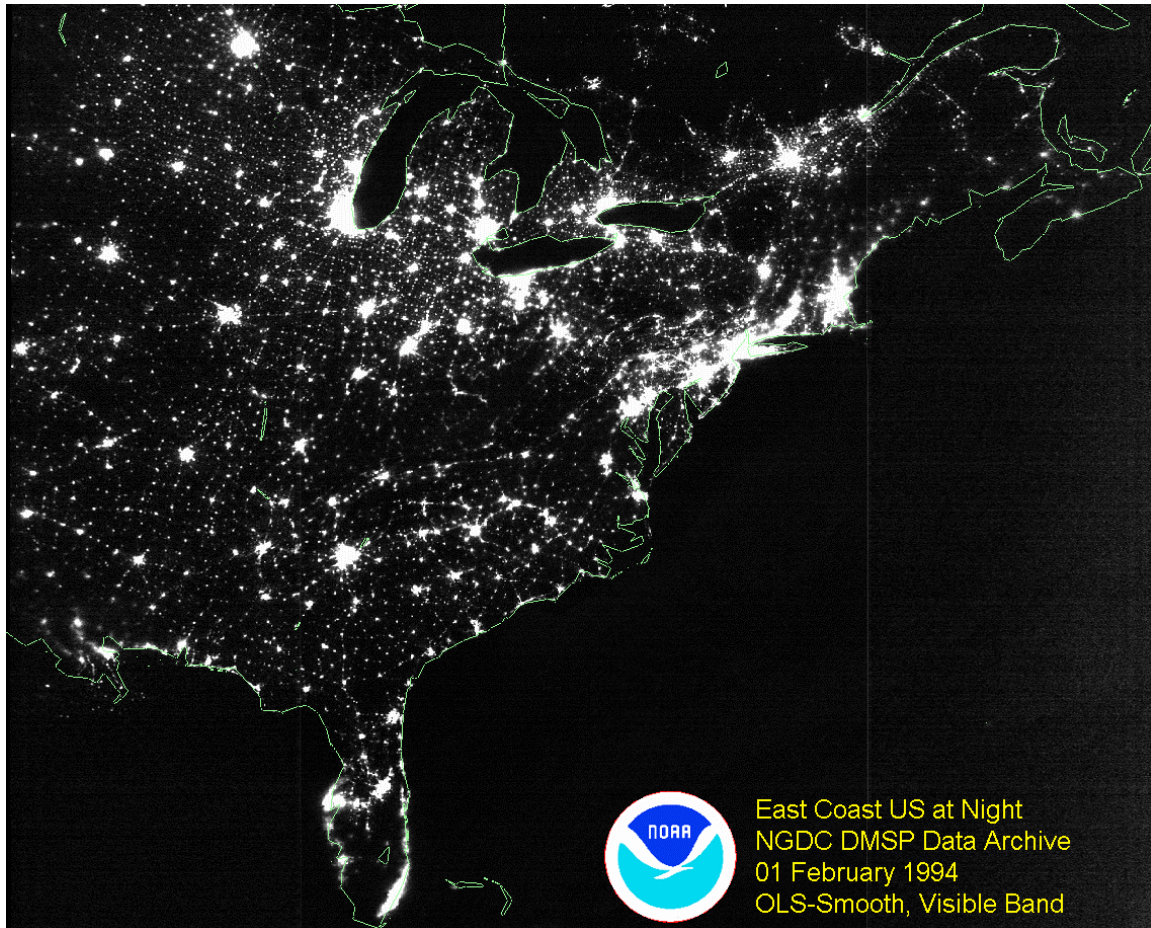
Figure 1-8. DMSP image of the East Coast at night.

By contrast with GOES, the DMSP imager only visits a given geographic region a few times a day. Orbiting at an altitude of 800 km or so, the daylight visible imager can take data at 1 km resolution. It provides coverage at high latitudes which cannot be obtained from the geosynchronous systems.

c UoSAT (100m)- San Francisco 18:59:15 29 August 1998

As the spatial resolution is increased, different sorts of features become more obvious. This image was taken by TMSAT, owned and operated by the Thai Microsatellite Company (TMSC), Bangkok, Thailand. TMSAT was designed and built by Surrey Satellite Technology Limited (SSTL) (http://www.sstl.co.uk/) a spin off from the University of Surrey, and the Surrey Space Centre. (http://www.ee.surrey.ac.uk/)

The TMSat microsatellite captured the image shown here on 29 August 1998 at 18:54:15 UTC (38.3°N 122.6°W) when over the cities of Oakland and San Francisco in California. This multispectral image was produced by combining the data from the three Narrow Angle Cameras, sensing in the green, red and near-IR spectra. Each image has 1020 x 1020 pixels, covering an area of 100 x 100 km at a mean ground resolution of 98 meters/pixel.

This imagery is a remarkable testimony to the possibilities inherent in small satellites.

Figure 1-9. TMSat image of San Francisco Bay.

Various man-made features are discernable. The Bay Bridge connecting San Francisco and Oakland is visible, but the Golden Gate Bridge is shrouded in sea mist. The runways at San Francisco and Oakland Airports stand out as long straight lines on the shores of the Bay. The variety of wavelengths gives additional information.

Red areas indicate healthy vegetation (due to the strong near-IR reflectance of chlorophyll), mainly forests on the Santa Cruz and Diablo mountains. Urban areas are generally blue-gray. To the right of the image, the intense agriculture of the Sacramento and San Joaquin valley is visible in the patchwork of fields. The different colors of these fields provides an indication of the state of vegetation (bare soil, marsh, young or mature vegetation, etc).

d Landsat 5 (30m)- San Diego - 7 May 1996 full scene and subset at full resolution

Multiple wavelength images (or multi-spectral) are most commonly applied to earth resources. Landsat provides higher spatial and spectral resolution than the previous example. Landsat has been the premiere earth resources satellite for two decades, providing 30-meter resolution imagery in 7 spectral bands. Imagery shown here has been taken from the three visible wavelength sensors, and combined to make a 'true' color image. The top frame is one complete Landsat scene. A small segment showing San Diego harbor has been extracted to illustrate the highest resolution of the TM sensor.

Figure 1-10 a

LANDSAT 5 - 7 May 1996

Figure 1-10 b
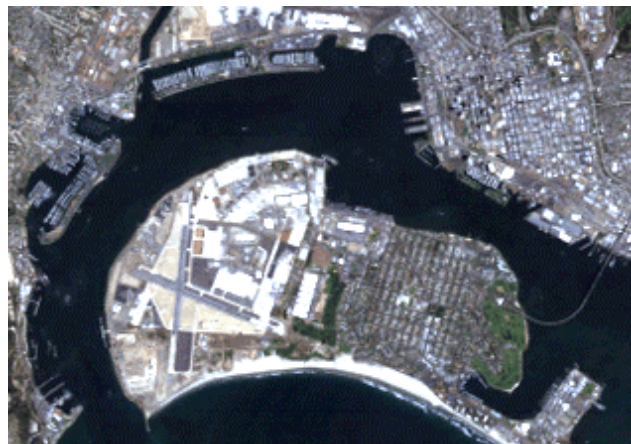
The penalty paid for this high spatial resolution is a relatively reduced field of view – nominally 100 km across in any given image. The low-altitude, polar orbiting satellite revisits each such region only once every 16 days.

e Shuttle 'handheld'

Just for comparison, the handheld Hasselblad camera on the space shuttle has produced a variety of noteworthy images over the years, such as this image of Egypt and Saudi Arabia. Spatial resolution is comparable to that of Landsat.

Figure 1-11. Eastern Egypt, the Red Sea, and Saudi Arabia, 4/29/90
NASA Photo ID: STS031-79-01, Film Type: 70mm.

Eastern Egypt, the Red Sea and Saudi Arabia can all be seen in this single view of the Near East (26.5N, 36.5E) from 330 nautical mile orbit. Easily seen from this vantage point is eastern Egypt, the Nile River, Lake Nassar, the Red Sea and almost half of Saudi Arabia.

http://images.jsc.nasa.gov/images/pao/STS31/10063614.htm

Resolution varies with the lenses used. The 'standard' telephoto, a 250 mm optic, gives resolution similar to that of Landsat, as illustrated on the left below.

Figure 1-12. a) STS064-080-021 (STS064 launch September 9, 1994),

b) Landsat (subset of image shown in Figure 1-10)

f Spot (10 m)

For many years, the highest resolution commercial imagery available was from the French SPOT satellite. Featuring resolution with 10-meter resolution, SPOT data have often been combined with LANDSAT data in order to provide a sharper image. Here an image of San Diego County is shown to illustrate a full frame of data, and a chip is shown of the harbor area and downtown San Diego.

Figure 1-13a.

Figure 1-13b. San Diego Harbor, SPOT image.

Notice the implicit conflict that emerges here between coverage and spatial resolution, along with the total data volume associated with the image. Higher spatial resolution implies more pixels, and hence more bits.

g IRS - 5 meter resolution

The Indian Remote Sensing Satellite, IRS-1C, launched in December 1995, has provided some of the highest resolution unclassified images to date. The inset to figure 1-8 is the entire 'scene' - note the substantially reduced area of coverage compared to a Landsat scene as shown in figure 1-10a.

IRS-1C - 23 March 1996 - San Diego, CA

Figure 1-14. San Diego Harbor, IRS image.

Relate these scenes of San Diego Harbor to AOB and NOB. What can you see (and not see) at 5-10 meter resolution? Can you see ships at the piers? If you can, do you need to resolve them to identify them? What can you tell about San Diego airport? Coronado Naval Air Station? Lines of Communication?

h IKONOS - San Diego/Coronado Island

The recent launch of the IKONOS satellite has dramatically changed the stakes in the resolution fight. IKONOS offers 1-meter spatial resolution panchromatic imagery, and 4-meter resolution multi-spectral (color) imagery. Shown here is a color image of San Diego, California, taken on November 17, 1999.

Figure 1-15. Coronado Island, San Diego, California. Space Imaging, Inc.

i High resolution airborne - F-16, Recon-Optical

Still higher resolution is possible, primarily from airborne platforms. In the last few years, electronic cameras have been able to provide high resolution imagery, which historically was the domain of film.

RCI	CA-260/4 Imagery	
SENSOR		KS-87 E_O
LENS		12-inch fl
ALTITUDE		4,500 ft
SLANT RANGE		9,585 ft
SPEED		350 kn
LOCAL TIME		1330
PLATFORM		ANG F-16

Figure 1-16. Recon-optical air photo

2 Infrared (IR)

Infrared imagery offers several differences with respect to visible imager. Two big ones:
a) Thermal IR works at night, and
b) Mid-wave infrared (MWIR) and Long-wave infrared (LWIR) data allow for non-literal information - meaning temperature, and associated interesting things like thermal inertia.

a GOES 9 - whole earth, 11 July 1995, 1800 UTC

Wavelength bands: 3.9, 11, and 12 microns encoded as red, green blue. Note that per the usual convention with the weather satellites, the 'gray' scales have been inverted - colder is brighter, dark is hotter. This is so the cold clouds will appear white.
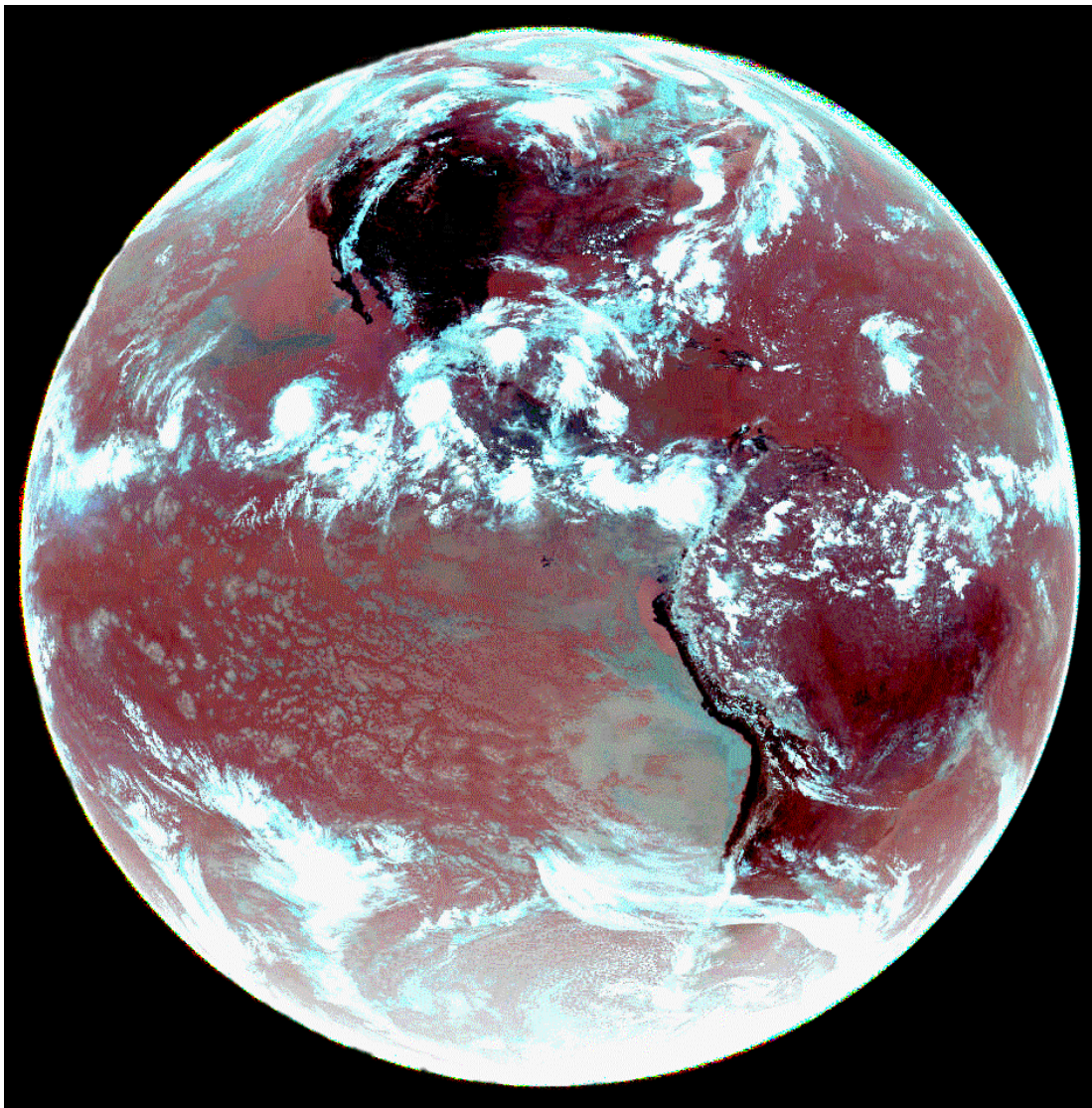
Figure 1-17. GOES infrared imagery. The different cloud colors tell you something about their height and water content.

b Landsat - IR San Diego - 7 May 1996 (bands 6, 5 and 7)

Reflective infrared and thermal infrared data from LANDSAT 5 (the same scene shown above in Figure 1-10) are shown encoded as an RGB triple in Figure 1-18. Note how the hot asphalt and city features are bright in the red (thermal), while the park (grass) areas are green (cool, and highly reflective in short-wave IR)

Figure 1-18. Landsat image - Infrared wavelengths. (Red: 11 micron, Green: 1.65 micron, Blue: 2.2 micron)

c DMSP - IR and Microwave

Thermal radiation extends beyond the traditional region defined by SWIR, MWIR, and LWIR. Indeed, the thermal emission from blackbodies extends out to microwave wavelengths.

INFRARED IMAGE FROM DMSP SATELLITE F-10

SIMULTANEOUS VISIBLE IMAGE

SIMULTANEOUS MICROWAVE IMAGE AT 85 GHz

"Blizzard of 93" March 13, 1993

The distribution of clouds are displayed in the infrared image (top left) recorded by Defense Meteorological Satellite Program (DMSP) F-10 Satellite around 10:30 PM. The visible image (top right), recorded at the same time, showed city lights, oil and gas flares and cloud top lightning associated with thunderstorms across the Gulf of Mexico. The simultaneous microwave image (bottom left) monitors the amount of liquid water within an atmospheric column along a conical scan that is half the width of the other two images. (Graphics courtesy of S.Goodman-NASA/MSFC, K. Knowles-NSIDC, R. Ferraro-NOAA/ORA)

NOAA/NGDC
DMSP Digital Archive
325 Broadway (E/GC2), Boulder, CO 80303
Phone: 303-497-6126; FAX: 303-497-6513
Email: dmsp@mail.ngdc.noaa.gov

Figure 1-19 - DMSP: Visible, infrared, and microwave wavelengths. Microwave wavelengths are also emitted by 'thermal' or 'blackbody' radiators. Here, the 85 GHz band (0.3 cm) gives additional information on atmospheric water content.

3 Radar (SAR)

There are two civilian radar systems in current operation, the Canadian Radarsat, and the European ERS-2. NASA has flown the Shuttle Imaging Radar C mission twice (and now a third time as the Topographic Mapping Mission). The Japanese had a successful radar mission named JERS.

a RADARSAT - Maui - and the airport

Canada launched RADARSAT on November 4, 1995. The spacecraft is equipped with a C-Band (5.6cm), HH polarization, Synthetic Aperture Radar (SAR) capable of acquiring high-resolution (25m nominal - 8-100 m depending on the mode) imagery, with a swath width in the 50 - 500 km range.

a)

b)
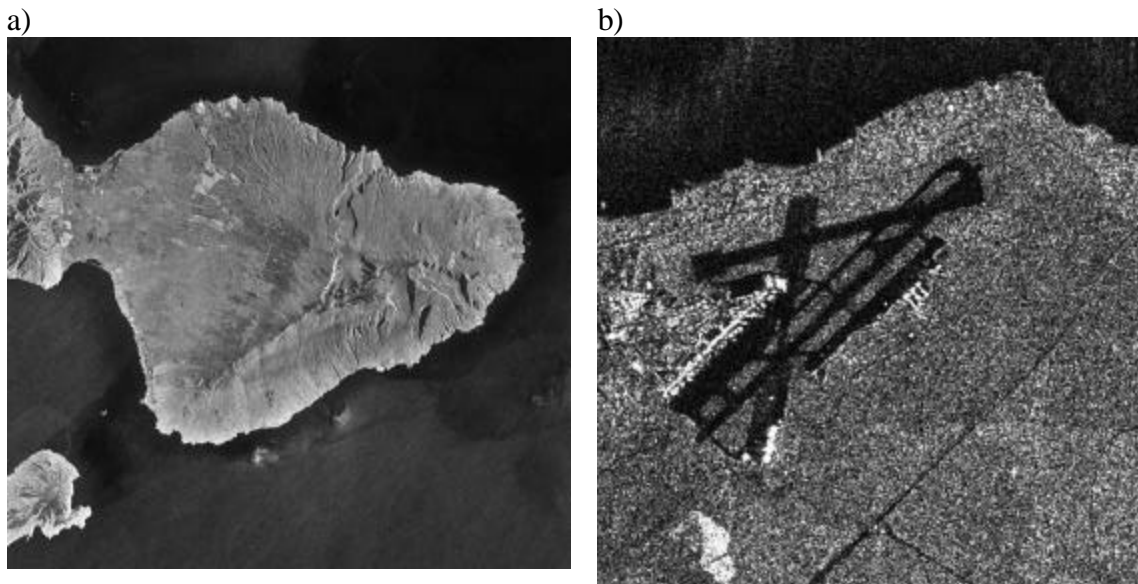
Figure 1-20. RADARSAT image of Maui, Hawaii

The SAR data 'look' substantially different at high resolution, which bothers some people. Note that the airfield on Maui is very dark, because the runway surfaces are very smooth compared to the wavelength of the radar - the radar energy bounces away from the satellite, and is not returned. Note the variations in grey level in the water in the left hand image. Differing wind-speeds on the surface cause variations in the scattering coefficient of the water.

b SIRC - Multi-wavelength/polarization
Maui

By comparison, the Shuttle Imaging Radar - C mission carried multi-wavelength, multi-polarization capabilities. A scene similar to the one above from RADARSAT is shown here, for Maui, Hawaii. Resolution is similar to that of RADARSAT.
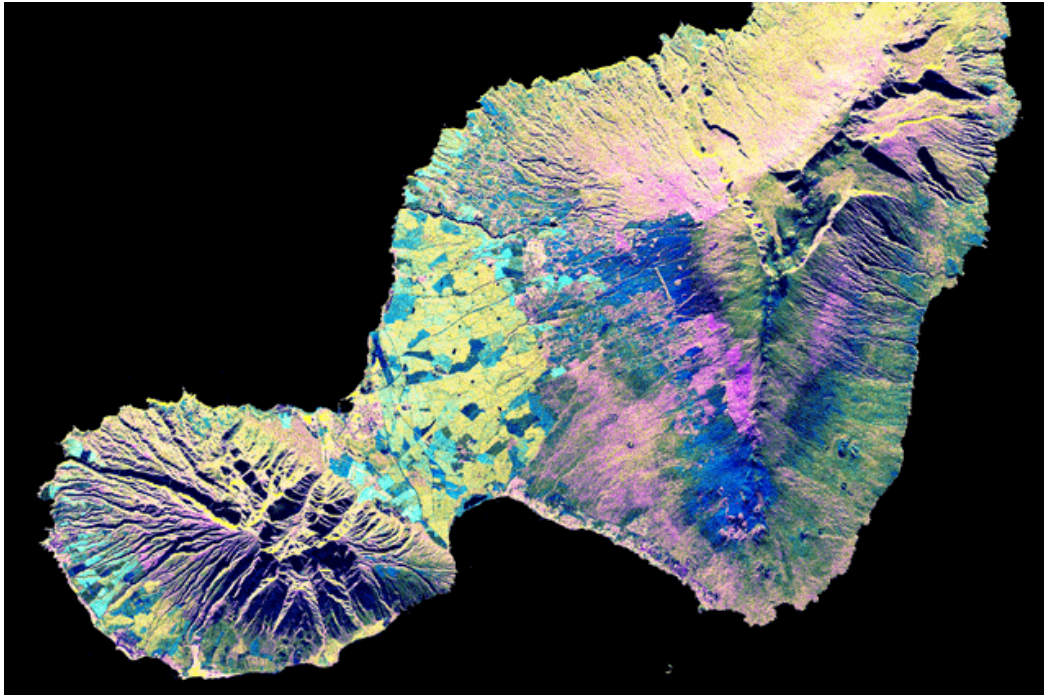
Figure 1-21. SIR-C image of Maui. This image was acquired by Spaceborne Imaging Radar-C/X-Band Synthetic Aperture Radar (SIR-C/X-SAR) onboard the space shuttle Endeavor on April 16, 1994. The image is 73.7 kilometers by 48.7 kilometers (45.7 miles by 30.2 miles) and is centered at 20.8 degrees North latitude, 156.4 degrees West longitude. North is toward the upper left. The colors are assigned to different radar frequencies and polarizations of the radar as follows:
red is L-band, horizontally transmitted and received;
green is C-band, horizontally transmitted and received; and
blue is the difference of the C-band and L-band channels.
http://www.jpl.nasa.gov/radar/sircxsar/maui.html)

Figure 1-20 shows the "Valley Island" of Maui, Hawaii. The cloud-penetrating capabilities of radar provide a rare view of many parts of the island, since the higher elevations are frequently shrouded in clouds. The light blue and yellow areas in the lowlands near the center are sugar cane fields. The three major population centers, Lahaina on the left at the western tip of island, Wailuku left of center, and Kihei in the lower center appear as small yellow, white or purple mottled areas.

West Maui volcano, in the lower left, is 1800 meters high (5900 feet) and is considered extinct. The entire eastern half of the island consists of East Maui volcano, which rises to an elevation of 3200 meters (10,500 feet) and features a spectacular crater called Haleakala at its summit. Haleakala Crater was produced by erosion during previous ice ages rather than by volcanic activity, although relatively recent small eruptions have produced the numerous volcanic cones and lava flows that can be seen on the floor of the crater. The most recent eruption took place near the coast at the southwestern end of East Maui volcano in the late 1700s. The multi-wavelength capability of the SIR-C radar also permits differences in the vegetation cover on the middle flanks of East Maui to be identified. Rain forests appear in yellow, while grassland is shown in dark green, pink and blue.

SIRC - San Diego Harbor

This radar image shows the city of San Diego, California and surrounding areas. San Diego Bay is in the bottom left of the image and is separated from Mission Bay by the Point Loma Peninsula. North Island, home of the U.S. Naval Air Station and Silver Strand are on the left side of San Diego Bay. This image was acquired on October 3, 1994 by the Spaceborne Imaging Radar-C/X-Band Synthetic Aperture Radar (SIR-C/X-SAR) onboard the space shuttle Endeavour.
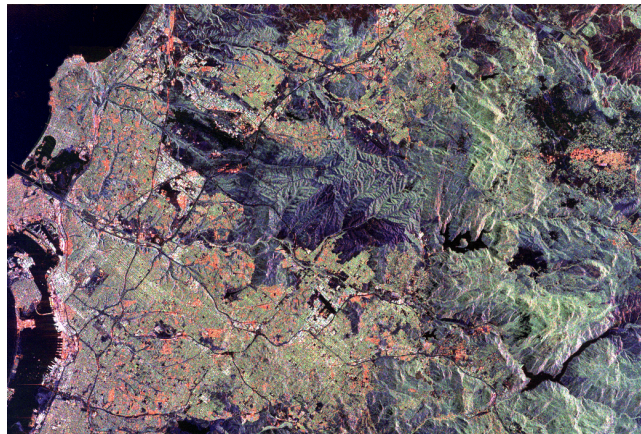
Figure 1-22a. Image P48773

R: L-HH
G: L-HV
B: C-HV

Image rotated 45°
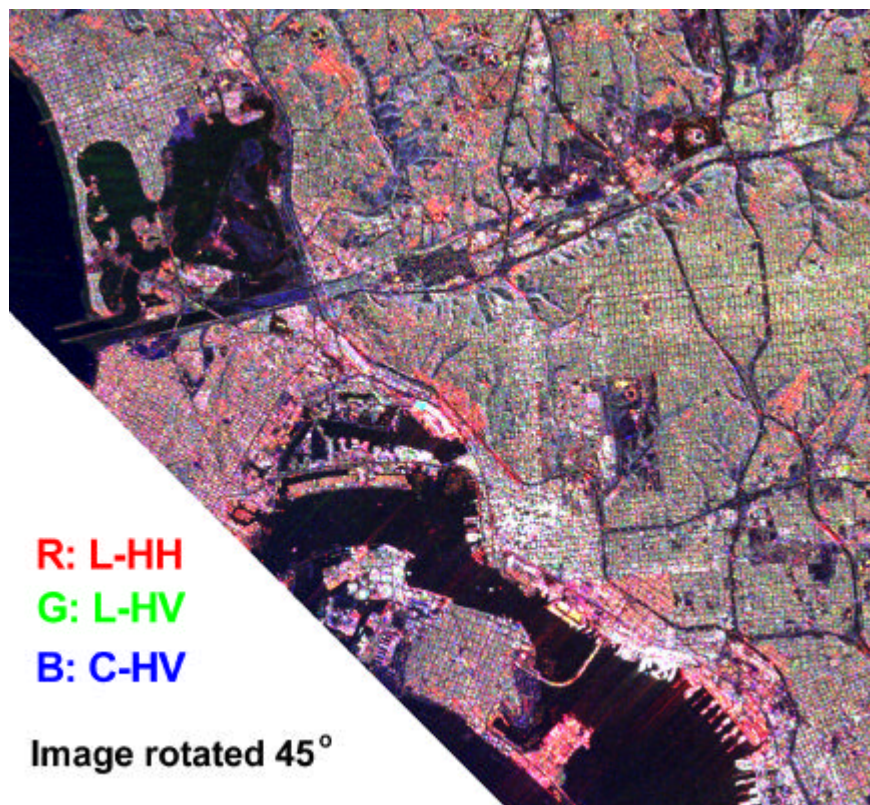
Figure 1-22b. San Diego image from the Shuttle Imaging Radar, L-band and C-band data. Subset of image P48773.

C Three Axes

One of the themes we will see as we progress is that there are three dimensions associated with remote sensing imagery - spatial, spectral, and temporal. These are in general somewhat mutually exclusive. One can have high spatial resolution, but only at low temporal coverage (like Landsat - decent pictures, but only once every 15 days or so). You can have high temporal coverage (like GOES, once every 30 minutes), but then your spatial resolution is only 1 kilometer. If you want spectral coverage (multi-spectral or hyperspectral), you will pay a penalty in the other dimensions.

Similarly, there is a conflict between resolution and field of view - image a larger area, and in general you will have lower spatial resolution.

Spatial Resolution

SPOT

Landsat

Hyperspectral

Spectral

Geosynchronous Weather

Missile Warning

Temporal
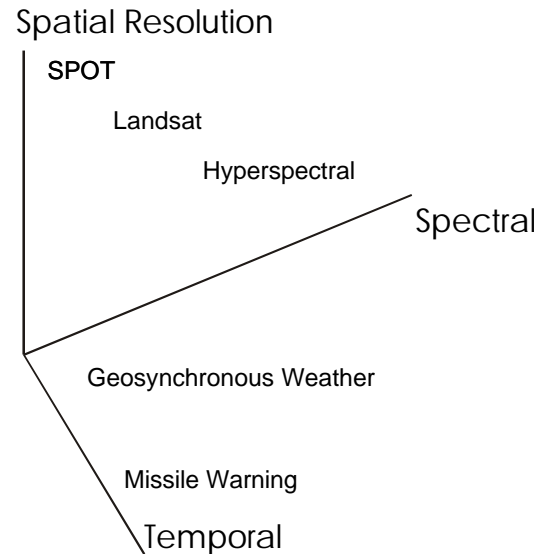
Figure 1.23

D Problems

1) List 10 elements of information that could be determined for NOB from imagery.

2) What wavelengths of EM radiation are utilized in the images shown in this chapter? (This is really a review question, best answered after completing chapter 2).

3) Construct a table/graph showing the relationship between ground resolution and area of coverage for the sensors shown in this chapter. (Also a review question, really.)

4) Compare the various images of San Diego Harbor. What are the differences in information content for the high-resolution panchromatic systems (SPOT, IRS-1C), the multispectral system (LANDSAT, visible and infrared), and the radar system. Which is best for lines of communication? Terrain categorization? Air order of battle? NOB?

Chapter 2 ELECTROMAGNETIC BASICS

A The Electromagnetic Spectrum - EM Wave theory

An understanding of the electromagnetic spectrum, and electromagnetic (EM) radiation is the first essential item we must address. Light, radar waves, radio waves, and all the rest are at their core, electromagnetic radiation. We briefly describe the underlying physical equations, and the nature of the wave equation that results from them.

The fundamental principles that define electricity and magnetism were codified by Maxwell in the late 1800's in four equations that bear his name:

1) $\oiint \vec{\mathbf{E}} \bullet d\vec{\mathbf{S}} = \dfrac{Q}{e_o}$ or $\nabla \bullet \vec{\mathbf{E}} = \dfrac{r}{e_o}$ (Eqn. 2.1 a)

2) $\oiint \vec{\mathbf{B}} \bullet d\vec{\mathbf{S}} = 0$ or $\nabla \bullet \vec{\mathbf{B}} = 0$ (Eqn. 2.1 b)

3) $\oint \vec{\mathbf{E}} \bullet d\vec{\mathbf{l}} = -\dfrac{\partial}{\partial t} \iint \vec{\mathbf{B}} \bullet d\vec{\mathbf{S}}$ or $\nabla \times \vec{\mathbf{E}} = -\dfrac{\partial \vec{\mathbf{B}}}{\partial t}$ (Eqn. 2.1 c)

4) $\oint \vec{\mathbf{B}} \bullet d\vec{\mathbf{l}} = m_o \, \mathbf{i} + m_o \, e_o \dfrac{\partial}{\partial t} \iint \vec{\mathbf{E}} \bullet d\vec{\mathbf{S}}$ or   (Eqn. 2.1 d)

$\nabla \times \underline{\mathbf{B}} = m_o \, \mathbf{J} + m_o \, e_o \dfrac{\partial \vec{\mathbf{E}}}{\partial t}$

These four equations respectively say:
1) that the electric flux through a "Gaussian" surface is equal to the charge contained inside the surface;
2) that in the absence of a magnetic point charge (we don't know of any), the magnetic flux through a Gaussian surface is equal to zero;
3) That the voltage induced in a wire loop is defined by the rate of change of the magnetic flux through that loop (the equation that defines electrical generators); and
4) That a magnetic field is generated by a current (typically in a wire), but also by a time varying electric field.

These equations can be manipulated in differential form to produce a new differential equation, the wave equation:

$$\nabla^2 \vec{\mathbf{E}} - e_o m_o \, \dfrac{\partial^2 \vec{\mathbf{E}}}{\partial t^2} = 0 \quad \text{and} \quad \nabla^2 \vec{\mathbf{B}} - e_o m_o \, \dfrac{\partial^2 \vec{\mathbf{B}}}{\partial t^2} = 0 \qquad \text{(Eqn. 2.2)}$$

Maxwell understood that the solutions to these equations were defined by oscillating electric and magnetic fields ($\vec{\mathbf{E}}$ and $\vec{\mathbf{B}}$). In particular, these equations immediately give the speed of light: $c = \dfrac{1}{\sqrt{e_o m_o}}$. The complexity of the solutions vary, but there are some fairly simple ones involving plane waves, propagating in a straight line. Like all wave phenomena, the solution involves the wavelength, frequency, and velocity of the radiation. In equation form, a typical solution looks like this:

$$\vec{\mathbf{E}}(z,t) = E\hat{\mathbf{x}}\,\cos 2\boldsymbol{p}\left(\frac{z}{\boldsymbol{l}} - f\,t\right) \quad \text{or} \quad \vec{\mathbf{E}}(z,t) = E\hat{\mathbf{x}}\,\cos(kz - \boldsymbol{w}t) \quad \text{(Eqn. 2.3)}$$

which is the equation for a wave propagating in the plus $\hat{\mathbf{z}}$ direction, with an electric field polarized in the $\hat{\mathbf{x}}$ direction. (More on polarization below.)

The various terms in this equation are defined as follows:

E	= Amplitude of the electric field
$\boldsymbol{l}$	= Wavelength (in meters)
k	= Wavenumber (meters^{-1})
f	= Frequency in Hz (cycles/sec)
ω	= Angular Frequency (radians/sec)
c	= Phase velocity of the wave (in m/sec)

Figure 2-1. Four cycles of a wave are shown, with wavelength λ, or period τ. The wave has an amplitude, A, equal to 3.
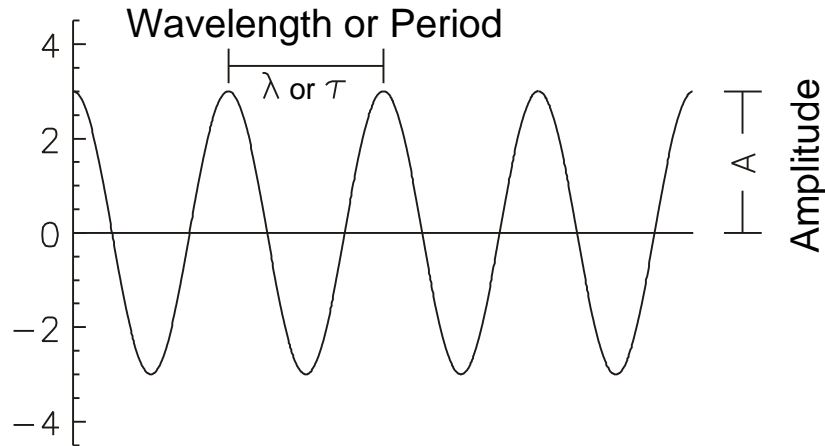
The solution depends upon the wavelength and frequency, which are related by:

$$\boldsymbol{l}\,f \;=\; c \qquad\qquad\qquad\qquad \text{(Eqn. 2.4)}$$

Note that the period, τ, is the inverse of the frequency, since for a wave it must be true that: $f \cdot \tau = 2\pi$. One can also define the angular frequency: $\boldsymbol{w} = 2\boldsymbol{p}\,f$, and the wavenumber: $k = 2\boldsymbol{p}/\boldsymbol{l}$.

For vacuum the value of c = 2.998 x 10⁸ (m/s), an important constant of physics. The range of wavelengths, which will be of interest to us, covers a very large range of about 20 orders of magnitude. This range is illustrated in Figure 2-2.

This construct was the initial one for light and other forms of EM radiation, but at the turn of the 20$^{\text{th}}$ century, it became obvious that a different perspective was needed to explain some of the interactions of light and matter - in particular processes such as the photo-electric effect (and similar processes which are important for the detection of light). This led to a resurgence of the idea that light, or electromagnetic radiation, might better be thought of as a particle, dubbed the photon. The energy of an individual photon is given by

$$E = hf \quad \text{(Joules or eV)} \qquad \text{(Eqn. 2.5)}$$

where   f = frequency of the EM wave (in Hz) and

$$h = \text{Planck's Constant} = \begin{cases} 6.626 \times 10^{-34} \text{ Joule - seconds} \\ 4.136 \times 10^{-15} \text{ eV - seconds} \end{cases}$$

The electron-volt (eV) is a convenient unit of energy and is related to the usual unit (Joule) by:
1 eV = 1.602 x 10^{-19} Joules

The photon energy, E, is determined by the frequency of the electromagnetic radiation. The higher the frequency, the higher the energy. Photons move at the speed of light, as expected for electromagnetic radiation. They have zero rest mass, however, so the rules of special relativity are not violated.
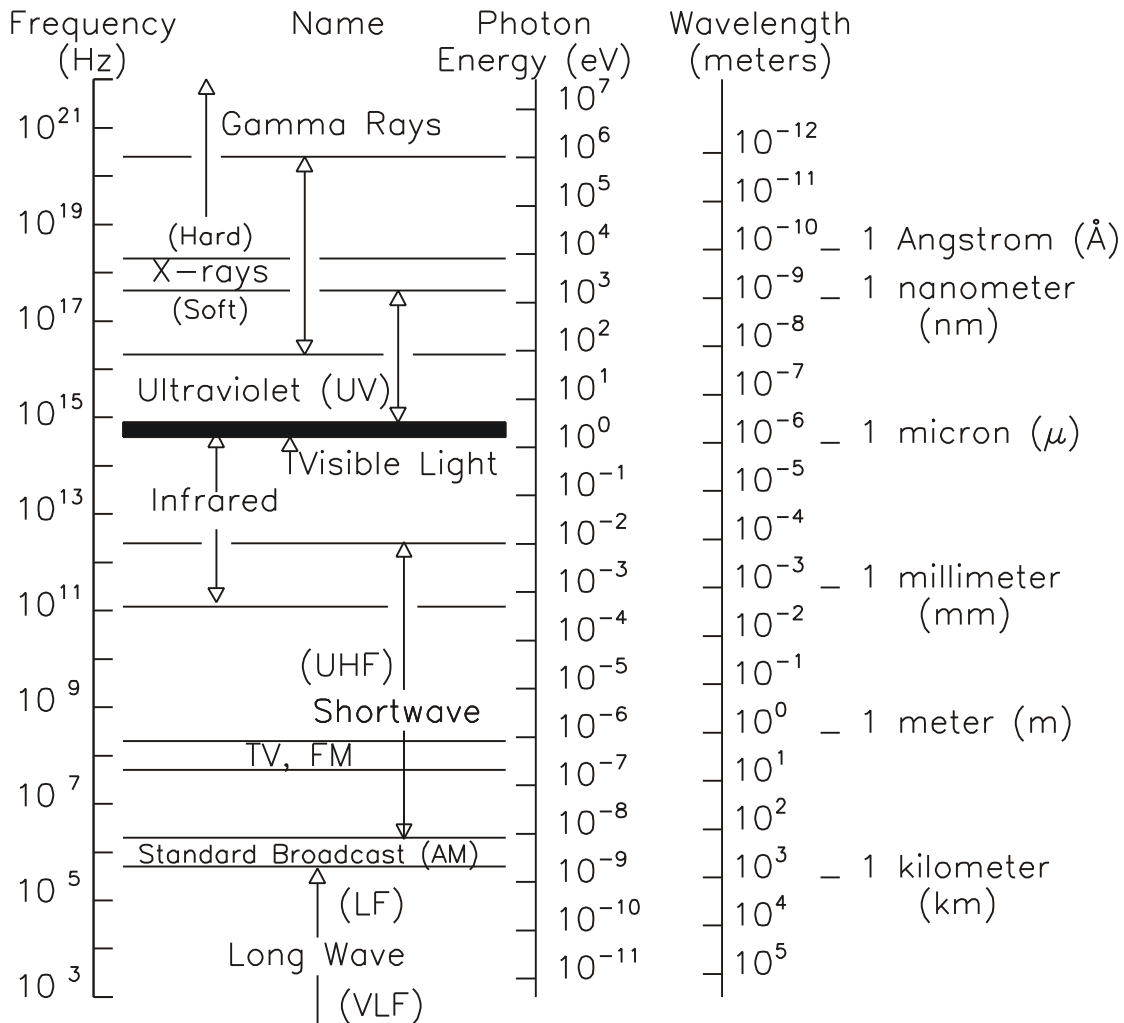
Figure 2.2 The spectrum of electromagnetic radiation.

Example:

The energy of the photons making up an electromagnetic wave (light wave) in the visible part of the spectrum (green color) is

$$E = hf = (4.14 \times 10^{-15})(6 \times 10^{+14}) = 2.48 \text{ eV}$$

which is on the order of (or slightly less than) typical atomic binding energies.

Energies of typical x-ray photons are in the 10^4 to 10^5 eV range, while the photons of a 100 MHz radio signal are only about 4×10^{-7} eV.

This business of energy in photons shows up as being very important for detector technology.   One illustration of this is in the photoelectric effect.   This is the one for which Albert Einstein won the Nobel Prize.   The process that can be observed is illustrated here.   If you shine light on a metal surface in a vacuum, electrons are liberated from the surface, and can be collected on a second surface, here, the collector plate.   This process results in a flow of current that depends on the intensity of the light.

The energy of the electrons can be measured by applying a back bias (a negative voltage) to the collector plate, repelling the electrons.   Voltages of a volt or so are typically sufficient to zero out the current.   Traditional wave theory predicts that the amplitude of the current would vary with the amplitude of the light, which it does, but does not provide a way to explain an observed dependence on the wavelength (frequency) of the light. The higher the frequency of the light (the bluer the light), the more energy the electrons have.   Einstein combined the above concept, E = hf, with the idea of a "work function", a fixed amount of energy necessary to liberate electrons from a metal surface - typically a volt or 2.   In short, the light must possess enough energy to overcome the work function. If the wavelength is too large (the frequency too low), then no electrons are emitted from the surface.
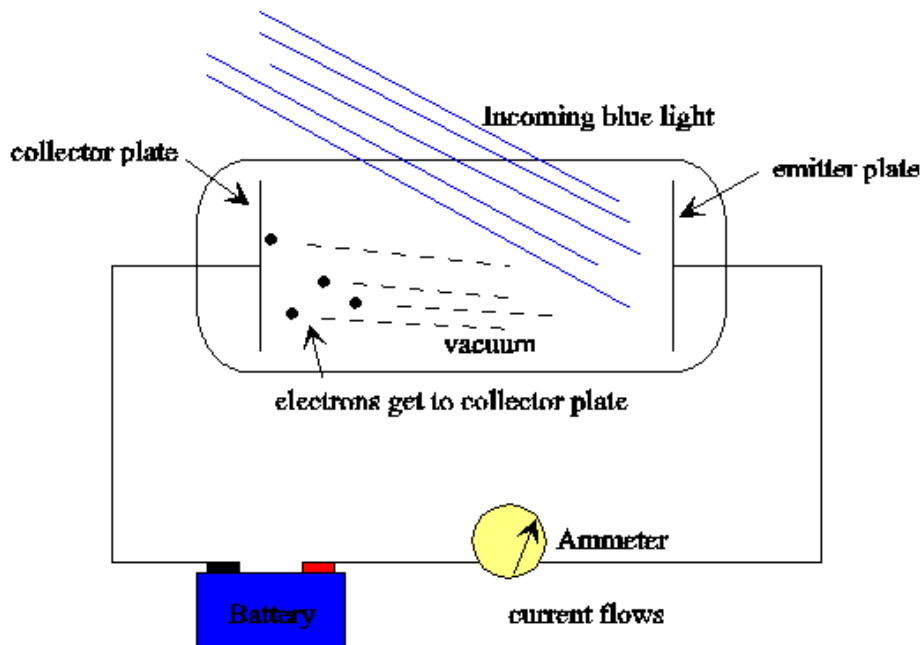
Figure 2.3 Layout for demonstration of the photoelectric effect.

In our illustration here, light at three wavelengths is used:
λ= 435.8 nm, 546.1 nm, and 632.8 nm. (blue, green, and red).
Calculating the energies corresponding to these wavelengths, we get:

$$E = hf = \frac{hc}{l} = \frac{4.136 \times 10^{-15} \text{ eV-s} \bullet 3\times10^{8} \frac{m}{s}}{435.8 \times10^{-9} \text{ m}} = \frac{1.24\times10^{-6}}{4.358 \times10^{-7}} = 2.85 \text{ eV}$$

Similarly, we get E=2.27 eV and E = 1.96 eV for 546.1 and 632.8 nm respectively. The experimental data shown below show that if the total photon energy = the electron energy plus the work function, or

$$E = hf = qW + \Phi \qquad \text{(Eqn. 2.6)}$$

Wavelength (nm)	Photon Energy (eV)	Electron Stopping Potential, W (Volts)	Work Function, Φ(eV)
435.8	2.85	1.25	1.6
546.1	2.27	0.7	1.6
632.8	1.96	0.4	1.6
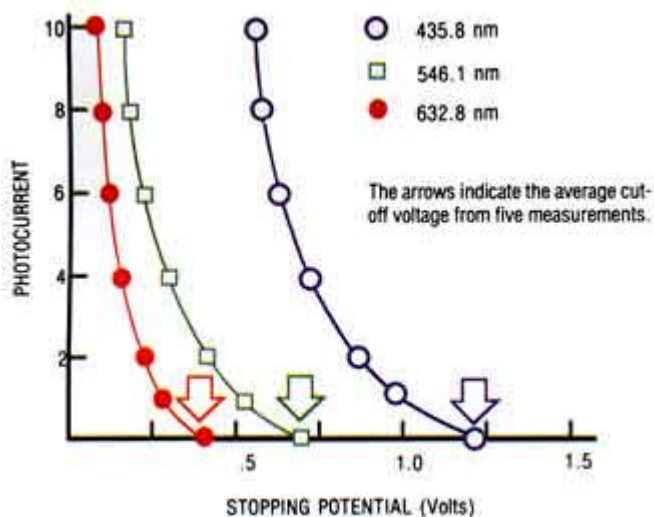
Figure 2.4   Results from typical demonstration of the photoelectric effect.

The brief introduction above does little justice to the diversity of processes that have produced these differing interpretations of light, and may leave the student confused. Is light a wave or a particle? Sadly, the correct answer is "yes".   The interpretation to be used really depends upon the process being observed (the experiment being done). Often, the correct perspective depends upon the energies of the photons (frequencies). It is generally found that the wave aspects dominate at frequencies below about 10^{15} Hz and the particle aspects at higher frequencies.   In the visible part of the spectrum both descriptions are useful.

Illustration of images at varying wavelength (energy).
As a conclusion to this segment, an unusual view of the electromagnetic spectrum is given by this illustration of the milky way galaxy as observed by a variety of instruments.

1) Radio Continuum (408 MHz) - Intensities: 10-4250 K
Intensity of radio continuum emission from hot, ionized gas in the Milky Way, from surveys with ground-based radio telescopes (Jodrell Bank MkI and MkIA, Bonn 100 meter, and Parkes 64 meter). At this frequency, most of the emission is from the scattering of free electrons in interstellar plasmas. Near some discrete sources, such as the supernova remnant Cas A near 110 degrees longitude, a significant fraction of the emission also comes from electrons accelerated in strong magnetic fields. The emission from Cas A is so intense that the diffraction pattern of the support legs for the radio receiver on the telescope is visible as a 'cross' shape.
Reference: Haslam, C. G. T., Salter, C. J., Stoffel, H., & Wi lson, W. E. 1982, Astron. Astrophys. Suppl. Ser., 47, 1
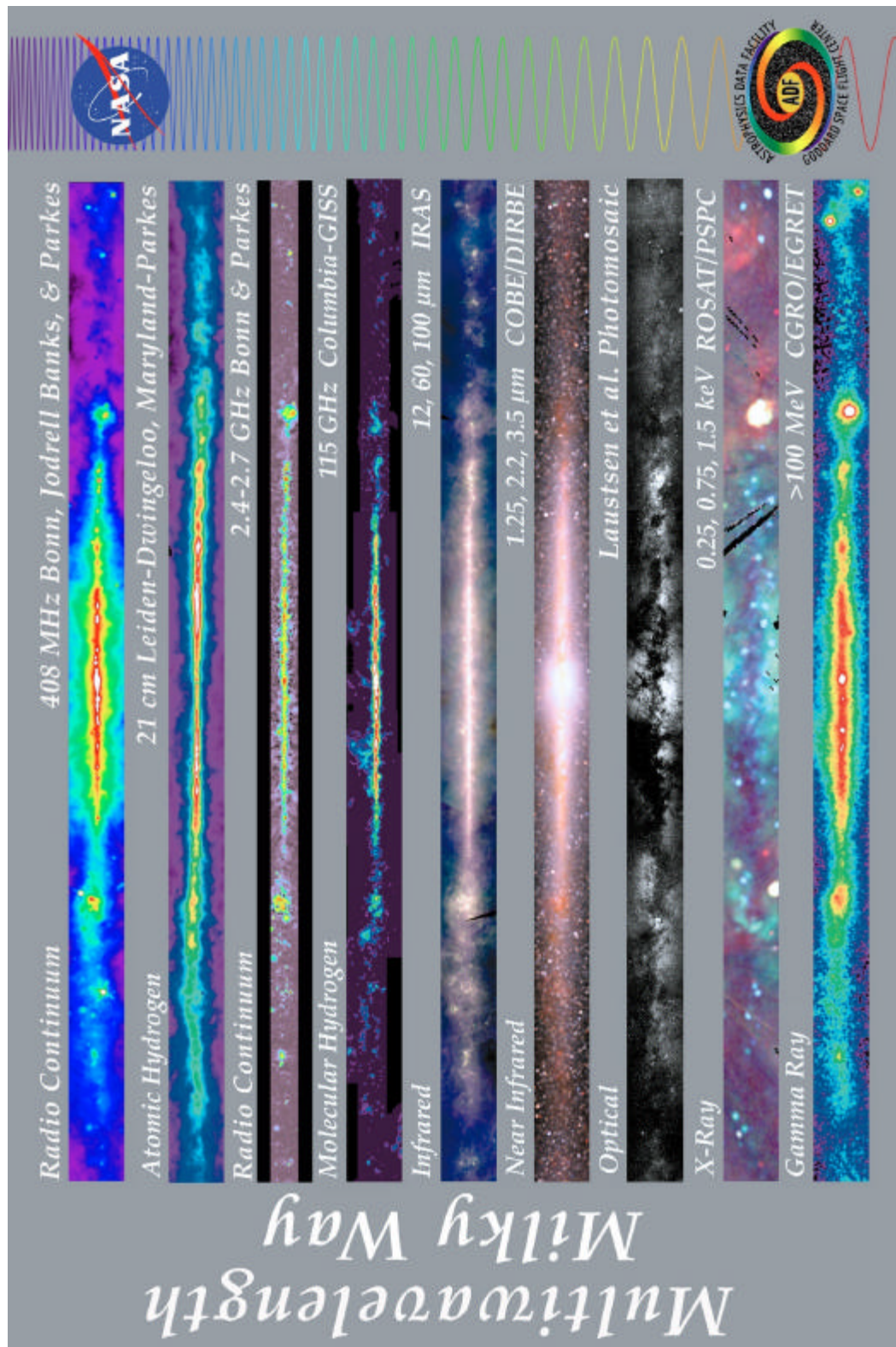
Figure 2.5 Multiwavelength Milky Way http://adc.gsfc.nasa.gov/mw/milkyway.html

2) Atomic Hydrogen - 1.4 GHz - Column densities: 10 x 10^{20} -230 x 10^{20} cm^{-2}

Column density of atomic hydrogen, derived on the assumption of optically thin emission, from radio surveys of the 21-cm spectral line of hydrogen. On a large scale the 21-cm emission traces the "warm" interstellar medium, which is organized into diffuse clouds of gas and dust that have sizes of up to hundreds of light years. Most of the image is based on the Leiden-Dwingeloo Survey of Galactic Neutral Hydrogen, made available by the authors in advance of publication. This survey was conducted over a period of 4 years using the Dwingeloo 25-m radio telescope, operated by the Netherlands Foundation for Research in Astronomy. The data were corrected for sidelobe contamination in collaboration with the University of Bonn.

*References: Burton, W. B. 1985, Astron. Astrophys. Suppl. Ser., 62, 365 ; Hartmann, Dap, & Burton, W. B., "Atlas of Galactic Neutral Hydrogen," Cambridge Univ. Press, (1997, book and CD-ROM); Kerr, F. J., et al. 1986, Astron. Astrophys. Suppl. Ser.*

3) Radio Continuum (2.4-2.7 GHz)

Intensity of radio continuum emission from hot, ionized gas and high-energy electrons in the Milky Way, from surveys with both the Bonn 100 meter, and Parkes 64 meter radio telescopes. Unlike the other views of our Galaxy presented here, these data extend to latitudes of only 5° from the Galactic midplane. The majority of the bright emission seen in the image is from hot, ionized regions, or is produced by energetic electrons moving in magnetic fields. The higher resolution of this image, relative to the 408 MHz picture above, shows Galactic objects in more detail. Note that the bright "ridge" of Galactic radio emission, appearing prominently in the 408 MHz image, has been subtracted here in order to show Galactic features and objects more clearly.

References:
Duncan, A. R., Stewart, R. T., Haynes, R. F., & Jones, K. L. 1995, Mon. Not. Roy. Astr. Soc., 277, 36
Fuerst, E., Reich, W., Reich, P., & Reif, K. 1990, Astron. Astrophys. Suppl. Ser., 85, 691
Reich, W., Fuerst, E., Reich, P., & Reif, K. 1990, Astron. Astrophys. Suppl. Ser., 85, 633

4) Molecular Hydrogen - Frequency: 115 GHz

Column density of molecular hydrogen inferred from the intensity of the J = 1-0 spectral line of carbon monoxide, a standard tracer of the cold, dense parts of the interstellar medium. Such gas is concentrated in the spiral arms in discrete "molecular clouds" and most molecular clouds are sites of star formation. The molecular gas is predominantly H2, but H2 is difficult to detect directly at interstellar conditions and CO, the second most abundant interstellar molecule, is observed as a surrogate. The column densities were derived on the assumption of a constant proportionality between the column density of H2 and the intensity of the CO emission. Black areas in the image indicate regions not yet surveyed for CO.

References: Dame, T. M., et al. 1987, Astrophysical Journal, 322, 706; Digel, S. W., & Dame, T. M. 1995, unpublished update

5) Infrared - Frequencies: 3.0 x 10^3-25 x 10^3 GHz

Intensities: 0.25-100 (12 microns), 1.5-750 (60 microns), 12-750 MJy sr^{-1} (100 microns)
Composite mid and far-infrared intensity observed by the Infrared Astronomical Satellite (IRAS) in 12, 60, and 100 micron wavelength bands. The images are encoded in the blue, green, and red color ranges, respectively. Most of the emission is thermal, from interstellar dust warmed by absorbed starlight, including that in star-forming regions embedded in interstellar clouds. The image here is a mosaic of IRAS Sky Survey Atlas plates; emission from interplanetary dust in the solar system, the "zodiacal emission," was modeled and subtracted in the production of the Atlas at the Infrared Processing and Analysis Center (IPAC). The black, wedge-shaped areas indicate gaps in the IRAS survey.

Reference: Wheelock, S. L., et al. 1994, IRAS Sky Survey Atlas Explanatory Supplement, JPL Publication 94-11 (Pasadena: JPL) Order: CASI HC A08/MF A02

6) Near Infrared - Frequencies: 86 x 10³-240 x 10³ GHz

Intensities: 0.5-9 (1.25 microns), 0.35-20 (2.2 microns), 0.22-4.5 MJy sr⁻¹ (3.5 microns)
Composite near-infrared intensity observed by the Diffuse Infrared Background Experiment
(DIRBE) instrument on the Cosmic Background Explorer (COBE) in the 1.25, 2.2, and 3.5 micron
wavelength bands. The images are encoded in the blue, green, and red color ranges,
respectively. Most of the emission at these wavelengths is from cool, low-mass K stars in the disk
and bulge of the Milky Way. Interstellar dust does not strongly obscure emission at these
wavelengths; the maps trace emission all the way through the Galaxy, although absorption in the
1.25 micron band is evident in the general direction of the Galactic center.
Reference: Hauser, M. G., Kelsall, T., Leisawitz, D., & Weiland, J. 1995, COBE Diffuse Infrared Background
Experiment Explanatory Supplement, Version 2.0, COBE Ref. Pub.
No. 95-A (Greenbelt, MD: NASA/GSFC)

7) Optical - Frequency: 460 x 10³ GHz

Intensity of visible light from a mosaic of wide-field photographs by Laustsen, Madsen, & West
(1987). Scanned images of the original prints were kindly provided by C. Madsen (European
Southern Observatory, cmadsen@eso.org). The images are copyright (1987) by ESO. Owing to
the strong obscuration by interstellar dust the light is primarily from stars within a few thousand
light-years of the Sun, nearby on the scale of the Milky Way, which has a diameter on the order of
100,000 light years. Nebulosity from hot, low-density gas is widespread in the image. Dark
patches are due to absorbing dust clouds, which are evident in the Molecular Hydrogen and
Infrared maps as emission regions. The mosaic is constructed from eight photographs. Narrow,
vertical gaps are evident between some photographs, as are slight discontinuities in brightness.
Reference: Laustsen, S., Madsen, C., West, R. 1987, Exploring the Southern Sky, (Berlin: Springer-Verlag)

8) X-Ray - Frequency: 60-360 x 10⁶ GHz

Intensities: 0-20 (0.25 keV), 0-10 (0.75 keV), 0-10 x 10⁻⁴ photons arcmin⁻² s⁻¹ (1.5 keV)
Composite X-ray intensity observed by the Position-Sensitive Proportional Counter (PSPC)
instrument on the Röntgen Satellite (ROSAT). Images in three broad, soft X-ray bands centered
at 0.25, 0.75, and 1.5 keV are encoded in the red, green, and blue color ranges, respectively. In
the Milky Way, extended soft X-ray emission is detected from hot, shocked gas. At the lower
energies especially, the interstellar medium strongly absorbs X-rays, and cold clouds of
interstellar gas are seen as shadows against background X-ray emission. Color variations
indicate variations of absorption or of the temperatures of emitting regions. The black regions
indicate gaps in the ROSAT survey.
Reference: Snowden, S. L., et al. 1995 Astrophys. J., 454, 643

9) Gamma Ray - Frequencies: >2.4 x 10¹³ GHz

Intensities: 4×10^{-5} - 93×10^{-5} photons cm⁻² s⁻¹ sr⁻¹
Intensity of high-energy gamma-ray emission observed by the Energetic Gamma-Ray Experiment
Telescope (EGRET) instrument on the Compton Gamma-Ray Observatory (CGRO). The image
includes all photons with energies greater than 100 MeV. At these extreme energies, most of the
celestial gamma rays originate in collisions of cosmic rays with hydrogen nuclei in interstellar
clouds. The bright, compact sources near Galactic longitudes 185°, 195°, and 265° indicate high-
energy phenomena associated with the Crab, Geminga, and Vela pulsars, respectively.
References: Hunter, S. D., et al. 1997, Astrophys. J., 481, 205; Thompson, D. J., et al. 1996, Astrophys. J. Suppl., 107,
227

B Polarization of radiation

The discussion above treats electric and magnetic fields as scalars - that is, amplitudes only. The alert students probably noticed at the beginning of this section that $\vec{\mathbf{E}}$ and $\vec{\mathbf{B}}$ are both vectors. This vector character to EM radiation becomes important when we consider the concept of polarization. Familiar to most as an aspect of expensive sunglasses, polarization shows up in visible light observations and radar. A brief illustration of how EM waves propagate becomes necessary at this point.

Figure 2.6 shows how the electric and magnetic fields oscillate with respect to one another in an EM wave (in vacuum).
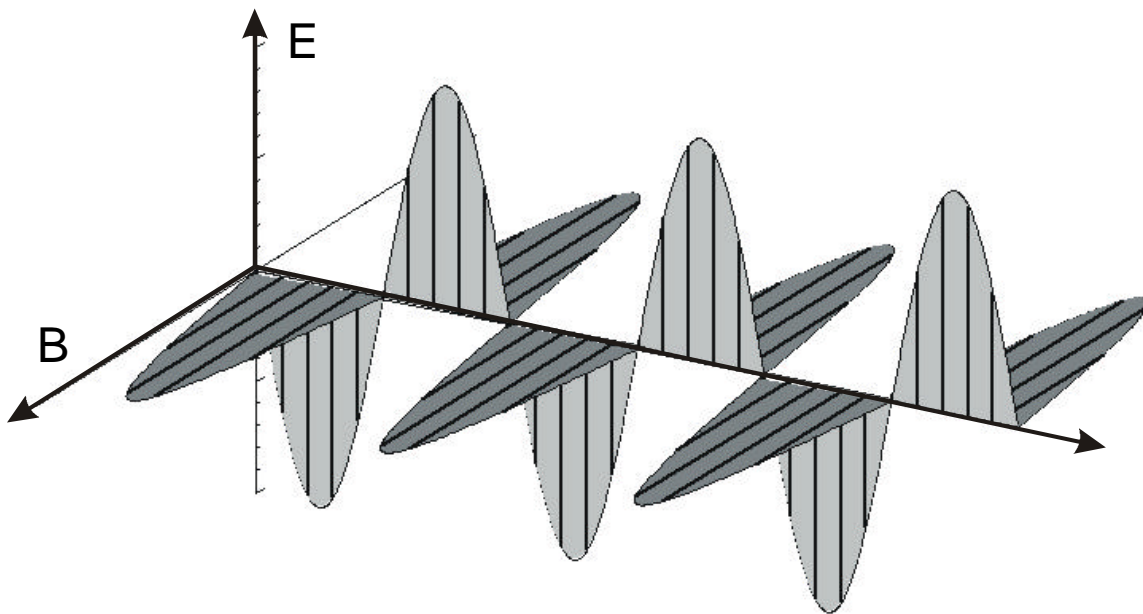

Figure 2.6 An electromagnetic wave. Note E⊥B, and both are perpendicular to the direction of propagation. Following a typical convention, E is in the x direction, B is in the y direction, and the wave is propagating in the z direction.

Other forms of polarization are possible, but harder to illustrate.

C Sources of Electromagnetic Radiation

There are several major sources of electromagnetic radiation, all ultimately associated in some for with the acceleration (change of energy) of charged particles (mostly electrons). For purposes of remote sensing, these can be distinguished into three categories:

(1) Individual atoms or molecules which radiate line spectra
(2) Hot, dense bodies which radiate a continuous "black-body" spectrum
(3) Electric currents moving in wires (aka antenna)

The first two of these sources of radiation are now considered in somewhat more detail.

1 Line spectra

Single atoms or molecules emit light in a form termed "line spectra". An atom or molecule, which is reasonably isolated (such as in a gas at ordinary temperatures and pressures) will **radiate** a discrete set of frequencies called a line spectrum. If, on the other had, we pass radiation having a continuous spectrum of frequencies through a gas we find that a discrete set of frequencies is **absorbed** by the gas leading to a spectrum of discrete absorption lines

The wavelengths radiated (absorbed) are characteristic of the particular atom or molecule and thus represent a powerful tool for determining the composition of radiating (or absorbing) gases. Much of our knowledge of the chemical composition of stars (including our sun) comes from detailed analysis of such line spectra.

The process is reasonably well explained by the Bohr model of the atom, as developed at the beginning of this century. The model, developed analytically in an appendix, uses the somewhat familiar construct of the atom as a small solar system, with a nucleus at the center composed of the heavy protons (+) and neutrons. The lighter electrons (-) orbit the nucleus at well-defined radii, which correspond to different energy levels. The closer they orbit to the nucleus, the lower (more negative) their energy levels are. As energy is given to the electrons, the radii of their orbits increase, until they finally break free. Bohr hypothesized that the radii of the orbits were constrained by quantum mechanics to have certain values (really, a constraint on angular momentum). This produces a set of discrete energy levels that are allowed for the electrons. Bohr then said that the emission and absorption of energy (light) by an atom could only occur for transitions between the discrete energy levels allowed to the electrons.

A few pages of mathematics (see appendix) gives the formula for the energy of the electrons orbiting in hydrogen-like atoms:

$$E = -\frac{1}{2}\left(\frac{Z\,e^2}{4\pi\,\varepsilon_0\,\hbar}\right)^2 \frac{m}{n^2} = Z^2\,\frac{E_1}{n^2} \qquad \text{(Eqn. 2.7)}$$

where $\quad\quad\quad\quad\quad E_1 = -\dfrac{me^4}{32\pi^2\varepsilon_0^2\ \hbar^2} = -13.58\ eV$

(here, n = the quantum number: 1, 2, 3, ….; Z - the atomic number;
 m = the electron mass; e= the electron charge; the remaining terms are constants.)
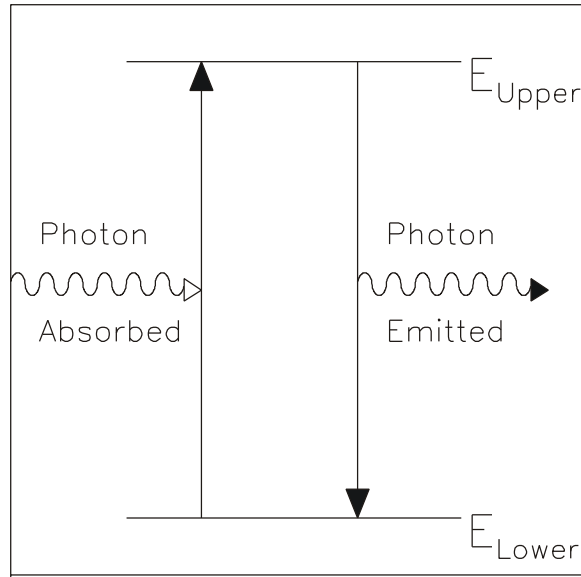
Figure 2.7 Bohr Postulate - photons produced/destroyed by discrete transition in energy.

Figure 2.8 illustrates the energy levels for the Bohr model of the hydrogen atom. We find that the ionization energy, the energy necessary to remove the electron from its "well", is 13.58 eV. The concept of a "work function", described above for the process of photoemission, derives from the same physics.

Within an atom, if the electron gains somewhat less energy, it may move up to an "excited state", where n > 1. For example, if an electron beginning in the ground state gains 10.19 eV it will move up to the n = 2 level. Dropping down from n = 2 to n = 1, it will emit a photon of 10.19 eV energy, at a wavelength:

$$\lambda = \frac{hc}{\Delta E} = 121.6\,nm = 1216\,\mathring{A}$$
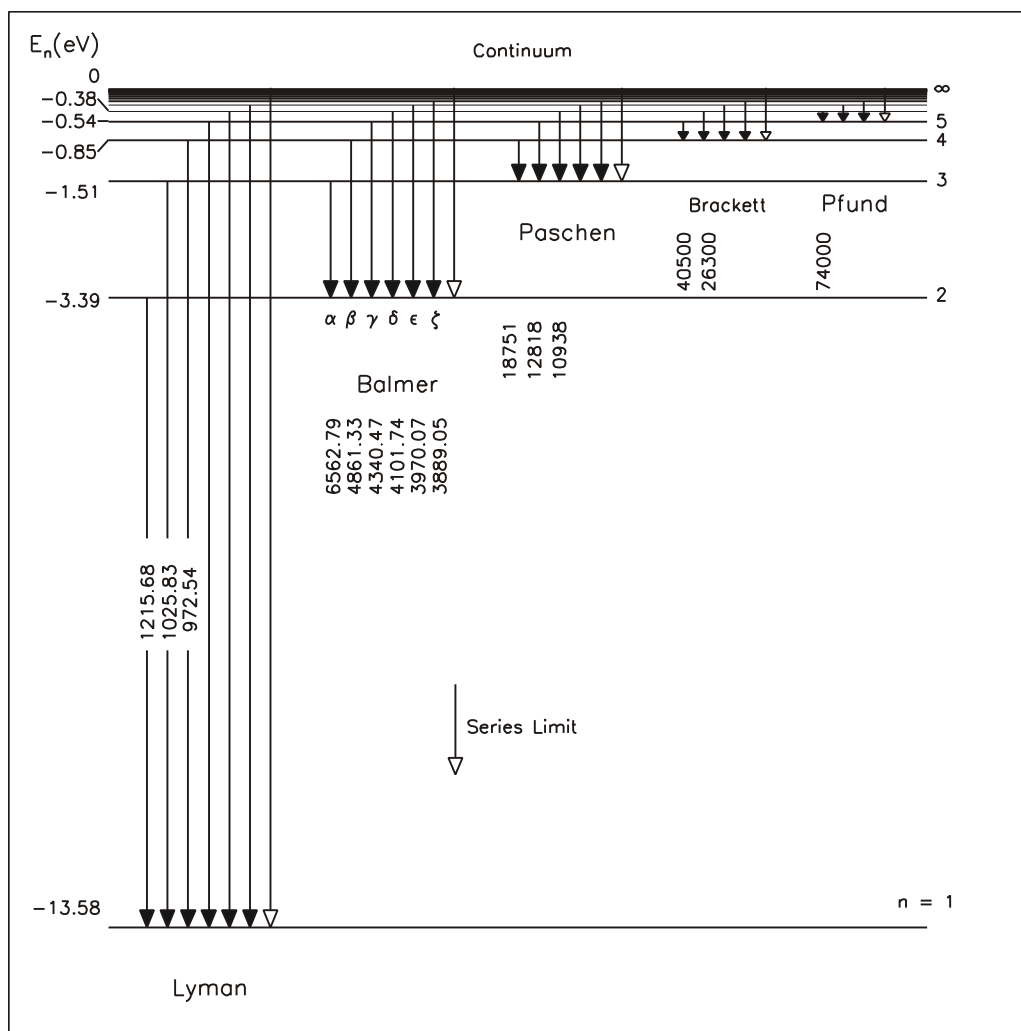
Figure 2.8. The energy level diagram of the hydrogen atom, showing the possible transitions corresponding to the different series. The numbers along the transitions are wavelengths. (Wavelengths are in units of Angstroms, where 1 nm = 10 A)
Adapted from: Fundamentals of Atomic Physics, Atam P. Arya, p264, 1971.

If ΔE is expressed in electron-volts (eV), which it usually is, then the constant "hc" in the numerator can be written as:

$$hc = 4.14 \times 10^{-15} \bullet 3 \times 10^{8} = 1.24 \times 10^{-6} \ (eV \ m)$$

and thus the wavelength λ (in meters) is given by:

$$\mathbf{\mathit{l}} \ (m) = \frac{1.24 \times 10^{-6}}{\Delta E \ (eV)} \quad or \quad \mathbf{\mathit{l}} \ (nm) = \frac{1240}{\Delta E \ (eV)} \qquad (Eqn. \ 2.8)$$

In general, transitions will occur between different energy levels, resulting in a wide spectrum of discrete spectral lines. Transitions from (or to) the n = 1 energy level (the ground state) are called the Lyman series. The n = 2 to n = 1 transitions is the Lyman

alpha (α) transition. This ultraviolet (UV) emission is one of the primary spectral (emission) lines of the sun's upper atmosphere.   The emission (or absorption) lines in the visible portion of the sun's spectrum are the Balmer series, transitions from n > 2 to n = 2. Higher order series are of less importance for our purposes.

The Bohr model is successful in predicting the observed energy levels for one-electron atoms. It is useful for illustrating the quantum nature of the atom, and the associated energy levels. It is also a good beginning for understanding all of the interesting spectral characteristics reflected and radiated light may exhibit in remote sensing applications. The Bohr model was ultimately replaced by the solution of the Schrödinger equation, and a more general form of quantum mechanics.

2 Black body radiation

Black Body Radiation is emitted by hot solids, liquids or dense gases and has a continuous distribution of radiated wavelength as shown in Figure 2.9. The curves in this figure give the radiance, L, in dimensions of $\dfrac{Power}{unit\ area\ \text{-}\ wavelength\ \text{-}\ solid\ angle}$, or units of $\dfrac{Watts}{m^2\ \mu\ ster}$. The radiance equation is:

$$Radiance = L = \frac{2\ hc^2}{\lambda^5} \frac{1}{e^{\frac{hc}{\lambda\,kT}} - 1} \qquad\qquad \text{(Eqn. 2.9)}$$

where $c = 3 \times 10^8\ \frac{m}{s};\ h = 6.626 \times 10^{-34}\ joule - s;\ k = 1.38 \times 10^{-23}\ \frac{Joule}{Kelvin}$

Planck Theory of Radiation
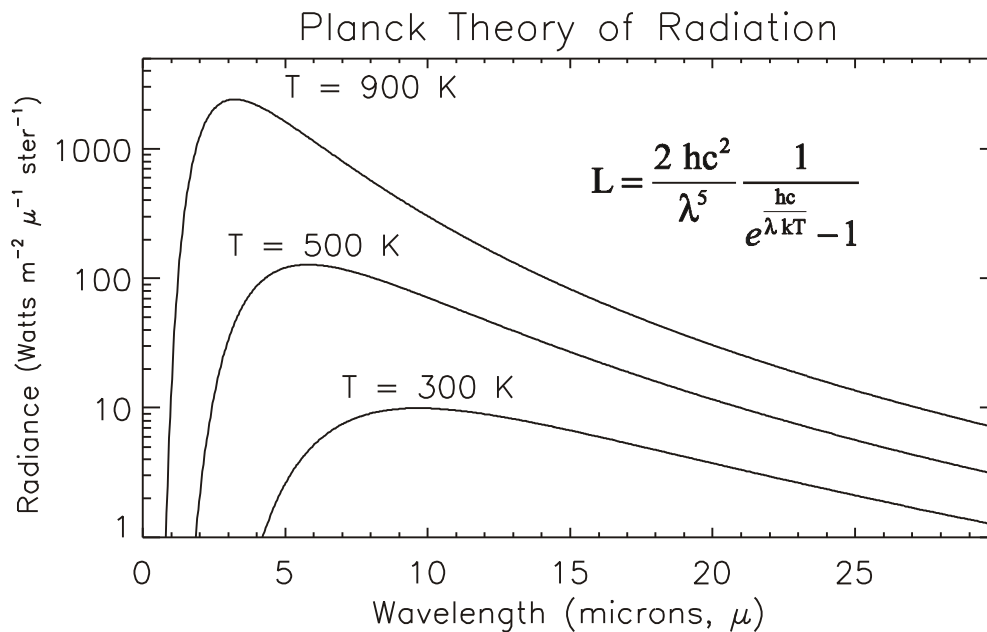
Figure 2.9 Blackbody radiation as a function of wavelength.

It is a little easier to decipher the nature of the formula if it is rewritten slightly:

$$L = \frac{2}{c^3 h^4} \frac{\left(\frac{hc}{\lambda\,kT}\right)^5}{e^{\frac{hc}{\lambda\,kT}} - 1} \left(kT\right)^5 \qquad = \frac{2}{c^3 h^4} \frac{x^5}{e^x - 1}\left(kT\right)^5 \qquad \text{(Eqn. 2.10)}$$

where the dimensionless term: $x = \left(\frac{hc}{\lambda\,kT}\right)$ is defined. We see that the shape of this function of wavelength (λ) is unchanging as temperature changes - only the overall amplitude changes (and of course, the location of the peak in wavelength).

Real materials will differ from the idealized black body in their emission of radiation. The emissivity of a surface is a measure of the efficiency with which the surface absorbs (or radiates) energy and lies between 0 (for a perfect reflector) and 1 (for a perfect absorber). A body which has $\varepsilon = 1$ is called a black body. In the infrared, many objects are nearly black bodies, in particular vegetation. Materials with $\varepsilon < 1$ are called gray bodies. Note that the emissivity (ε) will vary with wavelength.

Note that in some textbooks, a slightly different form of Planck's Law may be found, where an extra π is included:

$$\text{Radiant Exitance} = M = \frac{2\,\pi\,hc^2}{\lambda^5} \frac{1}{e^{\frac{hc}{\lambda\,kT}} - 1} \quad \frac{\text{Watts}}{m^2\,\mu} \qquad \text{(Eqn. 2.11)}$$

The difference is that the dependence on angle of the emitted radiation has been removed by integrating over the solid angle. You can do this for black-bodies because they are 'Lambertian' surfaces by definition - the emitted radiation does not depend upon angle, and $M = \pi L$.

For our purposes we are particularly interested in two aspects of the Planck curves:
   a) the total power radiated which is represented by the area under the curve, and
   b) the wavelength at which the curve peaks, λ_{max}.

The power radiated (integrated over all wavelengths) is given by

$$R \;=\; \sigma\,\varepsilon\,T^4 \;\left[\text{Watts}\middle/{m^2}\right] \quad \text{(Stefan Boltzmann Law)} \qquad \text{(Eqn. 2.12)}$$

where R = Power radiated / m²

      ε = Emissivity (taken as unity for black body)

      σ = 5.67×10^{-8} $\left[W\middle/{m^2\,K^4}\right]$ (Stefan's Constant)

      T = Temperature of the radiator (in K)

Wien's Displacement Law gives the wavelength at which the peak in radiation occurs:

$$\lambda_{max} = \frac{a}{T} \qquad \text{(Eqn. 2.13)}$$

for a given temperature T. The constant "a" has the value

$$a \;=\; 2.898 \times 10^{-3} \; [m\ K]$$

which gives λ_{max} in meters if T is K.

_____

Example:

Assume that the sun radiates like a blackbody, which is not a bad assumption, though we must choose two slightly different temperatures to match the observed quantities.

(a) Find the wavelength at which this radiation peaks, λ_{max}. The solar spectral shape in the visible is best matched by a temperature of ~ 6000 K.
(b) Find the total power radiated by the sun. The Stefan-Boltzmann law is best served by an "effective temperature" of ~ 5800 K.

$$\text{(A)} \quad \lambda_{max} = \frac{a}{T} = \frac{2.898 \times 10^{-3} \ (m/K)}{6000 \ K} = 4.83 \times 10^{-7} \ m$$

The spectrum peaks at ~500 nm, as illustrated below in figure 2.10.
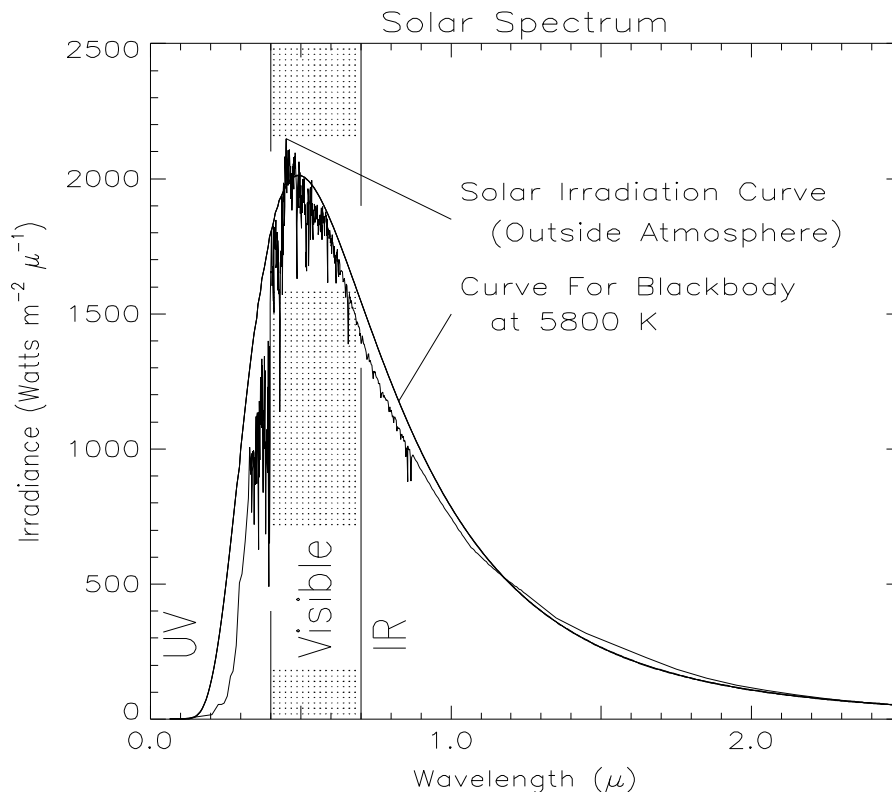
Figure 2.10 - The solar spectrum, based on the spectrum of Neckel and Labs "The solar radiation between 3300 and 12500 Angstrom", <u>Solar Physics</u>, <u>90</u>, 205-258, 1984. Data file courtesy of Bo-Cai Gao, NRL. The peak occurs at about 460 nm (blue).

(B) Next we can calculate R, the power emitted per-square-meter of surface. We use:

$$R = \sigma \varepsilon T^4$$

and we assume that $\varepsilon = 1$ (Black Body). Evaluating, we get:

$$R = 5.67 \times 10^{-8} \bullet 1 \bullet 5800^4 = 6.42 \times 10^7 \frac{\text{Watts}}{\text{meter}^2}$$

To find the total solar power output we must multiply by the solar surface area, $S_\odot = 4\pi R_\odot^2$, where $R_\odot = 6.96 \times 10^8$ m is the mean radius of the sun. Hence the total solar power output is:

$$P_\odot = R \ (4\pi R_\odot^2)$$

$$= 4\pi (6.96 \times 10^8)^2 \times (6.42 \times 10^7)$$

$$P_\odot = 3.91 \times 10^{26} \ W$$

(Not bad for a little star.)(See Kenneth Phillips, Guide to the Sun, Cambridge Press, 1992, pages 83-84) The sun's spectrum is shown in figure 2.10, with the spectrum of a 5,800 K black body superimposed.

_____

A slightly different perspective on the visible portion of the solar spectrum is obtained from an illustration created at the University of Hawaii. The dark lines superimposed on the rainbow scale are the solar absorption features, also known as Frauenhofer lines. These are due to the cool hydrogen and helium and other elements just above the surface of the sun. These correspond to the dips in the solar irradiation curve illustrated above.

Figure 2.11 - Solar spectrum as observed on Mount Haleakala, courtesy of the University of Hawai`i, Institute for Astronomy, C.E.K. Mees Solar Observatory,
http://www.solar.ifa.hawaii.edu/mees.html

D EM Radiation matter interactions
(This section from Avery and Berlin)

Electromagnetic radiation manifests itself only through its interactions with matter, which can be in the form of a gas, a liquid, or solid. This concept is clearly illustrated by shining a flashlight beam of visible light on a white wall in a darkened room. If we stand at a right angle to the long axis of the beam, the light is visible only at its source **E** and where it strikes the wall and is reflected to our eyes. The beam cannot be seen from the side and can be made visible only when its optical path contains particles large enough to scatter some of the light beam sideways. This can be accomplished by adding chalk dust or smoke to the invisible beam. Their large particles will scatter a portion of the EMR to our eyes, enabling the beam to be seen from the side. This side scattering of visible light along a beam path is known as the **Tyndall effect.**

EMR that impinges upon matter is called **incident radiation.** For the earth, the strongest source of incident radiation is the sun. Such radiation is called **insolation** a shortening of <u>in</u>coming <u>sol</u>ar rad<u>iation</u>. The full moon is the second strongest source, but its radiant energy measures only about one millionth of that from the sun. When EMR strikes matter, EMR may be **transmitted, reflected, scattered,** or **absorbed** in proportions that depend upon:
      1)   the compositional and physical properties of the medium,
      2)   the wave- length or frequency of the incident radiation, and
      3)   the angle at which the incident radiation strikes a surface.
The four fundamental energy interactions with matter are illustrated in Figure 2-12.
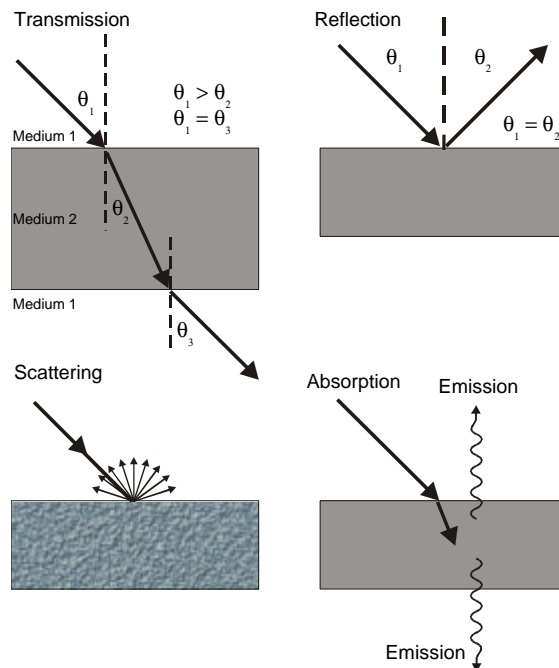

Figure 2-12
Citation: Thomas Eugene Avery and Graydon Lennis Berlin, Fundamentals of Remote Sensing and Airphoto Interpretation, Macmillan Publishing Company, NY, NY, 10022, 1992

1 Transmission

Transmission is the process by which incident radiation passes through matter without measurable attenuation; the substance is thus transparent to the radiation. Transmission through material media of different densities (e.g., air to water) causes the radiation to be refracted or deflected from a straight-line path with an accompanying change in its velocity and wavelength; frequency always remains constant. In Figure 2-10, it is observed that the incident beam of EMR (θ_1) is deflected toward the normal in going from a medium of low density to a denser medium (θ_2). Upon emerging from the other side of the denser medium, the beam is refracted away from the normal (θ_3). The angle relationships in Figure 2-9 are $q_1 > q_2$ and $q_1 = q_3$.

The change in EMR velocity is explained by the **index of refraction** (n), which is the ratio between the velocity of EMR in a vacuum (c) and its velocity in a material medium (v).

$$n = \frac{c}{v}$$ (Eqn. 2.14)

The index of refraction for a vacuum (perfectly transparent medium) is equal to 1, or unity. Because v is never greater than c, n can never be less than 1 for any substance. Indices of refraction vary from 1.0002926 for the earth's atmosphere, to *1.33* for water, to 2.42 for a diamond. The above relation leads to Snell's Law:

$$n_1 \sin q_1 = n_2 \sin q_2$$ (Eqn. 2.15)

2 Reflection

Reflection (also called specular reflection) describes the process whereby incident radiation "bounces off" the surface of a substance in a single, predictable direction. The angle of reflection is always equal and opposite to the angle of incidence ($q_1 = q_2$ in Figure 2-10). Reflection is caused by surfaces that are smooth relative to the wavelengths of incident radiation. These smooth, mirror-like surfaces are called specular reflectors**.** Specular reflection causes no change to either EMR velocity or wavelength.

3 Scattering

Scattering (also called diffuse reflection) occurs when incident radiation is dispersed or spread out unpredictably in many different directions, including the direction from which it originated (Figure 2-10). In the real world, scattering is much more common than reflection. The scattering process occurs with surfaces that are rough relative to the wavelengths of incident radiation. Such surfaces are called diffuse reflectors. EMR velocity and wavelength are not affected by the scattering process.

4 Absorption

Absorption is the process by which incident radiation is taken in by the medium (Figure 2-10). For this to occur, the substance must be opaque to the incident radiation. A portion of the absorbed radiation is converted into internal heat energy, which is subsequently **emitted** or **reradiated** at longer thermal infrared wavelengths (Figure 2-10).

5 Energy Balance

The interrelationships between energy interactions, as a function of wavelength (λ), can be expressed in the following manner:

$$E_I(\lambda) = E_T(\lambda) + E_R(\lambda) + E_A(\lambda)$$

where: $E_I(\lambda) = $ incident radiant energy,

$E_T(\lambda) = $ fraction transmitted,

$E_R(\lambda) = $ fraction reflected (specular and diffuse) , and

$E_A(\lambda) = $ fraction absorbed.

Most opaque materials transmit no incident radiant energy; hence, $E_T(\lambda) = 0$, and $E_R(\lambda) + E_A(\lambda) = 1 = E_I(\lambda)$. In regard to visible light,

1)   clear glass would have a high transmission value and low reflection and absorption values;

2)   fresh snow would have a high reflectance value and low transmission and absorption values; and

3)   fresh asphalt would be characterized by a high absorption value and minimal transmission and reflection values.

Because only the part of incident radiation that is absorbed by an object is effective in heating it, there would only be a minuscule rise in temperature for glass and snow, whereas the asphalt's temperature would be markedly higher.

E Problems:

1. MWIR radiation covers the 3-5μ portion of the EM spectrum. What energy range does this correspond to, in eV.

2. What frequency is an x-band radar? What wavelength?

3. What is the ground state energy for an He+ ion, in eV. (Note, Z=2)

4. Calculate the energy (in eV), frequency (in Hz), and wavelength (in meters, microns, and nano-meters) for the n=4 to n=2 transition in a hydrogen atom (note, Z=1). This is the Balmer-β transition.

5. Student exercise: check long wavelength behavior - use the fact that for small x: $e^x - 1 \approx x$ to get rid of the exponential term in the denominator. Also, which term dominates L for small wavelength?

6. Calculate the radiance, $L(\lambda)$, for T = 1000 K, from λ=0-20μ, and plot. Note that this is an exercise in calculation, and you should be sure you can obtain the correct answer with a hand calculator at a minimum of 2 wavelengths - say 3 and 10 μ.

7. Calculate the peak wavelength for radiation at T=297 K, 1000 K, and 5800 K, in microns and nano-meters.

8. Calculate the radiated power for a black body at 297 K, in Watts/m^2.

9. Calculate the radiated power for a gray body at 297 K, ε=0.8, in Watts/m^2. Assume a surface area of 2 m^2, and calculate the radiated power, in Watts

10. Snell's law in optics is normally given as:

$$n_1 \sin\boldsymbol{q}_1 = n_2 \sin\boldsymbol{q}_2$$

Where the angles are defined as in Figure 2.10. For an air/water interface, one can use the typical values: $n_1 = 1$; $n_2 = 1.33$. For such values, calculate $\boldsymbol{q}_2$ if $\boldsymbol{q}_1 = 30°$. What is the speed of light in water?

1 Black Body Problem

Calculate the equilibrium temperature of the earth, or any satellite orbiting the sun.

a How much energy is radiated by the sun, and how much then reaches earth orbit?

($R_{sun} = 6.96 \times 10^8$ m; $T_{sun} = 5800$ K; $\sigma = 5.67 \times 10^{-8}$ W$/$m^{2}K^4)

The radiated power is: $P_{sun} = \varepsilon \; \sigma \; T_{sun}^4 \bullet 4\pi R_{Sun}^2 =$

_____

Textbook Answer: 3.83×10^{26} Joules/s

_____

b The radiation spreads as the electromagnetic energy moves outwards, according to Gauss' Law (conservation of energy, really). What is the radiation at earth's orbit?

$\left(R_{Earth\;Orbit} = 150 \times 10^9 \text{ m, aka 93 million miles} \right)$

$R = P_{solar} / \left(4\pi \; R_{Earth\;Orbit}^2 \right) =$

The textbook value is: 1381 Watts/m^2

_____

c How much power does the earth receive?

The radiation is incident on a cross-section area which is the area of the earth's disk: $\pi \; R_{Earth}^2$. $\left(R_{Earth} = 6380 \text{ km} \right)$. One question which can be left open at this point is the question of the earth's albedo - the factor which determines what fraction of the sunlight incident on the earth is absorbed, vs reflected. Here, we will use the symbol "α" for albedo.

$$P_{Solar} = \alpha \; \sigma \; T_{Sun}^4 \bullet \left(\frac{R_{Sun}}{R_{Earth\;Orbit}} \right)^2 \bullet \pi \; R_{Earth}^2 = \text{Watts}$$

where you can nominally take α to be one for now.

_____

d This power has to be re-radiated by the earth - once a steady state temperature has been reached. Hence, you can derive a temperature for the earth.

$$P_{Solar} = \alpha \; \sigma \; T_{Sun}^4 \bullet \left(\frac{R_{Sun}}{R_{Earth\;Orbit}} \right)^2 \bullet \pi \; R_{Earth}^2 = \varepsilon_{Earth} \; \sigma \; T_{Earth}^4 \bullet 4\pi \; R_{Earth}^2$$

$T_{Earth} = 280$ K

The earth will freeze if the number drops to 273 K. If the emissivity of the earth is one, what does α have to drop to for this to happen?

This page intentionally left blank

Chapter 3 VISIBLE IMAGERY

We begin by looking in the part of the electromagnetic spectrum most familiar to humans - the visible spectrum. As an illustration, images from the first remote sensing satellite system are presented, from the CORONA spy satellites. Subsequent elements of the chapter look at elements of recognition (photo-interpretation), some basic optics, and the details of two high resolution imaging systems.

A The first remote sensing satellite - CORONA

1 A little history

CORONA was America's first operational space reconnaissance project. Its first successful mission was on August 18, 1960, and it operated for almost twelve years during the Cold War. It was developed as a highly classified program under the joint management of the CIA and the USAF, a relationship that evolved into the National Reconnaissance Office (NRO). For context, note that the first Soviet satellite, SPUTNIK, was launched on 14 October 1957. President Eisenhower endorsed the program in February 1958. This proved to be very foresighted, when Francis Gary Powers was shot down in a U-2 on 1 May 1960.

The first CORONA test launch was attempted 28 February 1959, followed by 12 failed missions. The Discover series (a cover name) had a dozen failures, 7 involving launch, 5 involving satellite/camera malfunctions. Mission number 13 produced the 1st successful recovery from space on 10 August 1960. The 1st image from space was taken on the next mission, on 18 August 1960. The last, #145, was launched 25 May 1972; the last images of the series were taken 31 May 1972.

Imaging resolution was originally 8 meters (25 feet), but improved to 2 meters (6 feet). Individual images on average covered an area approximately 10 miles by 120 miles. Operated for nearly 12 years, over 800,000 images were taken from space.   The declassified collection includes 2.1 million feet of film in 39,000 cans.

2 The technology

The Corona vehicle was launched by a THOR booster and used the AGENA spacecraft as the upper stage. While in orbit, Corona took photographs with a constant rotating stereo panoramic camera system and loaded the exposed photographic film into recovery vehicles. The vehicles were de-orbited and recovered by Air Force C-119 aircraft while floating to earth on a parachute.

The cameras, designated with the codename Keyhole, began as variants on cameras designed for airphotos. The first cameras, the "C" series, were designed by Itek, and built by Fairchild. They used long film strips, 2.2" x 30", and an f/5.0 Tessar lens, with a focal length of 24". The first images hand a ground resolution of 40 feet, based on a film resolution of 50-100 lines/millimeter. (Advances in film technology by Kodak were some of the most important technology advances in the CORONA program.)

Improved camera, lens, and film design led to the KH4 series cameras, with Petzval, f3.5 lenses, still at 24" focal length. With film resolutions of 160 lines/mm, it was possible to resolve ground targets of six feet. (Negatives could be enlarged some 40 times.) CORONA ultimately used film ranging in speeds from ASA 2 to ASA 8 - 1% the speed of 'regular' film. This is the tradeoff for high film resolution, and is one reason the very large optics were needed. (Day et al, 1998, page 65). Infrared film was flown on Mission 1104 and used to photograph the Vandenberg AFB area. "Color film was flown on Mission 1105 and 1108…. By 1970, the CIA concluded that color film's decreased resolution made it relatively useless for intelligence purposes - black and white film had a resolution approximately twice as good as high resolution color film. But the color film could be useful for mineral resources exploration." (Day et al, 1998, page 82) The results indirectly led to the earth resources program, and hence, the Landsat satellites.
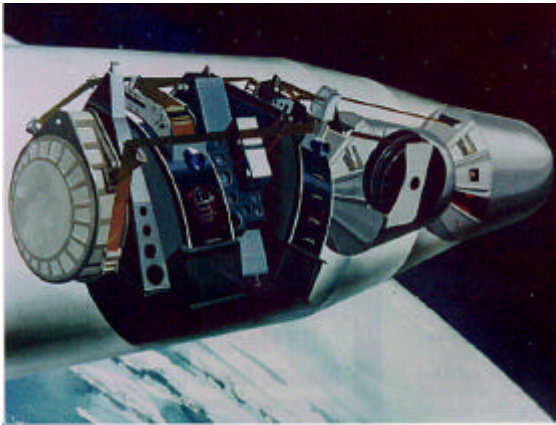
Figure 3-1 KH4B - artists concept
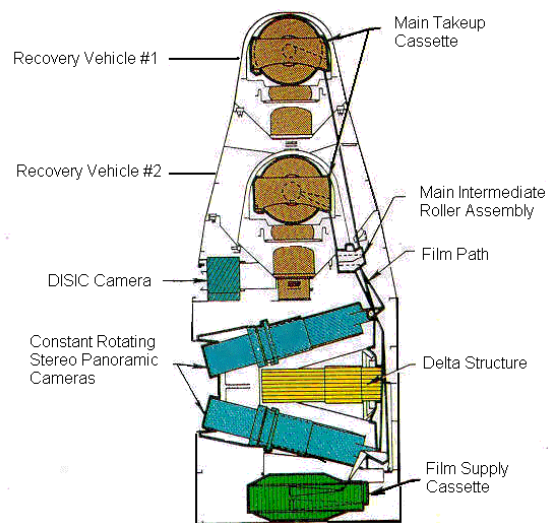
Figure 3-2 KH4B, or J3 camera. DISIC=Dual Improved Stellar Index Camera
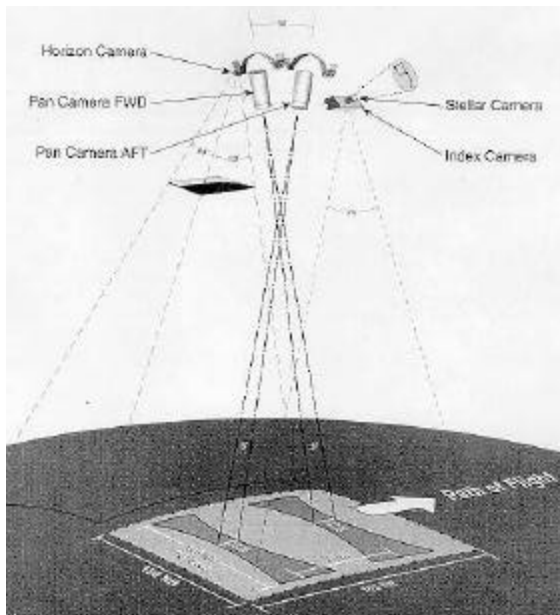
Figure 3-3. The KH4B cameras operated by mechanically scanning to keep the ground in focus. The paired cameras provided stereo images, which are very helpful for estimating the heights of cultural and natural features.

Figure 3-4. A U.S. Air Force C-119, and later, a C-130 (shown here) modified with poles, lines and winches extending from the rear cargo door captures a capsule ejected from a Discoverer satellite. Reportedly, this was considered by some to be the least likely part of the whole process - catching a satellite in midair.

3 Some illustrations

The first CORONA image, of the Mys Shmidta airfield, had high enough resolution to show the runway, and an adjacent parking apron.

Figure 3.5 Mys Shmidta Air Field, USSR. This August 18, 1960, photograph is the first intelligence target imaged from the first CORONA Mission. It shows a military airfield near Mys Schmidta on the Chukchi Sea in far-northeastern Russia.

Eventually, the systems got better, and higher resolution images were acquired

a) One always popular target - the Pentagon

b) Notice the shadow cast by the Washington monument.

Figure 3.6 Washington DC

Of course, the whole point was to spy on the Soviet Union. Here is Severodvinsk Shipyard, a North Sea port for the USSR, on 10 February 1969. The largish rectangular building in the center is the construction hall, and the square courtyard to the right is where vessels (submarines) are launched. The disturbed snow/ice (curved) trail is where they are floated into the river. The satellite is on a southbound pass over the port facility. (Eye in the Sky, The story of the Corona Spy Satellites, edited by Dwayne A Day, John M. Logsdon, and Brian Latell, 1998, page 224)

Figure 3.7 Severodvinsk Shipyard
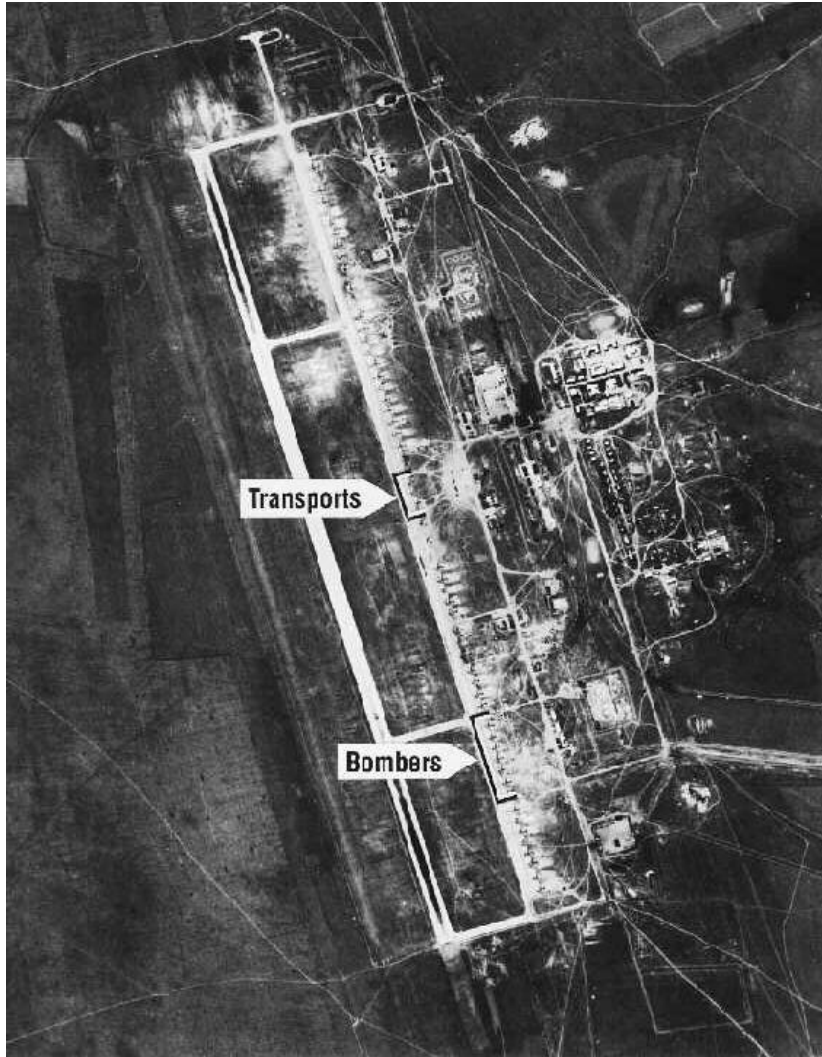
Figure 3.8
a) Air order of Battle is a fairly natural element of such imagery. The 5-10 foot resolution of the Keyhole camera systems was sufficient to distinguish classes of aircraft.

b) An image chip for the bombers indicated in the lower portion of the figure is displayed here.

B Interpretation keys (Elements of Recognition)

Having seen some of the early imagery, we now proceed to consider a few elements on the interpretation of imagery. The perspective used here is one developed for airphoto interpretation. (Avery and Berlin, pages 52-57)

1 Shape

One of the most useful elements of recognition is shape. One of the classic examples is the Pentagon, shown earlier in Figure 3-6. Note that in Figure 3-5, the airfield can be identified by the shape, even though it is not well resolved.

2 Size

Relative size is helpful in identifying objects; mensuration, the absolute measure of size, is extremely useful in extracting information from imagery. Illustrations at the beginning of Chapter 1 showed how runway length can be obtained from properly calibrated imagery. The Hen House radar sites (Figure 1-4) have characteristic shapes and sizes.

3 Pattern

Related to shape is pattern, the overall spatial form of related features. Figure 3-9 shows a Russian SAM site, with characteristic patterns that help detect the missile sites. A common illustration is the Russian propensity for putting three concentric fences around important installations.
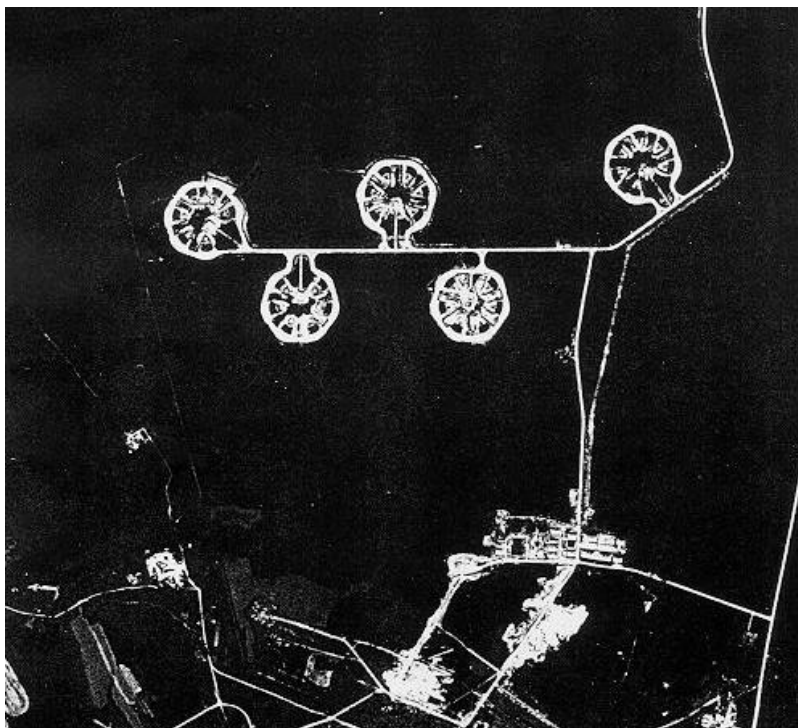
Figure 3.9 SA-2 SAM Base, KH-4 CORONA Product

4 Shadow

Shadows can be very helpful in separating targets from background. They can also be used to measure height. See the Washington monument illustration (Figure 3-6b).

5 Tone or color

Tone and color are the product of the target albedo, and illumination. The Landsat images in chapter 1 are good illustrations of this element. Consider the difference in tone between the runway (asphalt?) and adjacent regions in Figure 1-10b. The green regions on the south end of Coronado island can be distinguished from regions of similar brightness by the color. On a larger scale, the distinction between dirt and vegetation in San Diego County can also be made in color.

6 Texture

Texture depends upon the image scale, but can be used to distinguish objects which may not otherwise be resolved. The relative coarseness or smoothness of a surface becomes a particularly important visual clue with radar data. (Figure 1-19 b)

7 Association

"Certain objects are genetically linked to other objects, so that identifying one tends to indicate or confirm the other. Association is one of the most helpful clues for identifying cultural features." Avery and Berlin (1992). Things like nuclear power plants, for example, tend to be near source of cooling water, though this can also be associated with our last characteristic, which is site or location.

8 Site

This element is the location of an object relative to its environment.

C Some very simple geometric optics

1 Focal Length/Geometry

The most fundamental equation in optics is the thin lens equation:

$$\frac{1}{f} = \frac{1}{i} + \frac{1}{o} \qquad\qquad \text{(Eqn. 3-1)}$$

Here, f is the 'focal length', and intrinsic characteristic of the lens determined by the radius of curvature and the index of refraction of the lens material(s). The distances from the center of the lens to the object (o) and to the image (i) then are the other two parameters. We see that the focal length defines the image distance when o, the object distance, is infinity (∞). In the illustration here, the object distance is twice the focal length, so the image distance is also twice the focal length (I=O=2f).
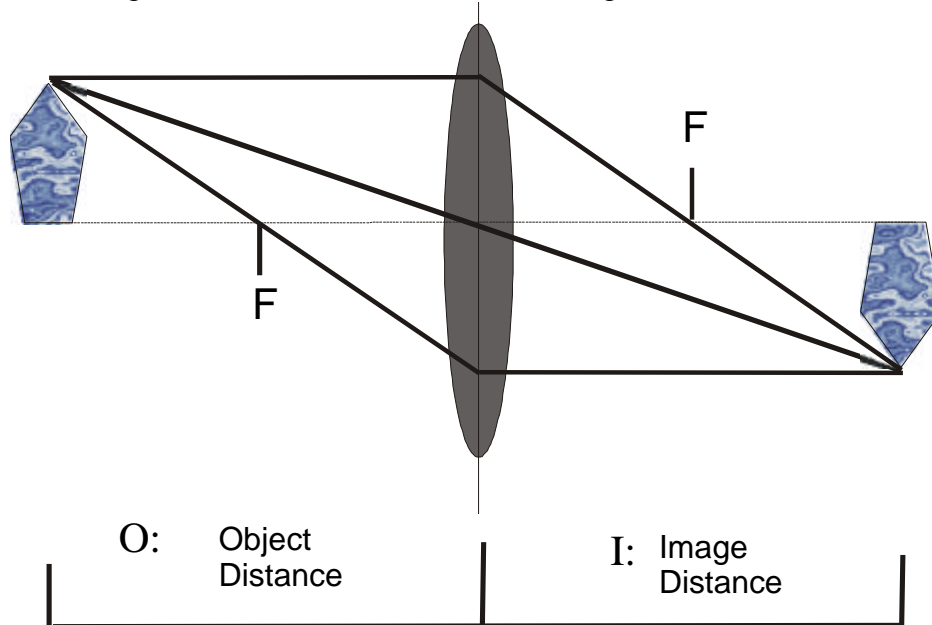
Figure 3.10 Thin lens law

2 Optical Diagram - Similar Triangles - Magnification

The size of the image is determined by the old geometry law of similar triangles - the magnification is equal to the ratio of the object distance to the image distance. In the example above, the two are equal so the image has the same size as the object. Normally, in remote sensing, the object distance is a large number, while the image distance is roughly the focal length. For example, the handheld camera on the shuttle is typically used with a 250 mm lens, at an altitude of 150 km. So, the ratio of the image size to the object is $\frac{250\times10^{-3}}{150\times10^{3}} = 1.6\times10^{-6}$ - a pretty small number.   The Monterey Peninsula

(extending some 20 km from north to south) would be imaged on a piece of film 0.032 m in length (32 mm - roughly the width of normal 35 mm film).
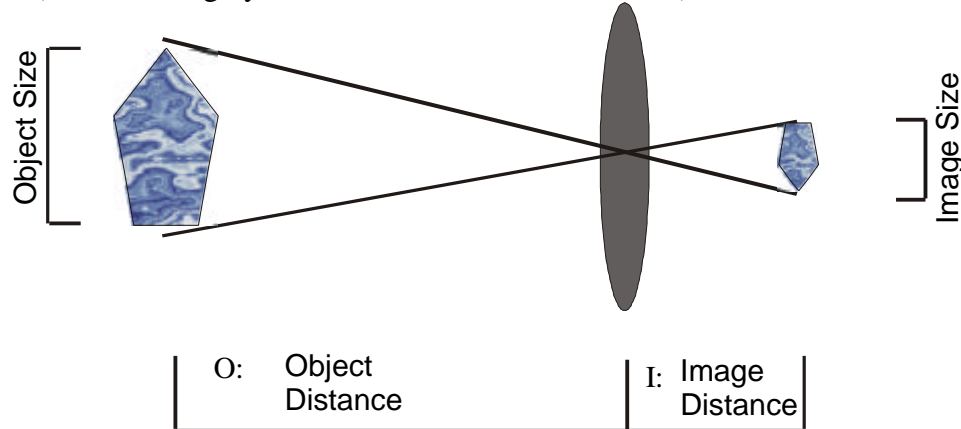
Figure 3.11 Magnification - similar triangles

3 Aperture (F/stop)

The light gathering ability of a lens is defined by the diameter of the lens - the bigger the better in optics! Still, the effectiveness of a given aperture depends upon the focal length (magnification). This dependence is defined by the concept of the f number, or f/stop. It is defined as the ratio of the focal length to the lens (or mirror) diameter.

$$f/\# = \frac{\text{Focal Length}}{\text{Diameter of the Primary Optic}} \qquad \text{(Eqn. 3-2)}$$

Typical camera lenses found on amateur cameras will vary from f/2.8 to f/4. High quality 'standard' lenses will be f/1.2 to f/1.4 for 35mm cameras. The longer the focal length (higher magnification), the large the lens needs to be. A typical telephoto for a sports photographer might be 500 mm, and might at best be f/8. (What is the diameter implied by that aperture?)

D Diffraction Limits

Light propagates as a wave, and hence does not propagate exclusively in straight lines. In common experience, this is more commonly encountered in situations where sound waves bend around barriers. A short theoretical development of the concept is given here. The foundation concept of interference is developed using the classic Young's Double Slit experiment.

Young's Double Slit experiment is based on the wave theory of light, and the understanding that waves can interfere with one another. In the drawing below, light can pass through either of the two small apertures shown, and travel to the right, hitting the screen at x, which is some distance in the vertical direction from the center line. The two

light rays will travel different distances, R_1 and R_2. Because of this difference, the two sets of waves will be somewhat out of phase. The difference in phase is just:

$$\Delta\Phi = 2p\frac{R_2 - R_1}{l} \qquad \text{(Eqn. 3-3)}$$

We want to relate this difference in phase to the distances R and x. Note that for satellites, R is the altitude, x will be the distance between two targets on the ground.
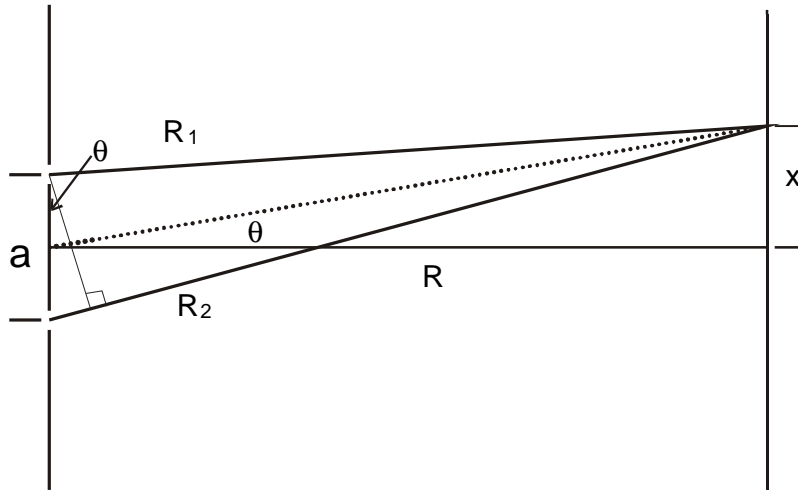
Figure 3.12 Young's Double Slit Experiment

Because the distance R is large compared to x or a, we can approximate:

$$q \approx \sin q \approx \tan q \approx \frac{x}{R} \qquad \text{(Eqn. 3-4)}$$

The two triangles shown are similar, and so we get the ratios:

$$\frac{R_2 - R_1}{a} = \frac{x}{R} \qquad \text{(Eqn. 3-5)}$$

From this, we can get the difference in phase between the light from the two slits:

$$\Delta\Phi = 2p\frac{R_2 - R_1}{l} = 2p\frac{a}{l}\frac{x}{R} = 2p\frac{a}{l}\sin q \qquad \text{(Eqn. 3.6)}$$

If the phase difference is π, the waves will cancel, and there will be a dark spot on the screen. The next bright spot will appear when the phase difference is 2π, followed by a minimum at 3π, and so on. If the intensity is plotted, a pattern like this occurs:
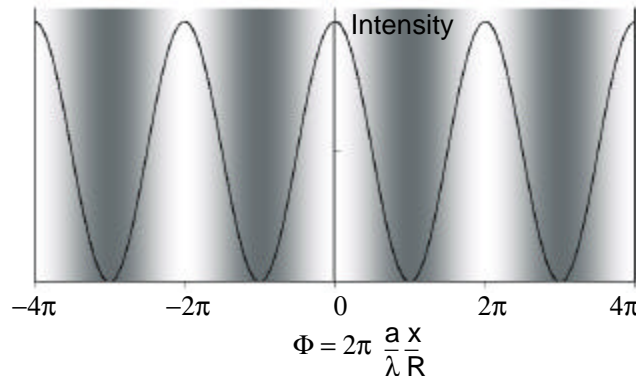
$$\Phi = 2\pi \ \frac{a}{\lambda} \frac{x}{R}$$

Figure 3.13 Double slit diffraction pattern. *Intensity* $\propto \ \mathrm{sinc}^2 \Phi$

The distance between two peaks is 2π, so the separations will be such that

$$\Delta\Phi = 2\pi = 2\pi \ \frac{a \ x}{\lambda \ R} = 2\pi \ \frac{a}{\lambda} \sin\theta; \ \ \text{or} \ \ \frac{a \ x}{\lambda \ R} = 1 \ \ \ \Rightarrow \qquad\qquad \text{(Eqn. 3.7)}$$

$$\Delta \ x = \frac{l \ R}{a}$$

What does this have to do with optical instruments?   The real answer lies in a fair amount more work, unfortunately. The extrapolation of this idea to optical systems is fairly simple, however. The above illustration considers light from two small sources (slits).   Conceptually, however, these could be two of the many small points on the surface of a lens. Light passing through different parts of the lens can interact with itself, causing interference. The smaller the lens (the smaller a is, above), the larger this effect will be.   The quantity Δx above becomes the separation between two points on the ground, or two stars in the sky that can be resolved. Once the mathematics is completed, a formula for the intensity of light passing through a circular aperture can be obtained that uses Bessel functions:

$$I \ \propto \ \left[\frac{J_1(w)}{w} \right]^2 , \ \text{where } w = \ \frac{2\pi \ a \ r}{R \ \lambda} . \qquad\qquad \text{(Eqn. 3.8)}$$

J_1=the 'J' Bessel function of order 1.
a = lens radius,
 r = distance from center line,
 R = distance from lens to screen, and
λ = wavelength.

This function looks like this:
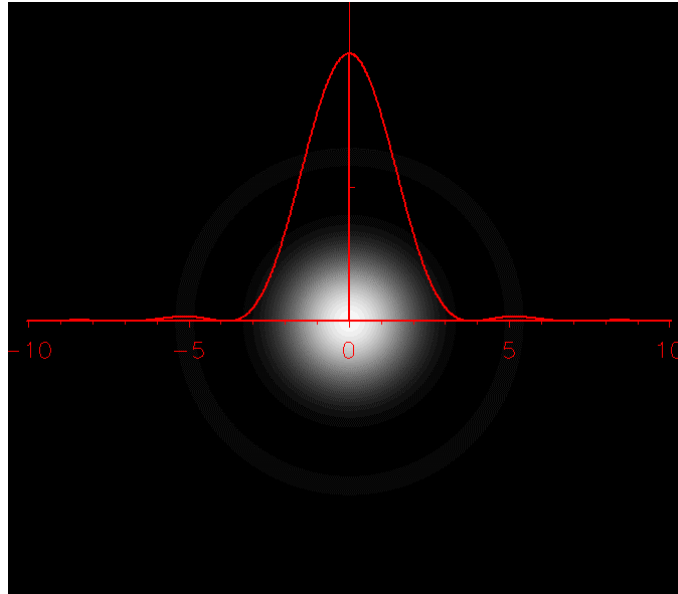
Figure 3.14

The first zero occurs where $w = 3.832$, which leads to a relatively famous result, that the radius of the 'Airy Disk' = 0.61*λ*distance/lens radius, or that the angular resolution of a lens is:

$$\Delta\theta = 0.61 \bullet \frac{\lambda}{a}, \text{ or } \Delta\theta = 1.22 \bullet \frac{\lambda}{\text{diameter}} \qquad \text{(Eqn. 3.9)}$$

For most purposes in these notes, we ignore the factor of 1.22.

Application:
  Hubble like system orbiting at 200 nautical miles = 370 km
  Mirror diameter = 96 inches = 2.43 meters (acts like lens diameter)
 wavelength = 5000 Angstroms = 5×10^{-7} m

Ground Separation Distance (GSD) =
$$\Delta x = \frac{\lambda R}{a} = \frac{5 \times 10^{-7} \bullet 370 \times 10^3}{2.43} = 7.5 \times 10^{-2} \text{ m } = 7.5 \text{ cm or 3"}$$

E Atmospheric Absorption, scattering, and turbulence

There are three limiting factors which the atmosphere introduces into remote sensing. These are absorption, typically by atomic and molecular processes; scattering, which is primarily due to aerosols (dust, fog, smoke); and turbulence, which is due to fluctuations in the temperature and density of the atmosphere. The first two terms combine to produce the effects illustrated in Figure 3.15, which shows a standard model for atmospheric absorption.
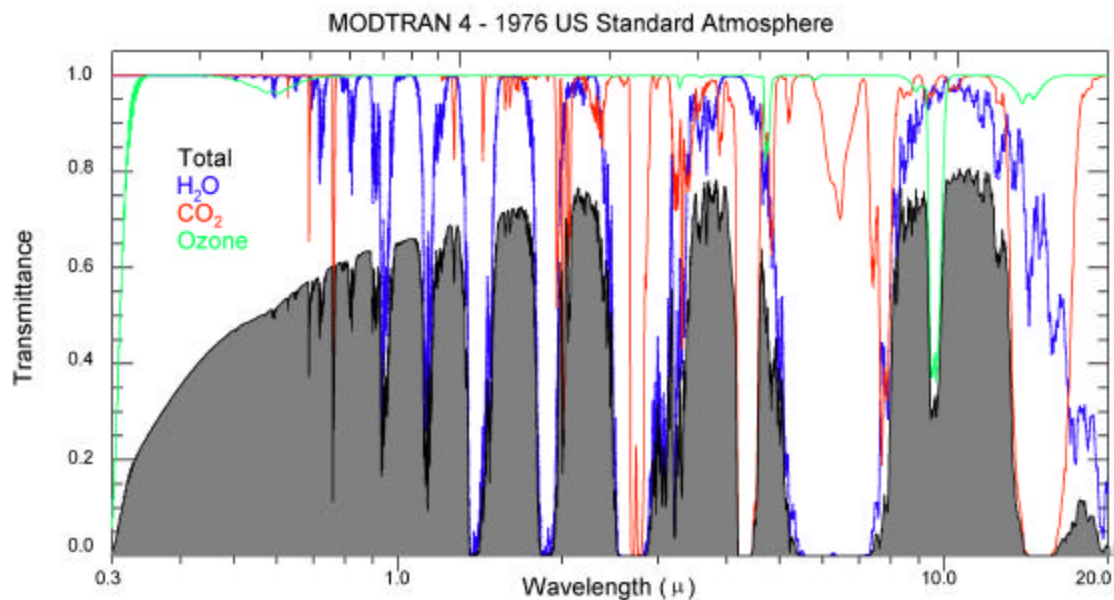
Figure 3.15 Atmospheric absorptions. Transmission curve calculated using MODTRAN 4.0, release 2. The total transmission is plotted, along with the effects for some of the primary atmospheric absorption elements - water, carbon dioxide, and ozone. Conditions are typical of mid-latitudes, with the 1976 US standard atmosphere assumed. The overall broad shape is due to scattering by molecular species and aerosols.

1 Atmospheric Scattering

Electromagnetic radiation within certain sections of the ultraviolet, visible, and reflected infrared bands is impeded in its direct journey through the atmosphere by the scattering process, which disperses the radiation in all directions. Important scattering agents include gaseous molecules, suspended particulates called aerosols, and clouds. Three types of atmospheric scattering are important to remote sensing.

Rayleigh, or **molecular, scattering** is primarily caused by oxygen and nitrogen molecules whose effective diameters are at least 0.1 times smaller than the affected wavelengths. Rayleigh scattering is most influential at altitudes above 4.5 km, occurring in what is called the **pure atmosphere.** The amount of Rayleigh scattering is highly selective, being inversely proportional to the fourth power of wavelength (λ^{-4}) (Figure 3-16). Consequently, invisible ultraviolet radiation, at a wavelength of 0.3 μ, is scattered 16

times as readily as red wavelengths at 0.6 μ [(0.6/0.3)^4]. In the visible spectrum, blue wavelengths at 0.4 μ are scattered about five times as readily as red wavelengths at 0.6 μ [(0.6/0.4)^4]. The preferential scattered of blue wavelengths explains why the clear sky (i.e., low humidity and few aerosols) appears blue in daylight. The blue wavelengths reach our eyes from all parts of the sky.

 Mie, or **nonmolecular, scattering** occurs when there are sufficient particles in the atmosphere that have mean diameters from about 0.1 to 10 times larger than the wavelengths under consideration. Important Mie scattering agents include water vapor and tiny particles of smoke, dust, volcanic ejecta, and salt crystals released from the evaporation of sea spray. The influence of Mie scattering is most pronounced in the lower 4.5 km of the atmosphere, where the larger Mie particles are most abundant (i.e., in the impure atmosphere).   Mie scattering influences longer radiation wavelengths than Rayleigh scattering. Depending upon the size distribution and concentration of Mie particles, the wavelength dependence varies between λ^{-4} and λ^0.

Figure 3.16 Atmospheric Scattering
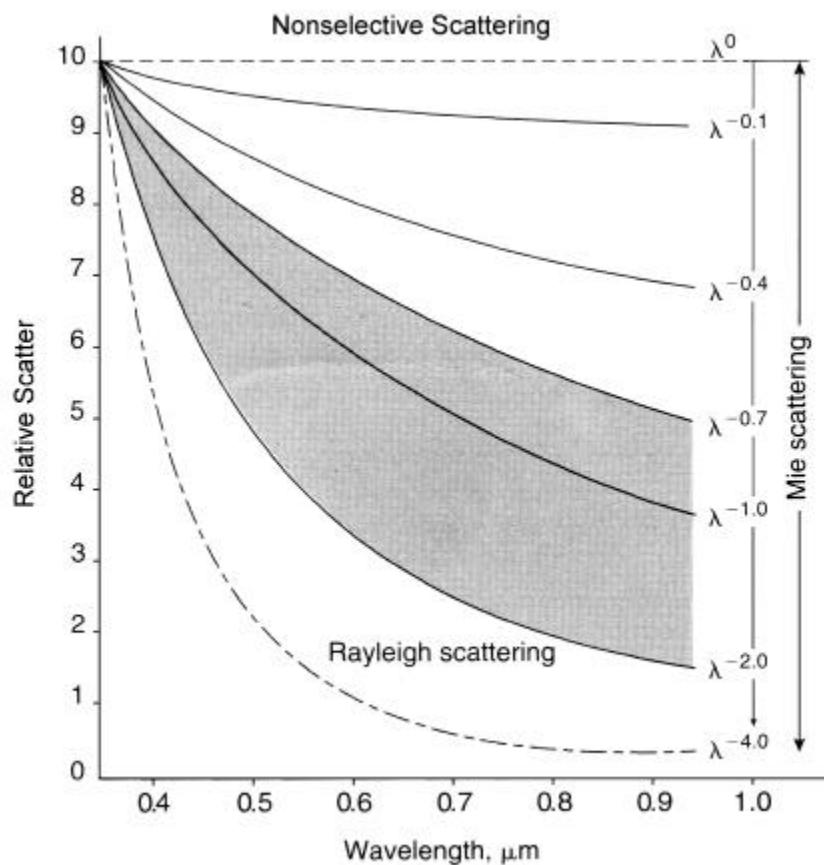
The clear atmosphere is a medium for both Rayleigh and Mie scattering. For a range of typical atmospheres, their combined influence is from about $\lambda^{-0.7}$ to λ^{-2} (Figure 3-16). Using a λ^{-2} relationship, blue wavelengths at 0.4 μ are scattered about three times as readily as red wavelengths at 0.7 μ [(0.7/0.4)$^{-4}$]. The observation of a red sunrise or

sunset is caused by the preferential treatment of Rayleigh and Mie scattering agents on sunlight. At these times, the solar beam, which starts out as white light, passes through its longest atmospheric path. This extended path causes the shorter wavelengths of sunlight to be scattered away (blue and green), leaving only the red wavelengths to reach our eyes.

Nonselective scattering becomes operative when the lower atmosphere contains a sufficient number of suspended aerosols having diameters at least 10 times larger than the wavelengths under consideration. Important agents include the larger equivalents of Mie particles plus the water droplets and ice crystals of which clouds and fog are composed. Non-selective scattering is independent of wavelength (λ^0). Its influence spans the near ultraviolet and visible bands and extends into the reflected infrared band (Figure 3-16).

Within the visible band, colorless water droplets and ice crystals scatter all wavelengths equally well, causing, for example, the sunlit surfaces of clouds to appear brilliant white. Also, large smog particles, if not possessing special absorption properties, will cause the color of the sky to go from blue to grayish white.

2 Atmospheric Turbulence

The third limiting factor in remote sensing through the atmosphere is atmospheric turbulence, which might also be termed the question: Why do stars twinkle? The answer is illustrated by Figure 3.17. This effect is much greater looking up out through the atmosphere than looking down at the earth.

Figure 3.17 a
Light propagating down through the atmosphere will encounter small perturbations of density and temperature, due to turbulent processes in the atmosphere. These small fluctuations produce variations in the index of refraction, which in turn cause small fluctuations in the direction in which the light is propagating.

Density/Temperature Fluctuations

Figure 3.17 b, c
First light for the adaptive optics system on the 3.5-m telescope at the Starfire Optical Range
occurred in September, 1997. This astronomical I Band (850 nm) compensated image of the
binary star Kappa-Pegasus (k-peg) was generated using the 756 active actuator adaptive optics
system. The two stars are seperated by 1.4544 microradians (4.85 microradians/arcsecond).
The images are 128x128 pixels - each pixel subtends 120 nano-radians, or 3.17 arcsec. The
FWHM of the uncompensated spot is about 7.5 microradians - about 5 times the separation of the
two stars.
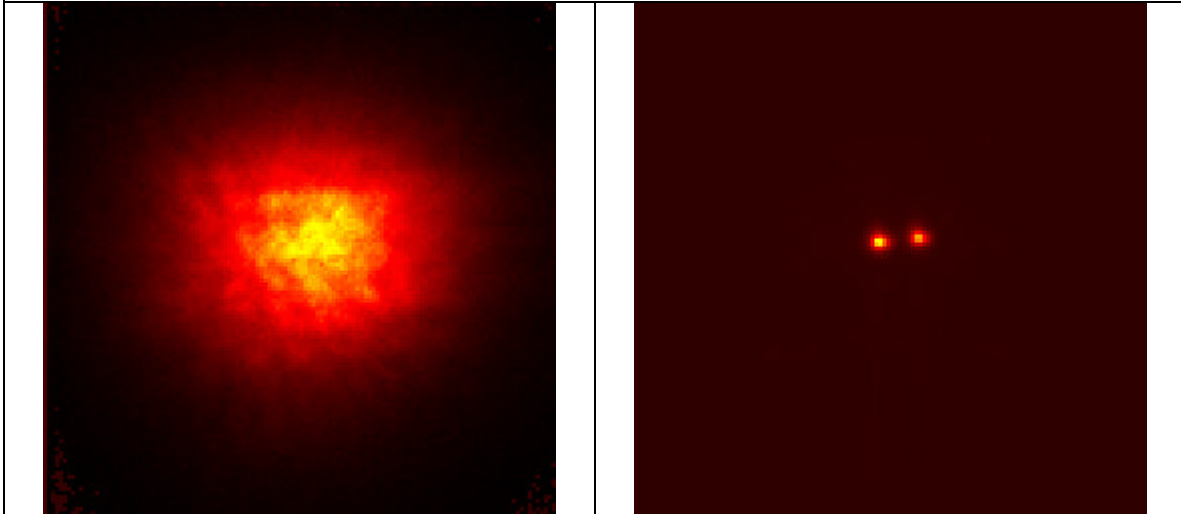
Note on nomenclature:
Astronomy IR Bands are: H (1.65 microns), I (0.834 microns),J (1.25 microns), K (2.2
microns).

Summary: there are three factors which constrain the resolution which can be obtained
with an imaging system: diffraction (the Rayleigh criterion), scattering, and turbulence.

F Detectors

The other primary element in any sensor system is the detector behind the optics. Historically, there have been two primary techniques: film and solid state.

1 Film

The role of film in remote sensing is an increasingly historical one, as the last of the space-based film systems (notably the Russian SPIN system) are being phased out. There is still a substantial airborne film imaging community, but this is also evaporating fairly rapidly, at least on the military side.

2 Solid State

Generally speaking, the detectors involved in remote sensing utilize arrays of solid-state detectors, much like the CCD detectors in modern video cameras, and digital still cameras. Though not a bad starting point, this rather broad statement about the class of sensors also termed focal plane arrays (FPA's), does not properly take into account the many sensors today flying linear arrays (1-dimensional focal planes) as on SPOT, and even the ongoing use of single detector sensors, such as on GOES and Landsat. Still, the underlying physics is similar for most such sensors.

Just as with the Bohr atom, as developed in Chapter 2, solid materials, and in particular semi-conductors, have a distribution of energy levels which may be occupied by electrons. Generally, the electrons reside in a state corresponding to the ground state of an individual atom, termed the Valence Band. There is then a gap in energy (a "bandgap"), which represents a range of energies that are forbidden for the electron to occupy.
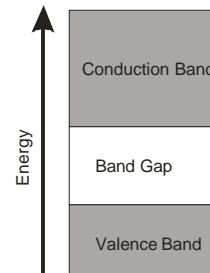
Figure 3.18

If a photon hits the semiconductor, however, it can give energy to an electron in the valence band, exciting it up into the conduction band. The significance of this is that it is now possible for the electron to move as though in a conductor, and it can be collected and measured. This is the essence of the detection mechanism for most solid state detectors. Such detectors have an efficiency that varies, but typically 40-80% of the incident photons with sufficient energy can be detected.

Material	Bandgap energy (eV) at 300 K
Silicon	1.12
Germanium	0.66
Gallium Arsenide	1.424
Indium Antimonide	?
Platinum Silicide	?
HgCdTe	0.1 to 0.3

This simple description makes it possible to quickly follow some of the more important constraints in the use of solid state detectors. First, one must match the energy bandgap to the energy of the photons you wish to observe. The photon energy must be at least

equal to the size of the bandgap, which varies with material. (Find the values for Platinum Silicide (PtSi), and Indium Antimonide (InSb))

What limits do these values place on the utility of different materials for use as detectors? Taking silicon as the most common example, we recall from Chapter 2 the equation which relates wavelength to the energy in a transition:

$$\lambda \ = \ \frac{hc}{\Delta E}$$

Here, ΔE is the band gap energy (in eV), and we use:

$$\lambda \ = \ \frac{hc}{\Delta E} \ = \ \frac{1.24 \times 10^{-6} \ (\text{eV m})}{1.12 \ \text{eV}} \ = \ 1.1 \times 10^{-6} \ \text{m, or 1.1 microns.}$$

So, the visible and the first part of the near-infrared spectrum can be detected with silicon detectors. This is reflected in their common usage in modern cameras.

The detection of longer wavelength photons requires the usage of materials such as HgCdTe, or InSb. The relatively small bandgaps cause a problem, however. At room temperature, the electrons tend to rattle around a fair amount, and every now and then one will cross the gap, just based on thermal excitation. This is a process which is largely controlled by the exponential term which comes from the "Maxwell-Boltzmann" distribution (bell-shaped curve) which describes the velocities, or energies, which will be found in any collection of objects (electrons, atoms, molecules) in a thermal equilibrium:

$$number \ \propto \ e^{-\frac{\text{Bandgap Energy}}{\text{Thermal Energy (kT)}}} \qquad\qquad\qquad \text{(Eqn. 3-10)}$$

If collected, this becomes part of a background noise termed the "dark current". In order to prevent this, the materials must be cooled - typically to 50-70 K, which requires liquid nitrogen cooling at least, and for some applications, liquid helium (4 K). Mechanical refrigerators can also be used, but are a concern in space applications.

Quick illustration of why cooling is important:

Use HgCdTe, assume a Bandgap of 0.1 eV, and compare the nominal number of electrons above the band gap at room temperature (300 K) and at 4 K.   Note that the conversion factor "k" in the term "kT" is:

$$1.38\times10^{-23} \; \tfrac{\text{Joules}}{\text{Kelvin}} \Big/ 1.6\times10^{-19} \; \tfrac{\text{Joules}}{\text{eV}} = 8.62\times10^{-5} \; \tfrac{\text{eV}}{\text{Kelvin}}$$

T = 300 K: $kT = 0.026$ eV ; T = 4 K , $kT = 0.00035$ eV

$$number \; \propto \; e^{-\frac{\text{Bandgap Energy}}{\text{Thermal Energy (kT)}}} = \begin{cases} e^{-\frac{0.1}{0.026}} = e^{-3.8} = 0.02 \quad @\,300\ \text{K} \\[2ex] e^{-\frac{0.1}{0.00035}} = e^{-286} \approx 0 \quad @\ \ 4\ \text{K} \end{cases}$$

At room temperature, the exponential is small, but reflects a non-negligible number of excitations of electron above the band gap energy. In liquid helium, the electrons sit quietly below the band gap.

Visible imaging cameras uniformly use silicon as the sensitive element. As of this writing, one finds that typical commercial infrared imaging systems that use InSb, PtSi, and HgCdTe. (e.g. FLIR systems family of cameras). In addition, there are two popular new technologies: quantum well (QWIP) and micro-bolometer detectors. The latter in particular offers a variety of advantages over the more traditional cooled semi-conductor systems.

3 Focal Plane Arrays

The photo-sensitive component of a detector can exist as a single element, and there are a number of operational systems which nominally have a single detector. A notable current example would be the GOES weather satellite, described in a subsequent chapter. Generally, however, newer systems are comprised of either linear arrays of pixels, as will be seen below for IKONOS, with an array which is 1x13,500 pixels, or by rectangular arrays. The latter currently would be something like the 640x480 CCD arrays found in a low-cost electronic camera.

A CCD (charge coupled device) is an array of sensitive elements,

The CCD imager evolved from a low-cost memory element in 1970, called a charge-coupled device (CCD). The CCD is an integrated circuit (IC) with the unique property that a charge held in one cell of the IC can be shifted to an adjacent cell by applying a suitable shift pulse. Information defined by the amount of charge can be shifted from cell to cell with virtually no loss. When it was further discovered that the construction could be altered so that individual cells also responded to incident light while retaining the ability to shift charges, the dream of a solid-state imager was born.

Many charge coupled cells or picture elements are arranged in a rectangular array. Each picture element, also called a pixel of the array, converts incoming light into a charge directly proportional to the amount of light received. This charge is then clocked (shifted) from cell to cell, to be finally converted to a video signal that represents the original image, at the output of the CCD.

4 Uncooled Focal Planes - Microbolometers

One of the problems with the traditional technology associated with semi-conductor detectors is the need for cooling. This is because cooling either requires a coolant (e.g. liquid nitrogen), or a mechanical refrigeration technique. The former is often awkward in the field, and for space use a finite supply of coolant defines a limit on detector lifetime. Mechanical devices are in general problematic for space use, because of a concern over mechanical failure.

Microbolometer techniques approach the detection process by sensing the change in temperature of a sensitive element, typically by measuring the resistance of that element. This allows the direct detection of "heat", as opposed to counting photons directly. As a consequence, the detectors do not need to be cooled. Commercial IR cameras are now being manufactured using these detectors, and they are very popular for applications such as fire-fighting. Such cameras at present are not quite as sensitive, and do not presently have the resolution of the more traditional technologies.

G Imaging system types

Remote sensing systems can generally be divided in to a handful of basic types, depending upon the form of imaging technology being used. These distinctions will affect the resolution and sensitivity of the system, and to a certain extent, the quality of the data.

1 Framing systems - mostly film systems (Corona)

Framing systems are those that snap an image, much like a common film camera, or a modern digital (still or video) camera. An image is formed on a focal plane, and the image is stored via chemical (film) or electronic (CCD) means. Variants on this technique are used by some air-photo systems, and the early Corona satellites, where the film is moved in concert with the satellite motion, to maintain a longer exposure time and better focus.
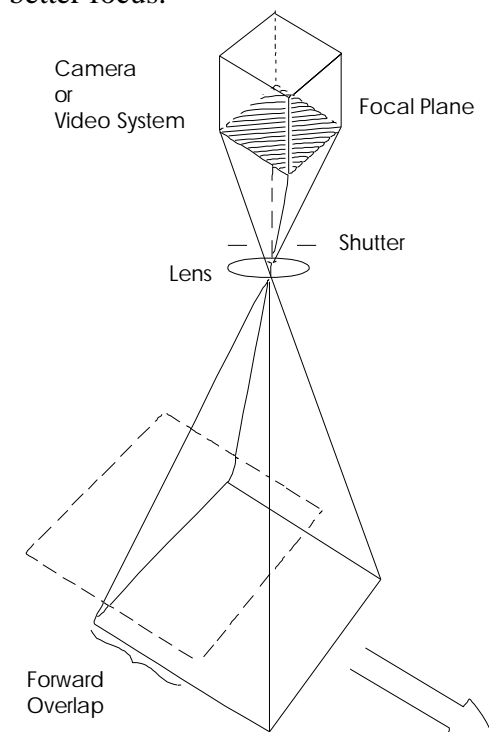
Figure 3-19. Framing System
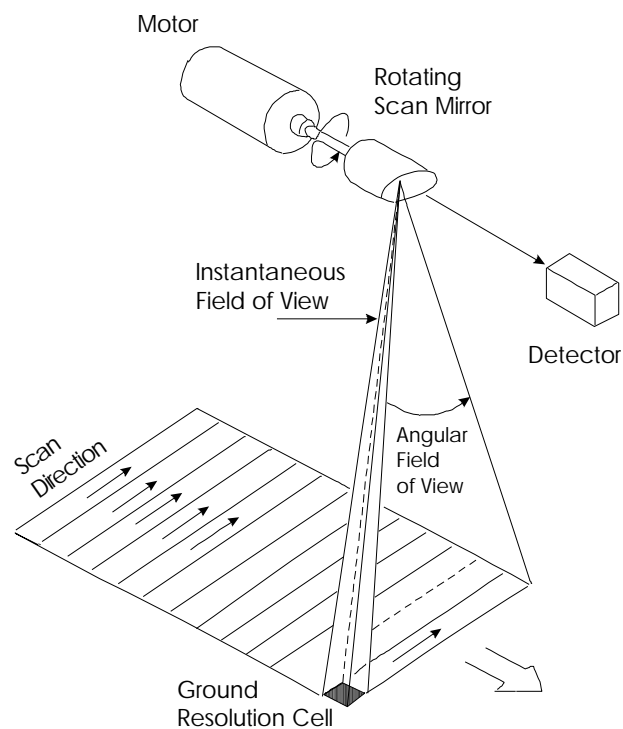
Figure 3-20. Cross-Track Scanner

2 Scanning Systems

a Cross Track (Landsat MSS, TM; AVIRIS)

Sensors such as those on the GOES weather satellite and the Landsat system consist of a small number of detectors - from one to 32 or so in the systems described later in the text. The sensor is swept from side to side, typically via an oscillating mirror, while the system flies along-track. The image is built up by the combined motion of the optic and the platform (aircraft or satellite).

b Along Track (SPOT HRV)

Linear detector arrays are used in systems such as the SPOT HRV sensor. The 'cross-track' dimension is covered by the linear array, while the along track direction is covered by the motion of the satellite.
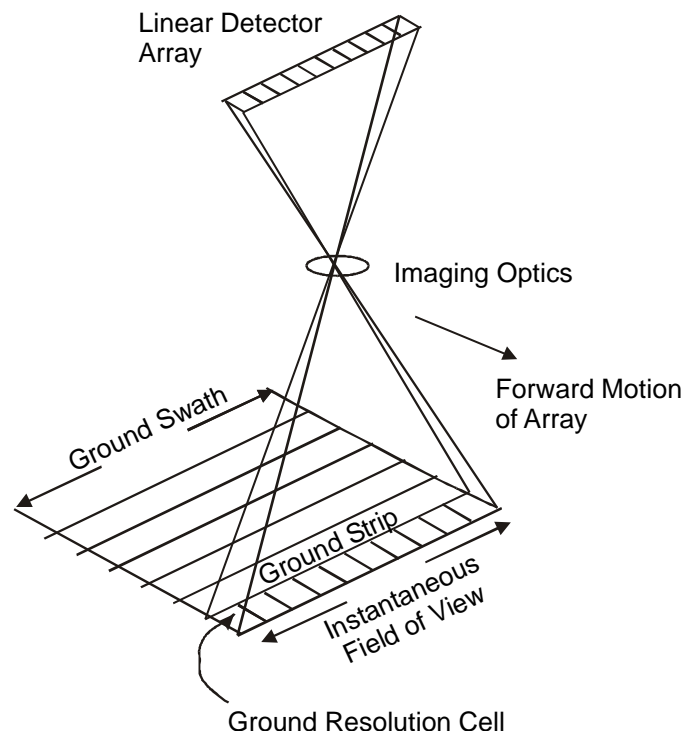
Figure 3.21 Pushbroom system

In subsequent sections we will consider how these techniques have been implemented in space imaging systems.

H Hubble - The Space Telescope

Three modern systems are described below, beginning with a fairly detailed consideration of the Hubble Space Telescope. Following that, the commercial IKONOS satellite will be briefly described, and a brief presentation of the low-light level imaging capability of DMPS will be made.

1 The Hubble Satellite

The Hubble Space Telescope (HST) was deployed April 25, 1990 from the space shuttle Discovery (STS-31). It has since been serviced three times, on the STS-61 shuttle mission launched on December 2, 1993, and then again on STS-82, launched on February 11, 1997, and on STS-103 launched on December 19, 1999.

Figure 3.22 The initial deployment of the Hubble Space Telescope.

STS 61 was the fifth flight of the Endeavour orbiter. Its objective was to repair, replace, and update the instruments on the Hubble Space Telescope. During several days of EVA, the crew installed corrective optics (COSTAR) in the light path after removing the High Speed Photometer (HSP) instrument; replaced the older Wide Field/Planetary Camera (WF/PC) with a newer version (WFPC 2); and replaced malfunctioning solar arrays.

The STS-82 mission had similar goals. During several days of EVA, the crew replaced a failed Fine Guidance Sensor (FGS), swapped one of the reel-to-reel tape recorders with a solid-state recorder, and exchanged two of the original instruments, the Goddard High-Resolution Spectrograph (GHRS) and the Faint Object Spectrograph (FOS), with two new instruments, the Space Telescope Imaging Spectrograph (STIS) and the Near Infrared Camera and Multi-Object Spectrometer (NICMOS). In addition to this planned work, astronauts discovered that some of the insulation around the light shield portion of

the telescope had degraded and attached several thermal insulation blankets to correct the problem.

The STS-103 mission was launched to replace the 6 gyroscopes, after the failure of 4 of the old gyros. In addition to the gyros, astronauts also replaced a guidance sensor and a transmitter, installed a new, advanced central computer, a digital data recorder, battery improvement kits, and new outer layers of thermal protection.
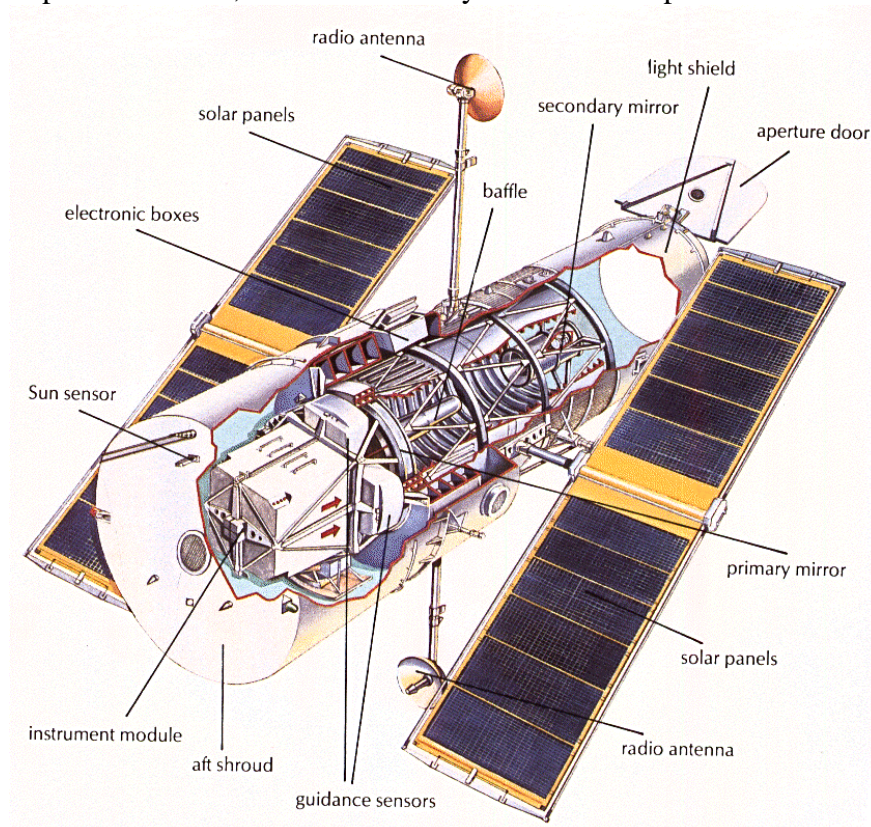
Figure 3.23 The Hubble satellite.

HST is roughly cylindrical in shape, 13.1 m end-to-end and 4.3 m in diameter at its widest point. The ten-ton vehicle is three-axis-stabilized. Maneuvering is performed via four of six gyros, or reaction wheels. Pointing can be maintained in this mode (coarse track) or the Fine Guidance Sensors (FGSs) can be used to lock onto guide stars (fine lock) to reduce the spacecraft drift and increase the pointing accuracy. It has a pointing accuracy of 0.007 arc-seconds.

Power to the two on-board computers and the scientific instruments is provided by two 2.4 x 12.1 m solar panels, which provide a nominal total power of 5 kW. The power generated by the arrays is used to power the satellite system (about 1.3 kW), and the science instruments (1-1.5 kW), and charge the six nickel-hydrogen batteries needed to provide power to the spacecraft during the roughly 25 minutes per orbit in which HST is within the Earth's shadow. (ref: e-mail from Dr. J. Keith Kalinowski, NASA/GSFC, 3 August, 1999)

Communications with the satellite are maintained with the TDRSS satellites. Observations taken during the time when neither TDRSS is visible from the spacecraft are recorded and dumped during periods of visibility. The spacecraft also supports real-time interactions with the ground system during times of TDRSS visibility. The primary data-link is at 1024 kbps.

There are two interesting constraints on the satellite behavior which are instructive, and which will affect most any LEO satellite.

South Atlantic Anomaly

Above South America and the South Atlantic Ocean lies a lower extension of the Van Allen radiation belts called the South Atlantic Anomaly (SAA). No astronomical or calibration observations are possible during passages of the spacecraft through the SAA because of the high background induced in the detectors. SAA passages limit the longest possible uninterrupted exposures, to about 12 hours (or 8 orbits).

Spacecraft Position in Orbit

Because HST's orbit is low, atmospheric drag is significant. Moreover, the amount of drag varies, depending on the orientation of the telescope and the density of the atmosphere, which depends on the level of solar activity. The chief manifestation of this effect is that it is difficult to predict in advance where HST will be in its orbit at a given time. The position error may be as large as 30 km within two days of a determination of the position of the spacecraft in its orbit.

Launch Date/Time	1990-04-25 at 12:33:51 UTC
On-orbit dry mass	11600.00 kg
Nominal Power Output	5000 W (BOL)
Batteries	Six – 60 Amp-hour NiMH
Orbital Period	96.66 m
Inclination	28.48 degrees
Eccentricity	0.00172
Periapsis	586.47 km
Apoapsis	610.44 km
Telemetry rates	0.500 - 1000.000 kbps
Effective Telemetry Rate	4.238 kbps

Figure 3.24 From STS82 - the second service mission - February 19, 1997
New solar arrays have not been deployed, yet. (S82E5937, 07:06:57)

2 The Hubble Telescope

The Hubble is an f/24 Ritchey-Chretien Cassegrain system with a 2.4 meter (94.5") diameter primary mirror, and a 0.3 m secondary mirror. The primary mirror is constructed of ultra-low expansion silica glass and coated with a thin layer of pure aluminum to reflect visible light. A thinner layer of magnesium fluoride is layered over the aluminum to prevent oxidation and to reflect ultraviolet light. The secondary mirror is constructed from Zerodur, a very-low thermal expansion (optical) ceramic material. The effective focal length is 57.6 m.

The distance between the two mirrors is 4.6 m, the focal plane is 1.5 m from the front of the primary mirror. The angular resolution at 500 nm is 0.043 arc-seconds. Note that the corresponding requirement for the spacecraft was a pointing accuracy (jitter) of 0.007 arc-seconds.   This was more easily achieved after the first set of solar arrays were replaced.
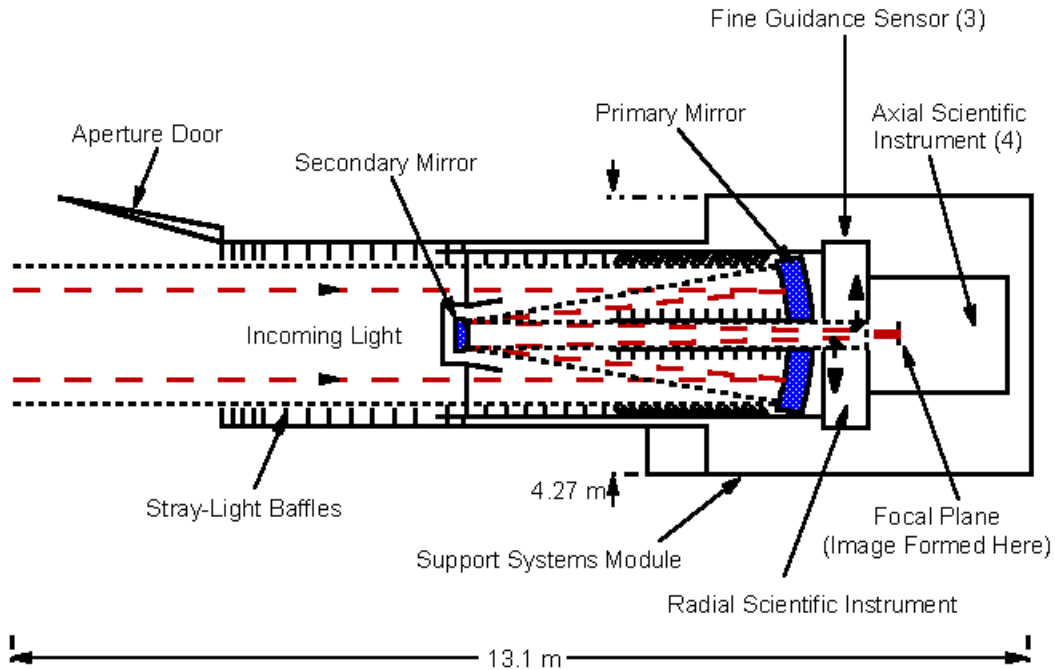
Figure 3.25 The Hubble Optics

There was just one small problem – the mirror was not ground to quite the right prescription, and it suffered from spherical aberration. As a consequence, new optics designs were created, and a very expensive corrective optic was applied for the existing instruments. Subsequent science instruments, such as the WFPC2, built corrections into their own optics.

Figure 3.26 The primary mirror of the Hubble telescope measures 2.4 m (8 ft) in diameter and weighs about 826 kg (1820 lbs). The center hole in the primary mirror has a diameter of 0.6 m.
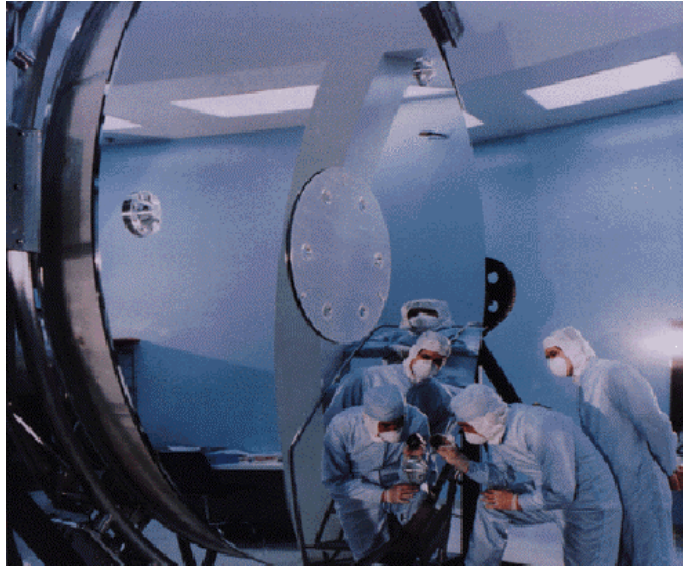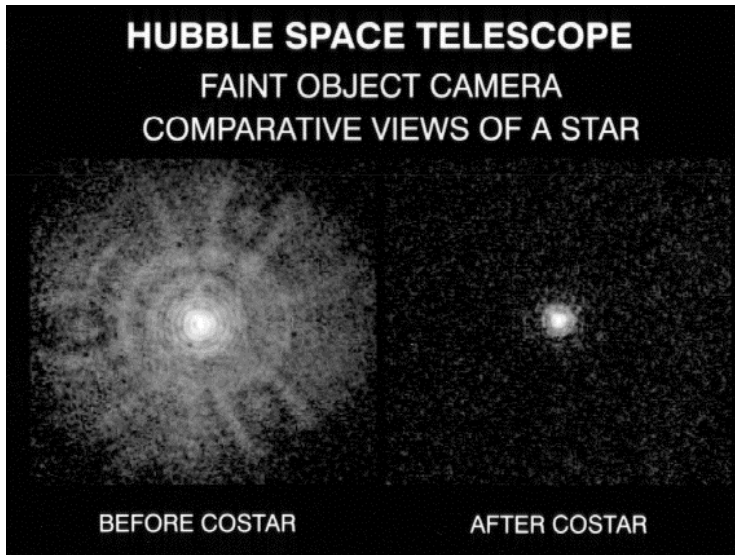
Figure 3.27: Left: An FOC image of a star taken prior to the STS-61 Space Shuttle mission to service the HST during which astronauts installed COSTAR. Right: Following the installation, deployment, and alignment of COSTAR, the starlight is concentrated into a 0.1 arc second radius circle.

3 Detectors - Wide Field Planetary Camera - 2

The Hubble normally carries 4 or 5 distinct sensors. For illustration purposes, the Wide Field and Planetary Camera 2 (WFPC2) is described here. *HST*'s Scientific Instruments are mounted in bays behind the primary mirror. The Wide Field Planetary Camera 2 occupies one of the radial bays, with an attached 45 degree pickoff mirror that allows it to receive the on-axis beam.
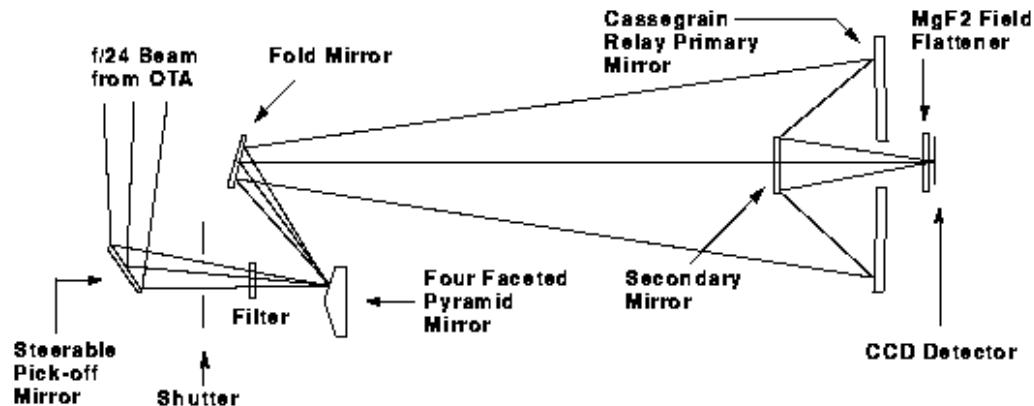
Figure 3.28 WFPC2 optics. Light enters the optical train from the main telescope at the left of the diagram.

The WFPC2 field-of-view is distributed over four cameras by a four-faceted pyramid mirror near the HST focal plane. Each of the cameras contains an 800×800 pixel Loral CCD detector. Three cameras operate at an image scale of 0.1" per pixel (F/12.9) and comprise the Wide Field Camera (WFC). The three cover an "L" shaped field-of-view of 150" x 150". The fourth camera operates at 0.046" per pixel (F/28.3) and is referred to as the Planetary Camera (PC). The fourth camera observes a smaller sky quadrant – a 34" x 34" square field. (Note that 34" is 34 arc-seconds, not 34 inches.)   The spectral range lies from approximately 1150Å to 10500Å.
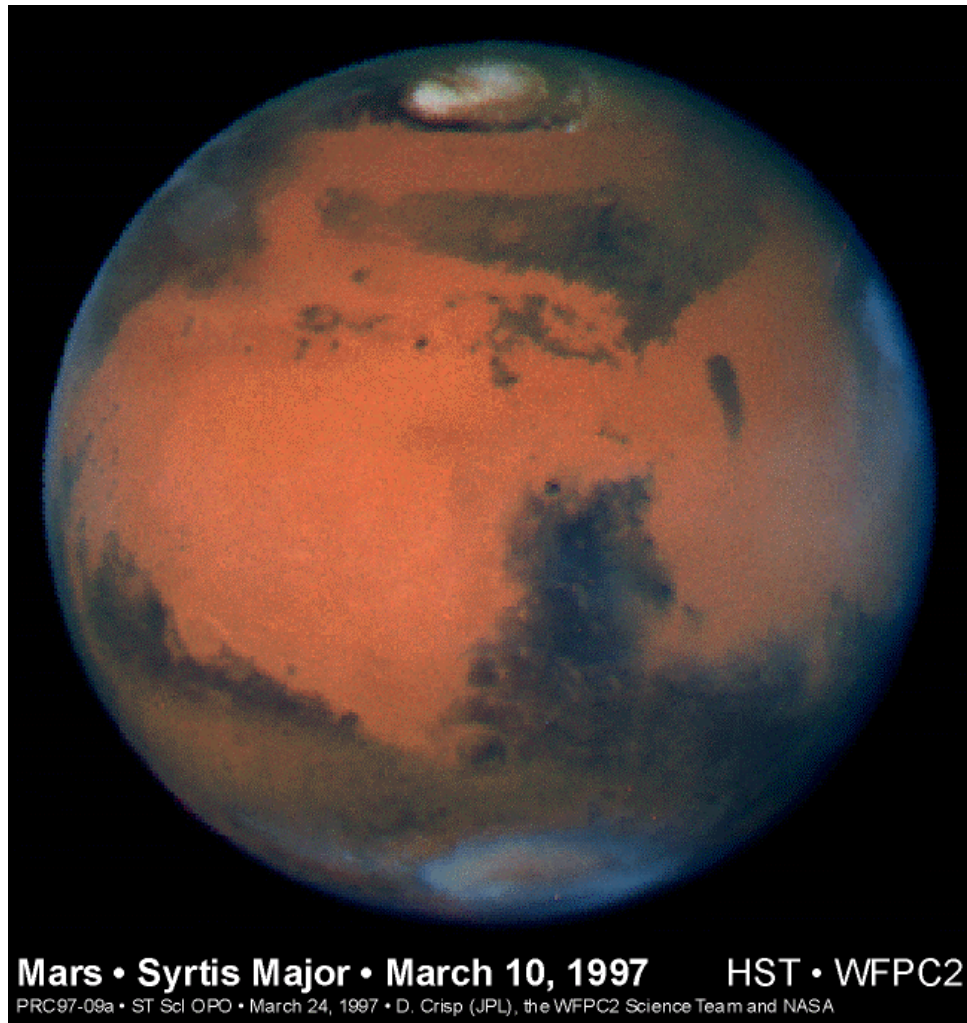
Figure 3.29 The sharpest view of Mars ever taken from Earth was obtained by the NASA Hubble Space Telescope (HST). This stunning portrait was taken with the HST Wide Field Planetary Camera-2 (WFPC2) on March 10, 1997, just before Mars opposition, when the red planet made one of its closest passes to the Earth (about 60 million miles or 100 million km). At this distance, a single picture element (pixel) in WFPC2's Planetary Camera spans 13 miles (22 km) on the Martian surface. The image is less than 335 pixels across - the Martian diameter is 6,794 km.

The WFPC2 was used to observe Mars in nine different colors spanning the ultraviolet to the near infrared. The specific colors were chosen to clearly discriminate between airborne dust, ice clouds, and prominent Martian surface features. This picture was created by combining images taken in blue (433 nm), green (554 nm), and red (763 nm) colored filters.

STScI-PRC97-09, March 20, 1997, David Crisp (JPL) and the WFPC2 Science Team

a Example: Diffraction and resolution limits
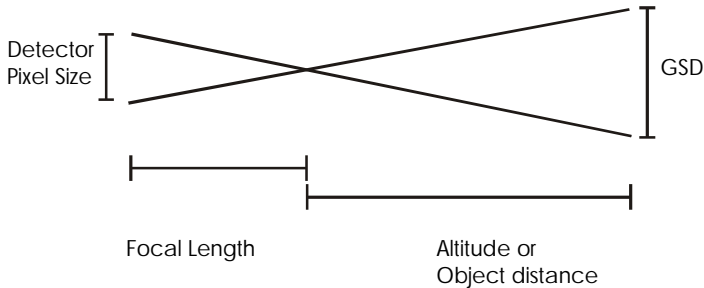
Figure 3.30 For the Hubble/WFPC2 combination, altitude is 600 km, detector size is 15 μ (microns), the focal length is 57 meters.

Rayleigh:

The angular resolution for the telescope is given as 0.043" (arc-seconds), with the slightly larger value of 0.046" for the combined Hubble/WFPC2 system. These values include all the effects which are ignored in the simplest approximation to the Rayleigh criteria,

$$\Delta q = \frac{l}{lens\ (mirror)\ diameter}.$$ A few numbers are tested here.

$$\Delta q = \frac{0.043\ \text{arc-seconds}}{60\ \text{sec}/\text{min}\ 60\ \text{min}/\text{degree}} \bullet \frac{2p\ \text{radians}}{360\ \text{degres}} = 2.08 \times 10^{-7}\ \text{radians}$$

comparing, we get $\quad \Delta q = \frac{5000 \times 10^{-10}\ \text{m}}{2.4\ \text{m}} = 2.08 \times 10^{-7}$

Applying to the hypothetical problem of the ground resolution Hubble would have if pointed down, we get: $GSD = \Delta q \bullet \text{altitude} = 2.08 \times 10^{-7} \bullet 600 \times 10^{3}\ (\text{meters}) = 0.125\ \text{m}$

If Hubble was pointed downwards, you would get a GSD of 12 cm. The calculations can be repeated for 0.046 arc-seconds, but the increase is only a few percent.

Resolution:

The above implies that the detector has infinite resolution. It does not, however. Using the concept of similar triangles shown previously, and the values for the detector pixel size given above, we can compare the detector resolution to the best resolution offered by the telescope.

$$\frac{GSD}{altitude} = \frac{Pixel\ Size}{Focal\ Length}; \text{ or}$$

$$GSD = \frac{Pixel\ Size}{Focal\ Length} \bullet altitude = \frac{15 \times 10^{-6}}{57} \bullet 600 \times 10^{3} = 0.16\ \text{m}$$

which is slightly worse than the best the telescope can do – the Airy disk from a distant star, or small bright light on the ground, would not quite fill one detector pixel. The detector is "undersampling" the image.

I IKONOS

The world of remote sensing changed in a dramatic way in late 1999, when the first commercial high spatial resolution imaging satellite, IKONOS, was launched. Imagery which was previously the domain of "spy" satellites was now available to any customer.

1 THE SATELLITE:

IKONOS was built by Lockheed Martin Commercial Space Systems in Sunnyvale, California for Space Imaging. Designed to take images of the earth from 400 miles up in space, and moving at a speed of 4.5 miles per second, the satellite can collect imagery that will distinguish objects on the earth's surface as small as 1-meter square. The IKONOS satellite also carries a 4-meter resolution multi-spectral sensor.
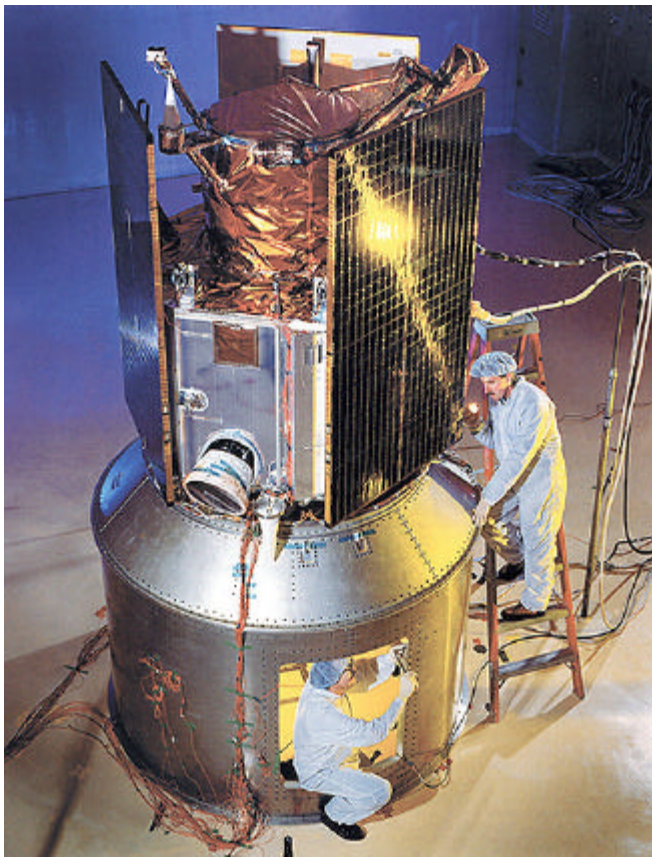

Figure 3.30. Image of the IKONOS satellite in the acoustic test cell at Lockheed Martin Missile & Space in Sunnyvale, CA.   The satellite weight on the ground was less than 1,600 pounds.

Launch Information	Vehicle: **Lockheed Martin Athena II** Rocket Location: **Vandenberg Air Force Base, California**
Resolution	• Ground resolution of each band: **1-meter panchromatic (nominal at <26° off nadir)** **4-meter multispectral**
Revisit frequency	**2.9 days at 1-meter resolution;** **1.5 days at 1.5-meter resolution.** These values are for targets at 40° latitude. The revisit times will be more frequent for higher latitudes and less frequent for latitudes closer to the equator
Spectral Bands	Panchromatic: **0.45 - 0.90 m** Multispectral: (same as Landsat TM Bands 1-4) **1: Blue 0.45 - 0.52 m** **2: Green 0.52 - 0.60 m** **3: Red 0.63 - 0.69 m** **4: Near IR 0.76 - 0.90 m**
Swath Widths & Scene Sizes	Nominal swath width: **• 11 km at nadir** Areas of interest: **• a single image at 11 km x 11 km** **• strips of 11 km x 100 km up to 11 km x 1000 km** **• image mosaics of up to 12,000 sq. km** **• up to two 10,000 square kilometer areas in a single pass within a region**
Metric Accuracy	**•12-meter horizontal and 10-meter vertical accuracy with no control** **• 2-meter horizontal and 3-meter vertical accuracy with GCP control** These are specified as 90% CE (circular error) for the horizontal and 90% LE (linear error) for the vertical
Orbital Information	Altitude: **681 kilometers / 423 miles** Inclination angle: **98.1°** Speed: **4 miles per second / 7 kilometers per second** Descending nodal crossing time: **10-11 a.m.** Revisit frequency**:** **3 days at 1-meter resolution;** **1.5 days at 1.5 meter resolution** Orbit time: **98 minutes** Orbit type: **sun-synchronous** Viewing angle: **Agile spacecraft - in-track and cross-track pointing** Weight: **1600 pounds**

2 Imaging Sensors and Electronics for the IKONOS Satellite

a The Camera System

The Kodak digital camera system for IKONOS consists of four major elements:

- The Optical Telescope Assembly captures the imagery across an 11-km to 13-km swath of the Earth's surface, and reflects it to the digital imaging sensors.
- The Focal Plane Unit contains panchromatic (black and white) and multispectral (color) imaging sensor arrays that transform the light into distinct picture elements (pixels). An analog signal processor converts the light striking each pixel into digital bits.
- The Digital Processing Unit compresses and formats the digital imagery for transmission to ground.
- The Power Supply Unit regulates power from the spacecraft to the camera electronics.

b Camera Telescope

Telescope design: The camera telescope has the equivalent resolving power of a 10,000mm telephoto lens. Three of the five telescope mirrors are curved, and are used focus the imagery onto the imaging sensors at the focal plane. Two flat mirrors, known as fold mirrors, bounce the imagery across the width of the telescope, thereby reducing overall telescope length from 10 meters to about two meters.

Weight reduction: To reduce overall telescope weight, Kodak cut out a significant portion of the glass from the telescope's largest (primary) mirror. The honeycomb glass core that remained was covered with thin, front surface mirror top and bottom glass faceplates, which were polished.

Surface polishing: To ensure the sharpest imagery possible, the surfaces of the three curved mirrors were polished to atomic level accuracy. The primary mirror surface is so smooth, if it were enlarged to 100 miles (160 km) in diameter, a car driven across its surface would not hit bumps any higher than 0.08in, or 2mm.

Mirror alignment: Two of the optics can be adjusted for focusing by command from the ground should correction be necessary. Mirror alignment, together with surface polishing accuracy, enable the telescope to deliver the sharpest possible image to the imaging sensors at the focal plane.

c Imaging Sensors & Electronics

Sensor arrays: The camera's Focal Plane Unit - attached to the back end of the telescope - contains separate sensor arrays for simultaneous capture of panchromatic (black and white) and multispectral (color) imagery.

The panchromatic sensor array consists of thousands of 12-micron-sized pixels (picture elements) . To capture red, green, blue and near-infrared light, the multispectral array is coated with special filters.

Digitizing the light: The CCD sensor arrays convert the light striking each pixel into discrete electronic charges. These charges are then measured as digital values by an analog signal processor in the Focal Plane Unit.

Image compression: The Digital Processing Unit compresses the digital image files from 11 bits per pixel data to an average value of 2.6 bpp at a speed of 115 million pixels per second.

Power: The Power Supply Unit converts electrical power from the spacecraft for use by the camera subsystems. Total camera system energy consumption is equivalent to a desktop PC.

d Quick Facts

Camera System

> Total system weight: 376 lbs. (171 kg.)
> Total system power consumption: 350 watts

Optical Telescope Assembly

> Assembly size: 61in. long x 31in. wide (1524mm) x (787mm)
> Assembly weight w/out focal plane unit: 240 lbs. (109 kg.)
> Optical design: Three mirror anastigmat
> Focal length / focal ratio: 10m / f14.3
> Image resolution (at nadir): one-meter panchromatic, four-meter multispectral
> Primary mirror: 27.5in. (0.7m) diameter x 4in. (100mm) thick, 29.5 lbs. (13.4 kg.)

Imaging Sensors & Electronics

Focal Plane Unit

> Unit size: 10in. x 9in. x 9in. (25cm x 23cm x 23cm)
> Panchromatic sensor: 12 micron pixel pitch, 13,500 pixels
> Multispectral sensor: 48 micron pixel pitch, 3375 pixels

Digital Processing Unit

> Unit size: 18in. x 7.5in. x 12.4in. (46cm x 19cm x 31cm)
> Compression rate: 11 bits per pixel compressed to 2.6 bpp
> Compression speed: 4 million pixels per second per processing channel

Power Supply Unit

> Unit size: 7in. x 8in. x 16in. (18cm x 20cm x 41cm)
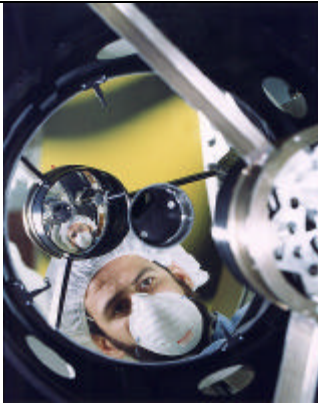
Figure 3.31.a IKONOS Camera:
A Kodak technician is reflected in the largest of three curved mirrors inside the compact IKONOS telescope assembly.

Figure 3.31.b
IKONOS Camera: Focal Plane array. A Kodak technician exposes the focal plane array at the base of the telescope

Figure 3.32 IKONOS Camera: Telescope

The IKONOS telescope has the equivalent resolving power of a 10,000mm telephoto lens. Designed and built by Kodak, the telescope features three curved mirrors, each precisely figured to capture and focus high-resolution Earth imagery onto the imaging sensors at the focal plane. Two additional flat mirrors 'fold' the imagery across the inside of the telescope, thereby significantly reducing telescope length and weight.

.
http://216.33.193.141/events/spaceimaging/aboutkodak2.html
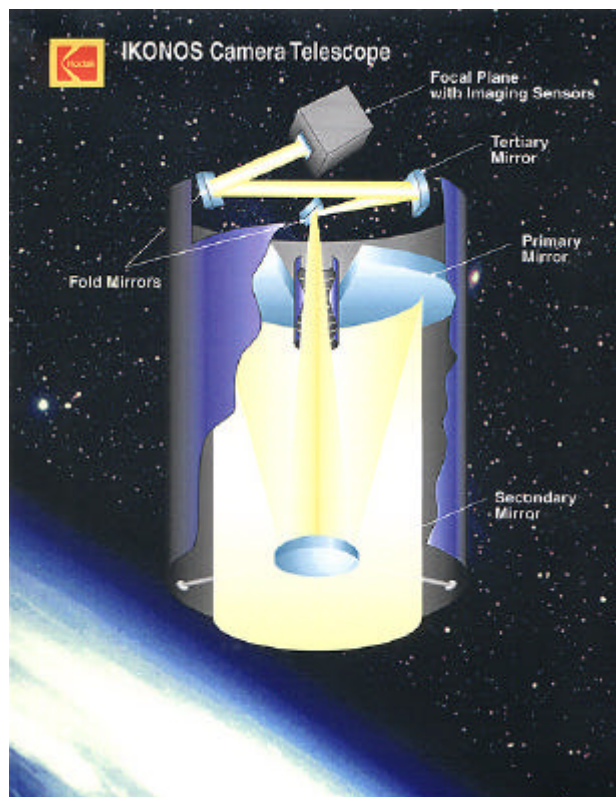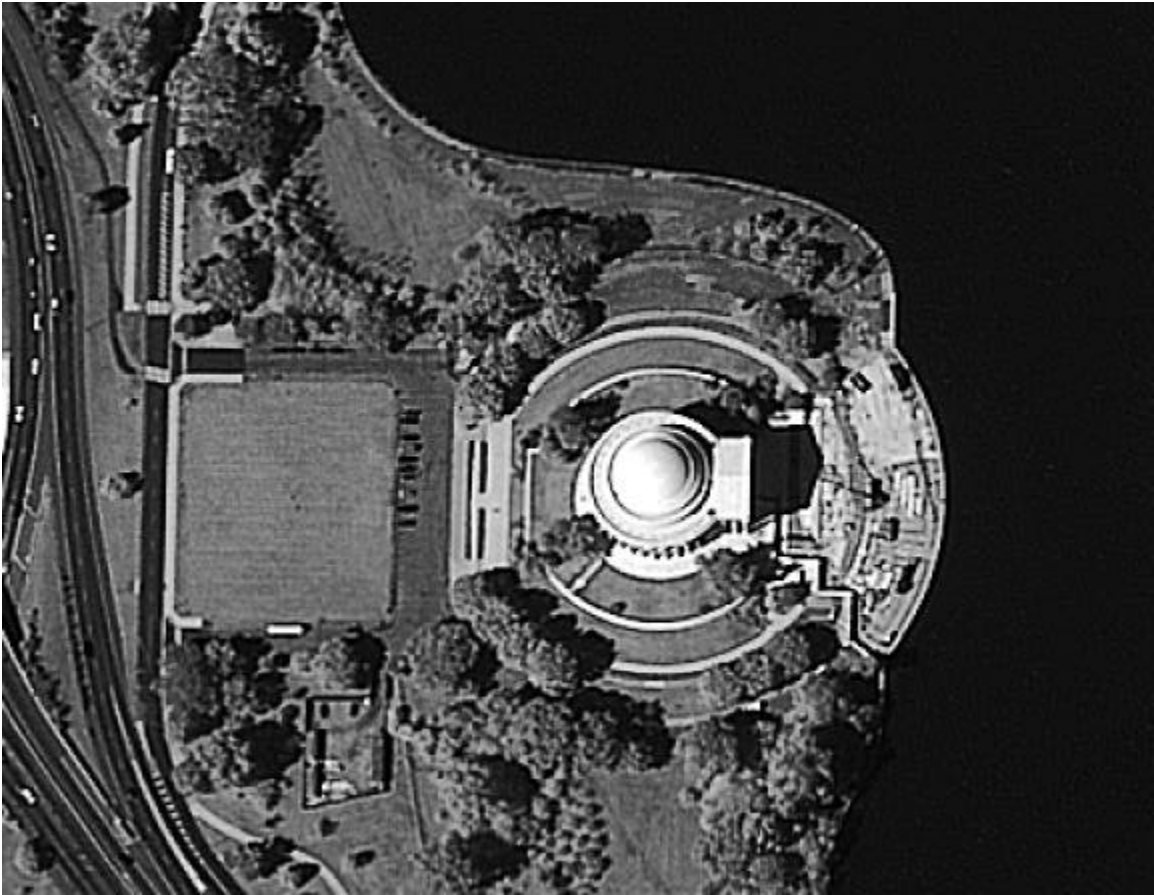
Figure 3.33 Washington DC - part of the first IKONOS image.

J DMSP - visible sensor - earth at night

Defense Meteorological Satellite Program (DMSP) satellites are primarily intended to gather weather data for military purposes. The system is presented here as an illustration of the concept of low-light level imaging. This system consists of platforms in sun-synchronous orbits with dayside equatorial crossings at 6:00 AM and 10:30 AM local times. Their purpose is to assist forecasters to identify and track developing patterns of weather so that imaging reconnaissance satellites do not waste film and flying time. Characteristics of some of the most recent 'Block 5D-2' missions are given here.

| Common Name	DMSP 5D-2-F11	DMSP 5D-2-F12	DMSP 5D-2-F13	DMSP 5D-2-F14
International Number	1991-082A	1994-057A	1995-015A	1997-012A
Launch Date (YYYY/MM/DD)	1991/11/28	1994/08/29	1995/03/24	1997/04/04
Launch Time	1323	1738	1405	1647
Mass	830.0 kg	823.0 kg	823.0 kg	850.0 kg
Apogee	853 km	858 km	855 km	855 km
Perigee	836 km	839 km	843 km	841 km
Period	101.8 min	101.9 min	101.9 min	101.8 min
Inclination	98.9°	98.7°	98.9°	98.8°

These satellites measure roughly $1.22m \times 6.4m$, with one solar wing of 8 panels generating one kW.

The OLS instrument consists of two telescopes and a photo multiplier tube (PMT). The scanning telescope of the OLS has a 20-cm aperture with an effective collecting area of 239 cm^2 and effective focal length of 122 cm. Light is split into two channels by a beam splitter. The system is designed to produce constant high resolution imaging rather than accurate radiometry.

The detectors sweep back and forth in a "whisk broom" or pendulum-type motion. The continuous analog signal is sampled at a constant rate so the Earth-located centers of each pixel are roughly equidistant, i.e., 0.5 km apart. 7,325 pixels are digitized across the 108° (???) swath from limb to limb.

Telescope pixel values are replaced by Photo Multiplier Tube (PMT) values at night. A telescope pixel is 0.55 km at high resolution (fine mode) and 2.7 km at low resolution (smooth mode). Low-resolution values are the mean of the appropriate 25 high resolution values. A PMT pixel is 2.7 km at nadir. Visible pixels are currently relative values ranging from 0 to 63 rather than absolute values in Watts/m^2. Instrumental gain levels are adjusted to maintain constant cloud reference values under varying conditions of solar and lunar illumination. Note that the combination of the two visible detectors allows a dynamic range of 2^5.

Swath (Scan Angle): 3000km @ 833km altitude

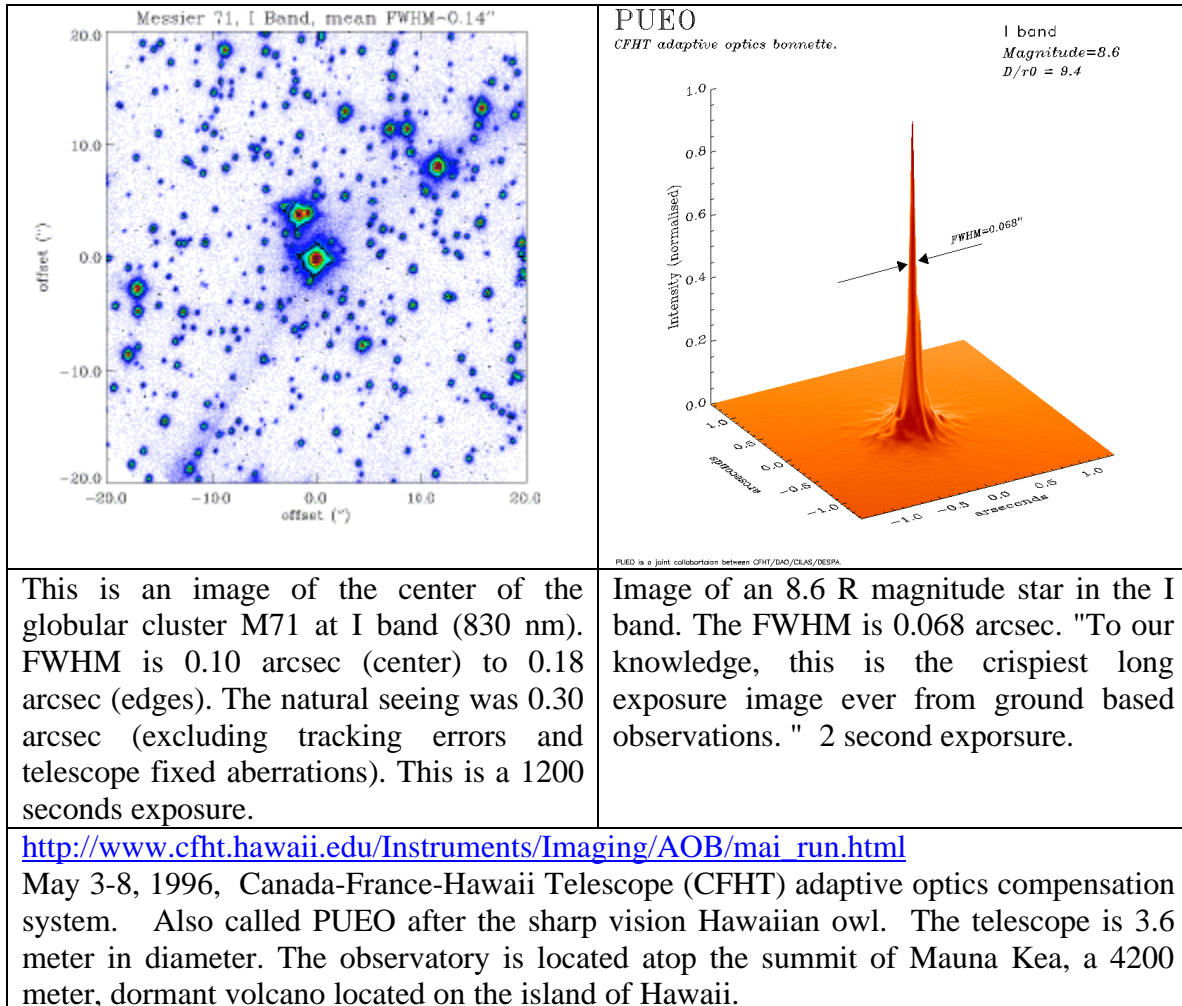| Spectral Channels	Wavelength (μm)	Wavelength (FWHM, μm)	Sensitivity	Spatial Resolution
OLS-L	0.40 - 1.10	0.58 - 0.91	10^{-3} - 10^{-5} Watts/cm^2 per sterradian	0.56 km[*]
OLS-PMT	0.47 - 0.95	0.51 - 0.86	10^{-5} - 10^{-9} Watts/cm^2 per sterradian	2.7 km
OLS-T	10. 0 - 13.4	10.3 - 12.9	190 to 310 K	5.4km

[*] stored data are resampled to 2.7km;

Figure 3.34 Several months of data, with cloudy data removed. The image is resampled to 1 km resolution.

.

K Problems

1. When was the first Corona launch ?

2. When was the first successful launch?   Which number was it?

3. How many launches before they had a successful film return?

4. How did the date of this launch compare to that of the U-2 incident with Gary Powers?

5. What was the best resolution (GSD) of the KH-4 cameras reported upon in this document?

6. What was the swath width associated with the 'best' resolution KH-4 images?

7. How many CORONA missions were there?

8. List 5 elements of recognition.

9. How could you tell that a road or rail-line was intended for missile transport.

10. When is the best time of week(day) to inventory an opponent's hardware (seems like it depends on religion...)

11. What is the focal length, diameter, and f/# for the Hubble Primary Optic?

12. Locate a high-quality 200 mm lens for a good 35 mm camera (say a Nikon or Canon). What is the f/#? What diameter is the primary optic?

13. For a 24" focal length camera, f/3.5, at an altitude of 200 km, calculate the GSD corresponding to a 0.01 mm spot on the film. Assume nadir viewing. Note that this is a geometry problem.

14. For a 24" focal length, f/3.5 lens, calculate the Rayleigh limit to GSD for a satellite at 200 km altitude. Assume nadir viewing, visible light (500 nm).

15. What diameter mirror would be needed to achieve 12 cm resolution (GSD) at geosynchronous orbit (6.6 Re, geocentric - note that this is **not** the altitude).

16. What are the three factors which constrain the resolution which can be obtained with an imaging system?

17. Adaptive optics: compare the Rayleigh criteria for the 3.5 m starfire observations in figure 3.17 to the results with and without the adaptive optics

18. Adaptive optics:

Messier 71, I Band, mean FWHM~0.14"

PUEO
CFHT adaptive optics bonnette.

I band
Magnitude=8.6
D/r0 = 9.4

FWHM=0.068"

PUEO is a joint collaboration between CFHT/DAO/CILAS/DESPA.

This is an image of the center of the globular cluster M71 at I band (830 nm). FWHM is 0.10 arcsec (center) to 0.18 arcsec (edges). The natural seeing was 0.30 arcsec (excluding tracking errors and telescope fixed aberrations). This is a 1200 seconds exposure.	Image of an 8.6 R magnitude star in the I band. The FWHM is 0.068 arcsec. "To our knowledge, this is the crispiest long exposure image ever from ground based observations. " 2 second exporsure.

http://www.cfht.hawaii.edu/Instruments/Imaging/AOB/mai_run.html
May 3-8, 1996, Canada-France-Hawaii Telescope (CFHT) adaptive optics compensation system. Also called PUEO after the sharp vision Hawaiian owl. The telescope is 3.6 meter in diameter. The observatory is located atop the summit of Mauna Kea, a 4200 meter, dormant volcano located on the island of Hawaii.

Compare the observed FWHM of 0.10 arcsec to the Rayleigh limit for such a mirror. Repeat for the "natural seeing" conditions of 0.3 arcsec.

Chapter 4 ORBITAL MECHANICS INTERLUDE

A Gravitational Force

Orbital mechanics is all about gravity, of course. You may be familiar with the relatively simple textbook case where the force due to gravity is given by the formula: f = mg, where m is the mass (generally in kilograms), and g is the acceleration due to gravity (approximately 9.8 $\frac{m}{s^2}$). Unfortunately, this simple form, appropriate near the surface of the earth, will not do for orbital motion, and a more complex form must be used. We find that the correct formula for this **'central force problem'** is:

$$\vec{F} = -G \frac{m_1 m_2}{r^2} \hat{r} \qquad\qquad \text{(Eqn. 4.1)}$$

where $G = 6.67 \times 10^{-11} \, N \frac{m^2}{kg^2}$ (Gravitational constant), m_1, and m_2 are the masses involved (the earth and the satellite, generally), r is the separation between the center of the earth and the satellite, and the vector elements (and sign) indicate that the force is along a line joining the centers (of mass) of the two bodies. As always, the force F is in Newtons, the masses again are in kilograms. At the surface of the earth, this equation becomes the familiar form:

$$F = g_o m \qquad\qquad \text{(Eqn. 4.2)}$$

where $g_o = G \frac{m_{Earth}}{R_{Earth}^2} = 9.8 \, \frac{m}{s^2}$ is the acceleration due to gravity at the earth's surface. Note that this can lead to a relatively convenient form of Eqn. 4.1:

$$F = g_o m \left| \frac{R_{Earth}}{r} \right|^2 \qquad\qquad \text{(Eqn. 4.3)}$$

where R_{earth} = 6380 km, and we have used $m_{earth} = 5.9736 \times 10^{24}$ kg.
[Rees (1990) notes that although the mass of the earth and G are not known to high accuracy, the product is: $GM_{Earth} = (3.98600434 \pm 2 \times 10^{-8}) \times 10^{14}$ $m^3 s^{-2}$. Note that the $\pm 2 \times 10^{-8}$ is the error in the last digit of the expression – we have 9 significant digits.

B Circular Motion

The force due to gravity results in a variety of possible solutions of the equations of motion. The simplest of these are the circular orbits, which objects like the moon approximate.

1 Equations of motion

The velocity of an object moving in a circular orbit is described by means of an **angular velocity** which determines the relationship between the radius of the circular motion, and the linear velocity.

$v = \boldsymbol{w}\, r$, where
v = velocity in meters/second,
r = distance from center of motion, ω=angular velocity (radians/second).
(If you are used to 'regular' frequency, f, then $\boldsymbol{w} = 2\boldsymbol{p}\, f$
Frequency is related to the period, τ, by the relation:

$$\tau \;=\; \frac{1}{f} \;=\; \frac{2\pi}{\omega} \tag{Eqn. 4.4}$$

a Example: Car going around in a circle of 200 m radius, at 36 km/hour. What is w?

$$\boldsymbol{w} = \frac{v}{r} = \frac{\left(36\times10^{3}\,m/3600\;s\right)}{200\;m} = 0.05 \;\; radians\!\big/\!s$$

b Example: a satellite is going around the earth once every 90 minutes. What is w?

Period (τ) = 90*60=5400 seconds.

$$f = \frac{1}{t} = \frac{1}{5400} = 1.85\times10^{-4}\,s^{-1}; \;\; \boldsymbol{w} = 2\boldsymbol{p}\, f = 1.16\times10^{-3}\;\; radians\!\big/\!s$$

2 Centripetal Force:

Newton said that if a mass is going to move in a trajectory other than a straight line, a force must be applied. In particular, circular motion requires the application of a force termed a 'centripetal force', or

$$F_{centripetal} = m\,\frac{v^{2}}{r} = m\boldsymbol{w}^{2}r \tag{Eqn. 4.5}$$

C Satellite Motion:

A consequence of the centripetal force applied to a satellite by gravity, for an object in circular motion, is the following balance:

$$F_{centripetal} = m\frac{v^2}{r} = F_{gravity} = g_o m \left(\frac{R_{Earth}}{r}\right)^2 \qquad \text{(Eqn. 4.6)}$$

Note that the mass cancels out - the orbital motion does not depend on the mass of the satellite.

$$\frac{v^2}{r} = g_o \left(\frac{R_{Earth}}{r}\right)^2 \Rightarrow v^2 = \frac{g_o R_{Earth}^2}{r} \Rightarrow$$

$$v = \sqrt{\frac{g_o}{r}} R_{Earth} \qquad \text{(Eqn. 4.7)}$$

There is a direct, inverse, relationship between the radius and velocity of a satellite in a circular orbit around the earth. This simple derivation is sufficient to introduce some of the most basic concepts of orbital motion - in particular Kepler's laws.

1 Illustration: Geosynchronous Orbit

What is the radius of the orbit of a geo-synchronous satellite - that is, a satellite with an orbital period of 24 hours. First: $w = \dfrac{2p}{24 \text{ hours}} = \dfrac{2p}{86400 \text{ s}}$

$$v = \sqrt{\frac{g_o}{r}} R_{Earth} \Rightarrow w = \frac{v}{r} = \sqrt{\frac{g_o}{r^3}} R_{Earth} \Rightarrow \frac{w^2}{R_{Earth}^2} = \frac{g_o}{r^3}, \text{ or}$$

$$\frac{r^3}{R_{Earth}^3} = \frac{g_o}{w^2}\frac{1}{R_{Earth}^1} \Rightarrow$$

$$\frac{r}{R_{Earth}} = \left(\frac{g_o}{R_{Earth}}\frac{1}{w^2}\right)^{\frac{1}{3}} = \left(\frac{9.8}{6.38 \times 10^6}\frac{(86400)^2}{(2p)^2}\right)^{\frac{1}{3}} = (290.45)^{\frac{1}{3}} = 6.62$$

so we see that geo-synchronous orbit is 6.6 earth radii (geocentric)
What is the velocity of the satellite ?

2 Kepler's Laws

There are three "Kepler's Laws"
    a) the orbits are ellipses, with one focal point at the center of the earth,
    b) equal areas are swept out in equal times, and
    c) the square of the orbital period is proportional to the cube of the semi-major axis.

a Elliptical Orbits (circular is a special case)

An ellipse is characterized by the semi-major and semi-minor axes (a, b), or alternatively, the semi-major axis and the eccentricity (a, ε or e). In our case, the important point for orbital motion is the focus, which for satellite motion around the earth is the center of the earth.
Some useful formulas:

$$\frac{x^2}{a^2} + \frac{y^2}{b^2} = 1$$

$$\boldsymbol{e} = \frac{\sqrt{a^2 - b^2}}{a} \quad \text{or} \quad \boldsymbol{e} = \sqrt{1 - \frac{b^2}{a^2}}$$
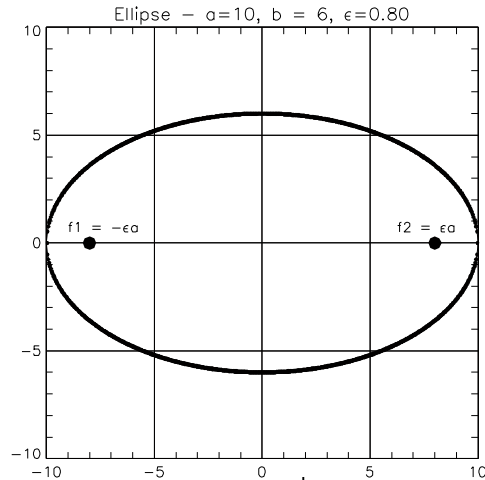
Distance from center to focus is

$$c = \boldsymbol{e}\, a = \sqrt{a^2 - b^2}$$

Figure 4-1 $r = \dfrac{a(1 - \boldsymbol{e}^2)}{1 + \boldsymbol{e}\cos\boldsymbol{q}}$

b Equal areas are swept out in equal times

This law is a consequence of the conservation of angular momentum;
$\vec{\mathbf{L}} = m\vec{\mathbf{v}} \times \vec{\mathbf{r}}; \; |\vec{\mathbf{L}}| = mvr\sin\boldsymbol{q}$ is a constant.
Hence, at each point along the orbit, the product of the velocity perpendicular to the radial vector $(v_{\boldsymbol{q}})$, and the radius is a constant. Note that at perigee and apogee, the radial velocity is zero (by definition), and if one checks the values to the right, one can see that:

    $2.709 \bullet 6.192 = 13.277 \bullet 1.263$

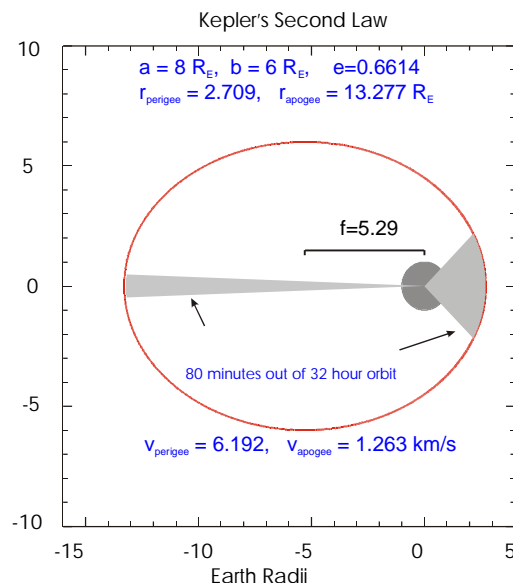A consequence of this law is that the satellite spends the great majority of its time at apogee.

Figure 4-2: Earth is at one focus, x=5.29; the x range is –13.29 to 2.71 R_E.

Note that the instantaneous velocity is given by:

$$v = \sqrt{GM\left[\frac{2}{r} - \frac{1}{a}\right]}$$ where r is the instantaneous radius, and a is the semi-major axis.

c Orbital Period: $t^2 \mu \, r^3$

As indicated above in the derivation of the period for a geosynchronous orbit,

$$v = \sqrt{\frac{g_o}{r}}R_{Earth} \Rightarrow w = \frac{v}{r} = \sqrt{\frac{g_o}{r^3}}R_{Earth} = \frac{2\boldsymbol{p}}{\boldsymbol{t}}$$

or $\boldsymbol{t} = \frac{2\boldsymbol{p}}{R_{Earth}}\sqrt{\frac{r^3}{g_o}} \Rightarrow \boldsymbol{t}^2 = \frac{4\boldsymbol{p}^2}{g_o R_{Earth}^2}r^3 = \frac{4\boldsymbol{p}^2}{M_{earth}G}r^3$ (Eqn. 4.8)

This result is obtained quickly here for a circular orbit, but is more generally true. Replace the radius of the circle with the semi-major axis, and you get the value of the orbital period.

D Orbital Elements

1 Semi-Major Axis – a

The size of the orbit is determined by this parameter, as illustrated in the above 2 figures. A is half of the longest axis of the ellipse. A related measure of size is the distance to the focus, c. (c = 8 and 5.29 in the two ellipses shown above.)

2 Eccentricity – e or e

This parameter determines the shape of the orbit, $\boldsymbol{e} = \frac{c}{a}$.   For a circle, $\varepsilon=0$, for a straight line, $\varepsilon=1$. (The latter would be a ballistic missile – straight up and straight down.)

3 Inclination Angle - I

This is the angle between the orbit plane and the equatorial plane of the earth. In the idealized case of a spherical earth, a geostationary satellite, at the earth's equator, would have an inclination of 0°. Reality differs slightly from this for modern geosynchronous satellites.

A polar orbiting satellite will have an inclination of 90° (more or less). The non-spherical earth exerts a torque on the satellite orbit plane. For an inclination of less than 90°, the orbit will precess west, for an inclination greater than 90°, the orbit will precess east. For the right choice, relative to the altitude, a polar orbiting satellite with the right inclination (greater than 90°) will be sun-synchronous- nominally 97°-98° for LEO satellites.

The remaining parameters determine the relative phase of the orbit.

4 Right Ascension of the ascending node - **W**

The right ascension of the ascending node is the angle between the plane of the satellite orbit and the line connecting the earth and the sun when the earth is located at the vernal equinox (first day of spring). (Alternately described as being measured from Aries.)

Alternative descriptions: the latitude at which the satellite crosses the terrestrial equator (longitude of the ascending node), or the point on the celestial equator (right ascension of the ascending node or celestial longitude of the ascending node – measured from Aries.)

5 Closest point of approach (argument of perigee or **w**)

This is the latitude for perigee, measured from the ascending node in the orbital plane in the direction of the satellite's motion. $\omega=0°$ corresponds to perigee occurring over the equator, 90° puts perigee over the northern pole. Again, because of the non-spherical earth, the argument of perigee precesses.

Inclination < 63.4°	ω precesses opposite satellite motion
Inclination = 63.4°	ω does not precess (Molniya orbit)
Inclination > 63.4°	ω precesses in the same direction as the satellite motion

E A few standard Orbits

There are a set of reasonably standard orbits used in the satellite industry, most of which have some use in the remote sensing community. In range of altitude, they range from low-earth-orbit (LEO) at altitudes of a few hundred miles, up to geosynchronous orbit, at an altitude of some 20,000 miles.

1 Low-earth orbit (LEO)

LEO is the domain of a large fraction of remote sensing satellites of various kinds: weather, earth resources, and reconnaissance. These satellites are typically in a sun-synchronous orbit. This means that they cross the equator at the same local time during each orbit, in order to maintain a constant solar illumination angle for their observations.
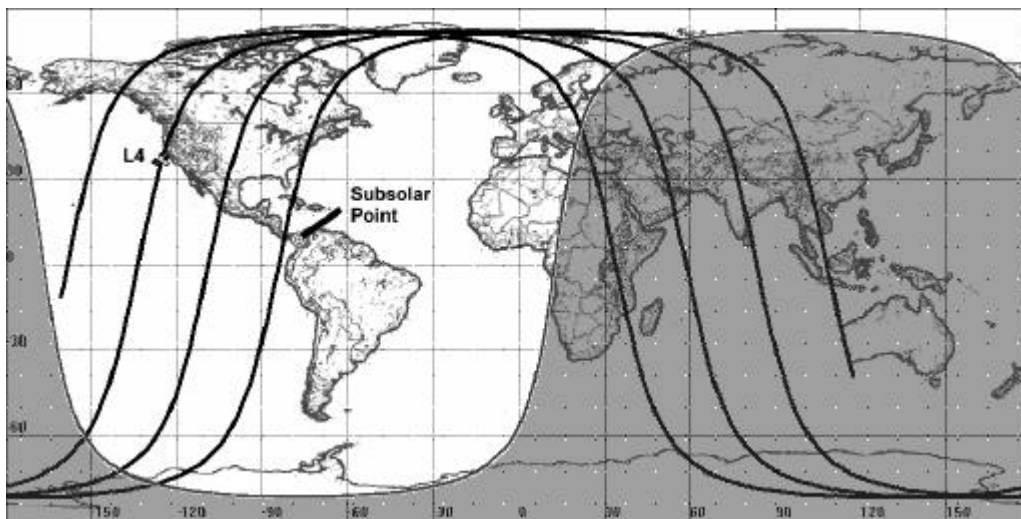

Figure 4.3 Ground track for 3 orbits by a LEO satellite, Landsat 4, crossing the equator during each orbit at 0940 local time. (Note the solar sub-point just above the coast of South America, corresponding to the time of the satellite crossing the equator). In the 98 minute orbit, the earth has rotated 24.5 degrees.
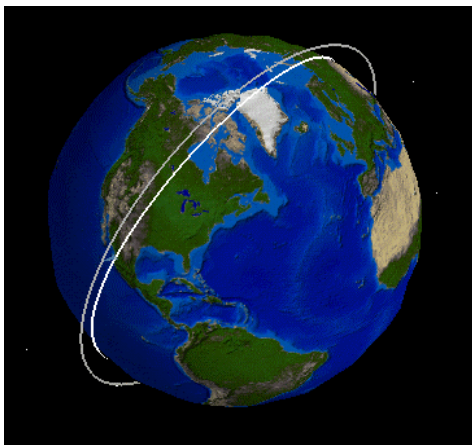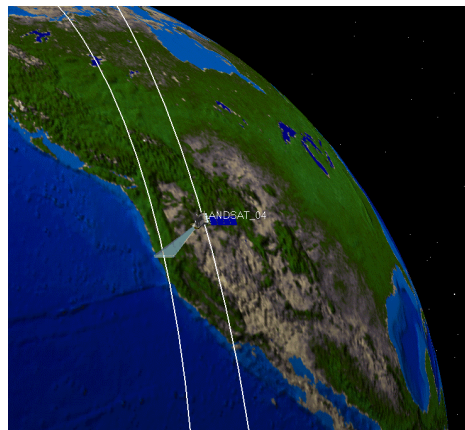

Figure 4.4a

Figure 4.4b The sensor on Landsat 4 sweeps along the orbit, aimed at the sub-satellite point (in the nadir direction) Over 15 days, the satellite will have observed the entire earth.

2 Medium Earth Orbit (MEO)

MEO is the domain of the Global Positioning Satellites (GPS). Though not directly used for remote sensing, they are increasingly important for mapping, and so do influence the interpretation of remotely sensed imagery. These satellites are in 4.15 R_E circular (26378 km geocentric) orbits, with 12 hour periods.
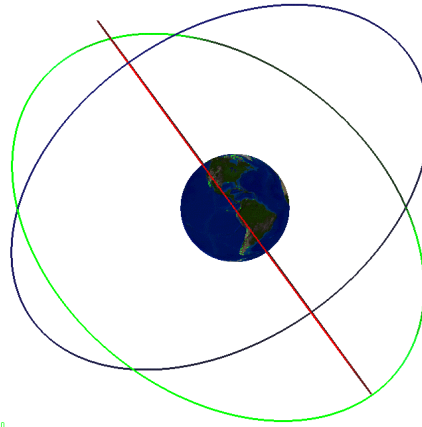
Figure 4.5

Figure 4.6 Orbit tracks for 3 GPS satellites

3 Molniya (HEO)

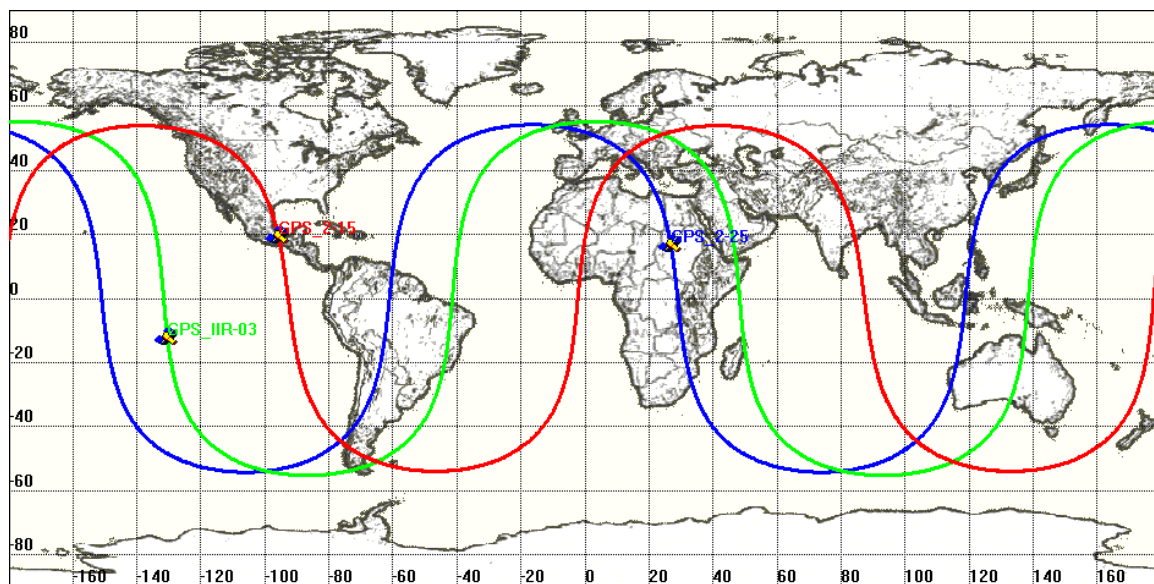The Molniya, or HEO orbits are useful for satellites that need to 'dwell' at high latitudes for an extended period. The careful match of inclination and eccentricity allows a balance of forces that keeps the orbit plane from precessing, that is, the latitude at which apogee occurs does not vary. This is the standard orbit for Russian communications satellites.
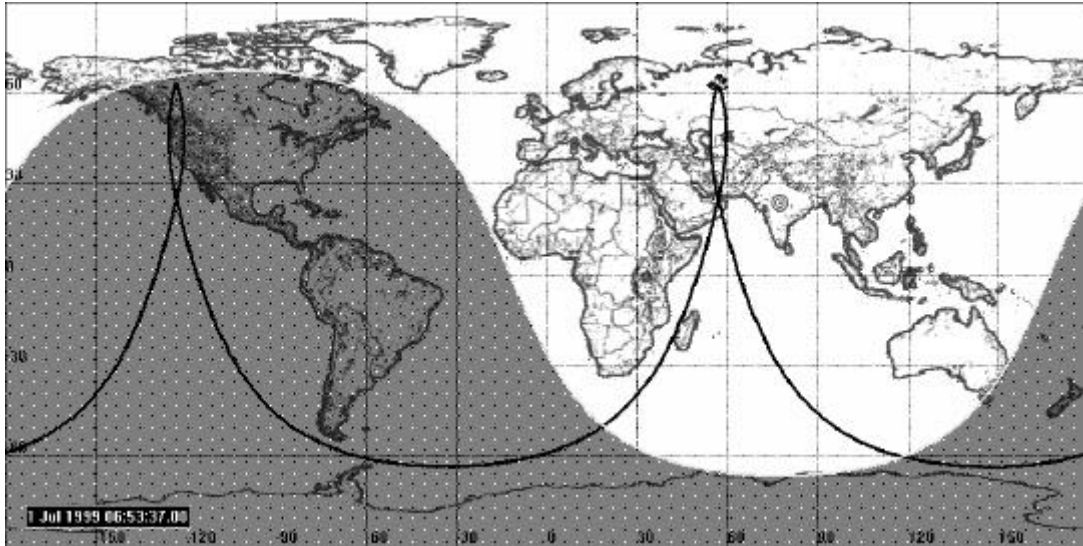
Figure 4.7 Molniya orbit, The subsolar point is centered on India.

Semi-major axis: a	26553.375 km	apogee radius	46228.612 km
Eccentricity: e	0.74097	perigee radius	6878.137 km
Inclination: I	63.40°	perigee altitude	500.000 km
argument of perigee	270.00°	RAAN	335.58°
Longitude of ascending node	230.043°	mean motion (revs per day)	2.00642615
period	43061.64 sec	Epoch	1 July 1999, 00:00:00

Figure 4.8a	Figure 4.8b

99
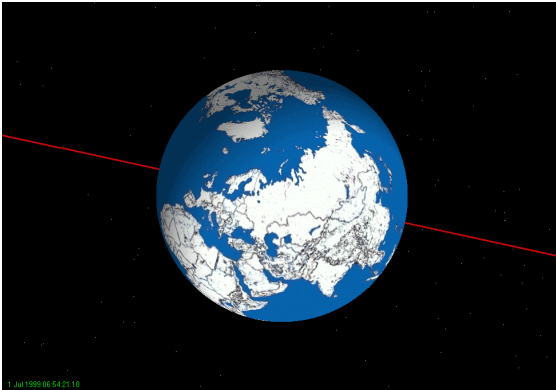
Figure 4.9a The view from Molniya orbit, corresponding to the location at apogee illustrated above. (06:54 UT)
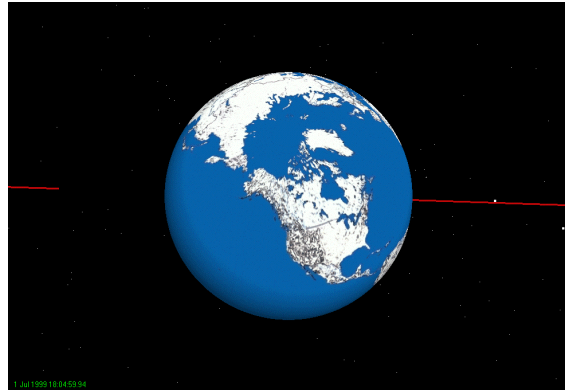
Figure 4.9b Some twelve hours later, the view from the apogee over the US – the subsolar point is in the Caribbean. (18:05 UT)

4 Geosynchronous (GEO)

Geosynchronous orbit is the standard orbit for most of the commercial and military communications satellites, the NASA telemetry system (TDRSS), and w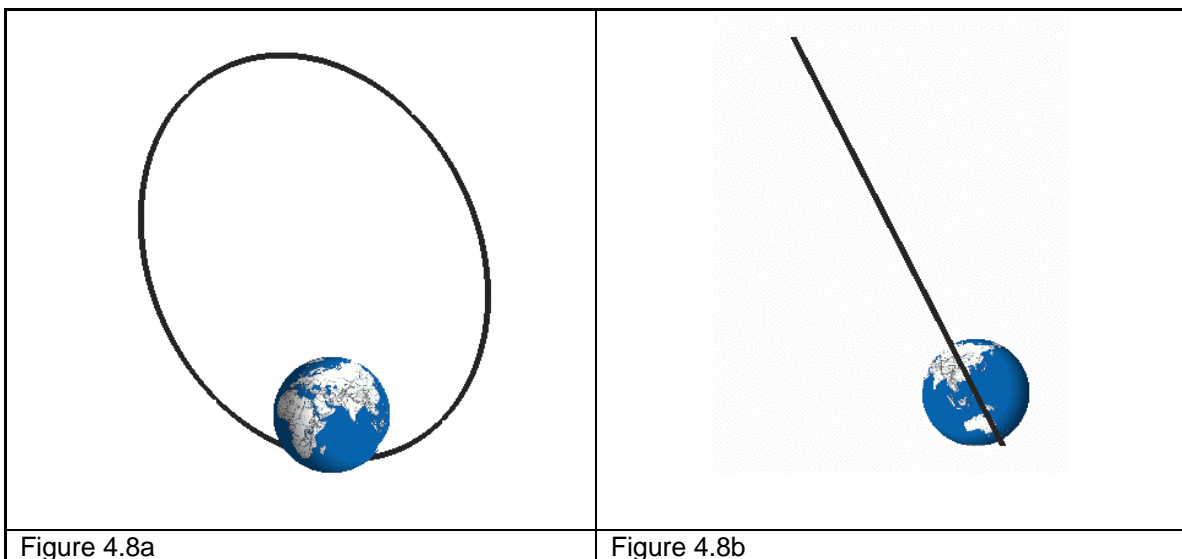eather satellites (GOES). There is some sloppiness in the usage of the term "geosynchronous", and it is frequently interchanged with geo-stationary. Most properly, the first really means an orbit with a 24 hour period, while the latter means that the satellite position with respect to the ground is unchanging. A truly geostationary orbit is difficult to obtain, and deviations from 0° inclination of a few degrees are typical. This leads to a modest amount of north-south motion during the day.
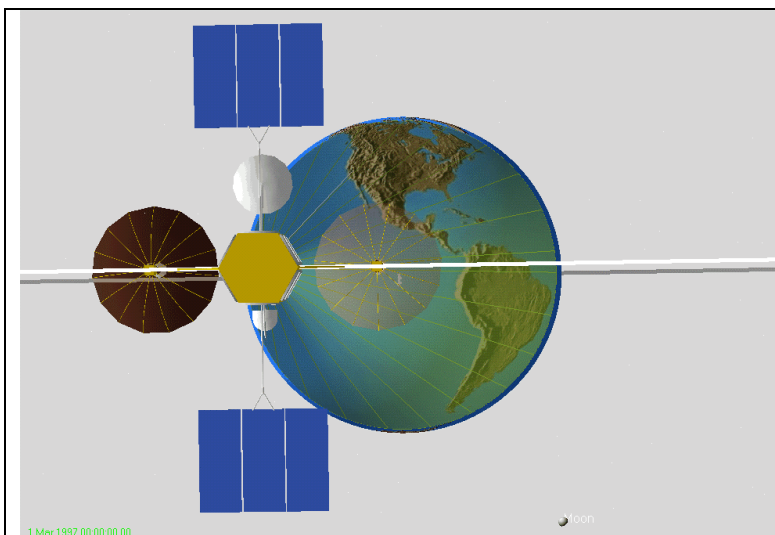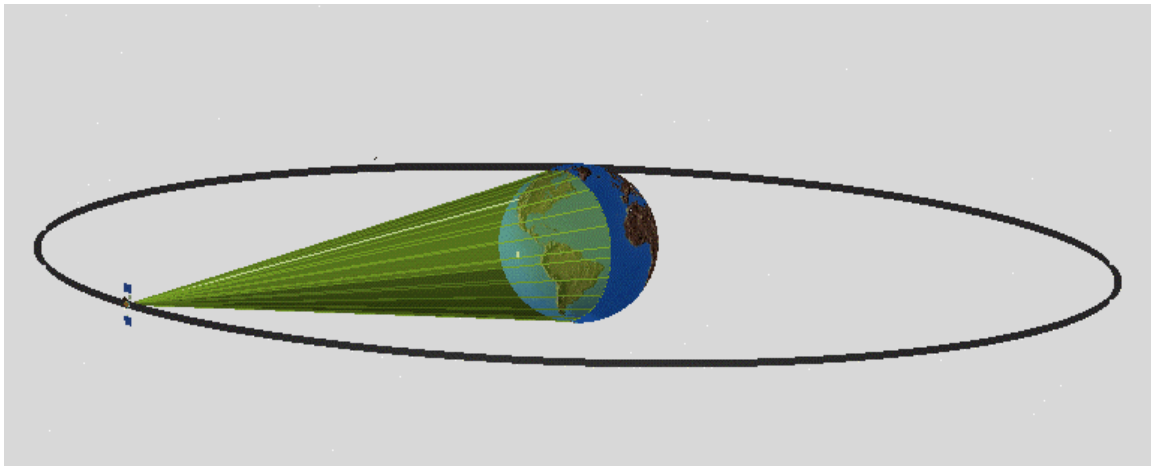
Figure 4.10
 The TDRSS orbit

TDRSS 7, launched in 1995
Mass   2225.0 kg
Apogee   35809 km
Perigee   35766 km
Period   1436.1 min
Inclination 3.0 deg

Orbit	LEO	MEO	HEO (Molniya)	GEO
Typical Satellite	Landsat 7	GPS 2-27	Russian communications	TDRSS 7
Launch Date	04/16/1999	09/12/1996		07/13/1995
Altitude: Apogee	703 km	20314 km	39850 km	5.6 R_E 35809 km
Perigee	701 km	20047 km	500 km	35766 km
Radius: Apogee		4.15 R_E	7.2 R_E 46,228 km	6.6 R_E
Perigee			6878.1 km	
Semi-major axis	1.1 R_E	4.15 R_E 26378 km	26553.4 km	6.6 R_E
Period	98.8 minutes	12 hour 717.9 min	~12 hours 717.7 min 43,061 s	24 hours 1436.1 min 86,164 s
Inclination	98.21°	54.2°	63.4	2.97°
Eccentricity	0.00010760	0.00505460	0.741	0.000765
Mean Motion (Revs/day)	14.5711	2.00572	2.00643	1.0027
Mass	2170 kg	1881.0 kg	-	2225.0 kg

Numbers primarily from Satellite Tool Kit data base

F Problems

1. Calculate the angular velocity for a geosynchronous orbit, in radians/second.

2. Calculate the period for a circular orbit at an altitude of 1 earth radius.

3. Calculate the period for a circular orbit at the surface of the earth. What is the velocity?   This is a "Herget" orbit, and is considered undesirable for a satellite.

4. Look up the orbits for the 9 planets, and plot the period vs. the semi-major axis. Do they obey Kepler's third law? Best done by using a log-log plot. Even better, plot the two-thirds root of the period vs the semi-major axis (or mean radius).

5. Derive the radius of orbit for a geosynchronous orbit.

This page intentionally left blank

Chapter 5 EO - SPECTRAL IMAGERY

The previous chapters have illustrated basics of optics, and panchromatic imagery. An increasingly important element in remote sensing is the ability to look beyond the purely "literal". This means making use of remote sensing information beyond elements such as size and shape, and looking at the 'color' of objects to identify them.

A Reflectance of Materials

The reflectance of most materials varies with wavelength. This allows spectral imagers, such as those on the Landsat missions, to distinguish between different materials. Distinguishing between different minerals is a fairly common goal for such work.

In figure 5-1 different aspects of reflective spectra are briefly illustrated. These spectra are the fingerprints of the elements, and derive from the fundamental atomic characteristics of the elements, as first indicated in chapter 2 for the Bohr model of the hydrogen atom. One of the more important, and dramatic spectral features found in remote sensing is the "IR ledge" at 0.7μ, as found in figure 5-2. This dramatic rise in reflectance with wavelength causes vegetation to be bright in the infrared. Old style black-and-white infrared film would show vegetation as bright, for example. In the military, one tries to design camouflage that can mimic this behavior.
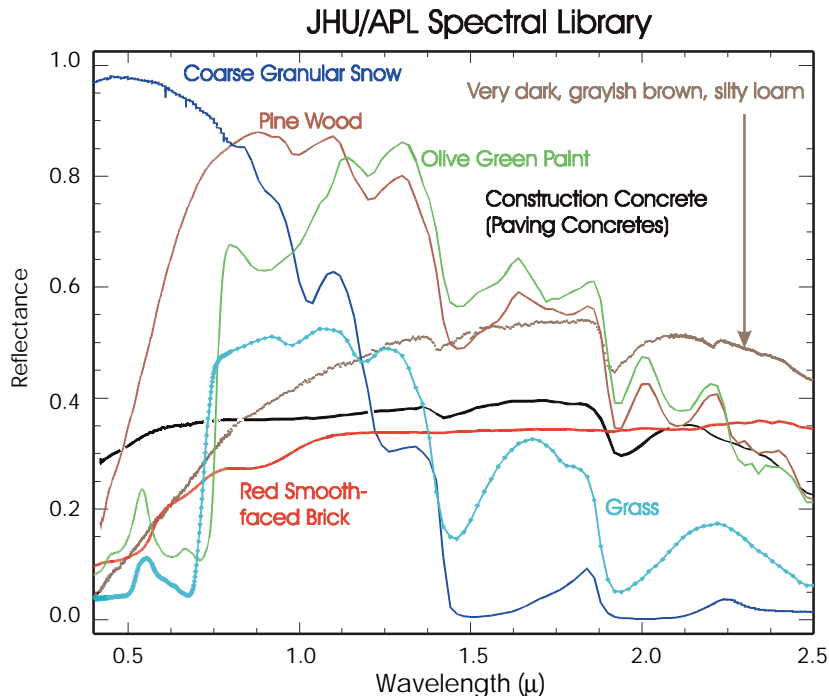
Figure 5.1 Comparison of some man-made and naturally occurring materials. Note how the olive green paint mimics the grass spectrum in the visible to NIR, but then deviates.

USGS Vegetation Library
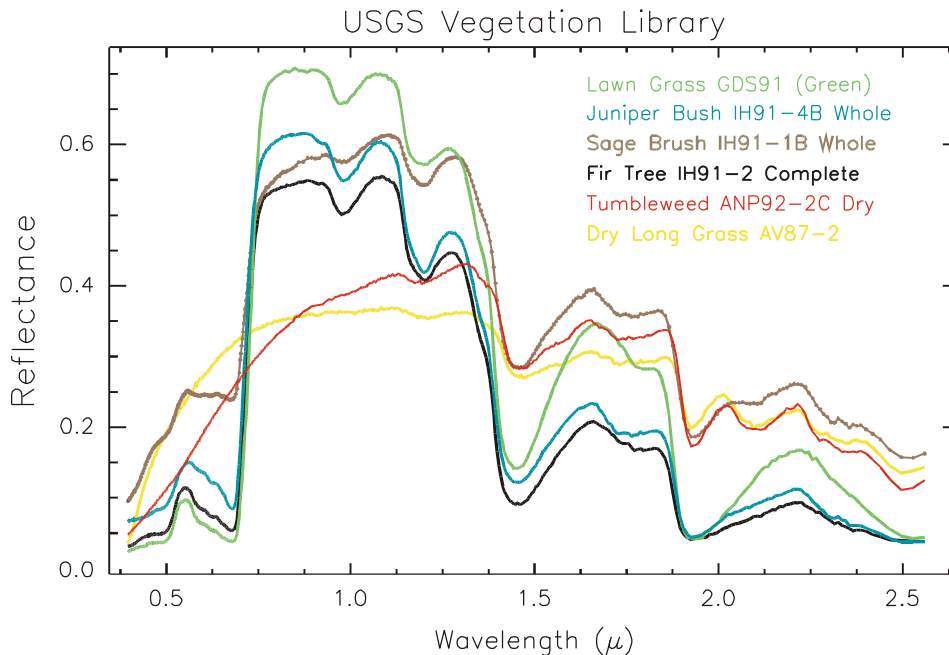
Figure 5.2 Sample vegetation spectra.
Clark, R. N., G. A. Swayze, A.J. Gallagher, T.V.V. King, and W.M. Calvin, 1993, The U. S. Geological Survey, Digital Spectral Library: Version 1: 0.2 to 3.0 microns, U.S. Geological Survey Open File Report 93-592, 1340 pages.

The sequence of vegetation spectra is meant to indicate some of the primary characteristics of vegetation:

a) the IR ledge at 0.7 µ, as noted above;
b) the lack of this feature in dry, brown, or senescent vegetation,
c) the dramatically higher reflectance in the IR vs. the small peak in the green (vegetation is dark as we normally see it).

Not indicated here, but important when viewing vegetation from above, is that the spectrum of a leaf is not the spectrum of a tree. This means that when foliage is viewed from above, observations will generally included the (shaded) ground below the vegetation, and the filtered sunlight reflecting from different elements of the foliage.

B Landsat

In late July 1972 NASA launched the first Earth Resources Technology Satellite (ERTS-1). The multispectral data provided by the on-board sensors led to an improved understanding of crops, minerals, soils, urban growth, and many other Earth features and processes. The name of the satellite, and those that followed, was soon changed to Landsat. These have been the primary earth resources satellites ever since, utilizing multispectral imagery with a spatial resolution of 30 meters. The most recent addition to the series is Landsat 7. At launch, this satellite, including the instrument and fuel, weighed approximately 4,800 pounds (2,200 kilograms). It is about 14 feet long (4.3 meters) and 9 feet (2.8 meters) in diameter. One of the first Landsat 7 images is shown below.

Figure 5-3 ERTS-1

Satellite	Launched	Sensors	Resolution (meters)	Altitude (km)	Data Link
Landsat 1 (ERTS-A)	July 23, 1972 - January 6, 1978	MSS RBV	80 80	917	Direct Downlink w/recorder (15Mbps)
Landsat 2	January 22, 1975 - February 25, 1982	MSS RBV	80 80	917	""
Landsat 3	March 5, 1978 - March 31, 1983	MSS RBV	80 30	917	""
Landsat 4	July 16, 1982 - *	MSS TM	80 30	705	Direct Downlink w/TDRSS (85Mbps)
Landsat 5	March 1, 1984 - date	MSS TM	80 30	705	""
Landsat 7	April 15, 1999 - date	ETM+ (pan)	30 15	705	Direct Downlink w/solid state recorders (150 Mbps)

*TM data transmission failed in August 1993, satellite used for maneuver testing

Landsat 6 was launched aboard a Titan II space launch vehicle from Vandenberg Air Force Base, Calif., Oct. 5, 1993. Indications were that the spacecraft separated from the booster at the appropriate time and location, but did not achieve orbit. The NOAA review board confirmed this and attributed the failure to a ruptured hydrazine manifold. The ruptured manifold rendered the satellite's reaction engine assemblies useless because fuel could not reach the engines. As a consequence, there was a failure to maintain attitude control during the apogee kick motor (AKM) burn. This failure caused the spacecraft to tumble during the AKM burn and not accumulate sufficient energy to attain orbit.

Figure 5-4. SF visible image from Landsat 7, April 23, 1999, flight day 9, orbit 117. ~1830Z With special thanks to Rebecca Farr, NESDIS/NOAA. Not yet on WRS, the scene is offset 31.89566 km east of nominal scene center. (Path 44 Row 34)

1 Orbit

The Landsat missions have been polar orbiters, in circular orbits, currently at an altitude of 705 km. An inclination of ~97° makes them sun-synchronous. Equatorial crossings were set at 0930 am for Landsats 1,2,3; 1030 AM for Landsats 4 and 5, 1000 AM for Landsat 7. These latter missions have orbit tracks set for 14.5 orbits per day, with 233 unique orbit tracks. The repeat cycle is every 16 days.
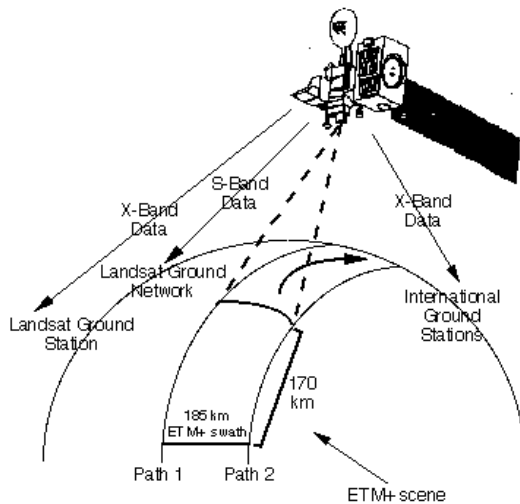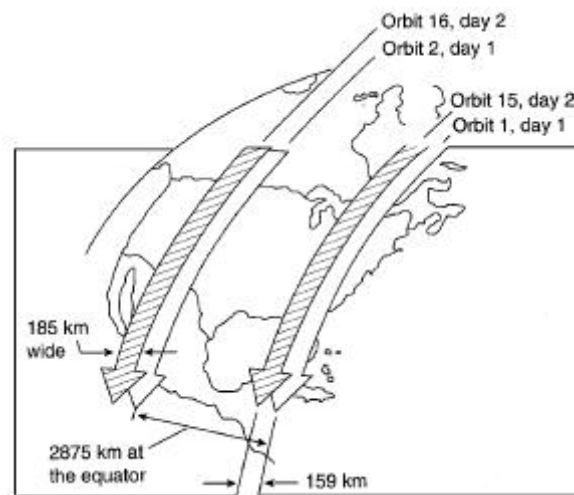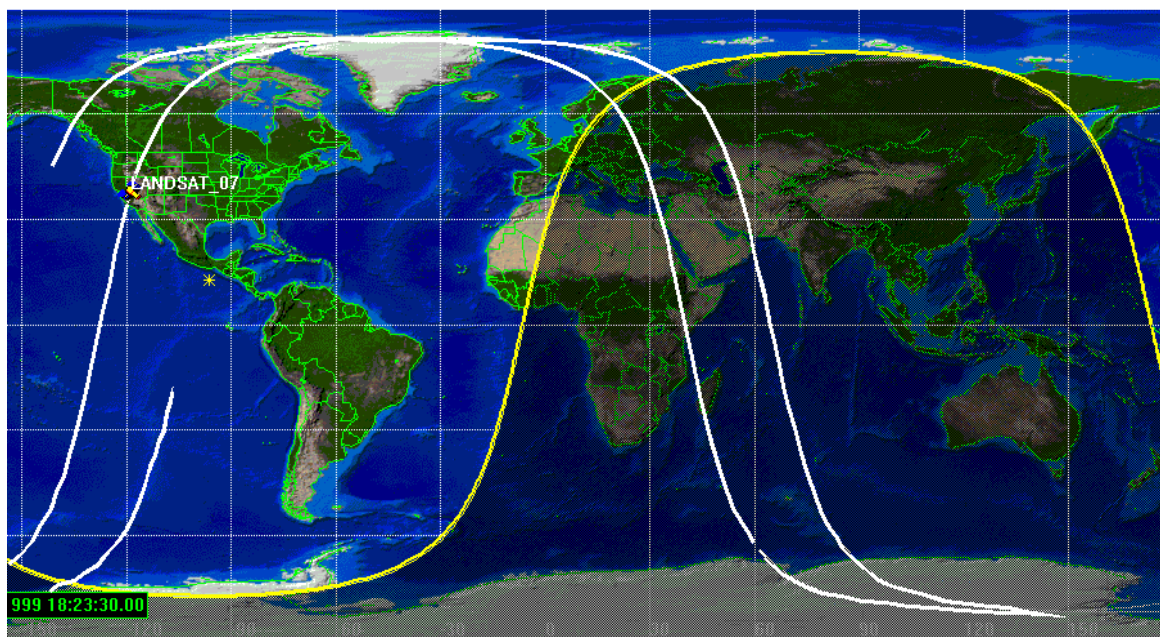

Figure 5.5

Figure 5.6

Figure 5.7 This is the orbit track corresponding to the San Francisco image shown above. The small yellow spot just below Mexico City is the sub-solar point, April 23, 1999, ~1830Z.

2 Sensor - Thematic Mapper

The first Landsats flew with a multispectral imager termed the MSS, and a TV-like sensor termed the Return Beam Vidicon. Beginning with Landsat 4, the prime instrument has been the Thematic Mapper, though the MSS was also carried to maintain continuity in archival, synoptic data sets. The TM sensor has provided 7 bands of spectral information at 30-meter resolution since 1982. On the most recent vehicle, Landsat 7, the instrument has been revised, and is termed the Enhanced Thematic Mapper - plus, or ETM+. The instrument has been revised to improve spatial resolution in the LWIR channel, and a new panchromatic band has been added with relatively higher spatial resolution (15 m). The discussion that follows addresses the most modern sensor.

a Optics

The optical path begins with a flat scan mirror oscillating with a period of 142.925 ms, scanning at 4.42 radians/s over a range of 0.2686 radians (15.39°). (60.74 ms scan, 10.72 ms to reverse.) The telescope is a Ritchey-Chretien design, a Cassegrain variant. The primary mirror (outer) aperture is 40.64 cm; the clear inner aperture is 16.66 cm. The effective focal length is 2.438 m, f/6. The mirror is ultra-low expansion glass, coated with silver. FOV: ±0.27°, IFOV: 42.5 μ radians.

The Relay Optics consists of a graphite-epoxy structure containing a folding mirror and a spherical mirror which are used to relay the imaged scene from the prime focal plane to the Band 5, 6 and 7 detectors on the cold focal plane. The characteristics of the relay optics are listed in the table below. The relay optics provides a magnification of 0.5. This magnification is used because of the reduced physical size of the band 6 detectors.
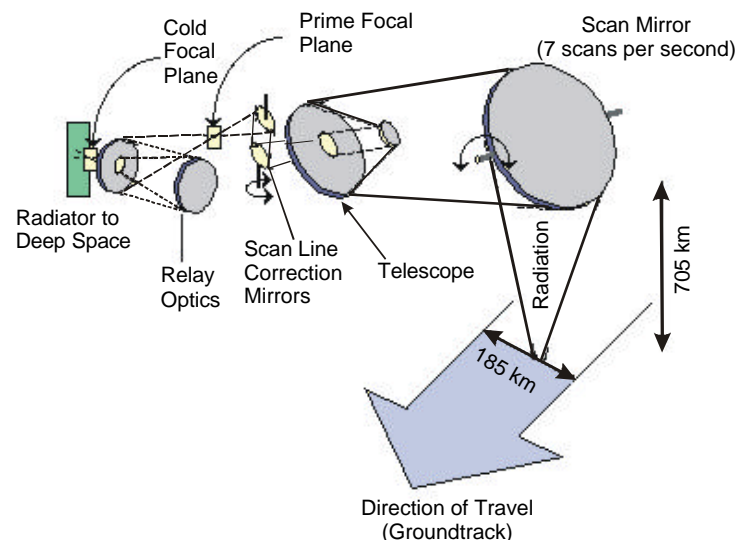
Figure 5.8 Landsat ETM+ Optical path.

Relay Optics Design Parameters	
Folding mirror clear aperture outer diameter	7.98 cm
Folding mirror clear aperture inner diameter	1.364 cm
Spherical mirror clear aperture diameter	14.067 cm
Magnification	0.5
F/#	3.0
Mirror material	ULE glass
Mirror coating	Aluminum, SiO overcoat

b Focal Planes

The ETM+ scanner contains 2 focal planes that collects, filters, and detects the scene radiation in a swath, 185 km wide, as it passes over the earth. The primary (warm) focal plane consists of optical filters, detectors, and preamplifiers for 5 of the 8 ETM+ spectral bands (bands 1-4, 8). The second focal plane is the cold focal plane (90 K), which includes the optical filters, infrared detectors, and input stages for ETM+ spectral bands 5,6, and 7.

Each band is comprised of two staggered rows of detectors with a center-to-center spacing between subsequent detectors in each row about twice the detector dimension and spacing between the rows just slightly more than that. This is done because there are readout electronics between the detectors. A scan mirror sweeps in the east-west direction as the spacecraft moves at about 6.7 km/s downtrack. The scan mirror operates at 7 Hz, so in half a period, or 71.4 msec, the spacecraft moves 480 meters downtrack.

Figure 5.9

c Prime Focal Plane

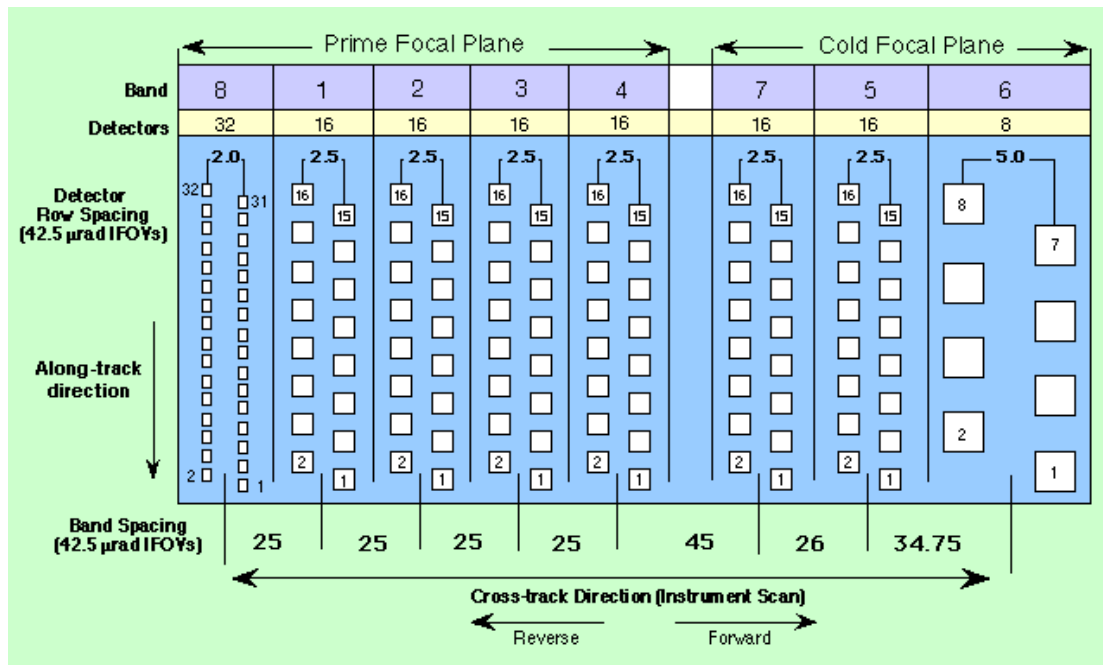The Prime Focal Plane Array is a monolithic silicon focal plane made up of five detector arrays: Band 1 through Band 4 and the Pan Band (8). The arrays for Bands 1 through 4 contain 16 detectors divided into odd-even rows. The array for the Pan Band contains 32 detectors also divided into odd-even rows. The system focus is optimized for the Pan Band which has the highest spatial resolution. The preamplifiers are mounted on the Prime Focal Plane Assembly, and consist of two stacks of flat hybrid modules. On top of each stack is a cylindrical black radiative cooling tower to help dissipate the heat from the preamplifiers.

Prime Focal Plane Assembly Design Parameters		
Parameter	Bands 1 through 4	Pan Band
Number of detectors	16 per band	32
Detector Size	103.6μ ×103.6μ	51.8 μ × 44.96μ
Detector Area	1.074×10^{-4} cm^2	2.5×10^{-5} cm^2
IFOV size	42.5 μ	21.3 μ× 18.4 μ
Center to center spacing along track	103.6 μ	51.8 μ
Center to center spacing between rows	259.0 μ	207.3 μ

The addition of a higher spatial resolution 'pan' band required the addition of a single staggered pair of rows of 16 detectors (32 detectors total making an equivalent 32 element line array downtrack) to the warm focal plane, each detector one-half the dimensions of the existing visible/near-IR band detectors. Of course, the new detectors also required the necessary preamplifiers, readout circuitry, and off-FPA electronics to produce the data. This band has a data rate four times that of the other visible bands. This increased the data rate of the sensor by about 70%.

d Cold focal Plane

There are 16 cooled indium antimonide (InSb) detectors for bands 5 and 7. Finally, for the LWIR, there are 8 cooled mercury cadmium telluride (HgCdTe) photo-conductive detectors for band 6. The detectors for bands 1-4, 5, and 7 each have 30-m resolution, the LWIR detector has 60 m resolution (an improvement over the 120 m resolution on TM). The detectors are arranged to have the same 480-m coverage downtrack.

Cold Focal Plane Design Parameters		
Parameter	Bands 5 and 7	Band 6
Number of detectors	16 per band	8
Detector Size	48.3μ × 51.82 μ	104μ × 104 μ
IFOV size	42.5 μ	42.5 μ × 85.0 μ
Center to center spacing along track	51.8 μ	104 μ
Center to center spacing between rows	130 μ	305 μ

With thanks to Dr. Carl Schueler, Director Advanced Concepts, Raytheon, May 1999.

And   http://ltpwww.gsfc.nasa.gov/IAS/handbook/

e Spectral Response
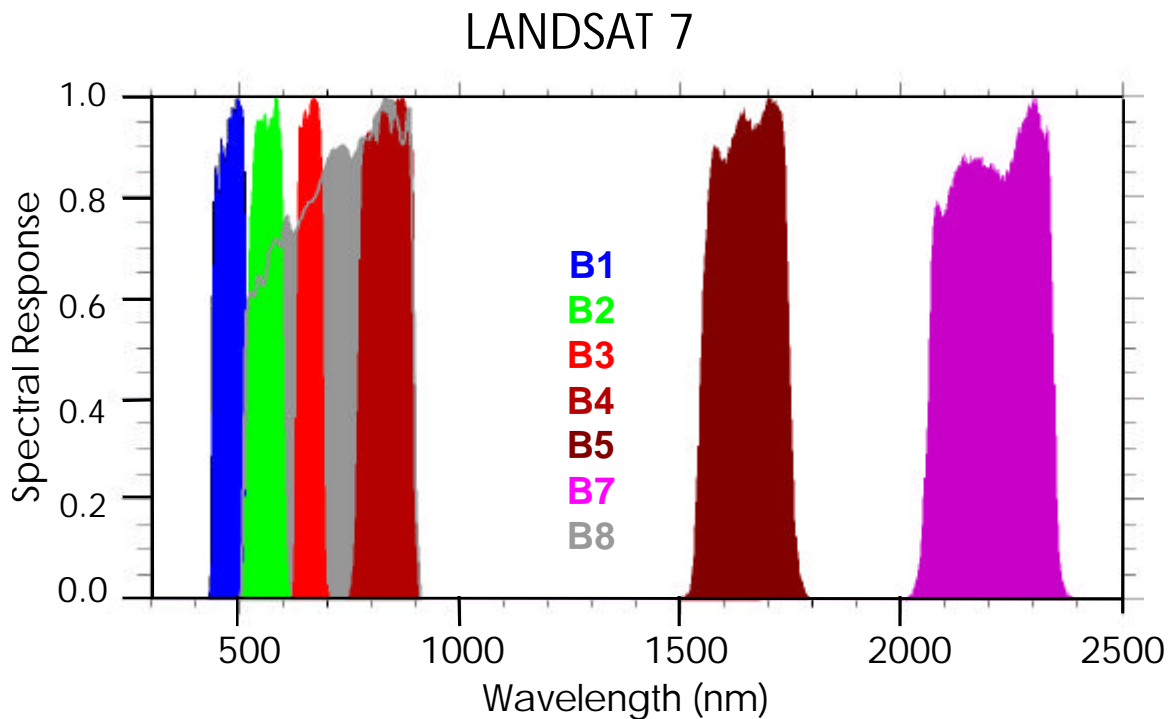
LANDSAT 7

Figure 5.10 The Landsat 7 spectral bandbass response functions are plotted here as a function of wavelength. These values are from the ground calibration numbers provided by NASA/GSFC. Note that the higher resolution pan-chromatic band cover the same region as bands 2,3, and 4, but does not extend into the blue. This is to avoid the scattering effects in the atmosphere at shorter wavelengths.
Above: Bands 1-5, 7 (VNIR, SWIR).
Right: Band 6 (LWIR)
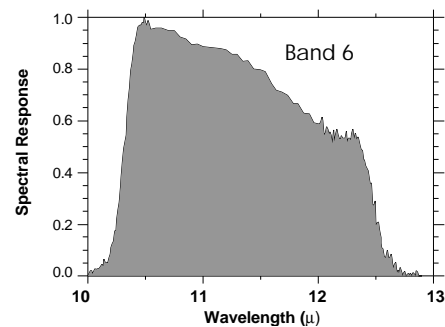
IKONOS multispectral data are taken over the same four bands as shown here for Landsat Bands 1-4, at 4-meter resolution.

f Spatial resolution - swath

Summarizing the above figures, the wavelength bands and spatial resolution for the ETM+ are as given here:

Band	Detector	Wavelength (nanometers)	Resolution (m)
1	Si	450-520 (VIS, blue)	30
2	Si	520-600 (VIS, green)	30
3	Si	630-690 (VIS, red)	30
4	Si	760-900 (NIR)	30
5	InSb	1550-1750 (SWIR)	30
6	HgCdTe	10.40 to 12.5 microns, thermal	60*
7	InSb	2090-2350 (SWIR)	30
Pan	Si	520-900	15

* 60 meter resolution for band 6 on Landsat 7 - 120 m on earlier missions.

g Dynamic range

An important element of all imagery is the question of dynamic range - the range of values from dark to bright that characterize the data. Landsat provides a fairly traditional 8 bit dynamic range - 0 to 255 DN. (The Landsat 7 ETM, Band 6 is now telemetered in two ranges, HI and LO, to extend the dynamic range of the data in that channel). Note that by contrast IKONOS data are 11 bit, enabling a dynamic range of 0-2047. Since most systems are designed for the brightest nominal targets, this difference in dynamic range is an indication of the sensor's ability to "see" into shadows, and to discriminate structure on dark targets.

h Data Rate

The Landsat missions have been designed to work with direct downlinks, suupplemented with some form of storage. Earlier missions carried tape recorders, which have all the undesirable characteristics of any moving, mechanical system on a satellite - ultimately they wear out. Beginning with Landsat 7, a solid state recorder (SSR) has been implemented.

The ETM+ instrument takes the data and separates the data into two formats. Format 1 (channel 1 also referred to as channel I contains bands 1-6 and format 2 (channel 2 also referred to as channel Q contains bands 6, 7, and 8 (PAN). Each format is transferred at 75 Mbps to a baseband switching unit (BSU) where the data is modulated. The data are then either downlinked in real-time to the Landsat Ground Station located at Sioux Falls, South Dakota, via an X-band link at a combined aggregate rate of 150 Mpbs, or recorded on the SSR. The data recorded on the SSR can be played back using one or two 150 Mbps bitstreams and downlinked to the LGS via the X-band link. When the spacecraft flies over LGS, it downlinks two 150 Mbps data streams, either 1 real-time and 1 playback, or 2 playbacks. Therefore, when the data is transmitted to the LGS, it is a combined rate of 300 Mbps, 150 Mbps bitstreams from the ETM+ and 150 Mbps bitstreams from the SSR or two 150 Mbps bitstreams from the SSR.

Reference:
http://caster.gsfc.nasa.gov/lps/ExtIntFaces/satellite.html

i Brief Review exercise - data rates

How do the various numbers described above relate to one-another? Let us estimate the data rate implied with a 185 km swath width, at 30-m resolution.

1)   First, how many pixels per "line" for one of the standard channels? $\frac{185 km}{30 m / pixel} = 6000 \, pixels / scan \, line$ (The correct answer is 6928 - there is some overlap in the pixels)

2) How many bits, or bytes, are there per scan line? $8 \; bits / pixel \; \times 6000 \; pixels / line$ $= 4.8 \times 10^4$ bits per scan line

3) How long is the satellite accumulating photons for one scan line?

$\tau = \dfrac{30m}{7 \times 10^3 m/s} = 0.0043s$ or 4.3ms (The actual time is 16 times longer, because of the focal plane design, but this answer will do for our purposes.)

4) So what is the implicit data rate? $\dfrac{4.8 \times 10^4 bits}{4.3 \times 10^{-3} s} = 11.2 \times 10^6 \dfrac{bits}{s} \approx 1.4MB/s$. So, one channel produces data at the rate of 1.4 Megabytes per second. Historically there were 7 channels, so some 85 Megabits/s, or 10 MB/s.   This rate has gone up by the influence of the extra channel 6 gain setting, and the 4x panchromatic channel, leading to the 150 Mb/s found on Landsat 7, using a 8.2 GHz (X-band) downlink.

j Student assignment: What is the current TDRSS configuration?

number of satellites, locations
transponder(s) - frequency, bandwidth
ground station(s) locations

C SPOT (Systeme Probatoire d'Observa tion de la Terre)

The French have their own version of Landsat, the Systeme Probatoire d'Observation de la Terre, or SPOT. The spectral capability of SPOT is limited compared to Landsat, but SPOT carried the highest spatial resolution PAN sensor available to the civilian community for a number of years. The orbits are all at 822-km altitude, with a 26 day repeat cycle, sun-synchronous, 10:00 local time. SPOT 1, 2, and 4 are all working as of mid-1999.

	SPOT 1	SPOT 2	SPOT 3	SPOT 4
Launch Date (YY/MM/DD)	1986/02/22	1988/03/01	1993/09/26	1998/03/24
Mass	1750 kg	1810 kg	1907 kg	2700 kg
Solar Array	1 KW	1 KW	1 KW	2.1 KW
Solar Panels	8.14 m	8.14 m	8.14 m	8.03 m
Altitude (at equator)	822 km	826 km	822 km	824 km
Orbital period	101.4 min	98.8 min	101.4 min	101.4 min
Mean Motion (Revs/Day)	14.20	14.20	14.17	14.20
Inclination	98.79	98.73	98.64	101.4 min
Main Structure (meters)	$2 \times 2 \times 4.5$	$2 \times 2 \times 4.5$	$2 \times 2 \times 4.5$	$2 \times 2 \times 5.6$
Telemetry (carrier freq.)	8.253 GHz	8.253 GHz	8.253 GHz	8.253 GHz
Image data rate	2×25 Mbits/s	2×25 Mbits/s	2×25 Mbits/s	2×25 Mbits/s
Onboard storage capacity	2×22 minutes[*]	2×22 minutes[*]	2×22 minutes[*]	2×40 minutes[*] + 3 minutes[**]

[*]Tape, [**]Solid State memory
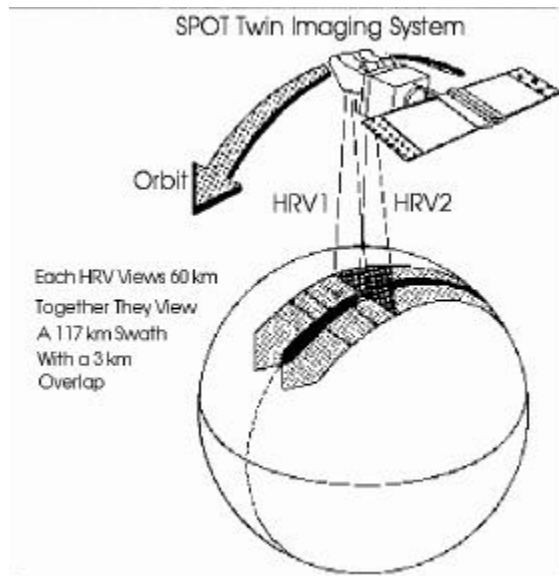
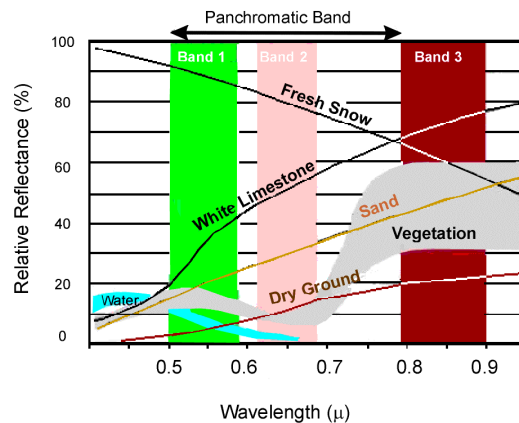Figure 5.10   Figure 5.11 SPOT 1, 2, 3

1 HRV sensor - pan/spectral - both are 60 km swath

The SPOT HRV sensors use paired linear arrays of 6000 pixels each for the high resolution panchromatic imager, as opposed to the single detector, scanning mirror with Landsat. The spectral channels use 3000 pixels each. The system uses 'Push broom' scanning, but with a significant off-nadir pointing capability (about 23° off-nadir). The two sensors can be pointed independently but apparently are normally operated to give a 120-km swath directly below the satellite (see Figure 5.10). The ability to use off-nadir pointing enhances the ability to do stereo pairs, and can be used to shorten revisit intervals.

a Imaging Modes - Spatial and Spectral Resolution

Note that on SPOT 4, an additional SWIR band was added, and a change in the spectral bandpass occurred for the panchromatic channel. On SPOT 4, the hi-resolution mode is in the red band. Compare this to the Landsat 7 panchromatic band.

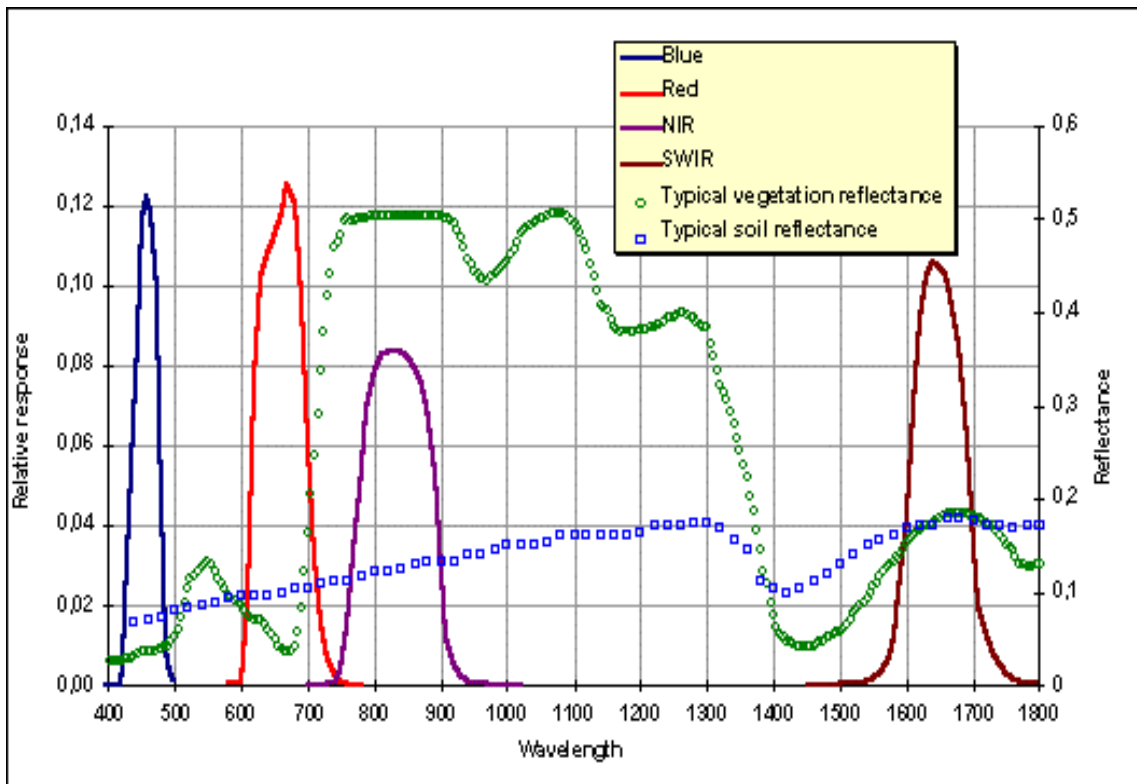|	Resolution	SPOT 1, 2, 3 (XS)	SPOT 4 (XI)
Band 1	20 m	500-590 nm (green)	500-590 nm (green)
Band 2	20 m	610-680 nm (red)	610-680 nm (red)
Band 3	20 m	790-890 nm (ir)	790-890 nm (ir)
Band 4	20 m	-	1580-1750 nm (SWIR)
Hi-Res	10 m	P mode - 510-730 nm	M mode - 610-680 nm

M - Monospectral, P- Panchromatic

Figure 5.12 SPOT 4 spectral responses. Notice that bands 2 and 3 are designed to distinguish the vegetation signature at the 700 nm IR ledge.

SPOT data from San Diego were illustrated in chapter 1 for the high-resolution pan-chromatic sensor. The spectral imagery from SPOT historically have been less widely used, when LANDSAT data are available.

D Indian Remote Sensing Satellites (IRS)

India has evolved a healthy remote sensing effort, and a substantial commercial presence beginning roughly with IRS-1C and IRS-ID. These vehicles mass ~1,350 kg, and are in 820 km polar orbits. The solar array generates more than 800 W. Both IRS-1C and 1D produce 5.8-meter panchromatic (0.50.75 µm - black and white) imagery, which is resampled to five-meter pixel detail, at 6 bit resolution. This spatial resolution, as of early 1998, was the best of any civilian remote sensing satellites in the world.

Figure 5.13 IRS

These satellites are also equipped with two-band Wide Field Sensors (WiFS) that cover a 774-square-kilometer (481-square-mile) area in a single image, as well as LISS-3 4-band sensors that provide 23.5-meter resolution multispectral coverage. The 23.5-meter resolution imagery is resampled to produce 20-meter pixel detail. The spacecraft also carry a 2-channel (0.62-0.68 and 0.77-0.86 µm) wide-field sensor (190 m resolution).
The IRS C, D Pan sensor sacrifices swath width for its higher resolution. However, it can be pointed off the orbit path which allows 2 to 4 day revisits to specific sites.
http://www.fas.org/spp/guide/india/earth/irs.htm

IRS-1C was launched into polar orbit on the 28th of December, 1995 by a Russian launch vehicle. Its payload was activated in the first week of January 1996. IRS-1D was launched 28 September 1997. It was also supposed to have gone into 800 km circular orbit, but initially went into an 821 × 327 km orbit. The orbit was corrected to 826 × 738 km using onboard fuel. This will shorten its operating life.

Sensor	PAN	LISS-III			WiFS		
Spatial resolution	5.8 m	23 m (VIS and NIR) 70 m (SWIR)			188 m		
Swath-width	70 km	142 km			810 km		
Spectral coverage	Pan-chromatic	Band 2 Band 3 Band 4 Band 5	520 - 590 nm 620 - 680 nm 770 - 860 nm 1550-1700 nm	green red NIR SWIR	Band 3 Band 4	620-680 nm 770-860 nm	red NIR
Radiometric Resolution, Quantisation	6 bit	7 bit			7 bit		

Note the modest dynamic range, and compare to Landsat and SPOT.

E Imaging Spectroscopy

Imaging Spectroscopy is the acquisition of images where for each spatial resolution element in the image a spectrum of the energy arriving at the sensor is measured. These spectra are used to derive information based on the signature of the interaction of matter and energy expressed in the spectrum. This spectroscopic approach has been used in the laboratory and in astronomy for more than 100 years.

AVIRIS: General Overview

AVIRIS is an acronym for the *A*irborne *V*isible *I*nfra*R*ed *I*maging *S*pectrometer. AVIRIS is a world class instrument in the realm of Earth Remote Sensing. It is a unique optical sensor that delivers calibrated images of the upwelling spectral radiance in 224 contiguous spectral channels (also called bands) with wavelengths from 400 to 2500 nanometers (nm). The instrument flies aboard a NASA ER-2 airplane (a U2 plane modified for increased performance) at approximately 20 km above sea level, at about 730 km/hr.
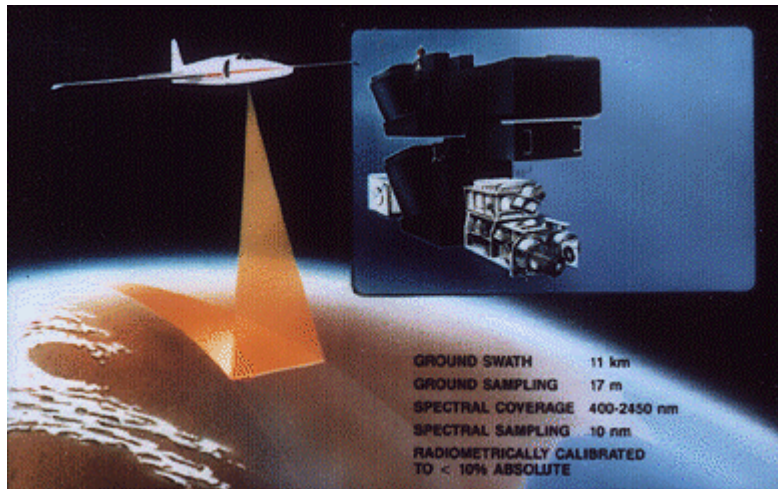

Figure 5.14

The AVIRIS instrument contains 224 different detectors, each with a wavelength sensitive range (also known as spectral bandwidth) of approximately 10 nanometers (nm), allowing it to cover the entire range between 380 nm and 2500 nm. When the data from each detector is plotted on a graph, it yields a spectrum. Comparing the resulting spectrum with those of known substances reveals information about the composition of the area being viewed by the instrument.

AVIRIS uses a scanning mirror to sweep back and forth ("whisk broom" fashion), producing 614 pixels for the 224 detectors each scan. Each pixel produced by the instrument covers an approximately 20 meter square area on the ground (with some overlap between pixels), thus yielding a ground swath about 11 kilometers wide.
http://makalu.jpl.nasa.gov/html/aboutav.html

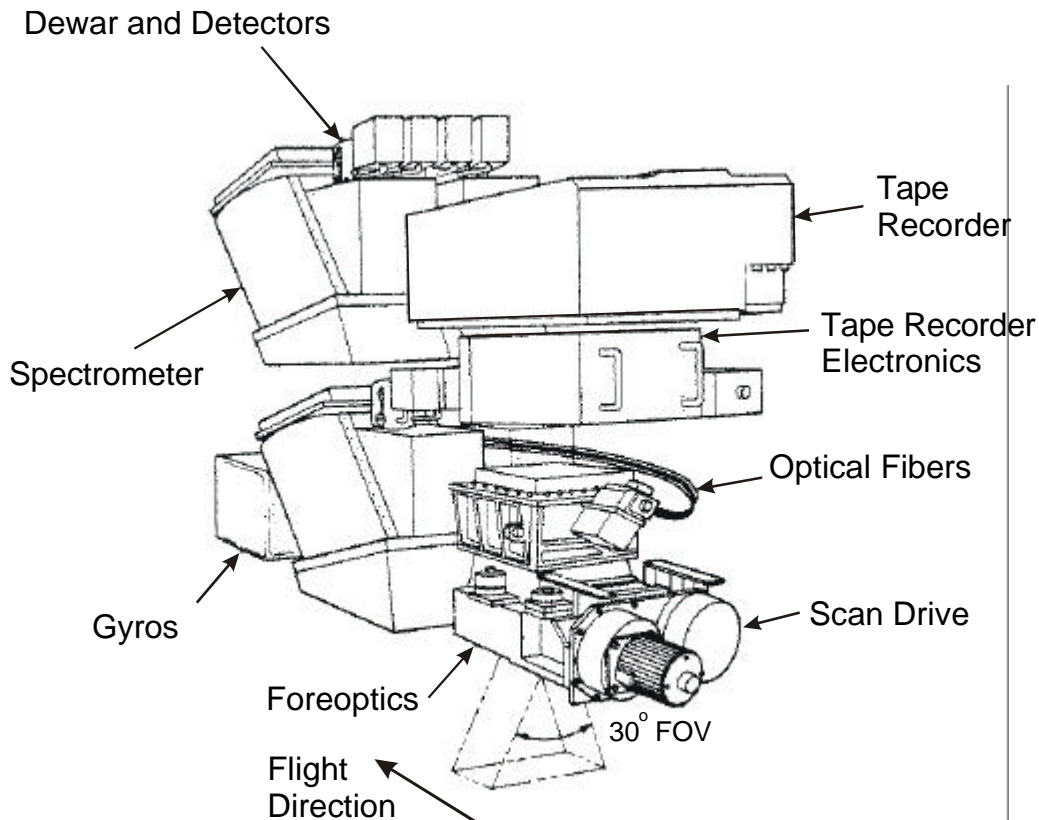Figure 5.15 The AVIRIS Instrument. Instrument mass is 340 kg.

10 bit data encoding through 1994, 12 bit from 1995.

Silicon (Si) detectors for the visible range, and indium-antimonide (InSb) detectors for the near infrared. (Liquid Nitrogen (LN2) cooled detectors)

30 degrees total field of view (full 614 samples); 1 milliradian Instantaneous Field Of View (IFOV, one sample), calibrated to within 0.1 mrad
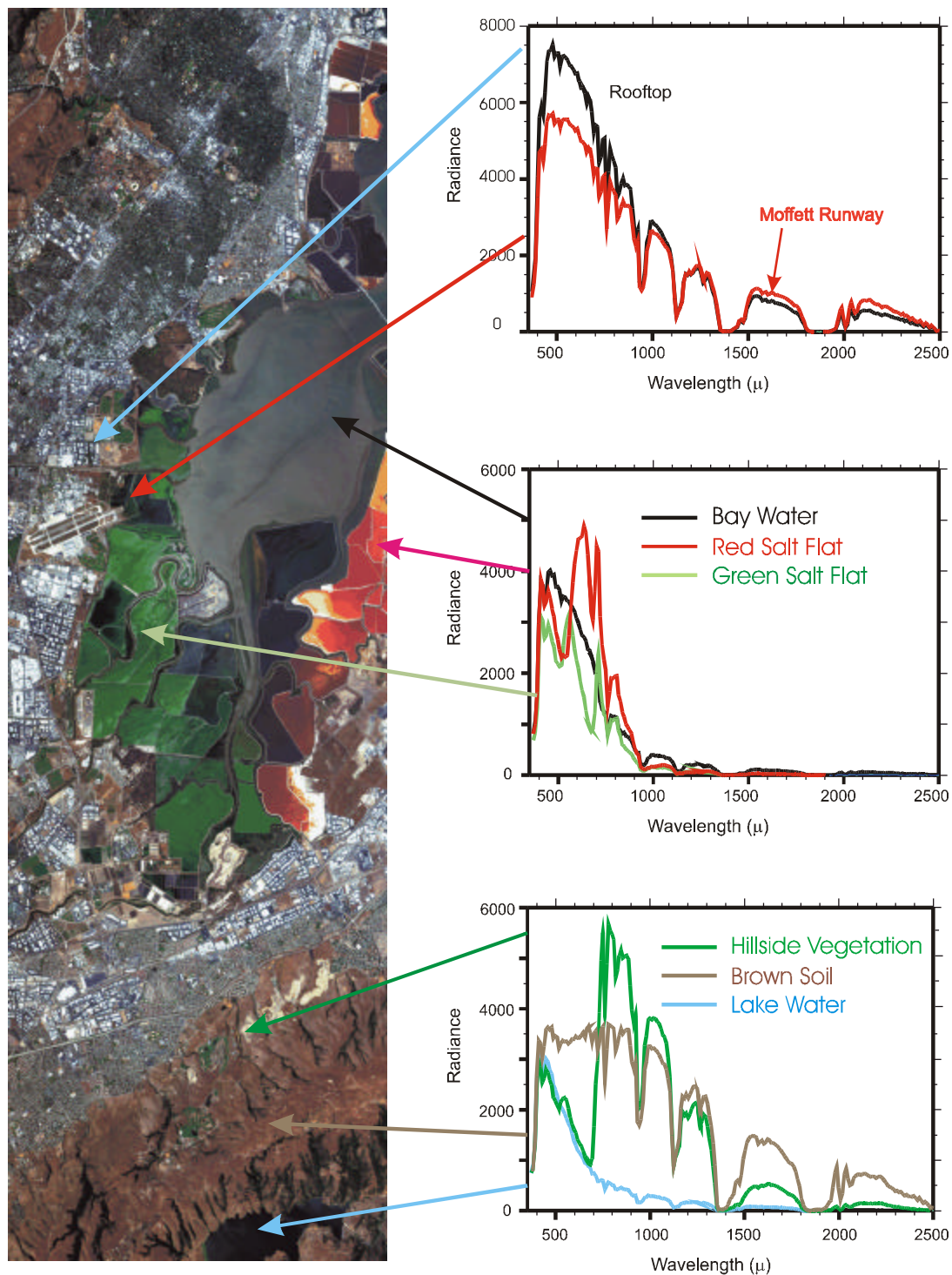
Figure 5.16 This image from AVIRIS shows elements of a scene acquired on August 20, 1992. The mission was flown on a NASA ER-2 plane at an altitude of 20,000 meters (65,000 feet) over Moffett Field, California, at the southern end of the San Francisco Bay. The image is a roughly 'true' color representation of the data. Blue: 458.46 nm, Green: 557.07 nm, Red: 655.84 nm (Bands 10, 20, and 30). The red area is real; it is due to the presence of 1-centimeter-long red brine shrimp in the evaporation pond.

F Problems

1. What wavelength does the 'IR ledge' for vegetation occur at? Is this in the bandwidth of a silicon detector?

2. When was the first Landsat launched?

3. How many spectral channels are used for the Thematic Mapper instrument? Over what wavelength ranges?

4. How wide is a standard Landsat 7 image? What is the spatial resolution for the 6 reflective bands? What is the spatial resolution for the thermal band? How many pixels wide does this make an image in the reflective band?

5. How does SPOT differ from Landsat 7?
    Spatial resolution (spectral bands, high-resolution panchromatic band)
    Wavelength for high-resolution panchromatic band
    Orbit
    Wavelengths of spectral bands
    Dynamic range

6. What is the nominal orbit for Landsat 7? (altitude, inclination, local time for equator crossing)

7. How long is the repeat cycle for Landsat 7?

8. What is the dynamic range for the visible detectors on Landsat 7 (6, 8, or 10 bits)?
    (you may need to go to the NASA/GSFC Landsat site on the WWW)

9. What is the nominal spectral resolution for AVIRIS (compare to Landsat).

This page intentionally left blank

Chapter 6 IMAGE PROCESSING - AND GIS

There are two elements of image processing for remote sensing – the techniques used to enhance images for presentation, and those used to extract information. Most work at the 'pixel' level, and many make use of the scene statistics. If the data inhabit more than one spectral dimension (that is, have color), then a broad range of techniques can be applied to reduce the spectral dimension of the data, and extract information. We begin with a prosaic example of a black and white image, chosen to maintain an intuitive grasp of the image at very high magnification.

A Structure of remote sensing data - DN - what is a pixel….

The image of a model shown on the left was chosen for illustration. The small region around the right eye was extracted, and is shown in an expanded view on the right. The data values associated with each 'eye' pixel are given in the table below the figure – the numbers run from 0 to 226, where 0 corresponds to a black pixel, and 226 to a nearly white pixel.
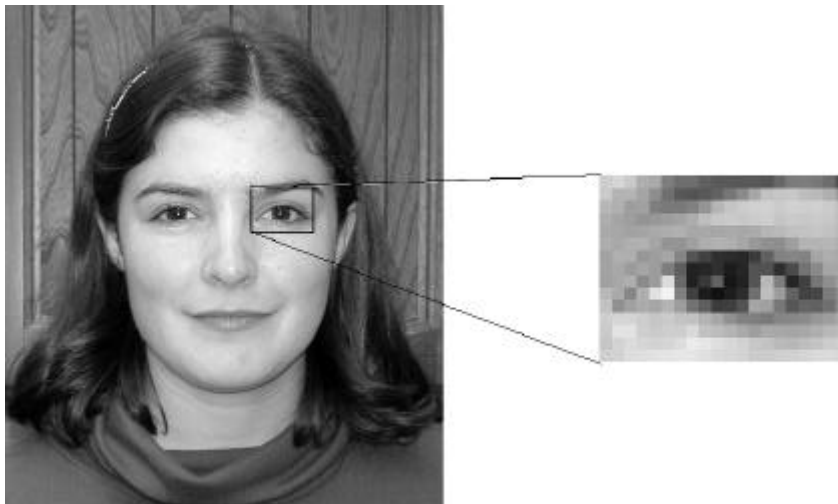

Figure 5-1. Model Susie Olsen

1	1	2	3	4	5	6	7	8	9	10	11	12	13	14	15	16	17	18	19	20
2	181	188	178	157	153	119	106	107	97	91	91	89	89	87	102	117	119	115	106	82
3	179	160	162	149	132	107	90	86	90	98	114	129	151	172	175	177	169	166	158	141
4	163	158	144	147	120	116	115	121	137	162	174	180	184	184	179	184	182	184	179	170
5	156	149	145	137	139	143	148	156	169	177	179	177	179	182	175	179	177	179	177	169
6	153	151	148	149	153	156	159	152	152	151	153	152	155	162	166	171	173	175	172	166
7	156	152	158	159	150	136	137	146	156	160	158	152	140	134	132	145	161	162	163	158
8	148	158	157	139	144	151	126	87	73	58	55	52	67	96	122	125	123	150	156	153
9	148	152	142	149	143	120	95	48	50	58	43	50	85	85	57	79	111	128	150	152
10	147	152	157	130	143	192	103	47	65	97	38	47	87	165	120	50	71	113	133	144
11	164	153	126	157	197	210	121	71	43	34	44	56	109	170	143	98	73	76	117	132
12	172	134	147	155	151	161	143	110	95	67	71	85	149	146	114	89	99	96	109	131
13	182	187	186	181	175	179	173	171	161	151	134	122	120	116	125	126	129	138	144	153
14	178	198	198	182	179	182	181	191	172	167	162	153	145	153	152	150	152	157	164	169
15	175	185	192	188	185	187	193	205	201	194	190	185	177	173	166	164	170	173	180	182
16	183	185	193	195	198	199	201	200	196	191	188	186	180	180	182	184	187	191	192	189

Many image processing techniques begin with an examination of the statistics of the scene or image, in particular, an important technique is to examine the histogram of occurrences in a scene
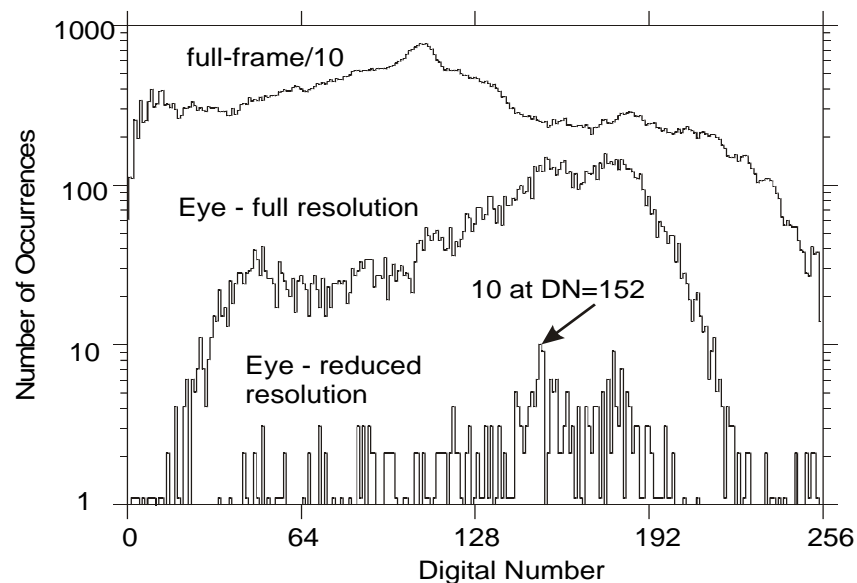

Figure 5-2 Histogram of DN occurrences. The reduced resolution curve corresponds to the image at the right of Figure 5-1, and the table above. The full resolution statistics for the same region are given, along with those for the complete 847×972 image.

This illustration is a little artificial – remote sensing scenes generally have a more even distribution of data values. The IRS-1C image of San Diego illustrated in Chapter 1, for example, has a nice Gaussian shape. Note the large number of near zero values for water.
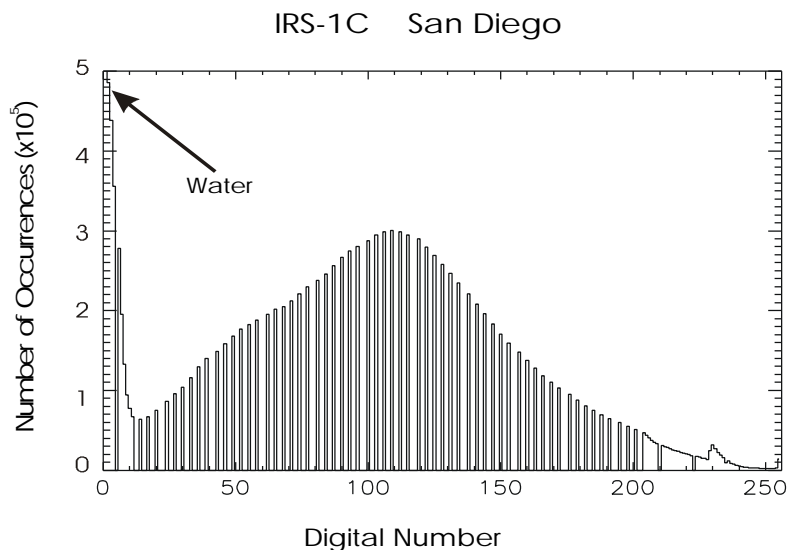

Figure 5-3 Histogram of DN occurrences

B What happens when you have spectr al data?

A fairly prosaic example is chosen from a picture of a red rose, taken with an electronic, digital camera. The image is composed of three bands, and can primarily be separated into red and green bands in this scene (plus a specular component reflecting from the leaves). The pixels from the flower lie along the horizontal axis, since the red rose has almost no green to its color. The diagonal line is the ensemble of pixels from the green leaves, starting at zero for the shadowed leaves, and rising up to a DN of 250. A few other spectral components in the scene reflect brown leaves (hidden in the shadows), and a less healthy rose near the top.
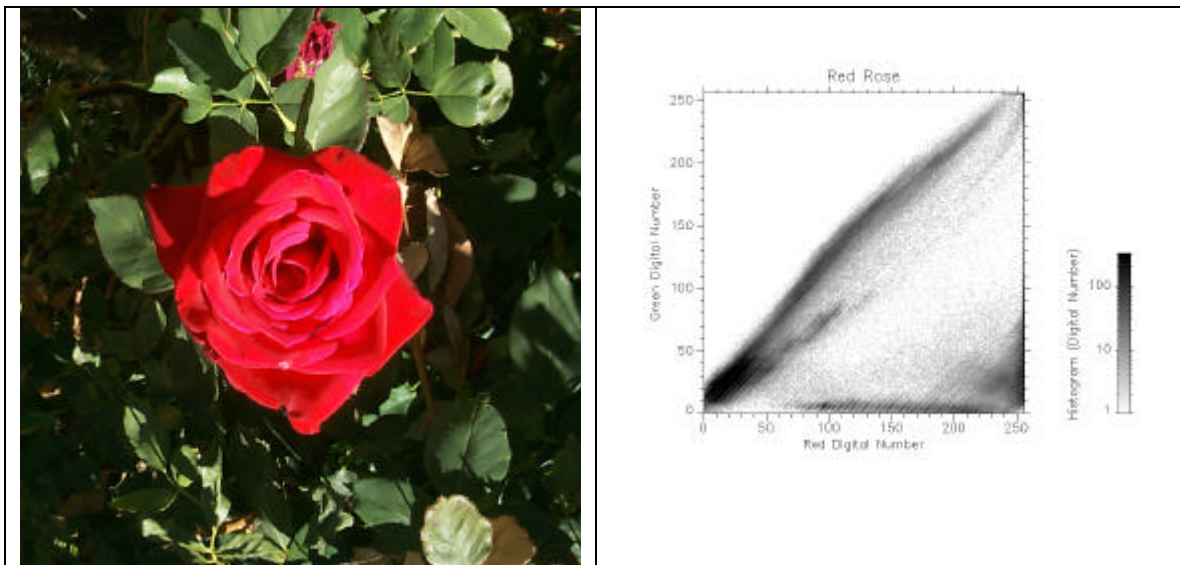

Figure 5-4 (a) Red rose, dark green leaves. (b) Scatter plot of green DN vs. red DN.
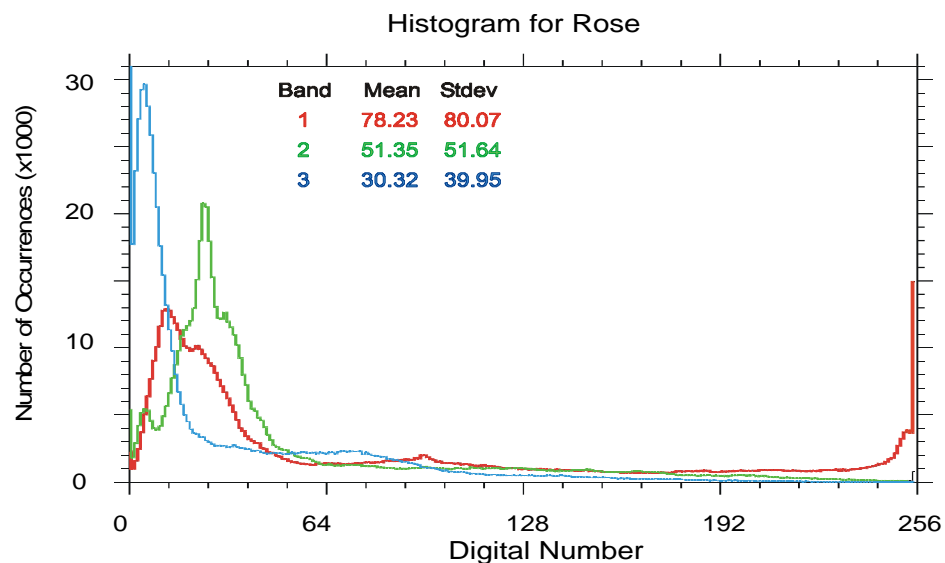

Figure 5-5 Histogram of red (1), green (2), and blue (3) bands from color image above.

One problem with any such data is the highly linear relationship between the different bands. Not really evident here, it becomes much more so when you have higher spectral dimensions to your data (6 or 7 bands with Landsat, 224 bands with AVIRIS). This can partly be understood by using the power of statistical measures such as covariance. If we calculate the covariance matrix for the 583696 points in our rose image, we get:

Covariance Matrix

Band	1	2	3
1	6411.7	1562.4	2127.8
2	1562.4	2666.6	1820.3
3	2127.8	1820.3	1596.0

This is a little hard to interpret without some sort of reference values for what represents large or small variance. The correlation coefficient is self-normalized, and allows us to obtain a measure of the relationship between the different bands.

Correlation Matrix

Band	1	2	3
1	1.000	0.378	0.665
2	0.378	1.000	0.882
3	0.665	0.882	1.000

We can see that the red and green bands are not well correlated (0.378), but green and blue are fairly highly correlated in this image (0.882). It is often helpful to completely decorrelate the different bands by taking just the right combination of bands – what I term a rotation in color space. The rotation that does this is the rotation which diagonalizes the covariance (or correlation) matrix. (Either can be done, which depends upon the nature of the problem at hand). This is called a principal components transform, also known as a Hotelling transform or a Karhunen-Loeve transform. If this is done for the above covariance matrix, the rotation we obtain is:

Eigenvectors

Eigenvector	PC 1	PC 2	PC 3
1 (Red)	0.845	-0.510	0.161
2 (Green)	0.374	0.778	0.505
3 (Blue)	0.383	0.366	-0.848

These eigenvectors have the eigenvalues:

PC Band	Eigenvalue
1	8066.72
2	2499.65
3	107.89

The eigenvalues tell us that the variance in the first two principal components is quite large (a large dynamic range in the data values), while the third component has an order of magnitude less variance. The third component is mostly noise. This becomes
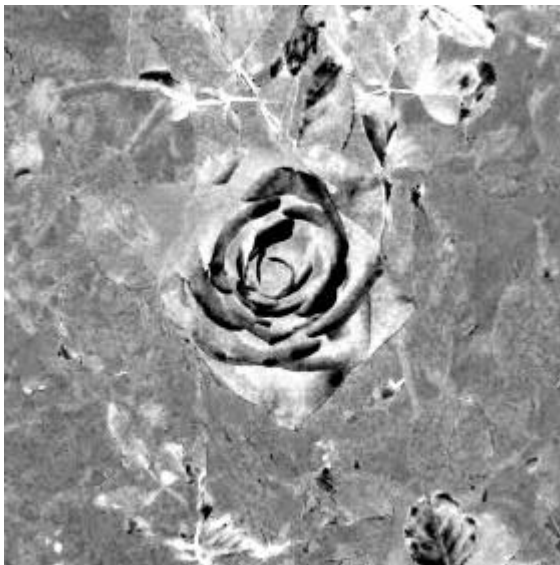
increasingly true with higher spectral dimensionality in the data, and can be used as a filter for noise in spectral imagers.


Principal Component 1

Principal Component 2

Principal Component 3

The first principal component is nominally the average of the three bands – not unlike a black & white photograph of the scene. For this particular scene, the first component is:
 0.845* red + 0.374 * green + 0.383 * blue. The second principal component breaks out the dark green leaves from the bright red rose: -0.510* red +0.778*green + 0.366* blue; basically the difference between green and blue, with things that are bright red very dark, things that are green or blue show up as bright. The third component is sort of the difference between green and blue, and has relatively little information content.

Part of the point, again, was to decorrelate the different bands. If we do a scatter plot in the new principal component space, we see that there is little obvious relationship between the different bands.
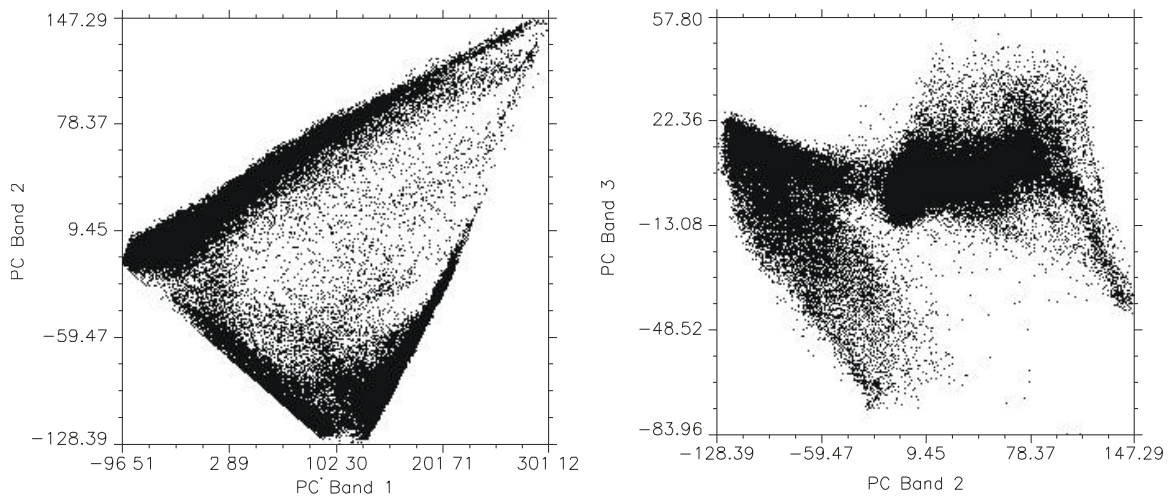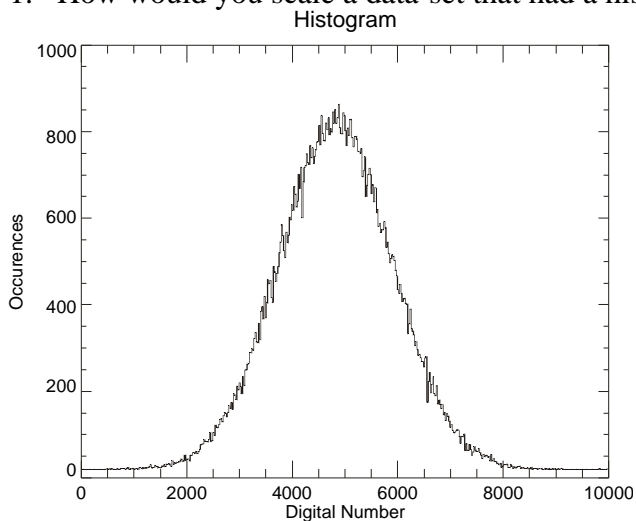
C Display vs. Analysis

1 Correcting for sensor artifacts (calibration), atmospheric effects

2 Image processing - histograms, contrast, color tricks

3 spectral processing - rotations in color space, classifiers

D Geographic Information Systems - GI S

E Problems

1. How would you scale a data-set that had a histogram distribution like this:

Chapter 7 THERMAL INFRARED

The above chapters largely describe the nature of data observed via reflected sunlight. Data from such systems have one obvious problem - they don't work well at night. This leads fairly promptly to a desire to work in the portion of the electromagnetic spectrum defined by the thermal emission intrinsic to all objects at a temperature above absolute zero. There are more subtle motivations, as well, because one can extract information from thermal imagery which is not available in the reflective domain - notably temperature.

A IR basics

Reflected vs. emitted radiation - in the visible, we mostly see by reflected (sun-light). In the IR, there is a reflected solar component (during the day), but much of the remote sensing is due to emitted IR, particularly in the mid-IR range (5 microns). Figure 2-9 in chapter 2 shows how the location of the peak in the spectrum and the amplitude of the radiation change with temperature. As a consequence of these curves, we can both 'see' in the ir, and obtain temperature measurements of remotely sensed scenes.

1 Stefan-Boltzman Law

We saw the Stefan-Boltzman law earlier in the text, and briefly repeat some elements here. Of particular interest is the difference between the sun as a black-body, and terrestrial objects.

Figure 7-1.
If you look at the radiation from the sun, the sun acts like a blackbody at about 6000 K. Of course, the radiation from the sun decreases as per the inverse square law, and the incident radiation observed at the earth is decreased by that factor: $\left(radius_{sun} / radius_{earth\ orbit} \right)^2$.
As a consequence, if you look at the 3-5 micron wavelength range, it is right in the middle of the transition region from dominance by reflected solar radiation to dominance by emitted thermal radiation for terrestrial targets.
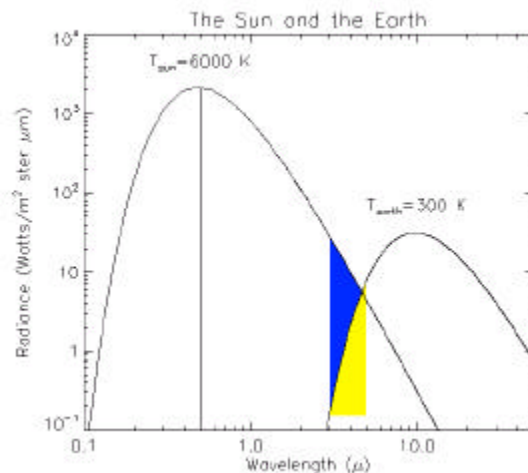
Two laws define the shapes shown in the upper figure.

2 Wien's displacement law

Wien's displacement law says that the wavelength of the peak is inversely related to the temperature:

$$\lambda_m = \frac{a}{T} \qquad\qquad\qquad (\text{Eqn. 7.1})$$

where a is a constant: $a = 2898\ \mu m/K$.

3 Stefan-Boltzmann: Radiance aT^4

The Stefan-Boltzmann law defines the total power:

$$S = \sigma \; T^4,$$
<div align="right">(Eqn. 7.2)</div>

where σ is again a constant: $\sigma = 5.669 \times 10^{-8}$ W m^{-2} K^{-4}.

4 Emissivity

The above numbers are for so-called 'black-bodies', which are perfect absorbers and emitters of radiation. Real objects all have an emissivity (ε) which is between 0 and 1, and modifies the emitted power, S - $power = \varepsilon \, \sigma \, T^4$. The table below shows some average values for the 8-12 micron wavelength range. Just as with reflective spectra, there are fine scale variations in the emissivity, which are unique to the materials.

Material	Emissivity
Granite	0.815
Sand, quartz, large-grain	0.914
Asphalt, paving	0.959
Concrete walkway	0.966
water, with thin layer of petroleum	0.972
Water, pure	0.993

Table 1. From Sabins, *Remote Sensing and Image Interpretation*, page 138.
His citation: Buettner and Kern, JGR, 70, p1333, 1965.
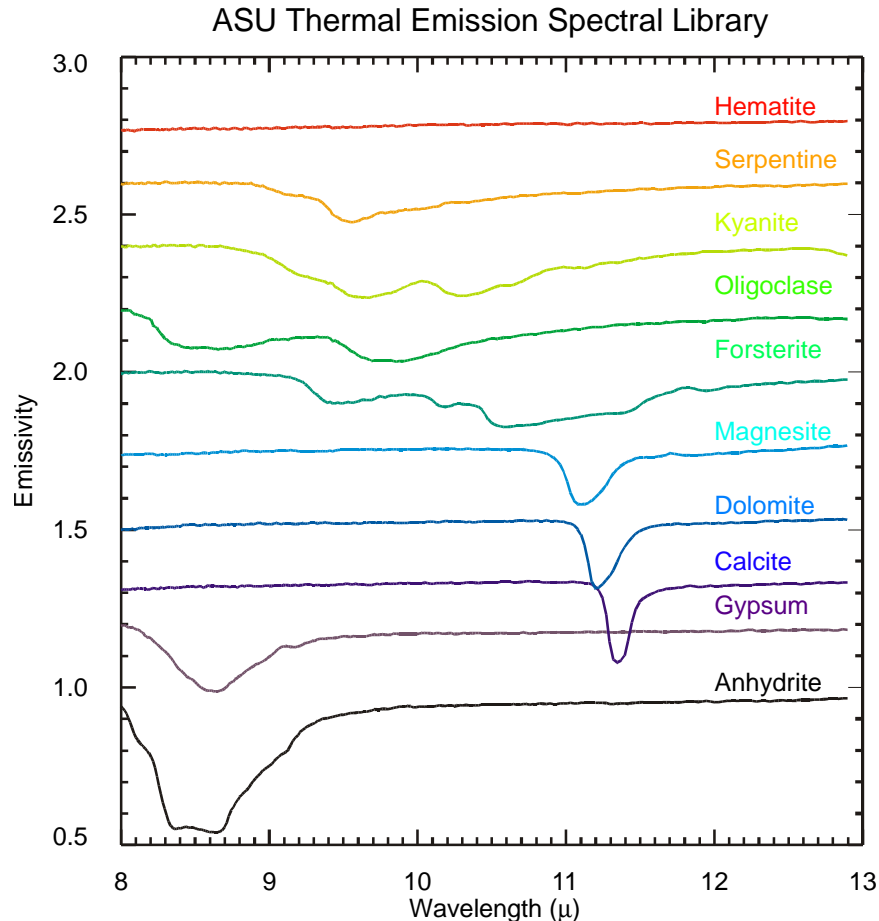
ASU Thermal Emission Spectral Library

Figure 7.2 Minerals have a number of interesting spectral characteristics that make the thermal IR region interesting for geological work. This figure is a "stack-plot" - the curves here are offset by a constant value of 0.2. Most of these materials have an emissivity near 1 at the high wavelength limit (13 μ). Notice how the variation in emissivity is fairly modest, in contrast for the much larger variation seen in the reflective bands (figures 5.1 and 5.2).

5 Atmospheric Absorption

In the infrared wavelength range, atmospheric absorption, due primarily to water (H_2O) and carbon dioxide (CO_2), becomes a very important consideration. (Figure 3.15)

B More IR

1 Kinetic Temperature

Resuming now with newer material, the concept of kinetic temperature appears. A remote sensing instrument, in general, will not be able to factor emissivity into the image analysis. As a result, although the radiated quantity is $\varepsilon\sigma\, T_{kinetic}^4$, the sensor data must be interpreted as $\sigma\, T_{radiated}^4$.   Here, $T_{kinetic}$ is the "real" temperature, meaning the temperature one would measure with a thermometer at the target. Setting the two equal, we obtain:

$\sigma\, T_{radiated}^4 = \varepsilon\sigma\, T_{kinetic}^4$, or $T_{radiated}^4 = \varepsilon T_{kinetic}^4$.   Note that ε is a number less than one, so $T_{kinetic} > T_{radiated}$ by a factor which is just the fourth root of ε, or

$$T_{radiated} = \sqrt[4]{e} \; T_{kinetic}$$

2 Thermal inertia, conductivity, capacity, diffusivity

Normal reflective observations depend primarily on the instantaneous values for the incident radiation, but thermal IR observations are very much dependent on the thermal history of the target region.

See: Physical Principles of Remote Sensing, W. G. Rees, p109-113

a Thermal Conductivity

Thermal Conductivity is the rate at which heat will pass through a material. It is measured as the amount of heat (calories) flowing through a cross-section area (cm^2), over a set distance (thickness in cm), at a given temperature difference (^{o}C). It is given the symbol:

$K \left(\dfrac{\text{calories}}{\text{cm s } ^o\text{C}} \right)$, where the nominal value for rocks is 0.006 in these peculiar units.

(compare water, ~0.001). Rocks are generally poor conductors of heat compared to metals, but are better than loose soil, which tends to have insulating air pockets.

b Thermal Capacity

Thermal Heat Capacity is a measure of the increase in thermal energy content (heat) per degree of temperature rise. It is measured as the number of calories required to rais the temperature of 1 gm of material by 1 ^{o}C. It is given the symbol: $C \left(\dfrac{\text{calories}}{cm^3 \; ^o\text{C}} \right)$

The specific heat is a closely related quantity, modifed by the mass density:

$c \left(\dfrac{\text{calories}}{gm \; ^o\text{C}} \right)$ where the value for water is very high (1.0), about 5 times that for rocks.

(Note: $C = \rho \, c$, where ρ is the mass density in $\dfrac{gm}{cm^3}$)

c Inertia

Thermal Inertia is the resistance of a material to temperature change, indicated by the time dependent variations in temperature during a full heating/cooling cycle.

$P = \sqrt{K \, \rho \, c} \left(\dfrac{\text{calories}}{cm^2 \; ^o\text{C} \; s^{\frac{1}{2}}} \right)$ varies by a factor of 4 or 5 for the range of materials shown

in figure 5-5 of Sabins.

d Thermal Diffusivity

Thermal diffusivity is a measure of the rate of internal heat transfer within a substance.

IT is related to the conductivity: $k = \dfrac{K}{c \, \rho} \left(cm^2 / s \right)$. In remote sensing, it relates the

ability of a substance to transfer heat from the surface to the subsurface during the day (heating period), and from the subsurface to the surface during the night (cooling period).

	Water	Sandy Soil	Basalt	Stainless Steel
K	0.0014	0.0014	0.0050	0.030
C	1.0	0.24	0.20	0.12
ρ	1.0	1.82	2.80	7.83
P	0.038	0.024	0.053	0.168

Table 2. From the remote sensing tutorial, http://eerst.gsfc.nasa.gov/Sect9/Sect9_3.html.
Units are cgs. See also table 6-4 in Avery and Berlin, page 123.

e Diurnal Temperature Variation:

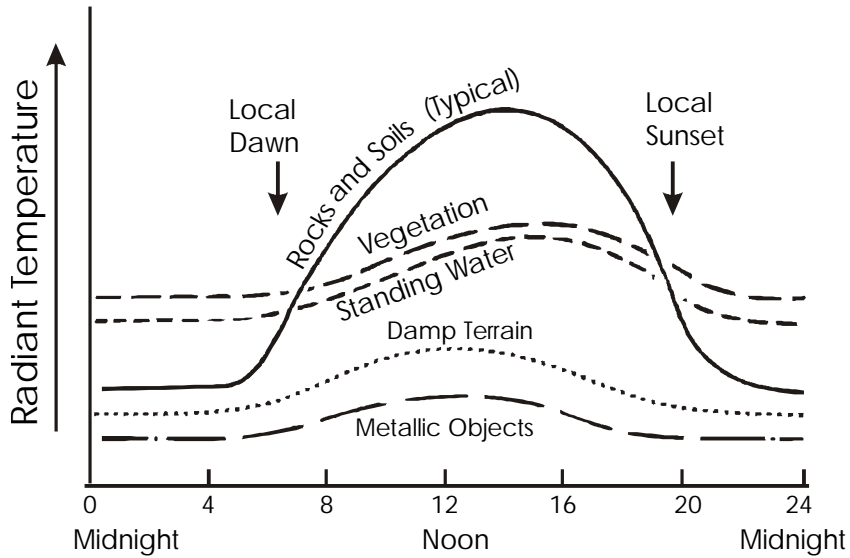The net result, and important when interpreting images.

Figure 7.3 Thermal inertia. Note the times of thermal "cross-over", where the rocks and vegetation have the same temperature. At such times, it will be difficult to distinguish such scene elements.

C LANDSAT

Infrared data from Landsat were shown in Chapter 1 for a San Diego scene. Here, a second example is shown where the Landsat 7 thermal band is used. The illustration is from over northern Greenland, at Thule AFB. In the color picture below, the 60-meter resolution data from Band 6 was resampled using cubic convolution to an effective pixel size of 5 meters. This was then combined with panchromatic band data into a Red-Green Blue picture below. Band 6 data are shown in red and the panchromatic band data are assigned to both the green and blue channels.

Note how some features are shown to be warmer than the surrounding snow due to heating from the 24-hour sunlight now being experienced at this high northern latitude. The runway and various buildings on the base show relative warmth. The southern sides of the storage tanks near the base show somewhat greater warmth than the northern sides. Exposed rock on the hillsides to the north are emitting greater thermal radiation than the snow.
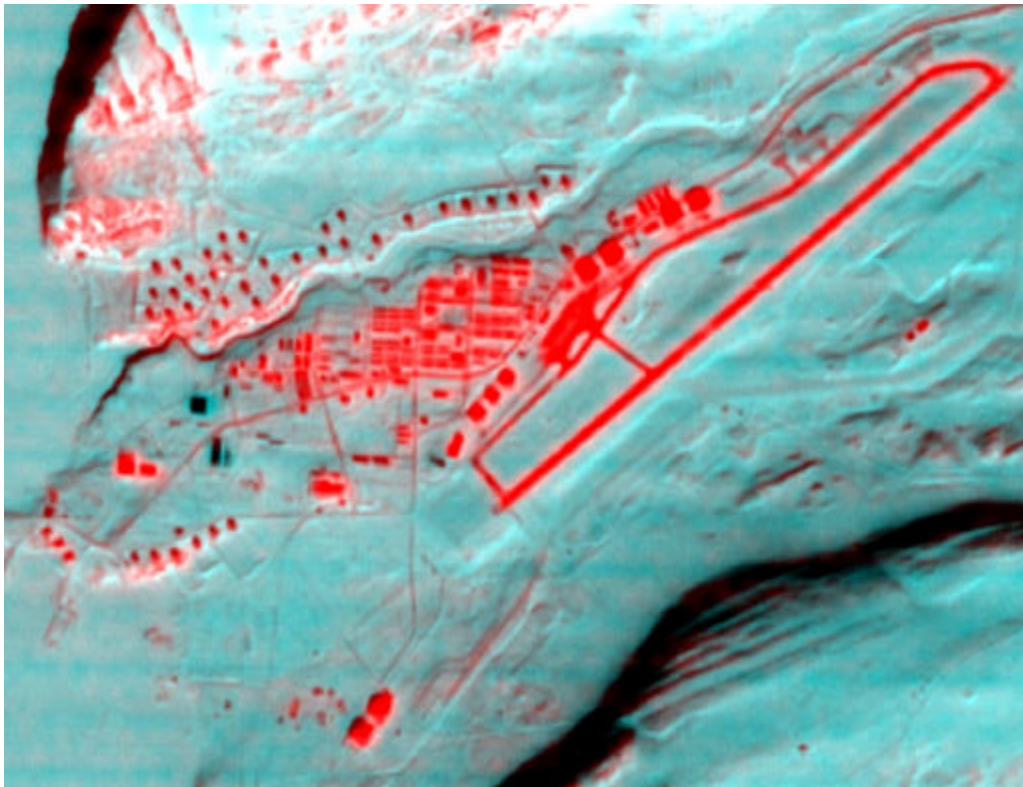

Figure 7-4. (Jim Storey of the EROS Data Center did the resampling and enhancement of this image, as part of the Landsat 7 calibration effort.)

D FLIR

Military airborne systems - see Recon-optical.

E Early Weather Satellites

Weather satellites are some of the primary IR platforms. Historically, the first were small polar orbiting platforms (TIROS, NIMBUS), followed by the first geosycnchronous platforms (ATS). The first illustrations here are in the visible wavelengths. These can be considered additional perspective on the question: can surveillance be done a the tactical or strategic level from high altitudes.

1 TIROS

The Television Infrared Observation Satellite (TIROS) was the first series of meteorological satellites to carry television cameras to photograph the Earth's cloud cover and demonstrate the value of using spacecraft for meteorological research and weather forecasting. The first TIROS was launched on 1 April 1960 and returned 22952 cloud cover photos. The satellite was tiny by modern standards: Mass: 120 kg. Perigee: 656 km. Apogee: 696 km. Inclination: 48.4 deg. RCA built the small cylindrical vehicle: 42" in diameter, 19" in height

TIROS has a complicated history of name changes and aliases, sensor packages, and other parameters. Between 1960 and 1965 ten TIROS satellites were launched. They were 18-sided cylinders covered on the sides and top by solar cells, with openings for two TV cameras on opposite sides. Each camera could acquire 16 images per orbit at 128 second intervals.
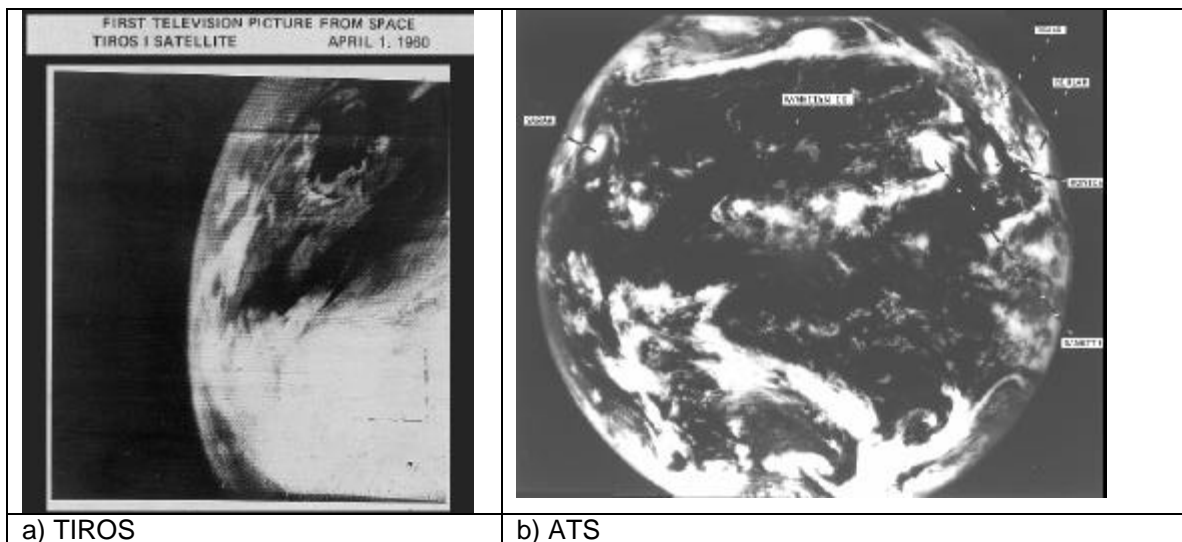

| a) TIROS | b) ATS |

Figure 7-5.

2 NIMBUS

Nimbus, a second-generation meteorological satellite, named for a cloud formation, was larger and more complex than the TIROS satellites. Nimbus 1 was launched on 28 August 1964 and carried two television cameras and two infrared cameras. Nimbus 1 had only about a one-month life span; six more missions were launched, with Nimbus 7 operating from 1978 through 1993.

The polar-orbiting spacecraft consisted of three major elements: (1) a sensory ring, (2) solar paddles, and (3) the control system housing. The solar paddles and the control system housing were connected to the sensory ring by a truss structure, giving the satellite the appearance of an ocean buoy. Nimbus, depending on the experiments carried, was 3.04 to 3.7 m tall, 1.52 m in diameter at the base, and 3 to 3.96 m across with solar paddles extended.

NIMBUS III HRIR DAYTIME ORBIT 711 6 JUNE 1969
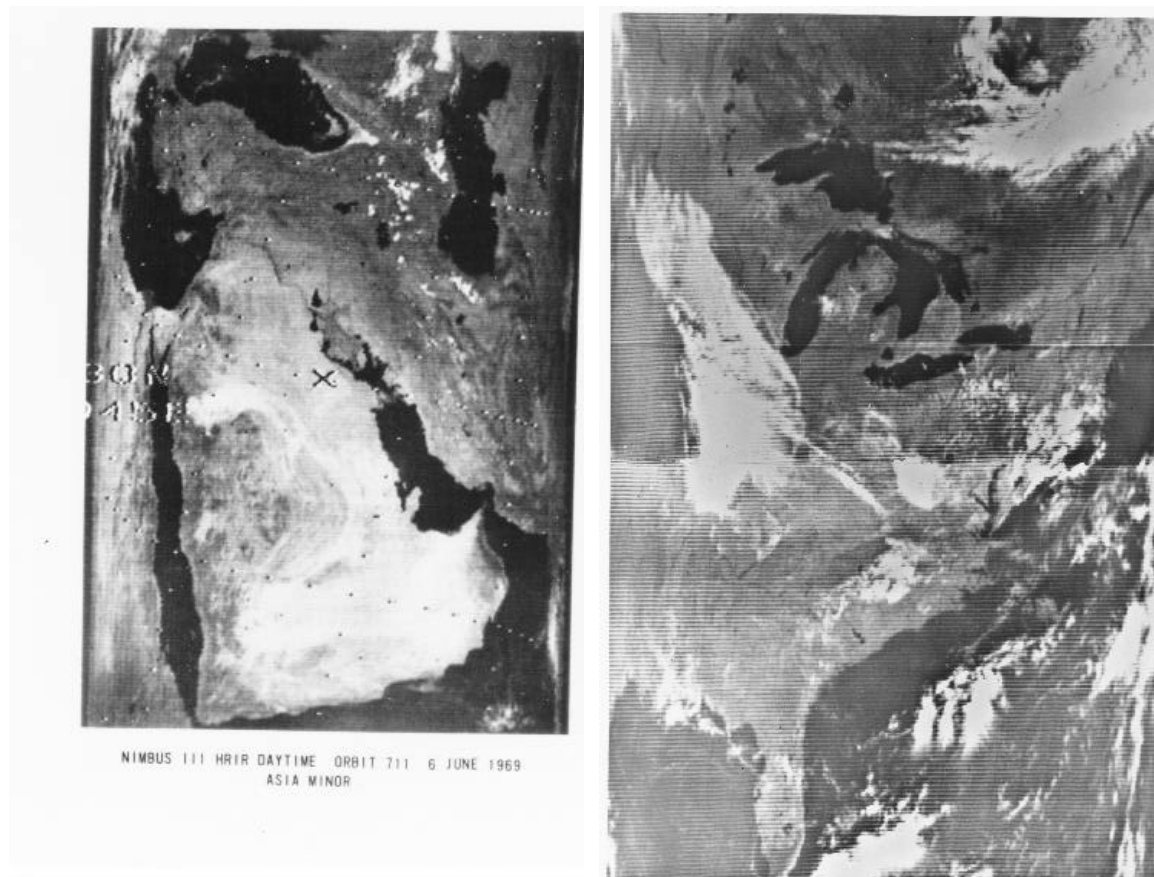ASIA MINOR

Figure 7-6 NIMBUS 1 Mass: 376 kg. Perigee: 429 km. Apogee: 937 km. Inclination: 98.7 deg. Returned 27,000 cloud cover images.

The spacecraft carried an advanced vidicon camera system for recording and storing remote cloudcover pictures, an automatic picture transmission camera for providing real-time cloud cover pictures, and a high-resolution infrared radiometer (3.4 to 4.2 micron) to complement the daytime TV coverage and to measure nighttime radiative temperatures of cloud tops and surface terrain.

3 Applied Technology Satellites (ATS)

The Applied Technology Satellite (ATS) series of satellites were designed to be geosynchronous orbiters, and were primarily communications technology testbeds. Several carried weather packages, however, and were precursors to today's GOES satellites.

a ATS-1

ATS-1 was launched in 1966. During its 18-year lifetime, ATS-1 examined spin stabilization techniques, investigated the geostationary environment, and performed several communications experiments. Its VHF experiment tested the ability to act as a link between ground stations and aircraft, demonstrated collection of meteorological data from remote terminals, and evaluated the feasibility of using VHF signals for navigation. The mission also provided the first full-Earth cloud cover images.

b ATS-3

ATS-3 was built by the Space Systems Division of Hughes Aircraft, El Segundo, CA. It was nearly identical to ATS-1. (ATS2 & 4 both failed to orbit properly.) The satellite was launched from NASA's Cape Kennedy on November 5, 1967, on top of an Atlas-Agena D launch vehicle. The satellite was initially placed in geosynchronous orbit at 47° West longitude, and was moved to several other locations to support various experiments before running out of fuel at 105° West longitude. The satellite remained in operation as a communications satellite for over 25 years.

Satellite Characteristics: THESE NUMBERS NEED SERIOUS CHECKING - look at GSFC

	ATS-1	ATS-3
Mass	295 kg. ?	352 kg.
Diameter	57.6" 1.42 m	57.6" 1.8 m
Height	54" 1.35 m	54" 1.42 m
Stabilization	Spin	Spin
Wavelength	0.475μm-0.630μm	0.39μm - 0.70μm
Spatial Resolution	>4km @ satellite subpoint	
Swath (Scan Angle): FOV	15° × 15°	

 Solar array providing 180W BOL, 2 6 Ah NiCd batteries,

c Spin Scan Cloud Cover Camera (SSCC)

The SSCC consisted of a 2-element Cassegrain-type telescope. Light entering the system was reflected from a 13.7cm diameter, 25.4cm focal length primary parabolic mirror onto a flat secondary quartz mirror to produce an image on the face of an aperture plate. The light was then passed through the 0.025mm diameter aperture and haze filter to impinge onto a photocathode backed by a photomultiplier tube. The entire assembly could be stepped ±7.5° to produce a N-S scan corresponding to 52° north and south latitude. It took 20 minutes to scan one scene.

The first full color picture at high enough altitude to see the full disk of the Earth
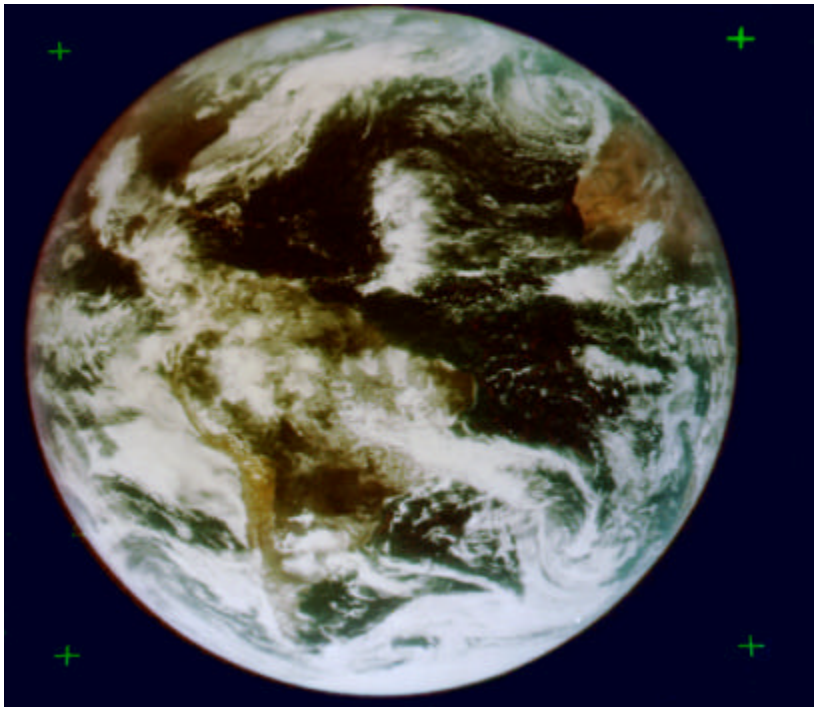

Figure 7-7. Earth in color from geosynchronous orbit - ATS-3

F GOES

1 Satellite and Sensor

The Geostationary Operational Environmental Satellite (GOES) mission provides the now-familiar weather pictures seen on newscasts worldwide. Each satellite in the series carries two major instruments, an imager and a sounder, which acquire high-resolution visible and infrared data, as well as temperature and moisture profiles of the atmosphere.

The GOES I-M system serves a region covering the central and eastern Pacific Ocean; North, Central, and South America; and the central and western Atlantic Ocean. Pacific coverage includes Hawaii and the Gulf of Alaska. This is accomplished by two satellites, GOES West located at 135 west longitude and GOES East at 75 west longitude. A common ground station, the CDA station located at Wallops, Virginia, supports the interface to both satellites.

Figure 7-8. GOES
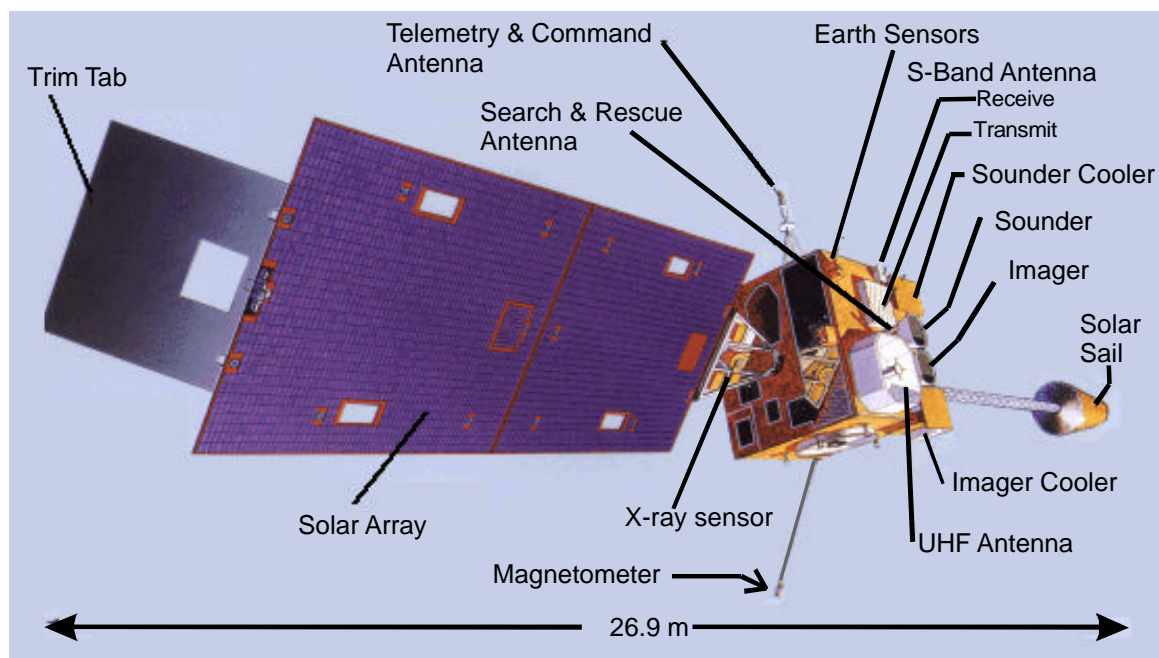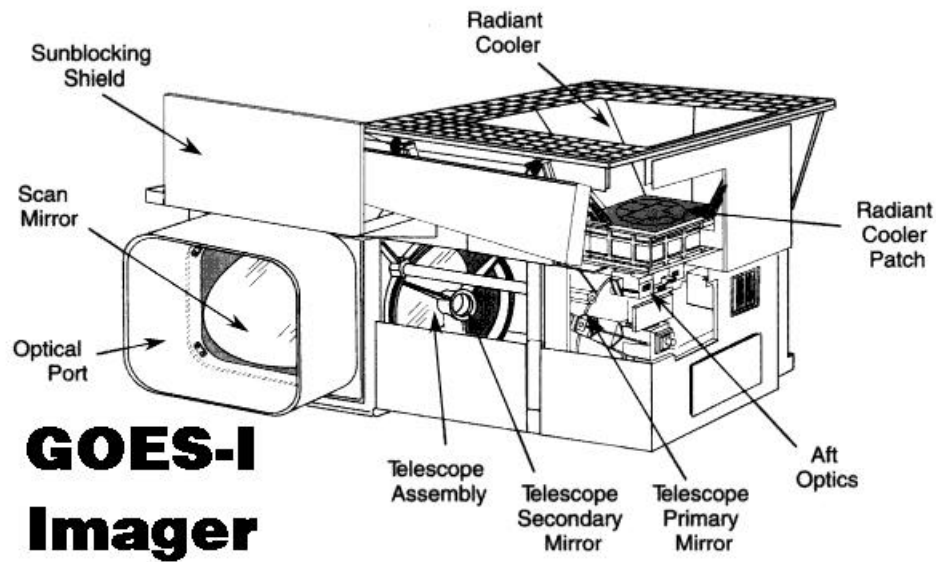
Figure 7-9

Figure 7-10. GOES-8 spectral response functions.
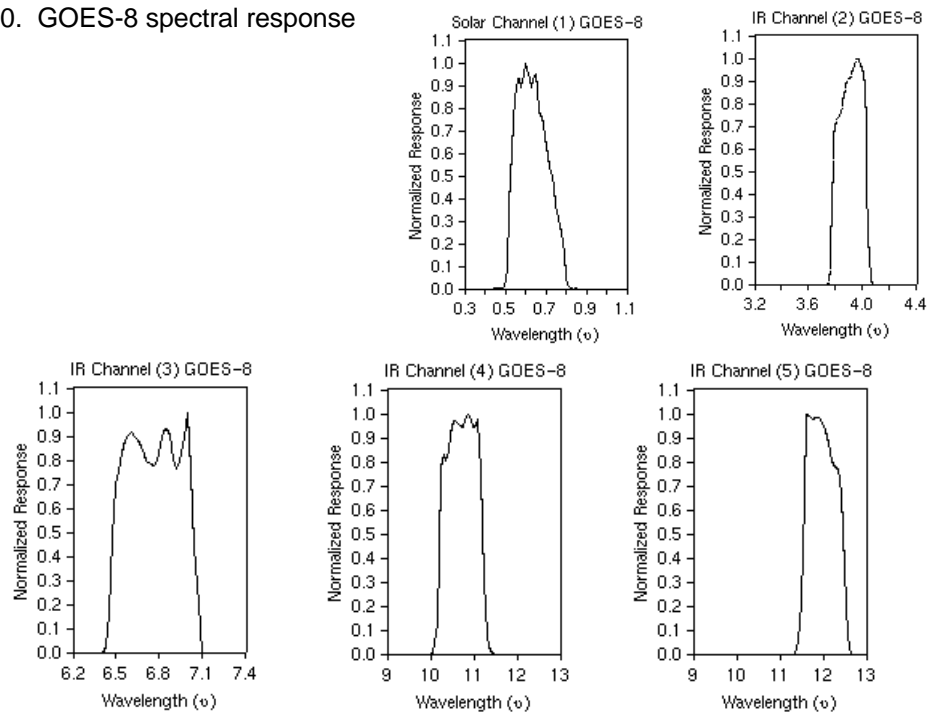
GOES 9 - 1930 UTC 4 April 1998
visible, 4 micron, 11 micron
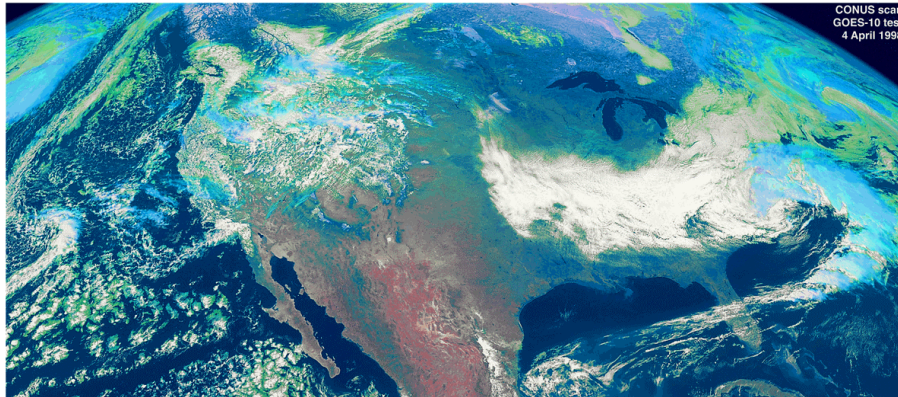
Figure 7-11 GOES vs NOAA : geosynchronous vs polar
Continuous view from geo - once every 15-30 minutes, 1 km resolution
Nadir view - worldwide coverage from polar orbiter.

2 Weather and storms - Hurricane Mitch

channel 1

IR: channel 4
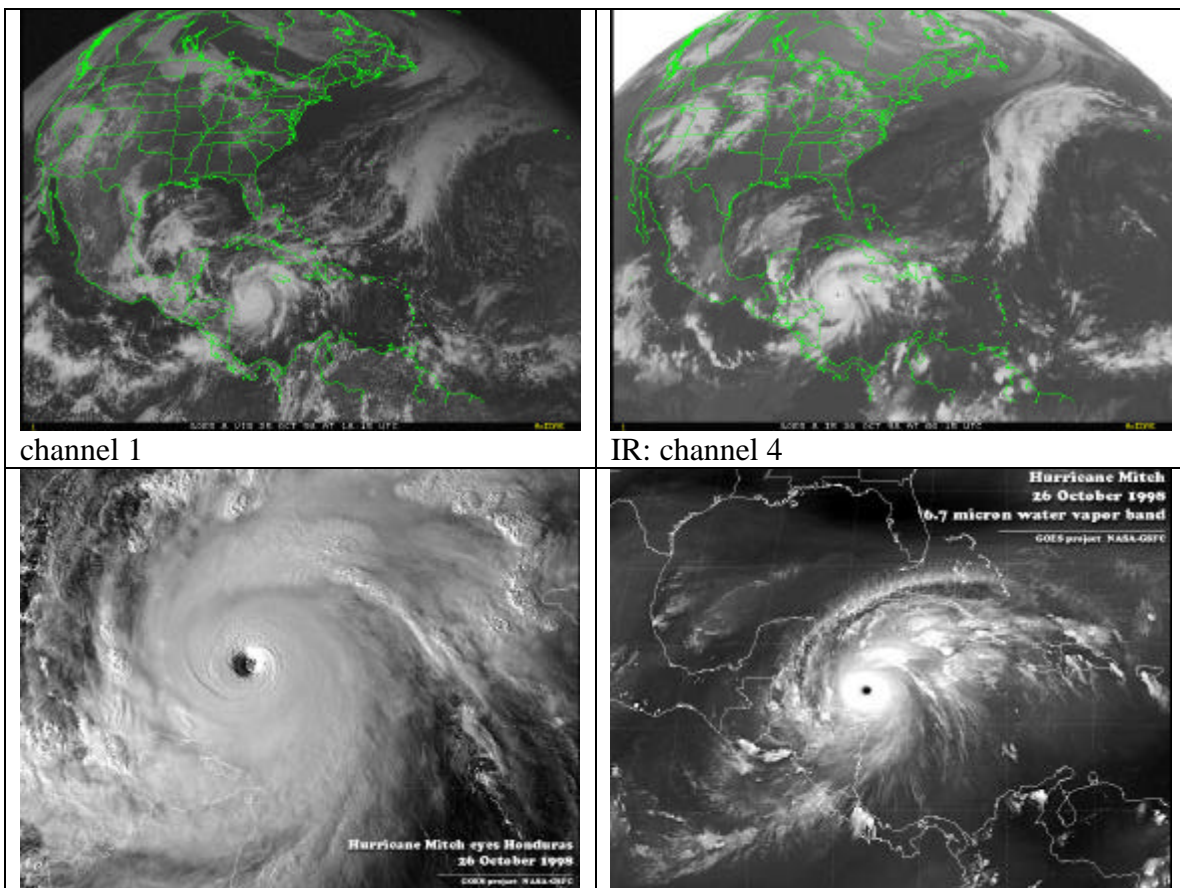
Figure 7-12 Weather

3 Volcanoes and ash clouds
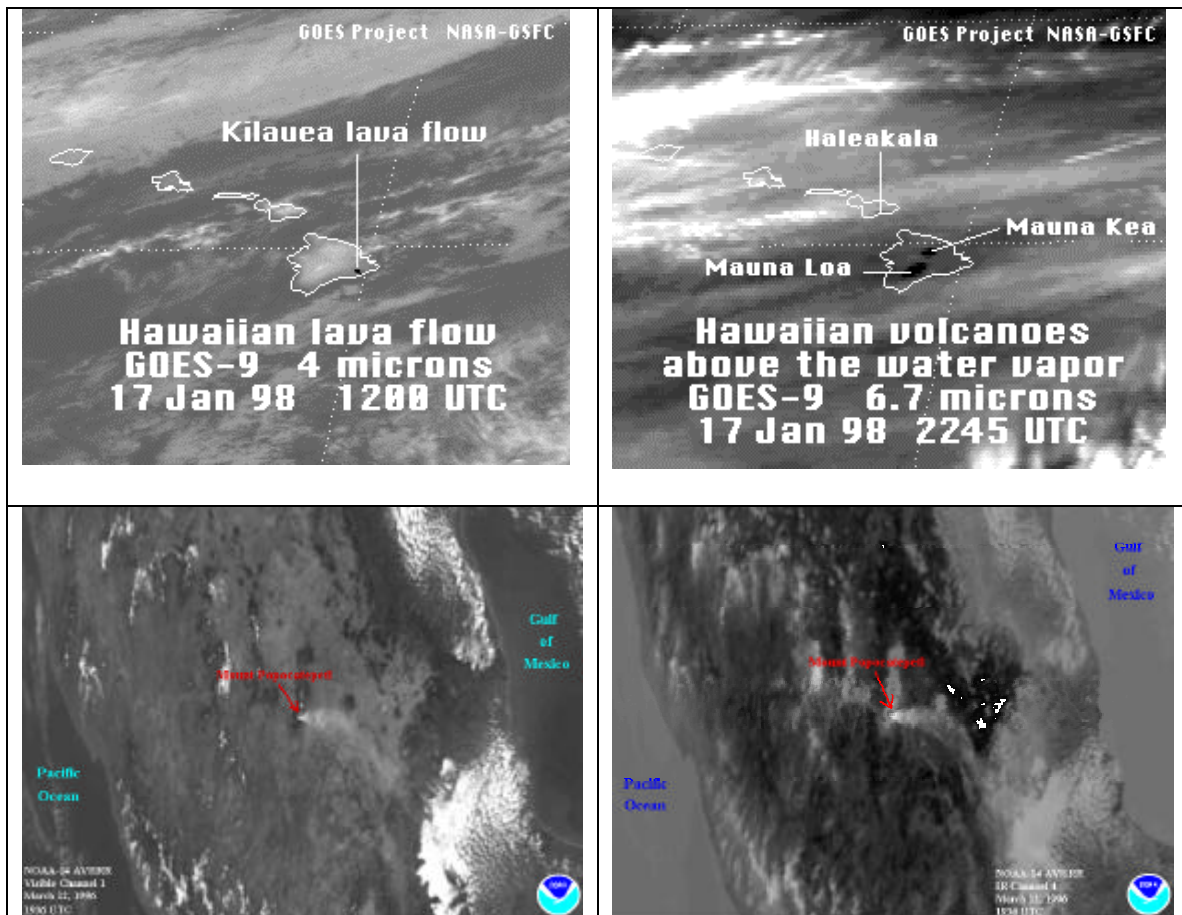
Figure 7-13. Volcanoes and volcanic ash clouds

The fact that the peaks of the Hawaiian volcanoes rise above the water vapor layer are a primary reason why they make good places for astronomical observatories. Volcanic ash clouds are a hazard for aviation, and are not easily detected by other means.

4 Shuttle launch - vapor trail, rocket

The GOES satellite makes a nice analogue for a missile warning satellite. The vapor trail is visible in the first trail (the white cloud you see from the ground). The hot, sub-pixel, target is visible in all 4 of the infrared channels. The long-wave channels (11, 12 µ) don't show very good contrast, because the earth is already bright at that wavelength. The highest contrast is in the 6.7 µ channel, because the atmospheric water vapor prevents the sensor from seeing the extensive ground clutter.

Figure 7-14.   The wavelength ranges used here were illustrated above in figure 7-7. Note that the third frame, from the 6.7µ channel shows the greatest signal-to-background.

5 SEBASS - thermal spectral

G Problems

1. At what wavelength does the radiation peak for targets at 300 K ?
    What is the ratio of the total power per unit area emitted by a person (300 K) and a hot vehicle (1000 K)?

2. What are the tradeoffs between using MWIR (3-5 µm) vs LWIR (8-13 µm)
Consider the radiated energy, the detector technology (cooling issues), Rayleigh Criteria concerns.

2. Of the materials in table 2, which will show the largest temperature fluctuation during a 24-hour heating/cooling cycle; which will show the smallest fluctuation?

This page intentionally left blank

Chapter 8 RADAR -

A Imaging radar

Radar, specifically imaging radar, provides a powerful tool for remote sensing. The two primary advantages are the 24 hour capability (independence from solar illumination), and all-weather (cloud penetration) capability. Radar can penetrate to modest depths into the earth, and can occasionally allow glimpses below the surface of the earth. This is useful for detecting buried objects, such as pipelines or mines. Polarization becomes a very powerful tool in the SAR domain.

Radar images were shown in Chapter 1, and an airborne image is shown here in Figure 8.1. The image of San Francisco is done in two wavelengths, encoded in complementary blue/yellow tones. Most of the urban surfaces reflect equally well in the two wavelengths, and much of the scene is shades of gray (white).

Figure 8-1. San Francisco, California, JPL AIRSAR, C and L band, VV polarization. October 18, 1996, 71351 seconds GMT. Ten meter GSD, aircraft tack -135°.

B Theory

1 Imaging Radar Basics

Before discussing the operation of an imaging radar system, it is appropriate to discuss the terminology and characteristics for imaging radar. Illustrations are used for Side-Looking Airborne Radar (SLAR). As shown in Figure 8-2, an airplane or spacecraft moves at some velocity and at some altitude in an azimuth, or along-track direction. Through a fixed antenna, pulses of microwave radiation are propagated outward in a perpendicular plane at the speed of light in the range, look or across-track direction. Slant range is the line-of-sight distance measured from the antenna to the terrain target, whereas ground range is the horizontal distance measured. along the surface from the ground track, or nadir line, to the target. The area closest to the ground track at which a radar pulse intercepts the terrain is the near range, and the area of pulse termination farthest from ground track is the far range.
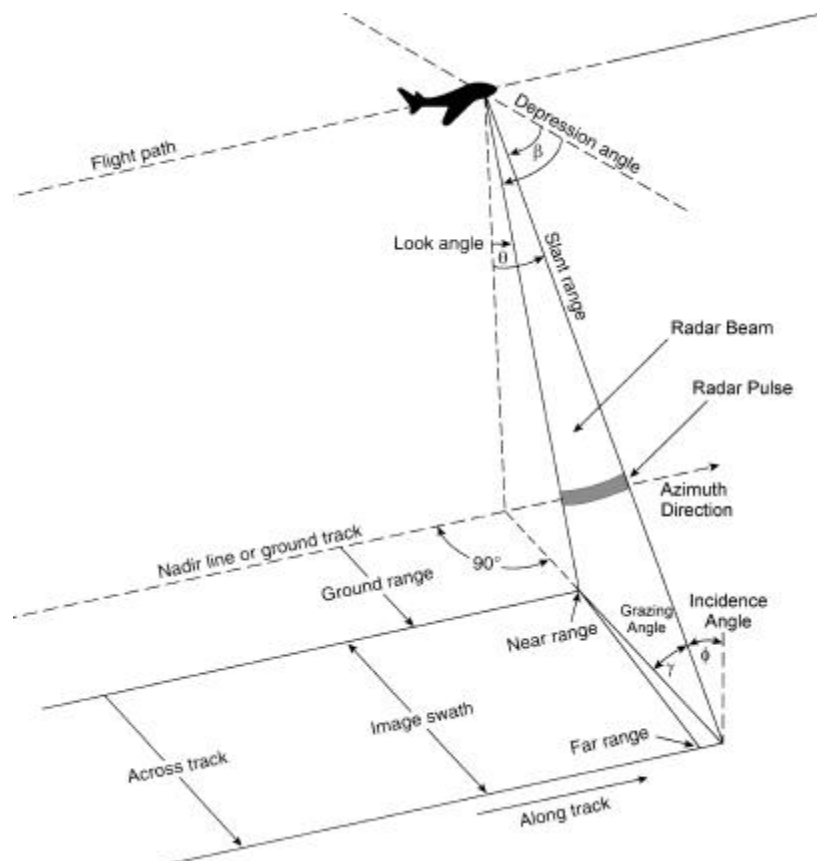
Figure 8-2. Definitions of terms for imaging radar.

The angle measured from a horizontal plane downward to a specific part of the radar beam defines the depression angle (β). The depression angle varies across the image swath from relatively steep (large angle) at near range to relatively shallow (small angle) at far range. The angle measured from a vertical plane upward to a specific part of the radar beam defines the look angle (θ). The look angle varies across the image swath from a relatively small angle at near range to a relatively large angle at far range. When

measured to the same part of the beam, the depression angle and the look angle are complementary angles ($\beta + \theta = 90°$).

The **incidence angle (f)** is the angle measured between the axis of the radar beam and a line perpendicular to the local ground surface that the beam strikes; the complement of the incidence angle is called the **grazing angle (g).** Consequently, the incidence angle and the grazing angle are a function of both the illumination angle (β or θ) and the slope of the terrain. When the terrain is horizontal, the depression and grazing angles are equal ($\beta = \gamma$) and the look and incidence angles are equal ($\theta = \phi$).

A key parameter often used to judge the quality of a radar image is resolution. Radar resolution is defined as the minimum separation between two objects of equal reflectivity that will enable them to appear individually in a processed radar image. The most important criterion for establishing resolution is the size of the pulse rectangle projected onto the ground at a given instant of time. The pulse rectangle is similar to the ground resolution cell associated with across-track scanners. When two or more objects fall within the same pulse rectangle they cannot be resolved as separate entities. Rather, they are presented as one echo to the radar system. If objects are separated by a distance exceeding the corresponding dimension of the pulse rectangle, they will be imaged separately. The size of the pulse rectangle is controlled by two independent resolutions: (1) Range resolution determines resolution cell size perpendicular to the ground track and (2) azimuth resolution establishes the cell size parallel to the ground track. These relationships are discussed in the following sections.

2 Detection

Radar detection is a measure of the smallest object that can be discerned on an image as a result of its ability to reflect microwave radiation. Detection is often associated with highly reflective metal objects such as vehicles, railroad tracks, fences, and power lines and poles, which are physically much smaller than the pulse rectangle. For example, a vehicle is normally a much better reflector of microwave than its surroundings, making it the dominant reflector in the pulse rectangle. When this composite reflectance value differs from those in surrounding cells, the radar system, in essence, detects the vehicle. However, to the radar, the vehicle is as large as the cell size. Users are often amazed by the detail seen in radar images because many small features are detected when resolution is not required to distinguish them from surrounding objects (Matthews 1975).

3 Range Resolution

Range, or **across-track, resolution** in **slant range (R_{sr})** is determined by the physical length of the radar pulse that is emitted from the antenna; this is called the **pulse length (t).** If not given, pulse length can be determined by multiplying the pulse duration (δ), or the length of time in microseconds (1 μs= 1×10^{-6}s) that the pulse was emitted from the antenna by the speed of light ($c = 3\times10^8$ m/s);

$$\tau = \delta c.$$ (Eqn. 8.1)

For a radar system to discern two targets in the across- track dimension all parts of their reflected signals must be received at the antenna at different times or they will appear as one large entity in an image. In Figure 8-3 it is seen that objects separated by a slant-range distance equal to or less than $\tau/2$ will produce reflections that arrive at the antenna as one continuous pulse, dictating that they be imaged as one large object (targets A, B, and C). If the slant-range separation is greater than $\tau/2$, the pulses from targets C and D will not overlap, and their signals will be recorded separately. Thus, slant-range resolution measured in the across- track dimension is equal to one-half the transmitted pulse length:

$$R_{sr} = \frac{c\,\tau}{2}.$$ (Eqn. 8.2)

To convert R_{sr} to ground-range resolution (R_{gr}), the formula is:

$$R_{gr} = \frac{c\,\tau}{2\,\cos\beta}$$ (Eqn. 8.3)

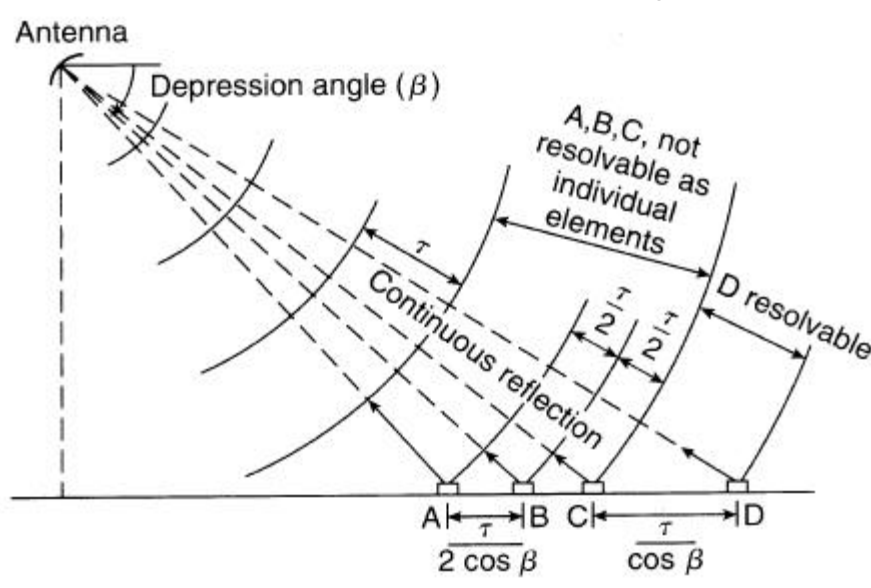where: τ= pulse length, c is the speed of light, and β= antenna depression angle.

Figure 8-3. Range resolution is a function of pulse length

It can be noted from the equation that:

(1) ground- range resolution improves as the distance from the ground track increases (i.e., across-track resolution is better in far range than in near range because β is smaller), and

(2) resolution can be improved by shortening the pulse length. However, a point will be reached when a drastically shortened pulse will not contain sufficient energy for its echoes to be detected by the receiver.

A closely related concept to the pulse duration is the pulse repetition rate, or frequency (PRF). This corresponds to the interval between pulses, and is relatively long compared to the pulse duration. Figure 8-4 illustrates the signals used for the SIR-C x-band radar. Here, the pulse width is 40-μs, the PRF is 1240-1736 Hz, or about 15 times the width of the pulses illustrated here.
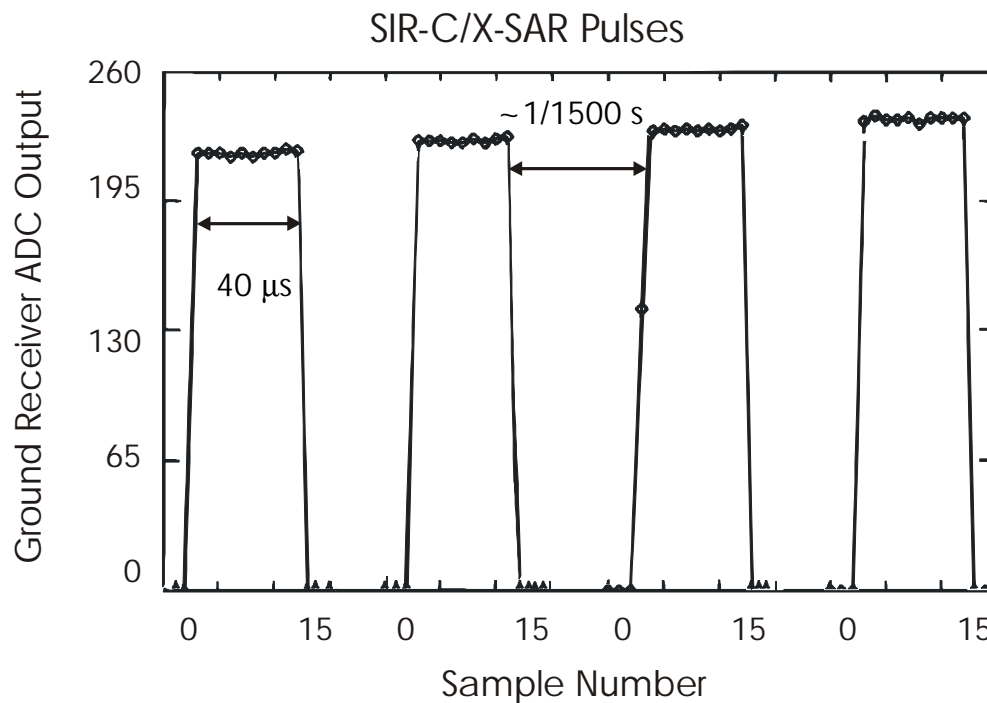
Zink & Bamler, X-SAR Radiometric Calibration and Data Quality, IEEE TGRS, July 1995

Figure 8-4. SIR-C X-SAR pulses recorded by a ground calibration receiver, sampling at 4 μs (250 kHz). Data Take 30 of SRL-1 (April, 1994). The slight variation in power seen over this interval is due to the progress of the shuttle over the ground site. Note that without signal shaping, the best range resolution which could be obtained from such pulses would be 6 km.

4 Signal Shape

Our ability to resolve targets basically revolves the length of the radar pulse - that is the spatial extent of the pulse. By manipulating the shape of the pulse, we can finesse the limitation which is imposed by our need to keep a fairly long pulse length, a requirement imposed by the power constraints of real radar.   The limitation is resolved by modulating the frequency of the pulse, or using FM chirp, invented by Suntharalingam Gnanalingam at Cambridge to study the ionosphere. (Professor Gnanalingam worked at NPS from ~1985-1995). To understand the process, we need to look at radar pulses in both time and frequency space.

A closely related concept is the bandwidth associated with the pulse length.   Figure 8-5 illustrates some basic features of signals, and the relationship between pulse length and the spread in frequencies associated with square pulses. Basically, if you have a very short pulse, a wide spectrum of frequencies is implicit, while a monochromatic signal implies a very long pulse. For an infinitely long pulse, one can have a monochromatic (single frequency) signal. For any square pulse, the transformed signal is a sinc function $\left(\dfrac{\sin x}{x}\right)$ centered at the carrier frequency.   The bandwidth is basically (twice) the inverse of the pulse length.
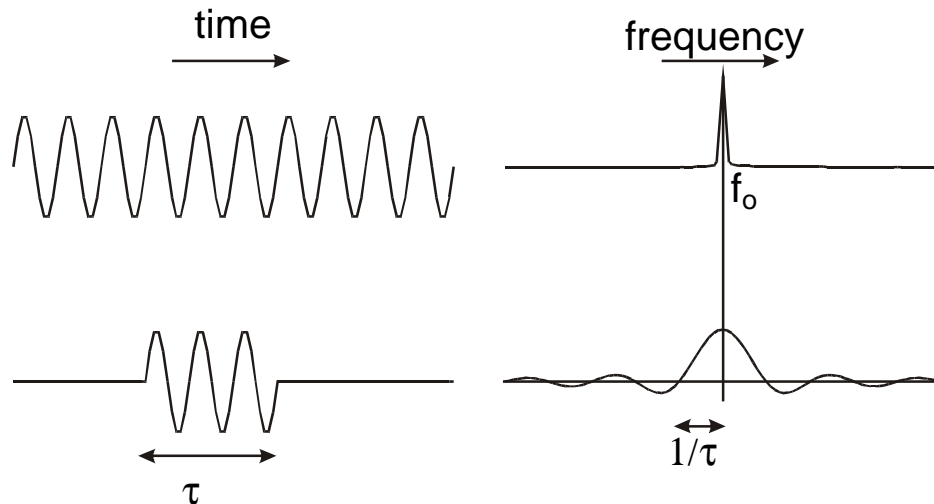
Figure 8.5 Continuous wave and pulsed signals. Note that bandwith = 2/pulse length. The plots on the right are Fourier transforms of the signals on the left.

Figure 8-6 illustrates the chirp concept - the frequency increases with time. Now, each cycle of the transmitted signal can by more or less uniquely identified by its frequency. Relatively long pulses can be used, and the width of the pulse in frequency space is now defined by the range of the chirp (Δf).   This is illustrated in Figure 8.6. The Fourier transform of this signal is a nicely defined signal again centered at the carrier frequency, and with a width of Δf.   Numbers for the SIR-C X-band were, for example $f_0 = 9.6$ GHz, and $\Delta f = 20$ MHz.   What does this buy you?   Though not shown here, the result you obtain from analysis is basically the same - the spatial resolution is defined by the pulse

length, which is the inverse of the bandwidth. With a chirped pulse, one replaces the bandwidth noted above (the inverse of the "real" pulse length), with the bandwidth of the chirp. One can obtain a spatial resolution which is defined by an effective time:

$$t = \frac{1}{\Delta f} .$$ (Eqn. 8.4)

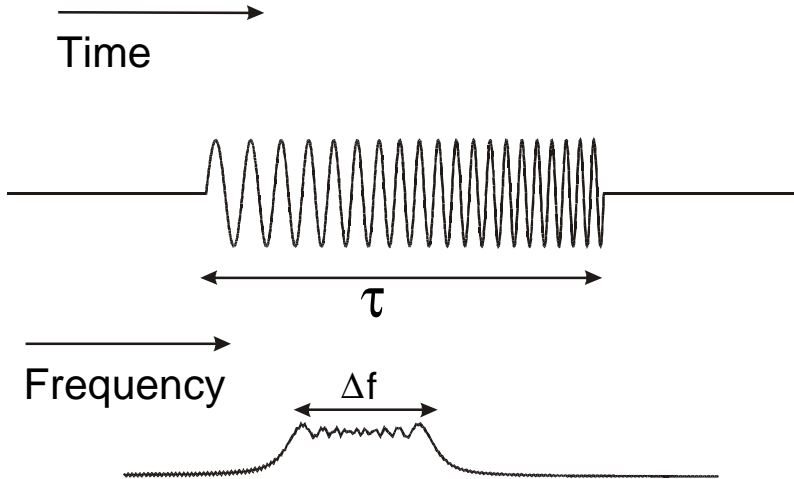which in turn gives a range resolution as given in Equation 8.2.

Figure 8.6 A pulse varies linearly in frequency from f to $f_o + \Delta f$, the power is then localized in frequency space (bandwidth). (Elachi, page 185)

_____

As an illustration, the SIR-C X-band pulse length is 40 μs, which implies a bandwidth of

$BW = \frac{1}{4 \times 10^{-5}} = 2.5 \times 10^4$ Hz , and a range resolution of

$R_{sr} = \frac{3 \times 10^8 \bullet 4 \times 10^{-5}}{2} = 6 \times 10^3$ m

using the 20 MHz chirp range for bandwidth, we get an effective pulse length of

$t = \frac{1}{\Delta f} = \frac{1}{2 \times 10^7} = 5 \times 10^{-8}$ s , and hence an effective slant range resolution of

$R_{sr} = \frac{3 \times 10^8 \bullet 5 \times 10^{-8}}{2} = 7.5$ m

The actual performance was not quite this good, as is generally found in real life.
The so-called "compression-ratio" is the ratio of the two times, which here is

$\frac{4 \times 10^{-5}}{5 \times 10^{-8}} = 8 \times 10^2$, or 800.   Just as a reference, the European ERS-1 systems has a

compression ratio of 575 on its 37.1-μs pulse, for an effective pulse duration of 64.5 ns.

_____

5 Azimuth Resolution

Azimuth, or along-track resolution (R_a) is determined by the width of the terrain strip illuminated by a radar pulse, which is a function of the beamwidth of a real-aperture radar (RAR). In Figure 8-6 it is shown that the beamwidth increases with range. Thus, two tank-like objects (at the same range) are in the beam simultaneously, and their echoes will be received at the same time. Consequently, they will appear as one extended object in an image. Two other objects, an A7 jet and T72 tank, are located outside the beam width as shown here. Since a distance greater than the beamwidth separates them; their returns will be received and recorded separately. Thus, to separate two objects in the along-track direction, it is necessary that their separation on the ground be greater than the width of the radar beam. What determines the beam width? Basically the length of the antenna.
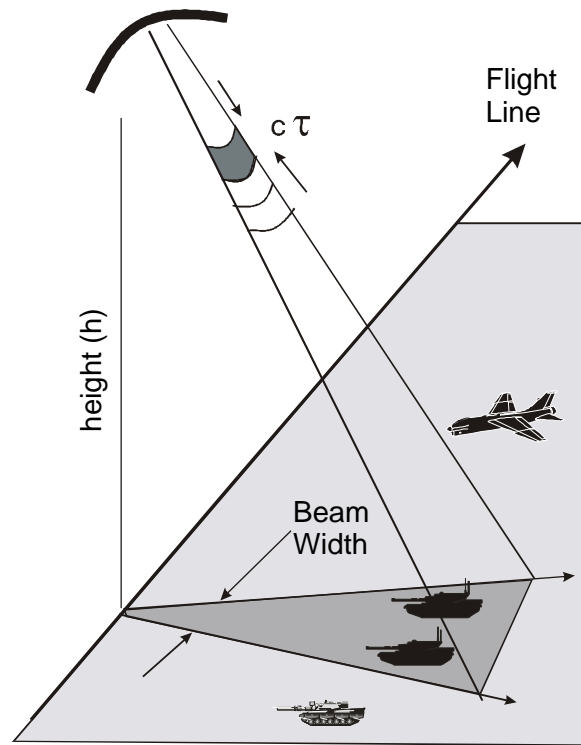
Figure 8-7

6 Beam Pattern and resolution

We need to look at the nature of the antenna radiation pattern briefly, in order to get a handle on the resolution characteristics of an imaging radar system. Following Elachi (pages 177-180), we consider the far field contribution of a radiator which is one member of a linear array.

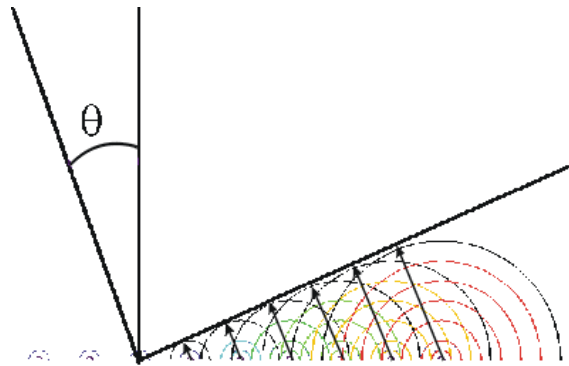$$E_n \approx \left(a_n e^{i\phi_n} \right) e^{-ikd_n \sin\theta} \qquad \text{(Eqn. 8.5)}$$

Figure 8-8. Elachi, page 177

The total field from all the radiators is the sum of the elements

$$E(\theta) \approx \sum_n a_n e^{i\phi_n - ikd_n \sin\theta} \qquad \text{(Eqn. 8.6)}$$

where each element contributes and amplitude a_n, and a phase ϕ_n. If the radiators are all identical in phase and amplitude, and equally spaced, then the total field is

$$E(\theta) \approx ae^{i\phi} \sum_{n=1}^{N} e^{-inkd \sin\theta} \qquad \text{(Eqn. 8.7)}$$

This sum is strongly dependent on the factor in the exponential, $\Psi = kd\sin\theta$. If the phase, Ψ, is zero, then all the elements add, and we get a strong signal. As Ψ increases, the vectors are out of phase, and the sum will decrease. For the case $N\Psi = 2\pi$, the sum is zero. This corresponds to: $Nkd\sin\theta = 2\pi$, or more generally

$$Nkd\sin\theta = 2m\pi, \qquad \text{where m= 1,2,3, ...} \qquad \text{(Eqn. 8.8)}$$

This defines the zeroes in the beam pattern. For a continuous antenna element, the sum is replace by an integral over an antenna of length L:

$$E(\theta) \approx \int_{-\frac{L}{2}}^{\frac{L}{2}} a(x) e^{-ik\sin\theta} dx = \int_{-\frac{L}{2}}^{\frac{L}{2}} e^{-ik\sin\theta} dx = L\frac{\sin(kL\sin\theta / 2)}{kL\sin\theta / 2} \qquad \text{(Eqn. 8.9)}$$

The power at any particular location will then be proportional to the square of the electric field strength.

Figure 8-9 shows this characteristic $\sin^2\alpha / \alpha^2$ shape, with zeros where the argument of sin is $m\pi$, or :

$$kD\sin\theta / 2 = m\pi$$
$$\Rightarrow kD\sin\theta = 2m\pi \qquad \text{(Eqn. 8.10)}$$

This leads to:

$$\frac{2\pi}{\lambda} D\sin\theta = 2m\pi \qquad \Rightarrow D\sin\theta = \lambda, \text{ or}$$

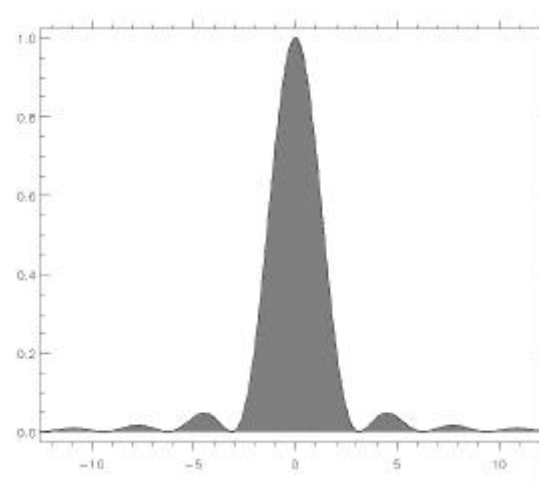$$\frac{\lambda}{D} = \sin\theta \qquad \text{(Eqn. 8.12)}$$

Figure 8-9. The square of the sinc function: $\sin^2(\alpha)/\alpha^2$

This is effectively the same result as we inferred for the resolution of diffraction limited optics- and the reasons are the same!

The equation for determining azimuth resolution (R_a) is

$$R_a = \frac{\lambda\, R_s}{D_a} \qquad \text{(Eqn. 8.13)}$$

where: λ= operating wavelength,
R_s = slant range to the target, and
D_a= length of the antenna.

The relationships expressed in Equation 8-13 show that:
(1) azimuth resolution decreases in proportion to increasing range (i.e., resolution is best in near range, where the width of the beam is narrowest), and
 (2) a long antenna or a short operating wavelength will improve azimuth resolution.
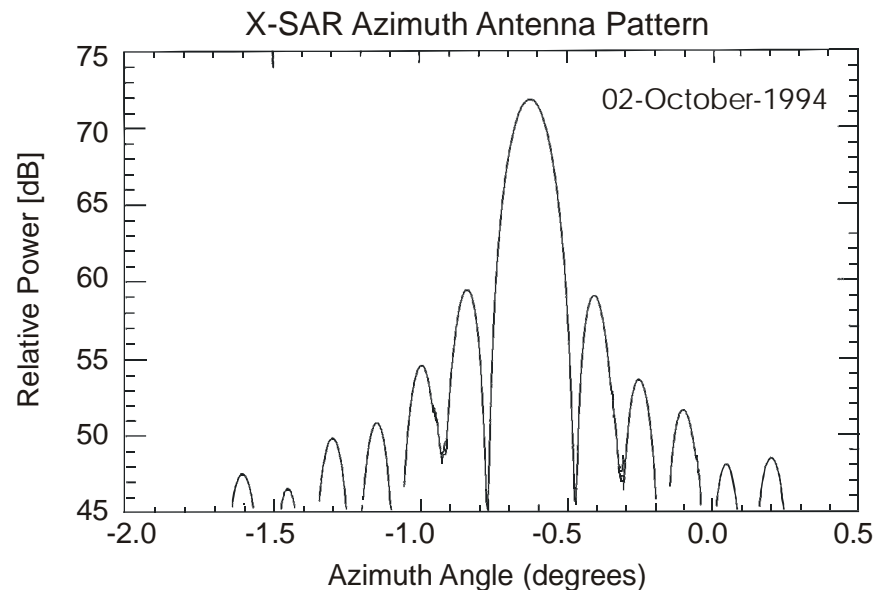
 The latter two parameters both enable the radar beam to be focused into a narrower angle; beam spreading is inversely proportional to antenna length and directly proportional to wavelength. There are several ways to obtain improved azimuth resolution with conventional RARs: a long antenna, a short operating wavelength, or a close-in range interval. However, the practical limit of antenna length for aircraft stability is about 5 m, and the all-weather capability of radar is effectively reduced when the wavelength is decreased below about 3 cm. Because of these limitations, RARs are best suited for low-level, short-range operations.

The resolution of a real aperture, imaging radar is, in the along track direction, given above can be rewritten as:

$$R_a = \frac{\lambda\, h}{L \cos\theta} \qquad\qquad \text{(Eqn. 8.14)}$$

For ordinary space kinds of numbers (antenna length L = 10 m, λ=3 cm, h = 800 km, θ=20°) we get a resolution of 2.5 km.   We need a bigger antenna!

Before proceeding to the method by which a long synthetic antenna can be constructed, we look briefly at some real antenna patterns, again from the SIR-C X-SAR instrument. Figure 8-10 shows what certainly appears to be a sinc^2 pattern, per the theory described above (note that the use of dB as a unit means that we have a logarithmic vertical axis). A companion figure, Figure 8-11, shows the data on a linear vertical scale (bottom), and divided by the expected factor of $\text{sinc}^2\left(\dfrac{f}{0.151^{\circ}}\right)$ in the top. Here, the model is for the 3-cm (9.6 GHz) waves, given the 12-meter antenna length ($0.151° = \dfrac{l}{L}$).

X-SAR Azimuth Antenna Pattern

02-October-1994

Relative Power [dB] vs Azimuth Angle (degrees)

Zink & Bamler, X-SAR Radiometric Calibration and Data Quality, IEEE TGRS, July 1995

Figure 8-10. SIR-C X-SAR azimuthal antenna pattern as observed from ground observations along the beam centerline (the center of the range antenna pattern).

One-Way Azimuth Antenna Pattern

Ratio to Sinc^2

Main Lobe

Azimuth Angle (degrees)
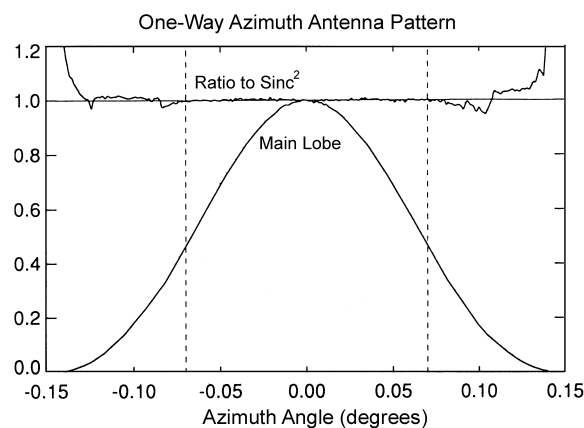
Zink & Bamler, X-SAR Radiometric Calibration and Data Quality, IEEE TGRS, July 1995

Figure 8-11. SIR-C X-SAR azimuthal antenna pattern on a linear scale, and compared to Sinc2. Note that the portion of the data processed come from the region between the dashed lines $\left(\pm 0.07^{\circ}\right)$, for which the model is very accurate.

For comparison, the range (or elevation) antenna pattern, synthesized from a number of observations like those shown in Figure 8-10, is given in Figure 8-12. Note that the width is considerably greater, given the relatively narrow dimension of the antenna in the corresponding direction (0.75 m)

X-SAR Elevation Antenna Pattern
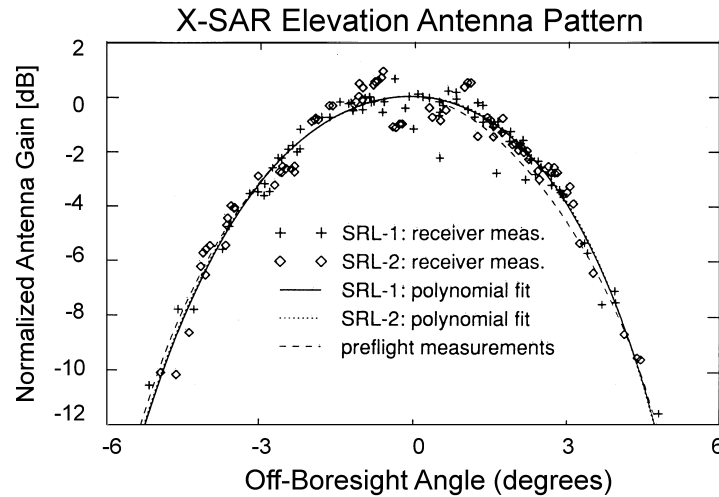
Figure 8-12. SIR-C X-SAR range antenna pattern. This beam pattern needs to cover the entire cross-track range of the system - here 20-70 km as illuminated from 222 km altitude.

C Synthetic Aperture Radar

The principal disadvantage of real-aperture radar is that its along-track or azimuth resolution is limited by antenna length. Synthetic-aperture radar (SAR) was developed to overcome this disadvantage. SAR produces a very long antenna synthetically or artificially by using the forward motion of the platform to carry a relatively short real antenna to successive positions along the flight line. The longer antenna is simulated by using the coherence of radar signals. If the sensor is moving at velocity v, and has an antenna length L, then the main beam footprint on the surface has a characteristic length $\ell = \dfrac{2\lambda h}{L}$. Data are accumulated for as long as a given point on the ground is in view (see figure 8-13)

Figure 8-13

Magically, the synthesized collection of measurements will have a beam width equal to

$$\theta_s \; = \; \frac{\lambda}{\ell} = \frac{L}{2h} \qquad\qquad \text{(Eqn. 8.15)}$$

and the resulting array footprint on the ground has the size:

$$R_a \; = \; h\theta_s \; = \; \frac{L}{2} \qquad\qquad \text{(Eqn. 8.16)}$$

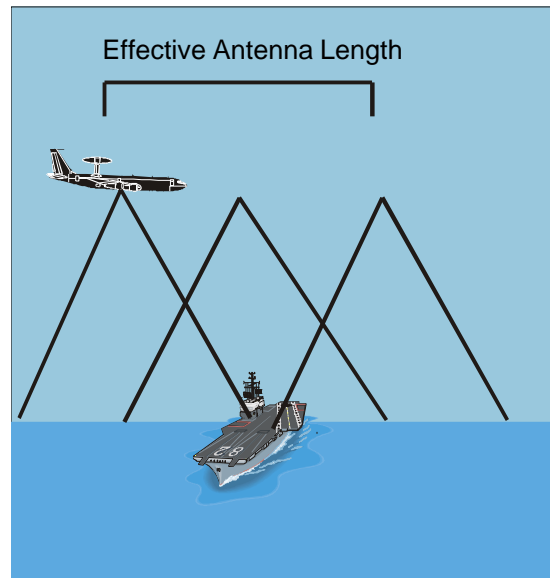This very counter-intuitive result is due to the fact that for a smaller antenna (small L), the target is in the beam for a longer time. The time period that an object is illuminated increases with increasing range, so azimuthal resolution is range independent
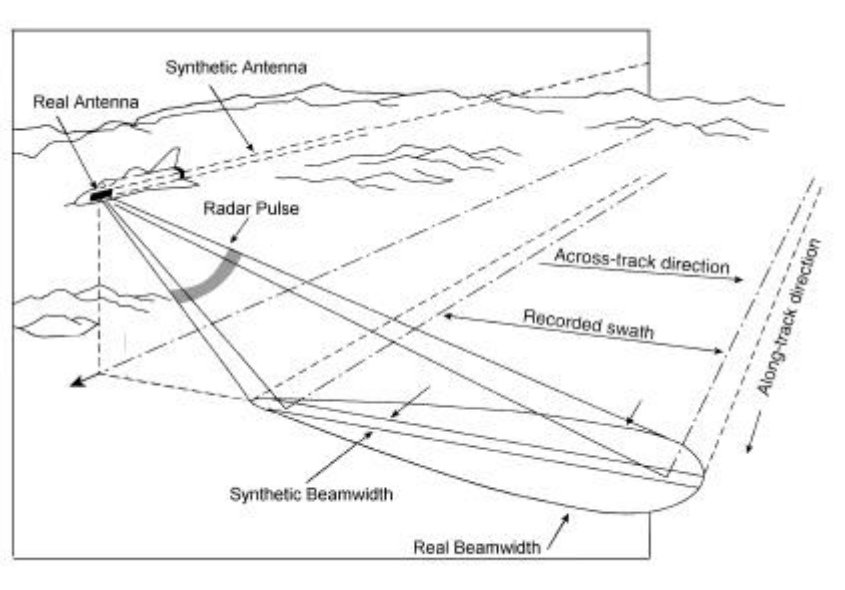
Figure 8-14 The synthetic antenna's length is directly proportional to range – as across-track distance increases, antenna length increases. This produces a synthetic beam with a constant width, regardless of range

The azimuth details are determined by establishing the position-dependent frequency changes or shifts in the echoes that are caused by the relative motion between terrain objects and the platform. To do this, a SAR system must unravel the complex echo history for a ground feature from each of a multitude of antenna positions. For example, if we isolate a single ground feature, the following frequency modulations occur as a consequence of the forward motion of the platform:

(1) The feature enters the beam ahead of the platform and its echoes are shifted to higher frequencies **(positive Doppler);**

(2) when the platform is perpendicular to the features position, there is no shift in frequency **(zero Doppler);** and

(3) as the platform moves away from the feature, the echoes have lower frequencies **(negative Doppler)** than the transmitted signal.

The Doppler shift information is then obtained by electronically comparing the reflected signals from a given feature with a reference signal that incorporates the same frequency of the transmitted pulse. The output is known as a **phase history,** and it contains a record of the Doppler frequency changes plus the amplitude of the returns from each ground feature as it passed through the beam of the moving antenna.

D Radar Cross Section (*s*)

The radar cross section, σ, is generally defined as the ratio of the backscattered energy to the energy that the sensor would have received if the target surface has scattered the energy incident on it in an isotropic fashion. The backscatter cross section is usually expressed in dB (decibels), which is given by: σ = 10 log (energy ratio) (Elachi, page 163). A rough idea of the magnitude of σ is given by Figure 8.15 (Elachi, page 175), which shows the scattering coefficients inferred from Skylab data at 13.9 GHz, at 33° incidence - something like 30% of the energy is returned (-10 dB±3dB), it would seem, though there are some subtleties to the reference point to be used.
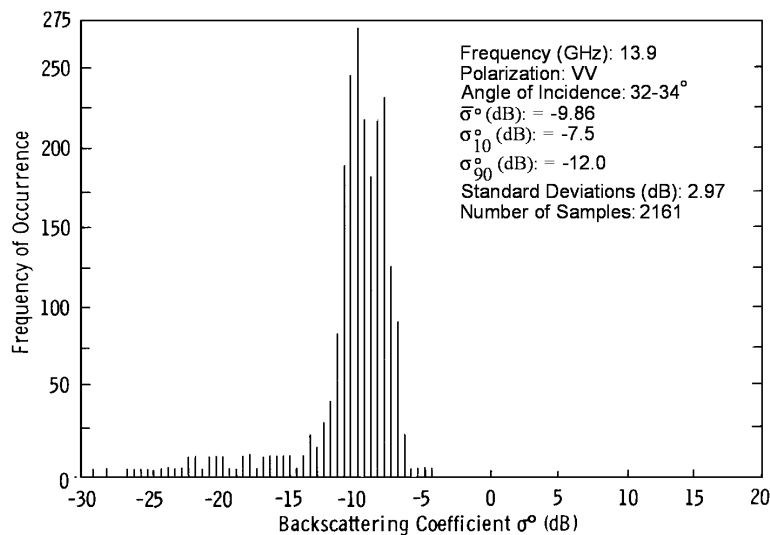
Figure 8-15

σ depends on any number of surface characteristics, with a strong dependence on the incident angle, and scattering angle. At scattering angles larger than about 30°, the surface scattering is dominated by the effect of small scale roughness (here, small scale means small compared to the wavelength). The "point scatterer" model is invoked here, and the small scatterers are assumed to make up a Lambertian distribution (an optics term)

$$\sigma(\theta) \propto \cos^2\theta \qquad\qquad \text{(Eqn. 8.17)}$$

This gives some idea of the type of functional dependence on angle one might obtain. The details are much messier. Observationally, the dependence is well illustrated by the Skylab results shown in Figure 8.16 (Elachi, page 176). The center line is the average, the two boundary lines show the 10 and 90 percentile bounds. Note the 10-15 dB variation in return with angle.
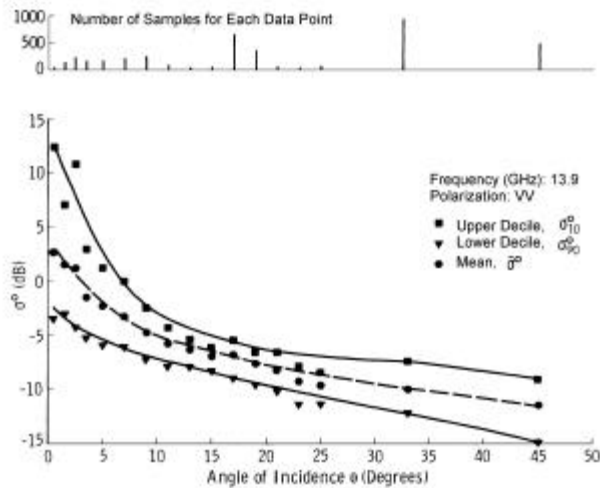
Figure 8-16

The point of this portion of the discussion is that the radar return has a strong dependence on the angle of incidence on the target surface. This differs fairly substantially from the optical case, where there are modest effects due to the illumination angle, aside from shadows. Note also that a sun-synchronous satellite (e.g. LANDSAT) always observes under roughly the same illumination conditions, whereas a radar satellite will not (theta varies).

Not included here is the form of the strong return which is observed if the wavelength of the incident radiation matches the characteristic scale length of features in the target. Strong returns are seen under this condition, termed Bragg scattering.

1 Dielectric Coefficient - soil moisture

The amplitude of the radar return depends strongly on the dielectric coefficient of the surface material (think index of refraction in normal optics, $n \sim \sqrt{\boldsymbol{e}_r}$, the index of refraction varies as the square root of the relative dielectric constant). Radar returns vary substantially as the surface materials go from insulator to conductor - which in the dielectric coefficient shows up as the imaginary component, $\boldsymbol{e}''$. In the illustration here, we see that soil moisture drives the imaginary term up, causing increased absorption of the radar energy. Note the wavelength dependence of this variation - higher frequencies (lower wavelengths) are affected more. This means lower frequencies are better for penetration of the ground and foliage.
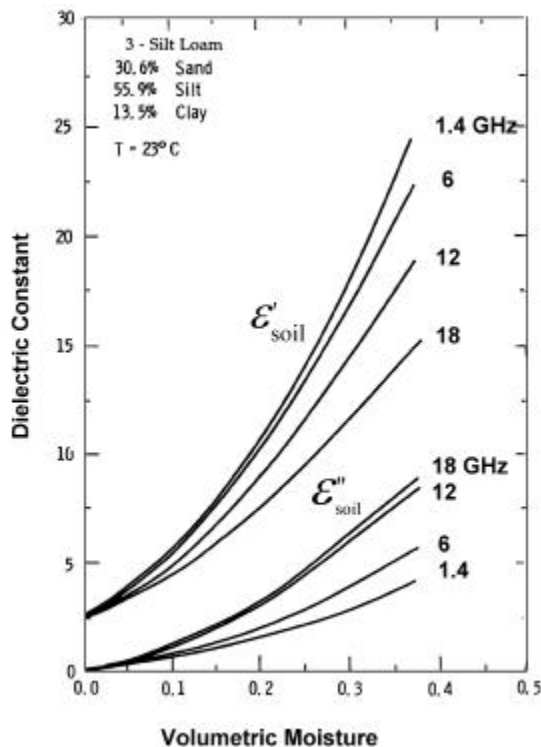
Figure 8-17. (left) The real $(\boldsymbol{e}')$ and imaginary $(\boldsymbol{e}'')$ components of the dielectric coefficient for a silty loam mixture, as a function of water content. Both refraction and absorption increase with moisture content.

Figure 8-18 (below) The concept of rough and smooth needs to take into account the wavelength of the radiation

A
Surface of pebbles,
specular reflection

B
Surface of cobbles,
diffuse reflection
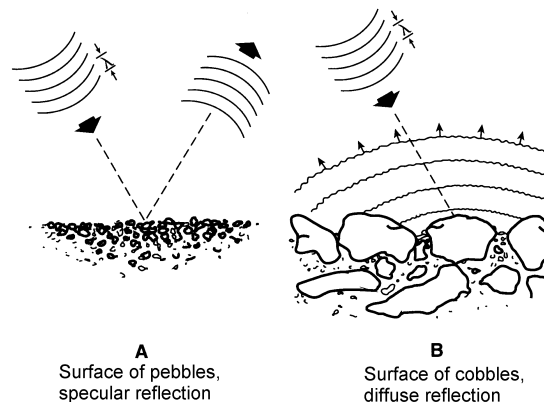
2 Roughness

The effect of surface roughness is illustrated by Figure 8-18. (Elachi, page 174, Sabins pages 197-201). The figure is somewhat schematic, but it emphasizes the variation in radar return with angle, and surface roughness. Note that this roughness is relative to the wavelength, so smooth means surfaces like concrete walls, (e.g. cultural objects), rough tends to mean things like vegetation.

3 Tetrahedrons / Corner Reflectors

Hard targets, meaning most man-made artifacts, generally have sharp corners and flat surfaces. These produce extremely bright returns, often saturating the images produced from SAR systems. The SIR-C flight over Death Valley included calibration sequences with retro-reflectors, which have as a characteristic that they return all incident radiation back in the direction of incidence - that is, they are nearly perfect reflectors. Figure 8-19 shows some SIR-C observations rendered in line graphics. In the SAR images, these correspond to a small white dot against the relatively flat background.

SIR-C Corner Reflector Signature
(Point Target Response)

Range Cut

Azimuth Cut

Figure 8-19. SAR impulse response

E Polarization

The above discussion ignores the important topic of polarization. Radar transmissions are polarized, with components normally termed vertical (V) and horizontal (H). Vertical means t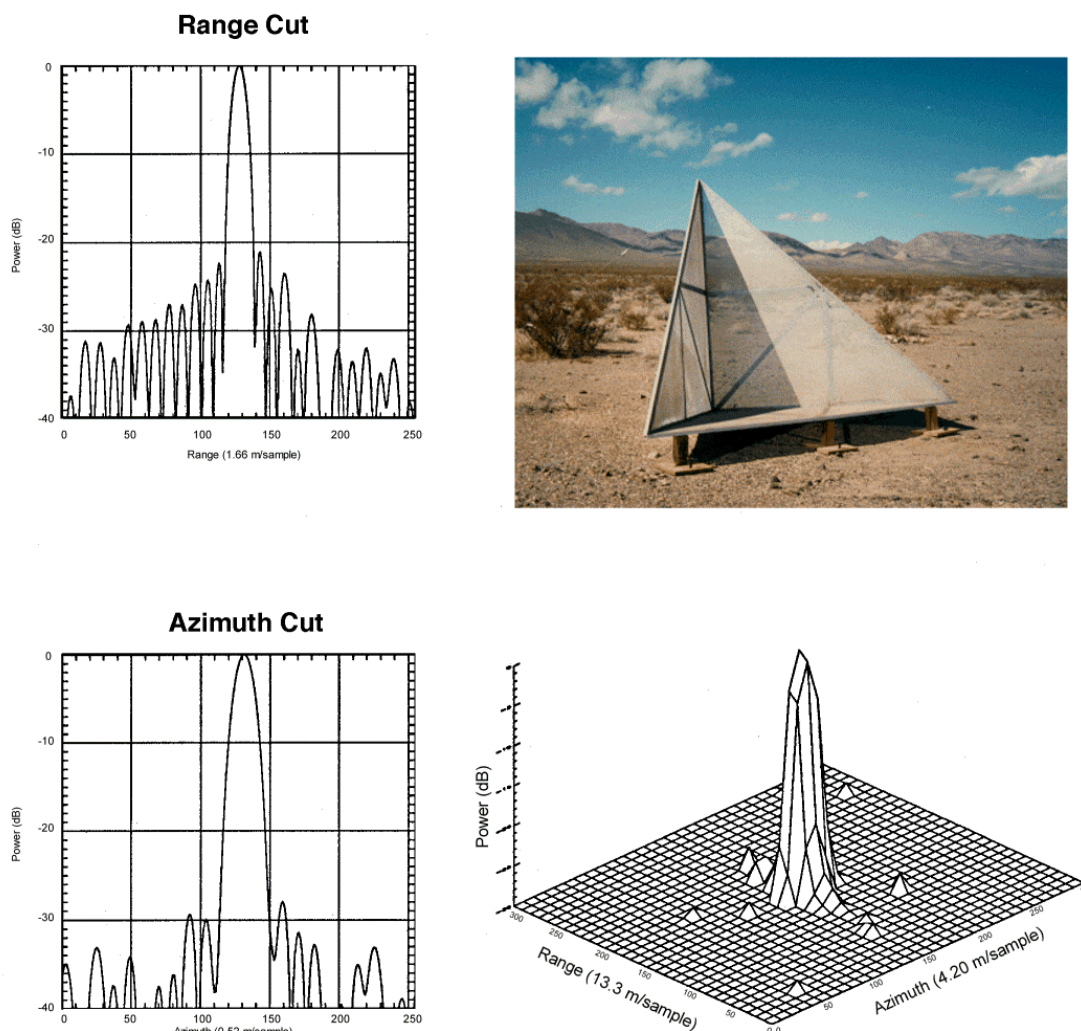hat electric vector is in the plane of incident, horizontal corresponds to the state where the electric vector is perpendicular to the plane of incidence. (Elachi, page 25). The receive antenna, in turn, can be selected for either V or H returns. This leads to a possible matrix of return values:

$$\boldsymbol{s} = \begin{pmatrix} \boldsymbol{S}_{HH} & \boldsymbol{S}_{HV} \\ \boldsymbol{S}_{VH} & \boldsymbol{S}_{VV} \end{pmatrix}$$

Where the first subscript is determined by the transmit state, the second by the receive state. These four complex (amplitude **and** phase) components of the scattering matrix give a wealth of information, much more than can be obtained from an optical system. Generally speaking, scatterers which are aligned along the direction of polarization give higher returns, rough surfaces produce the cross-terms. Water gives almost zero scattering in the cross terms. Several illustrations have been given above which show the difference in returns associate with the different polarizations.

F Wavelength

Notes on microwave wavelengths in RADARSAT/PCI notes, page 11, 43.
 1) Radar penetrates clouds, smoke rain, haze. There is some wavelength dependence for rain penetration - at 15 cm and longer (2GHz and below), rain is not a problem. At 5 GHz (6 cm), significant rain shadows are seen. At 36 GHz (0.8 cm) moderate rainfall rates can cause significant attenuation.
2) Response to macroscopic structure, bulk electrical properties: X, C band primarily interacts with surface, L&P penetrate canopy, soil.

Band Designation[*]	Wavelength (cm)	Frequency (GHz)
Ka (0.86 cm)	0.8 - 1.1	40.0 - 26.5
K	1.1 - 1.7	26.5 - 18.0
Ku	1.7 - 2.4	18.0 - 12.5
X (3.0, 3.2 cm)	2.4 - 3.8	12.5 - 8.0
C	3.8 - 7.5	8.0 - 4.0
S	7.5 - 15.0	4.0 - 2.0
L (23.5, 25 cm)	15.0 - 30.0	2.0 - 1.0
P	30.0 - 100.0	1.0 - 0.3

[*]Wavelengths commonly used in imaging radars are indicated in parenthesis.

G Vehicles

1 Shuttle Imaging Radar (SIR)

The shuttle imaging radar has flown in several versions (A, B, C), and twice as SIR-C on Endeavour - the first as SRL-1: STS-59, April 9 - 20, 1994, the second as SRL-2: STS-68, September 30 - October 11, 1994. Both missions were conducted with highly inclined orbits (57° inclination) in order to maximize the earth regions covered. The orbit was 222-km altitude, circular. The mission included X, C, and L band radar, and was capable of various modes including full polarimeteric (VV, VH, HV, and HH polarization).

Spatial resolution varied between the sensors, and with operating mode, but was generally from 10-25 meters, with a spatial extent of 30-50 km. The combined SIR-C/X-SAR payload had a mass (instruments, antennas, and electronics) of 10,500 kg filling nearly the entire cargo bay of the Shuttle.
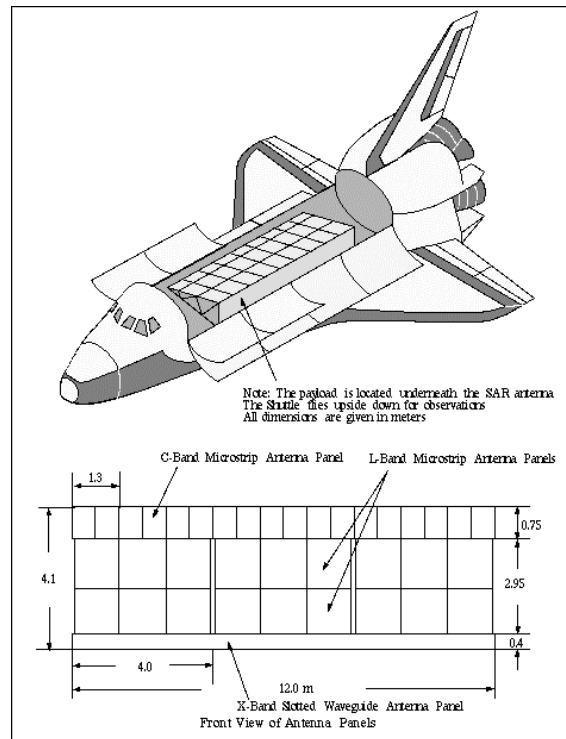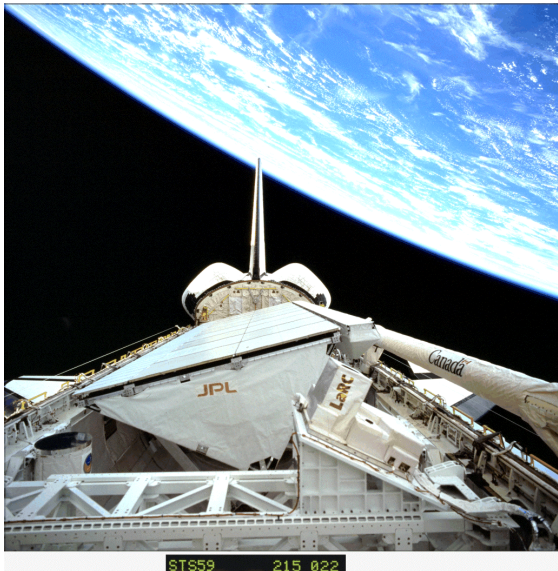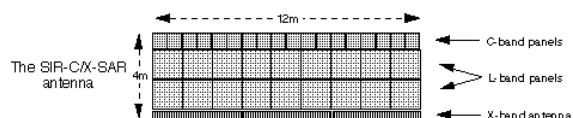
Figure 8-20.

Figure 8-21.

Figure 8-22.

Enormous data rates are implicit in these missions. Launched April 9, 1994, the STS-59 mission for SIR-C/X-SAR collected a total of 65 hours of data during the 10 day mission, roughly corresponding to 66 million square kilometers (26 million square miles).   All data were stored onboard the shuttle using high-density, digital, rotary-head tape recorders.   The data filled 166 digital tape cartridges (similar to VCR tape cassettes).

 The mission returned 47 terabits of data (47×10^{12} bits). When all the radars are operating they produce 225 million bits of data per second, or the equivalent of 45 simultaneously operating television stations. The raw data was processed into images using JPL's digital SAR processor and by processors developed by Germany and Italy for the X-SAR data.

The L-Band and C-Band SARs allow multifrequency and multipolarization measurements. Parallel image generation in L-Band and C-Band with HH, VV, HV, or VH polarization. Look angle = variable from 20 - 55°. Data rate = 90 Mbit/s for L-Band and 90 Mbit/s for C-Band (a total of 4 streams of V and H data, each data stream has a data rate of 45 Mbit/s).

X-SAR (SAR for X-Band measurement provided by DARA/DLR and ASI) X-SAR uses only vertical polarization (VV). Look angle (off nadir) = 15 - 55°. Data rate = 45 Mbit/s. The X-SAR antenna transmits and receives vertically polarized signals; it can be tilted to achieve a range of look angles from 15° - 55°. The ground area illuminated by the antenna is an ellipse of about 60 km x 0.8 km (altitude of 222 km). The X-SAR electronics are mounted underneath the antenna on a cold plate structure. A TWT (Travelling Wave Tube) amplifier is transmitting up to 1736 pulses/s at peak transmit power of 3.35 kW. The pulses are frequency modulated (chirp) with a pulse length of 40 μs and a programmable bandwidth of 9.5 or 19 MHz. The signal echoes are amplified in a coherent receiver, digitized (4 or 6 bit) and recorded together with auxiliary data.

Parameter	L-Band	C-Band	X-Band
Wavelength (cm)	23.5	5.8	3.1
Frequency	1.250 GHz	5.3 GHz	9.6 GHz
Aperture length	12.0 m	12.0 m	12.0 m
Aperture width	2.95 m	0.75 m	0.4 m
Architecture	Active Phased Array		Slotted waveguide
Polarization	H and V	H and V	V
Polarization isolation	25 dB	25 dB	39 dB
Antenna gain	36.4 dB	42.7 dB	44.5 dB
Mechanical steering range	N/A	N/A	±23°
Electronic steering range	±20°	±20°	N/A
Elevation beamwidth	5-16°	5-16°	5.5°
Azimuth beamwidth	1.0°	0.25°	0.14°
Peak radiated power	4400 W	1200 W	3350 W
System noise temperature	450 K	550 K	551 K
Mass of structure	3300 kg		49 kg

2 RADARSAT

Radarsat data were briefly illustrated in Chapter 1, in figure 1-19. Radarsat carries a C-band synthetic aperture radar, and operates in HH polarization only. Launched on November 4, 1995, it has a five-year design life. There are 7 beam modes offering a wide range of resolutions (8 - 100 meters) and swath widths (50 - 500 km). Incidence angles vary from 20-59°.   http://www.rsi.ca/classroom/cl_rsat.htm

The satellite is in a circular, sun-synchronous orbit (dawn-dusk), at 798-km altitude, 98.6° inclination, and with a 100.7-minute period. The circular orbit is maintained as accurately as possible to maintain repeatability in the imaging. This allows for the application of techniques in change detection, and interferometry.

The radar has a power transmission / duty cycle of 5 kW (peak); 300s W (average)/ up to 28%. The antenna is a 15 m x 1.5 m phased array. The pulse is 1270Hz - 1390Hz; PRF = 42 µs.

RADARSAT is a right-looking sensor, facing east during the ascending orbit and west during the descending orbit. The look direction can have a significant influence on the appearance of radar imagery especially when features have an organized linear structure (e.g., agricultural surfaces or geological structures).

3 European Radar Satellites, ERS-1, -2

The European Radar Satellites, ERS-1 and ERS-2, are also polar orbiting SAR systems. ERS-1 was placed in a near-polar orbit at a mean altitude of about 780-km, inclination of 98.52°, period of about 100 minutes. The instrument payload included active and passive microwave sensors and a thermal infrared radiometer. The satellite (see the figure) is large, weighing 2400 kg and measuring 12 m x 12 m x 2.5 m. ERS-1 ceased operation on 10 March 2000

Like Radarsat, the radar is C-band (5.3 GHz), but it operates in VV polarization. Incidence angle is 20-26°. It is somewhat more powerful than Radarsat, also; the peak power supplied to the payload is 2600 W, payload average power is at most 550 W - but the payload requires almost double that power when active. ERS-1 was launched on 17 July 1991 by an Ariane 4 from Kourou, French Guiana. The satellite masses are quite large: 2157.4 kg for ERS-1, 2516 kg for ERS-2. Over 320 kg of the mass goes to the SAR system.

Figure 8-23
ESA's ERS-1 satellite was photographed by the Spot-4 Earth observation satellite of the French space agency, CNES, at 09:56 UT on 6 May 1998. From its 820 km orbit, Spot-4 recorded ERS-1 passing by 41 km below at a relative speed of 250 km/h, over the Tenere Desert of Niger, Africa. Resolution of the ERS-1 spacecraft is 0.5 meters. The image was taken by one of the HRVIR (high-resolution visible-infrared) cameras during Spot's testing phase.
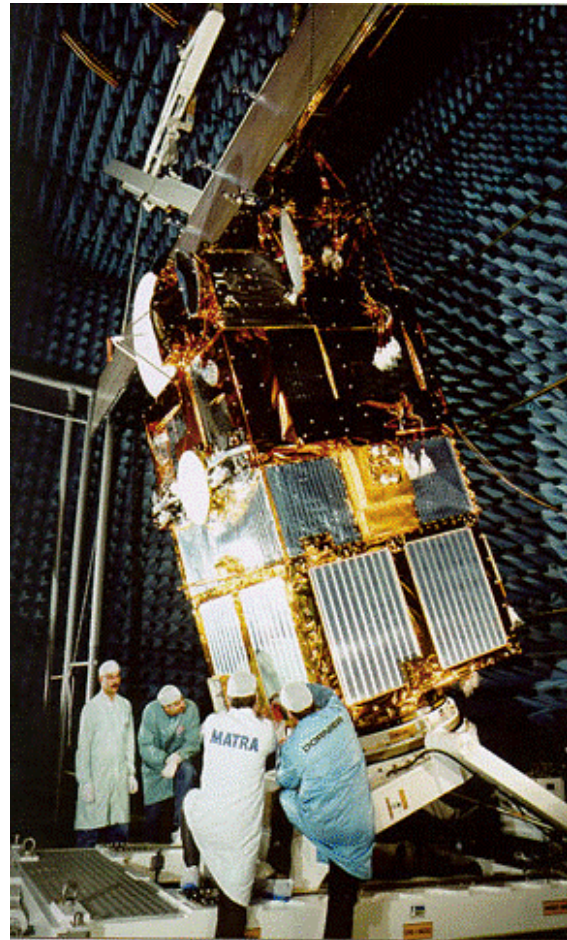

Figure 8-24 ERS-2

The satellite is 11.8 m in total height. The solar array consists of two 5.8 m x 2.4 m wings, manufactured from flexible reinforced Kapton, on which are mounted a total of 22,260 solar cells. The two solar array wings are deployed by means of a pantograph mechanism, and the whole array rotates through 360 degrees with respect to the satellite during each orbit in order to maintain its Sun pointing.

ERS-1 was launched on 17 July 1991 into a sun-synchronous, near polar, near circular orbit at a mean altitude of 785 km and an inclination of 98.5 degrees.   The vehicle was 3-axis stabilized, with orbit knowledge: 5 m (radial), 15 m (cross) 60 m (along). Substantial data-rates are again implicit. The data down link is x-band (105 Mbit/s high rate link for AMI image mode) X-band (15 Mbit/s low rate link for real-time and playback of LBR data) on-board recorders provide 6.5 Gbits storage S-band telemetry links for housekeeping data.

ERS-2 was built by a consortium led by Deutsche Aerospace and was launched on April 20, 1995 on an Ariane.   The ERS-2 satellite is essentially the same as ERS-1 except that it includes a number of enhancements and it is carrying a new instrument to measure the chemical composition of the atmosphere, named the Global Ozone Monitoring Experiment (GOME).

a Multi-temporal images - Rome

This multi-temporal image of Rome and the Castelli Romani hills to its southeast shows, by its colors, a variety of changes, both in the agricultural fields of the lowlands, and in the grasslands and forests of the hillier areas. The city, however, has not changed in the short interval between the capture of the first and the last of the images and thus appears more uniformly gray, as equal values of the RGB colors from which the image is made give a range of grayscales rather than of colors.
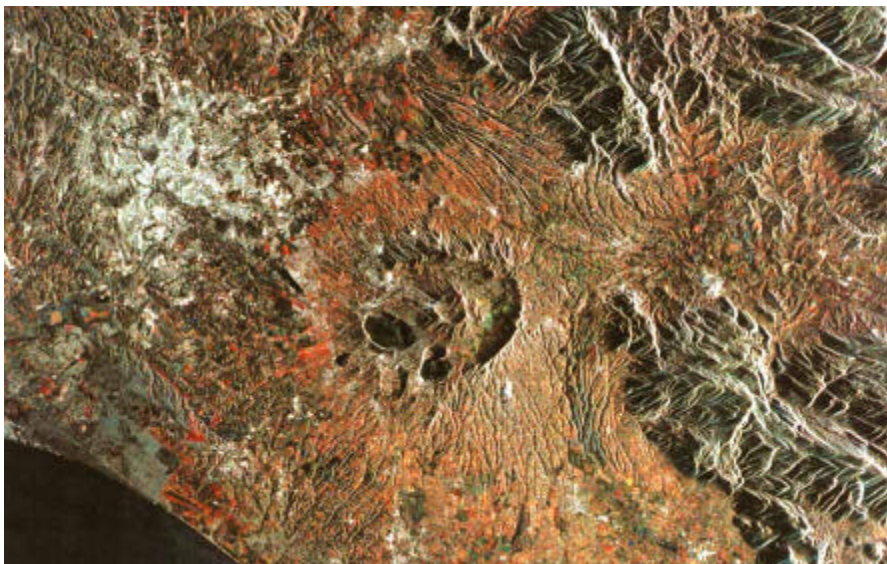
Figure 8-25. Incidence Angle: 23 degrees; Spatial Resolution: 30 meters; Swath Width: 100 kilometers. Copyright © ESA, 1995   Original data distributed by Eurimage
http://www.eurimage.it/Products/ERS/Msample_images.shtml

b SPAIN - MOROCCO - Strait of Gibraltar

This spectacular image of the Strait of Gibraltar shows internal waves (wavelength about 2 km) which seem to move from the Atlantic Ocean to the Mediterranean Sea, at the east of Gibraltar and Ceuta. Internal waves are usually created by the presence of two different layers of water combined with a certain configuration of relief and current. In the case of the Strait of Gibraltar, the two layers correspond to different salinities, whereas the current is caused by the tide passing through the Strait. As this current meets the ascending ocean bottom in the Strait, the internal waves are generated reaching the surface some kilometers behind the Strait. They are not directly visible to the observer but produce a perturbation at the surface that appears as strips of rough and calm water. ERS-1 therefore gives scientists the opportunity to observe and map such phenomena.

The image has been artificially colored - land encoded as shades of brown, water as shades of blue; the data were acquired at the Fucino ground station on 7-1-1992;

Figure 8-26. Straits of Gibraltar, Area covered 90 km x 100 km; C-VV; Resolution: 30 m.

H Problems

1. For a SAR system, such as SIR-C, does the nominal 12.5 meter azimuthal resolution for the German X-band system correspond well to the nominal antenna width? What pulse length would be required to match that in range resolution?

2. What wavelengths and polarizations are used for the commercial SAR systems (Radarsat, ERS)?

3. For a spotlight mode SAR system, what azimuthal resolution could be obtained with x-band for a 10 second integration interval (assume v = 7 km/s)

4. For the conditions illustrated in Figure 8-12, the shuttle was at 222 km altitude, and the antenna (shuttle) attitude was 27.1°. What range does the $27.1^{\circ} \pm 3^{\circ}$ (measured from nadir) correspond to?

5. During an earlier shuttle flight (SIR-B), observations similar to those shown in Figures 8-10 to 8-12 were made. Given a vehicle velocity of 7.5 km/s, convert the variations in time displayed here into a beam width in degrees. The wavelength is 23.5 cm. The local angle of incidence is 31°. (The incidence angle is measured down from the vertical.) What is the antenna length implied by this antenna pattern?

SIR-B Azimuth Pattern
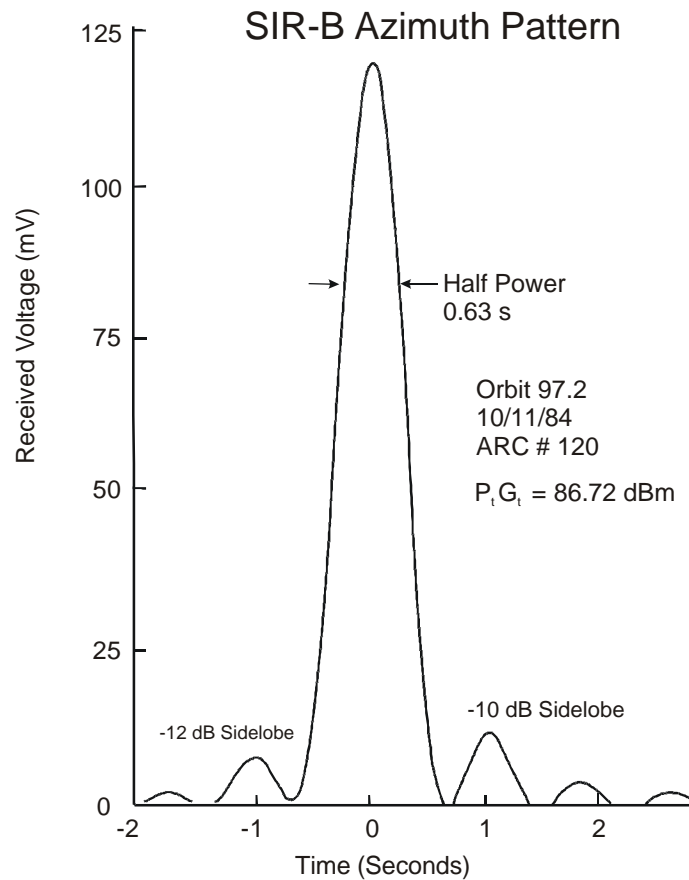
Dobson et al: External Calibration of SIR-B Imagery, IEEE TGRS, July 1986

Figure 8-27. SIR-B azimuth (along track) antenna pattern.

6. The decrease in radar energy as the beam propagates is illustrated by an example
    from the SIR-B mission, which shows the results of measuring the variation in power
    observed at depths of 12 and 35 cm in desert soil (near Mina, NV), from a paper by
    Farr et al. 1986. If the radar energy has decreased by 8 dB in the first 12 cm, what is
    the characteristic scale length, d, as defined here? This scale length is determined by
    the imaginary part of the dielectric coefficient.

$$I = I_o \ e^{-x/d}$$

Chapter 9 NON-TRADITIONAL FORMS

A LIDAR

Use the Kaman data, or get forest scene (and lake?) from David Evans at MSU.

B Milli-meter

C Other non-traditional forms

This page intentionally left blank

Appendix 1 NATIONAL IMAGE INTERPRETABILITY RATING SCALES

The aerial imaging community utilizes the National Imagery Interpretability Rating Scale (NIIRS) to define and measure the quality of images and performance of imaging systems. Through a process referred to as "rating" an image, the NIIRS is used by imagery analysts to assign a number that indicates the interpretability of a given image. The NIIRS concept provides a means to directly relate the quality of an image to the interpretation tasks for which it may be used. Although the NIIRS has been primarily applied in the evaluation of aerial imagery, it provides a systematic approach to measuring the quality of photographic or digital imagery, the performance of image capture devices, and the effects of image processing algorithms.
http://www.fas.org/irp/imint/niirs.htm

---

references:

Civil NIIRS Reference Guide, http://www.fas.org/irp/imint/niirs_c/index.html,

From the Imagery Resolution Assessments and Reporting Standards (IRARS) Committee.

Imagery Interpretability Rating Scales,

L. A. Maver, C. D. Erdman, K. Riehl, Itek Optical Systems, Lexington, MA, Society for Information Display, 1995, Applied Vision/Human Factors session,

 http://www.sid.org/sid95pdf/10-2x.pdf

 This paper describes the NIIRS and provides information on how the scale is developed and used to facilitate its application to other imaging scenarios.

1 NIIRS 0

Visible NIIRS	Radar NIIRS	Infrared NIIRS	Multispectral NIIRS
March 1994	August 1992	April 1996	February 1995
Interpretability of the imagery is precluded by obscuration, degradation, or very poor resolution	Interpretability of the imagery is precluded by obscuration, degradation, or very poor resolution	Interpretability of the imagery is precluded by obscuration, degradation, or very poor resolution	Interpretability of the imagery is precluded by obscuration, degradation, or very poor resolution

2 NIIRS 1 [over 9.0 m GRD]

Visible NIIRS	Radar NIIRS	Infrared NIIRS	Multispectral NIIRS
Detect a medium-sized port facility and/or distinguish between taxiways and runways at a large airfield.	Detect the presence of aircraft dispersal parking areas. Detect a large cleared swath in a densely wooded area. Detect, based on presence of piers and warehouses, a port facility. Detect lines of transportation (either road or rail), but do not distinguish between	Distinguish between runways and taxiways on the basis of size, configuration or pattern at a large airfield. Detect a large (e.g., greater than I square kilometer) cleared area in dense forest. Detect large ocean-going vessels (e.g., aircraft carrier, super-tanker, KIROV) in open water. Detect large areas (e.g., greater than I square kilometer) of marsh/swamp.	Distinguish between urban and rural areas. Identify a large wetland (greater than 100 acres). Detect meander flood plains (characterized by features such as channel scars, oxbow lakes, meander scrolls). Delineate coastal shoreline. Detect major highway and rail bridges over water (e.g., Golden Gate, Chesapeake Bay). Delineate extent of snow or ice cover.

3 NIIRS 2 [4.5 - 9.0 m GRD]

Visible NIIRS	Radar NIIRS	Infrared NIIRS	Multispectral NIIRS
Detect large hangars at airfields. Detect large static radars (e.g., AN/FPS-85, COBRA DANE, PECHORA, HENHOUSE). Detect military training areas. Identify an SA-5 site based on road pattern and overall site configuration. Detect large buildings at a naval facility (e.g., warehouses, construction hall). Detect large buildings (e.g., hospitals, factories).	Detect the presence of large (e.g., BLACKJACK, CAMBER, COCK, 707, 747) bombers or transports. Identify large phased array radars (e.g., HEN HOUSE, DOG HOUSE) by type. Detect a military installation by building pattern and site configuration. Detect road pattern, fence, and hardstand configuration at SSM launch sites (missile silos, launch control silos) within a known ICBM complex. Detect large non-combatant ships (e.g., freighters or tankers) at a known port facility. Identify athletic stadiums.	Detect large aircraft (e.g., C-141, 707, BEAR, CANDID, CLASSIC). Detect individual large buildings (e.g., hospitals, factories) in an urban area. Distinguish between densely wooded, sparsely wooded and open fields. Identify an SS-25 base by the pattern of buildings and roads. Distinguish between naval and commercial port facilities based on type and configuration of large functional areas.	Detect multilane highways. Detect strip mining. Determine water current direction as indicated by color differences (e.g., tributary entering larger water feature, chlorophyll or sediment patterns). Detect timber clear-cutting. Delineate extent of cultivated land. Identify riverine flood plains.

4 NIIRS 3 [2.5 - 4.5 m GRD]

Visible NIIRS	Radar NIIRS	Infrared NIIRS	Multispectral NIIRS
Identify the wing configuration (e.g., straight, swept, delta) of all large aircraft (e.g., 707, CONCORD, BEAR, BLACKJACK). Identify radar and guidance areas at a SAM site by the configuration, mounds, and presence of concrete aprons. Detect a helipad by the configuration and markings. Detect the presence / absence of support vehicles at a mobile missile base. Identify a large surface ship in port by type (e.g., cruiser, auxiliary ship, noncombatant/merchant). Detect trains or strings of standard rolling stock on railroad tracks (not individual cars)	Detect medium-sized aircraft (e.g., FENCER, FLANKER, CURL, COKE, F-15). Identify an ORBITA site on the basis of a 12 meter dish antenna normally mounted on a circular building. Detect vehicle revetments at a ground forces facility. Detect vehicles/pieces of equipment at a SAM, SSM, or ABM fixed missile site. Determine the location of the superstructure (e.g., fore, amidships, aft) on a medium-sized freighter. Identify a medium-sized (approx. six track) railroad classification yard.	Distinguish between large (e.g., C-141, 707, BEAR, A300 AIRBUS) and small aircraft (e.g., A-4, FISHBED, L-39). Identify individual thermally active flues running between the boiler hall and smoke stacks at a thermal power plant. Detect a large air warning radar site based on the presence of mounds, revetments and security fencing. Detect a driver training track at a ground forces garrison. Identify individual functional areas (e.g., launch sites, electronics area, support area, missile handling area) of an SA-5 launch complex. Distinguish between large (e.g, greater than 200 meter) freighters and tankers.	Detect vegetation/soil moisture differences along a linear feature (suggesting the presence of a fenceline). Identify major street patterns in urban areas. Identify golf courses. Identify shoreline indications of predominant water currents. Distinguish among residential, commercial, and industrial areas within an urban area. Detect reservoir depletion.

5 NIIRS 4 [1.2 - 2.5 m GRD]

Visible NIIRS	Radar NIIRS	Infrared NIIRS	Multispectral NIIRS
Identify all large fighters by type (e.g., FENCER, FOXBAT, F-15, F-14). Detect the presence of large individual radar antennas (e.g., TALL KING). Identify, by general type, tracked vehicles, field artillery, large river crossing equipment, wheeled vehicles when in groups. Detect an open missile silo door. Determine the shape of the bow (pointed or blunt/rounded) on a medium-sized submarine (e.g., ROMEO, HAN, Type 209, CHARLIE 11, ECHO 11, VICTOR II/III). Identify individual tracks, rail pairs, control towers,	Distinguish between large rotary-wing and medium fixed-wing aircraft (e.g., HALO helicopter versus CRUSTY transport). Detect recent cable scars between facilities or command posts. Detect individual vehicles in a row at a known motor pool. Distinguish between open and closed sliding roof areas on a single bay garage at a mobile missile base. Identify square bow shape of ROPUCHA class (LST). Detect all rail/road bridges.	Identify the wing configuration of small fighter aircraft (e.g., FROGFOOT, F- 16, FISHBED). Detect a small (e.g., 50 meter square) electrical transformer yard in an urban area. Detect large (e.g., greater than 10 meter diameter) environmental domes at an electronics facility. Detect individual thermally active vehicles in garrison. Detect thermally active SS-25 MSV's in garrison. Identify individual closed cargo hold hatches on large merchant ships.	Detect recently constructed weapon positions (e.g. tank, artillery, self-propelled gun) based on the presence of revetments, berms, and ground scarring in vegetated areas. Distinguish between two-lane improved and unimproved roads. Detect indications of natural surface airstrip maintenance or improvements (e.g., runway extension, grading, resurfacing, bush removal, vegetation cutting). Detect landslide or rockslide large enough to obstruct a single-lane road. Detect small boats(15-20 feet in length) in open water

6 NIIRS 5 [0.75 - 1.2 m GRD]

Visible NIIRS	Radar NIIRS	Infrared NIIRS	Multispectral NIIRS
Distinguish between a MIDAS and a CANDID by the presence of refueling equipment (e.g., pedestal and wing pod). Identify radar as vehicle-mounted or trailer-mounted. Identify, by type, deployed tactical SSM systems (e.g., FROG, SS-21, SCUD). Distinguish between SS-25 mobile missile TEL and Missile Support Vans (MSVS) in a known support base, when not covered by camouflage. Identify TOP STEER or TOP SAIL air surveillance radar on KIROV-, SOVREMENNY-, KIEV-, SLAVA-, MOSKVA-, KARA-, or KRESTA-II-class vessels.	Count all medium helicopters (e.g., HIND, HIP, HAZE, HOUND, PUMA, WASP). Detect deployed TWIN EAR antenna. Distinguish between river crossing equipment and medium/heavy armored vehicles by size and shape (e.g., MTU-20 vs. T-62 MBT). Detect missile support equipment at an SS-25 RTP (e.g., TEL, MSV). Distinguish bow shape and length/width differences of SSNS. Detect the break between railcars (count railcars).	Distinguish between single-tail (e.g., FLOGGER, F-16, TORNADO) and twin-tailed (e.g., F-15, FLANKER, FOXBAT) fighters. Identify outdoor tennis courts. Identify the metal lattice structure of large (e.g. approximately 75 meter) radio relay towers. Detect armored vehicles in a revetment. Detect a deployed TET (transportable electronics tower) at an SA-10 site. Identify the stack shape (e.g., square, round, oval) on large (e.g., greater than 200 meter) merchant ships.	Detect automobile in a parking lot. Identify beach terrain suitable for amphibious landing operation. Detect ditch irrigation of beet fields. Detect disruptive or deceptive use of paints or coatings on buildings/structures at a ground forces installation. Detect raw construction materials in ground forces deployment areas (e.g., timber, sand, gravel).

7 NIIRS 6 [0.40 - 0.75 m GRD]

Visible NIIRS	Radar NIIRS	Infrared NIIRS	Multispectral NIIRS
Distinguish between models of small/medium helicopters (e.g., HELIX A from HELIX B from HELIX C, HIND D from HIND E, HAZE A from HAZE B from HAZE C). Identify the shape of antennas on EW/GCI/ACQ radars as parabolic, parabolic with clipped comers or rectangular. Identify the spare tire on a medium-sized truck. Distinguish between SA-6, SA- I 1, and SA- 17 missile airframes. Identify individual launcher covers (8) of vertically launched SA-N-6 on SLAVA-class vessels. Identify automobiles as	Distinguish between variable and fixed-wing fighter aircraft (e.g., FENCER vs. FLANKER). Distinguish between the BAR LOCK and SIDE NET antennas at a BAR LOCK/SIDE NET acquisition radar site. Distinguish between small support vehicles (e.g., UAZ-69, UAZ-469) and tanks (e.g., T-72, T-80). Identify SS-24 launch triplet at a known location. Distinguish between the raised helicopter deck on a KRESTA II (CG) and the helicopter deck with main deck on a KRESTA I (CG).	Detect wing-mounted stores (i.e., ASM, bombs) protruding from the wings of large bombers (e.g., B-52, BEAR, Badger). Identify individual thermally active engine vents atop diesel locomotives. Distinguish between a FIX FOUR and FIX SIX site based on antenna pattern and spacing. Distinguish between thermally active tanks and APCs. Distinguish between a 2-rail and 4-rail SA-3 launcher. Identify missile tube hatches on submarines.	Detect summer woodland camouflage netting large enough to cover a tank against a scattered tree background. Detect foot trail through tall grass. Detect navigational channel markers and mooring buoys in water. Detect livestock in open but fenced areas. Detect recently installed minefields in ground forces deployment area based on a regular pattern of disturbed earth or vegetation. Count individual dwellings in subsistence housing areas (e.g., squatter settlements, refugee camps).

8 NIIRS 7 [0.20 - 0.40 m GRD]

Visible NIIRS	Radar NIIRS	Infrared NIIRS	Multispectral NIIRS
Identify fitments and fairings on a fighter-sized aircraft (e.g., FULCRUM, FOXHOUND). Identify ports, ladders, vents on electronics vans. Detect the mount for antitank guided missiles (e.g., SAGGER on BMP-1). Detect details of the silo door hinging mechanism on Type III-F, III-G, and 11-H launch silos and Type III-X launch control silos. Identify the individual tubes of the RBU on KIROV-, KARA-, KRIVAK-class vessels. Identify individual rail ties.	Identify small fighter aircraft by type (e.g., FISHBED, FITTER, FLOGGER). Distinguish between electronics van trailers (without tractor) and van trucks in garrison. Distinguish, by size and configuration, between a turreted, tracked APC and a medium tank (e.g., BMP-1/2 vs. T-64). Detect a missile on the launcher in an SA-2 launch revetment. Distinguish between bow mounted missile system on KRIVAK I/II and bow mounted gun turret on KRIVAK III. Detect road/street lamps in an urban residential area or military complex.	Distinguish between ground attack and interceptor versions of the MIG-23 FLOGGER based on the shape of the nose. Identify automobiles as sedans or station wagons. Identify antenna dishes (less than 3 meters in diameter) on a radio relay tower. Identify the missile transfer crane on a SA-6 transloader. Distinguish between an SA-2/CSA-1 and a SCUD-B missile transporter when missiles are not loaded. Detect mooring cleats or bollards on piers.	Distinguish between tanks and three-dimensional tank decoys. Identify individual 55-gallon drums. Detect small marine mammals (e.g., harbor seals) on sand/gravel beaches. Detect underwater pier footings. Detect foxholes by ring of spoil outlining hole. Distinguish individual rows of truck crops.

9 NIIRS 8 [0.10 - 0.20 m GRD]

Visible NIIRS	Radar NIIRS	Infrared NIIRS	Multispectral NIIRS
Identify the rivet lines on bomber aircraft. Detect horn-shaped and W-shaped antennas mounted atop BACKTRAP and BACKNET radars. Identify a hand-held SAM (e.g., SA-7/14, REDEYE, STINGER). Identify joints and welds on a TEL or TELAR. Detect winch cables on deck-mounted cranes. Identify windshield wipers on a vehicle.	Distinguish the fuselage difference between a HIND and a HIP helicopter. Distinguish between the FAN SONG E missile control radar and the FAN SONG F based on the number of parabolic dish antennas (three vs. one). Identify the SA-6 transloader when other SA-6 equipment is present. Distinguish limber hole shape and configuration differences between DELTA I and YANKEE I (SSBNs). Identify the dome/vent pattern on rail tank cars.	Identify the RAM airscoop on the dorsal spine of FISHBED J/K/L. Identify limbs (e.g., arms, legs) on an individual. Identify individual horizontal and vertical ribs on a radar antenna. Detect closed hatches on a tank turret. Distinguish between fuel and oxidizer Multi-System Propellant Transporters based on twin or single fitments on the front of the semi-trailer. Identify individual posts and rails on deck edge life rails.	

10 NIIRS 9 [less than 0.10 m GRD]

Visible NIIRS	Radar NIIRS	Infrared NIIRS	Multispectral NIIRS
Differentiate cross-slot from single slot heads on aircraft skin panel fasteners. Identify small light-toned ceramic insulators that connect wires of an antenna canopy. Identify vehicle registration numbers (VRN) on trucks. Identify screws and bolts on missile components. Identify braid of ropes (I to 3 inches in diameter). Detect individual spikes in railroad ties.	Detect major modifications to large aircraft (e.g., fairings, pods, winglets). Identify the shape of antennas on EW/GCI/ACQ radars as parabolic, parabolic with clipped corners, or rectangular. Identify, based on presence or absence of turret, size of aun tube, and chassis configuration, wheeled or tracked APCs by type (e.g., BTR-80, BMP- 1/2, MT-LB, Ml 13). Identify the forward fins on an SA-3 missile. Identify individual hatch covers of vertically launched SA-N-6 surface-to-air system. Identify trucks as cab-over-engine or engine-in-front.	Identify access panels on fighter aircraft. Identify cargo (e.g., shovels, rakes, ladders) in an open-bed, light-duty truck. Distinguish between BIRDS EYE and BELL LACE antennas based on the presence or absence of small dipole elements. Identify turret hatch hinges on armored vehicles. Identify individual command guidance strip antennas on an SA-2/CSA-1 missile. Identify individual rungs on bulkhead mounted ladders.	

Appendix 2 DERIVATION OF THE BOHR ATOM

The existence of line spectra can be explained by means of the first 'quantum' model of the atom, developed by Bohr in 1913. Although the Bohr model of the hydrogen atom was eventually replaced, it yields the correct values for the observed spectral lines, and gives a substantial insight into the structure of atoms in general. The following derivation has the objective of obtaining the energy levels of the Bohr atom.

It is an experimental fact that the force F between two point charges q_1 and q_2 separated by a distance r is given by:

$$F = \frac{q_1 q_2}{4\pi \varepsilon_0 r^2} \qquad \text{(Eqn. A4-1)}$$

where $\dfrac{1}{4\pi \varepsilon_o} = 8.99 \times 10^9 \left[\dfrac{N\ m^2}{C^2}\right]$ and q_1 and q_2 are in units of Coulombs. The distance, r, is in meters of course. The potential energy associated with these two charges is:

$$U = \frac{q_1 q_2}{4\pi \varepsilon_o r} \qquad \text{(Eqn. A4-2)}$$

taking $U\ (r = \infty) = 0$. Note that the charges may be positive or negative.

For a single electron atom, we take the charge of the nucleus, q_1, to be +Ze, where Z is the atomic number of the atom (the number of protons in the nucleus). Z equals 1 for hydrogen. The charge of the electron, q_2, is -e. Substituting these values into (A1-1) and (A1-2) above we obtain:

$$F = - \frac{Ze^2}{4\pi \varepsilon_0 r^2} \qquad \text{(Eqn. A4-3)}$$

and,

$$U = - \frac{Ze^2}{4\pi \varepsilon_0 r} \qquad \text{(Eqn. A4-4)}$$

The minus sign on the force term means the force is 'inward', or attractive. A negative potential energy means the electron is in a potential 'well'. Given this expression for the potential energy, we need a similar expression for kinetic energy.

Let us assume that the electron moves in a circular orbit around the nucleus. Then Newton's second Law (F=ma) (here: setting the Coulomb force equal to the centripetal force) can be written as:

$$\frac{-Ze^2}{4\pi \varepsilon_0 r^2} = -mv^2 / r \qquad \text{(Eqn. A4-5)}$$

The kinetic energy, T, is then easily obtained:

$$T = \tfrac{1}{2} mv^2 = \frac{1}{2} \frac{Ze^2}{4\pi \, \varepsilon_0 \, r} \qquad \text{(Eqn. A4-6)}$$

The total energy of the electron, E, therefore is obtained:

$$E = U + T = -\frac{Ze^2}{4\pi \, \varepsilon_0 \, r} + \frac{1}{2}\left(\frac{Ze^2}{4\pi \, \varepsilon_0}\right)\frac{1}{r} = -\frac{1}{2}\left(\frac{Ze^2}{4\pi \, \varepsilon_0}\right)\frac{1}{r} \qquad \text{(Eqn. A4-7)}$$

The total energy is negative - a general characteristic of bound orbits. This equation also tells us that if we know the radius of the orbit (r) we ca n calculate the energy E of the electron. Bohr now introduced the first of his two postulates, namely that the only allowed orbits were those for which the angular momentum, L, was given by:

$$L = mvr = n\hbar \qquad\qquad\qquad\qquad\qquad\qquad\qquad \text{(Eqn. A4-8)}$$

where:
m = electron mass
v = velocity
r = radius of the orbit
n = an integer (1,2,3,..)
and

$$\hbar = \frac{h}{2\pi} = 1.054 \times 10^{-34} \; [\text{Joule - seconds}]$$

$$= 0.658 \times 10^{-15} \; [\text{eV - seconds}]$$

where "h" is simply Planck's constant, as before. This is sufficient to give us:

$$v_n = \frac{n\hbar}{mr_n} \qquad\qquad \text{(Eqn. A4-9)}$$

for the velocity of the electron in its orbit. Note that there is an index n, for the different allowed orbits. It follows that:

$$\frac{m v_n^2}{r_n} = \frac{Ze^2}{4\pi \, \varepsilon_0 \, r_n^2} = \frac{mn^2 \, \hbar^2}{m^2 \, r_n^3} \qquad\qquad \text{(Eqn. A4-10)}$$

Upon solving for the radius of the orbit (r_n), we get:

$$r_n = \frac{n^2 \, \hbar^2}{m} \times \frac{4\pi \, \varepsilon_o}{Ze^2} = n^2 \left[\frac{4\pi \, \varepsilon_o \, \hbar^2}{Zme^2} \right] \qquad\qquad \text{(Eqn. A4-11)}$$

$$r_n \, [\text{meters}] = n^2 \times \; 0.528 \times 10^{-10} \; / Z.$$

This only works for one electron atoms (H and He$^+$ as a practical matter), but within that restriction, it works fairly well. For hydrogen (Z=1) we get the Bohr radius, $r_1 = 0.528 \times 10^{-10}$ meters as the radius of the smallest orbit.

Substituting the expression for r_n into Eqn. A4-7, we obtain for the energy:

$$E = -\frac{1}{2}\frac{Ze^2}{4\pi\varepsilon_0} \times \frac{1}{n^2}\frac{Zme^2}{4\pi\varepsilon_0\hbar^2}$$

or
$$E = -\frac{1}{2}\left(\frac{Z\,e^2}{4\pi\,\varepsilon_0\,\hbar}\right)^2\frac{m}{n^2} = Z^2\frac{E_1}{n^2} \qquad \text{(Eqn. A4-12)}$$

where
$$E_1 = -\frac{me^4}{32\pi^2\varepsilon_0^2\,\hbar^2} = -13.58\text{ eV}$$

is the energy of the electron in its lowest or "ground" state in the hydrogen atom.

This page intentionally left blank

Appendix 3 USEFUL EQUATIONS

EM Waves

$\lambda f = c; \quad E = hf; \quad \lambda = \dfrac{hc}{\Delta E}; \quad c = 2.998 \times 10^8; \quad 1 \text{ eV} = 1.602 \times 10^{-19} \text{ Joules}$

$h = \text{Planck's Constant} = \begin{cases} 6.626 \times 10^{-34} & \text{Joule - seconds} \\ 4.136 \times 10^{-15} & \text{eV - seconds} \end{cases}$

$\Delta E(\text{eV}) = \dfrac{1.24 \times 10^{-6}}{l\,(m)} = \dfrac{1.24}{l\,(\boldsymbol{m}m)}$

Bohr Atom:

$r_n\,[\text{meters}] = n^2 \times 0.528 \times 10^{-10} / Z.$

$E_n = -\dfrac{1}{2}\left[\dfrac{Z\,e^2}{4\boldsymbol{p}\,\boldsymbol{e}_0\,\hbar}\right]^2 \dfrac{m}{n^2} = Z^2 \dfrac{E_1}{n^2}; \qquad E_1 = -\dfrac{me^4}{32\pi^2\,\varepsilon_0^2\,\hbar^2} = -13.58 \text{ eV};$

$number \propto e^{-\frac{\text{Bandgap Energy}}{\text{Thermal Energy (kT)}}}$

Black Body Radiation

$c = 3\times10^8\,\tfrac{m}{s}; \quad h = 6.626\times10^{-34}\,joule - s; \quad k = 1.38\times10^{-23}\,\tfrac{Joule}{Kelvin}$

$Radiance = L = \dfrac{2\,hc^2}{l^5}\dfrac{1}{e^{\frac{hc}{l\,kT}} - 1}$

Stefan Boltzmann Law: $\quad R = \boldsymbol{s}\,\boldsymbol{e}\,T^4\,\left[\text{Watts}\big/\text{m}^2\right]$

$\varepsilon = \text{Emissivity}; \quad \boldsymbol{S} = 5.67 \times 10^{-8}\,\left[\text{W}\big/\text{m}^2\,\text{K}^4\right]; \quad T = \text{Temperature (K)}$

Wien's Law: $\quad l_{\max} = a\big/T \qquad a = 2.898\times10^{-3}\,[\text{m K}]$

PH3052   07/09/00

Optics
$$\frac{1}{f} = \frac{1}{i} + \frac{1}{o}; \quad f/\# = \frac{\text{Focal Length}}{\text{Diameter}}$$

Rayleigh Criteria: $\text{GSD} = \Delta q \bullet \text{altitude} = \dfrac{\lambda}{\text{diameter}} \bullet \text{altitude}$

Orbital Mechanics

$$\vec{\mathbf{F}} = -\text{G}\frac{\text{m}_1\text{m}_2}{\text{r}^2}\hat{\mathbf{r}}; \quad F = g_o m \left|\frac{R_{Earth}}{r}\right|^2 \quad \text{G} = 6.67 \times 10^{-11} \ \text{N}\frac{\text{m}^2}{\text{kg}^2}; \quad g_o = G\frac{m_{Earth}}{R_{Earth}^2} = 9.8 \ \frac{\text{m}}{\text{s}^2}$$

$\text{R}_{\text{earth}} = 6.38 \times 10^6$ m, $\text{m}_{\text{earth}} = 5.9736 \times 10^{24}$ kg.

$$\text{v} = w\,r; \quad w = 2p\,\text{f}; \quad t = \frac{1}{f} = \frac{2p}{w}$$

$$F_{centripetal} = m\frac{\text{v}^2}{r} = mw^2 r$$

circular motion: $\text{v} = \sqrt{\dfrac{g_o}{r}} R_{Earth}$

Ellipses: $\dfrac{x^2}{a^2} + \dfrac{y^2}{b^2} = 1; \quad e = \dfrac{\sqrt{a^2-b^2}}{a} \quad \text{or} \quad e = \sqrt{1-\dfrac{b^2}{a^2}}$

Distance from center to focus is $c = e\,a = \sqrt{a^2-b^2}$

Elliptical orbit: $\text{v} = \sqrt{\text{GM}\left[\dfrac{2}{\text{r}} - \dfrac{1}{\text{a}}\right]}$

$$t^2 = \frac{4p^2}{g_o R_{Earth}^2} r^3 = \frac{4p^2}{\text{M}_{\text{earth}}\text{G}} r^3$$

Radar Resolution:

Rayleigh Criteria: $\text{GSD} = \Delta q \bullet \text{altitude} = \dfrac{\lambda}{\text{diameter}} \bullet \text{altitude}$

Range Resolution: Scan Mode Sar: $\text{GSD} = \dfrac{L}{2}$

©Richard Christopher Olsen, Naval Postgraduate School